GROWTH OF NOVEL WIDE BANDGAP ROOM TEMPERATURE FERROMAGNETIC SEMICONDUCTOR FOR SPINTRONIC APPLICATIONS

A Dissertation
Presented to
The Academic Faculty

by

Shalini Gupta

In Partial Fulfillment
of the Requirements for the Degree
Doctor of Philosophy in the
School of Electrical and Computer Engineering

Georgia Institute of Technology
May 2009

GROWTH OF NOVEL WIDE BANDGAP ROOM TEMPERATURE FERROMAGNETIC SEMICONDUCTOR FOR SPINTRONIC APPLICATIONS

Approved by:

Dr. Ian Ferguson, Advisor
School of Electrical and Computer Engineering
Georgia Institute of Technology

Dr. David Citrin
School of Electrical and Computer Engineering
Georgia Institute of Technology

Dr. Ali Adibi
School of Electrical and Computer Engineering
Georgia Institute of Technology

Dr. Justin Schwartz
Department of Mechanical Engineering
Florida State University

Dr. Shyh-Chiang Shen
School of Electrical and Computer Engineering
Georgia Institute of Technology

Date Approved: March 6, 2009

Dedicated to my parents
for their unconditional love and support
and for always believing in me

ACKNOWLEDGEMENTS

Firstly, I would like to thank my advisor Ian Ferguson for his support and guidance throughout my Ph.D. career. I would like to thank the current and past members of my research group namely Ali Asghar, James Bain, Ming Pan, Adam Payne, Zaili Fang, Will Fenwick, Olivier Hamard, Yong Huang, Muhammad Jamil, Balakrishnam Jampana, Omkar Jani, Shalini Kandoor, Hun Kang, Nola Li, Enno Malguth, Dhariya Mehta, Andrew Melton, Jill Morris, David Nicol, Eun-Hyun Park, Petkov Petko, My Tran, June O Song, Peter Speirs, Martin Strassburg, Shenjie Wang, Vincent Woods, Tianming Xu, Hongbo Yu, and Tahir Zaidi. I would also like to thank Dr. Nikolaus Dietz, Dr. Z. C. Feng, Dr. Samuel Graham, Dr. Axel Hoffmann, Dr. Justin Schwartz, Dr. John Zhang, and their students for helping with the measurements for this project. I am grateful to all my past teachers and professors for their guidance and support.

I thank the National Science Foundation and the Air Force Office of Scientific Research for funding this project.

I thank all my friends for supporting me through the course of my Ph.D. Finally, I would like to thank my parents and my sister Jyoti for their unconditional love and support.

TABLE OF CONTENTS

LIST OF TABLES

LIST OF FIGURES

LIST OF SYMBOLS AND ABBREVIATIONS

Cr	Chromium
Eu	Europium
Fe	Iron
Gd	Gadolinium
Mg	Magnesium
Mn	Manganese
P_{spin}	Spin polarization
Si	Silicon
n↑	Spin-up states
n↓	Spin-down states
σ^{+}	Right polarized light
σ^{-}	Left polarized light
T_C	Curie Temperature
AFM	Atomic Force Microscopy
AlN	Aluminum Nitride
CB	Conduction Band
CBM	Conduction Band Minimum
DMNS	Dilute Magnetic Nanostructures
DMQDs	Dilute Magnetic Quantum Dots
DMS	Dilute Magnetic Semiconductors
EDS	Energy Dispersive X-ray Spectroscopy
FC	Field Cooled
FET	Field Effect Transistor

FM	Ferromagnetism
F-vdM	Frank-van der Merwe
FWHM	Full Width Half Maximum
GaAs	Gallium Arsenide
GaN	Gallium Nitride
HEMT	High Electron Mobility Transistor
HH	Heavy Hole
HR-XRD	High Resolution X-ray Diffraction
InAs	Indium Arsenide
InN	Indium Nitride
KKR-CPA	Korringa Kohn Rostoker Coherent Potential Approximations
LED	Light Emitting Diode
LH	Light Hole
LDA	Local Density Approximation
LT	Low Temperature
MBE	Molecular Beam Epitaxy
MOCVD	Metal Organic Chemical Vapor Deposition
NN	Nearest Neighbor
NNN	Next Nearest Neighbor
PL	Photoluminescence
PLD	Pulsed Layer Deposition
QD	Quantum Dot
QW	Quantum Well
RE	Rare Earth
RKKY	Ruderman-Kittel-Kasuya-Yosida

RT	Room Temperature
SEM	Scanning Electron Microscope
SIMS	Secondary Ion Mass Spectrometer
SK	Stranski-Krastanow
SO	Spin-Orbit
SQUID	Superconducting Quantum Interference Device
TM	Transition Metal
VB	Valence Band
VBM	Valence Band Maximum
V-W	Volmer-Weber
VP	Vapor Pressure
VSM	Vibrating Sample Magnetometer
ZFC	Zero Field Cooled
ZnO	Zinc Oxide
ZnSe	Zinc Selenide

SUMMARY

This work presents the development of a GaN-based dilute magnetic semiconductor (DMS) by metal organic chemical vapor deposition (MOCVD) that is ferromagnetic at room temperature (RT), electrically conductive, and whose magnetic properties can be tuned by doping the semiconductor n- or p-type. GaN is an excellent candidate for RT spintronic applications, as it has been theoretically predicted to have a Curie temperature (T_C) greater than RT. Additionally, the development of a GaN-based DMS is significant as it can be incorporated into optoelectronic devices such as light emitting diodes (LEDs) to create spin-LEDs, which provide a good platform for analyzing spin transport in heterostructures. This work employed a series of transition metals by a single epitaxial growth technique at the thin film and the nanostructure level with the aim of determining the magnetic mechanism in these materials. Additionally, this work presents the first report on gadolinium doping of GaN by MOCVD and also provides the first report on p-$Ga_{1-x}Gd_xN$.

The transition metal (TM) series, namely chromium, manganese, and iron, was investigated in this work in order to analyze the effect of the TM acceptor level and the number of unpaired spins on the magnetic and material properties of the semiconductor. This research presents a series of TM-dopants by a single growth technique, which eliminates the ambiguity present when comparing results from different growth techniques. Structural characterization revealed that single phase and strain free $Ga_{1-x}TM_xN$ films were obtained. Optical measurements revealed that Mn is a deep acceptor in GaN, while Hall measurements showed that these $Ga_{1-x}TM_xN$ films were semi-insulating, making carrier mediated exchange unlikely. Hysteresis curves were

obtained at RT for all the $Ga_{1-x}TM_xN$ films with the maximum saturation magnetization of 16 emu/cm^3 obtained for 1.5 % Mn doping in GaN. Furthermore, the effect of n- and p-doping on the magnetic properties was analyzed and in-depth magnetic measurements revealed that there is a high tendency for TMs to cluster in GaN and the observed magnetization is due to magnetic clusters rather than the double exchange mechanism previously proposed by experimentalists and theorists.

The TM elements were incorporated into GaN nanostructures to obtain a better understanding of the impact of size on the magnetic properties of the semiconductor. It was determined that TMs enhance nucleation and provide additional support for the TM clustering seen in thin films. Additionally, a clear superparamagnetic behavior is observed for the $Ga_{1-x}TM_xN$ nanostructures, which is consistent with the thin film observations.

Gadolinium is the only rare earth element with both unfilled d and f orbitals and thus has a very high atomic magnetic moment and provides an alternate route for creating a RT DMS. Molecular beam epitaxy growth studies have shown that Gd-doped GaN results in an extremely large magnetic moment at room temperature. However, the mechanism behind the large magnetic moment is not clear. Despite the observation of this large magnetic moment, no published reports exist on Gd doping of GaN by MOCVD. This work presents the first report of Gd (0-4 %) doping of GaN by MOCVD and presents the impact of n- and p-dopants on its magnetic and material properties. Gadolinium incorporation in GaN resulted in a large magnetization strength of 20 emu/cm^3 and the material displays n-type conductivity. Silicon was introduced to $Ga_{0.98}Gd_{0.02}N$ as an n-type dopant, which greatly enhanced the magnetization to

110 emu/cm^3 upon doping with 10^{18} cm^{-3} silicon atoms. Doping the Gadolinium-based DMS with 10^{19} cm^{-3} magnesium atoms (p-type dopant) increased the saturation magnetization to 500 emu/cm^3. All the $Ga_{1-x}Gd_xN$ films including the n- and p-type films were conductive and are suitable for integration into device structures. The ferromagnetic properties of $Ga_{1-x}Gd_xN$ are attributed to Ruderman-Kittel-Kasuya-Yosida (RKKY) indirect exchange interaction where the interactions between the magnetic ions are facilitated by the intrinsic donors (nitrogen vacancies) that are present in the material. Furthermore, the addition of electrons and holes results in spin-splitting of the conduction band and valence band respectively and the ferromagnetic phase is stabilized through s-f and p-d coupling. It has been experimentally shown that holes are more effective in stabilizing the ferromagnetic phase in $Ga_{1-x}Gd_xN$ providing an experimental answer to the theoretical debate over which carrier better facilitates ferromagnetic exchange interactions.

This work has provided many novel, experimentally based insights into GaN-based DMS, resulting in the development of semiconducting materials that show room-temperature ferromagnetism. These materials pave the way for development of multifunctional microelectronic devices that integrate electrical, optical, and magnetic properties. The development of spintronic devices by employing such a DMS can result in devices that provide higher information storage densities, higher speeds, and lower power consumption than current technology allows.

CHAPTER 1

INTRODUCTION

1.1. Introduction

The rapid advancement of microelectronic technology has created demand for compact, high performance devices that offer multiple functionalities. Moore's law has been an excellent predictor of integrated circuit density and performance since the 1970s. The result of decades of transistor size reduction is that quantum effects play a significant role in modern device operation. These effects make it very difficult for electronic device developers to continue the exponential performance improvements predicted by Moore's law. New semiconductor materials may enable next-generation electronic devices that exploit both the spin and charge of an electron for data processing, storage, and transfer. This field of study which is based on the manipulation of spin degree of freedom in solid state systems is known as "Spintronics" (SPIN TRansport electrONICS) [1]. Developments in this field could lead to the integration of electrical, optical, and magnetic properties thereby resulting in the creation of novel multifunctional devices. Spintronics can result in devices that have reduced power consumption and devices that result in faster data manipulation. Some examples of future spintronic devices include integrated chip-based magnetic memories, reconfigurable logic elements, polarized light emitting diodes (LEDs), and building blocks for quantum computing, communication and cryptography [2, 3].

The field of spintronics received great impetus by the discovery of the giant magneto resistance (GMR) effect in 1998 by Albert Fert and Peter Grünberg who received the

2007 Nobel Prize in physics for this work. A GMR is a layered structure consisting of a free magnetic layer and a pinned ferromagnetic layer separated by a non-magnetic spacer material (Figure 1.1) [1]. The pinning of the ferromagnetic layer is obtained by coupling it with an antiferromagnetic material. The resistance of the structure is lowest when the magnetic moments in the ferromagnetic layers are aligned and highest (giant magnetoresistance) when they are anti-aligned. Nearly all modern hard disk drives incorporate a GMR-based read head which has significantly increased the storage capacity of hard drives and resulted in the creation of a billion dollar industry [1]. The progress in GMR technology has been extrapolated to other device such as nonvolatile magnetic random access memory (MRAM) devices which are now commercially available.

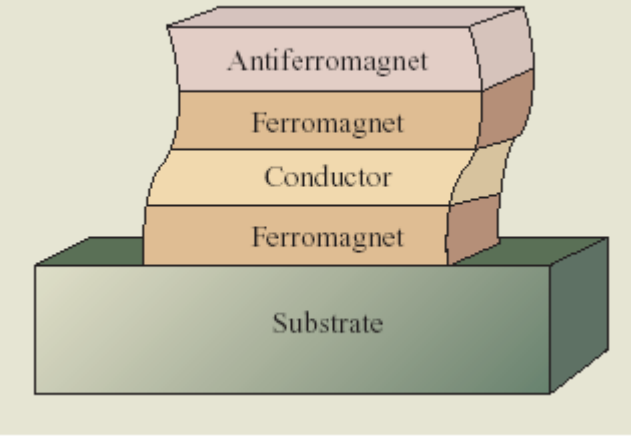

Figure 1.1: Schematic of a GMR structure [1].

In the field of spintronics there are two primary domains of interest. The first area focuses on improving existing GMR technology by developing new materials with large population of oriented spins or on improving device design to provide better spin filtering. The second area looks to develop new materials for spin injection, spin

detection, and for investigating spin transport. Integrating these new materials into existing microelectronics devices would make them more efficient and enable additional functionality. This research is focused on the latter of the two areas. Thus, this research will focus on developing a room temperature ferromagnetic semiconductor that can be potentially used to develop spintronic devices. Furthermore, the magnetic semiconductor developed will also be used to develop a spin-LED to analyze the spin transport properties and the magnetic semiconductor's performance in a device environment. In a spin-LED, polarized carriers from the magnetic semiconductor recombine with unpolarized carriers to produce circularly polarized light. By analyzing the degree of polarization of the emitted light, the spin injection efficiency can be determined.

1.2. Magnetic Semiconductors

There are two routes to develop a magnetic semiconductor. The first is to deposit a ferromagnetic metal onto a semiconductor with the aim of injecting spin polarized carriers. The second is to introduce magnetic ions into semiconductors which make the semiconductors ferromagnetic through various exchange mechanisms. These two approaches are described below.

1.2.1. Ferromagnetic Metals

The easiest way to make a magnetic semiconductor is to deposit a ferromagnetic metal onto a semiconductor and to use it as a spin injector. Ferromagnetic metals have been used in devices as Ohmic, Schottky, or tunneling contacts to create spin injection in LEDs. However, these metal contacts resulted in scattering of the spins at the metal-semiconductor interface due to conductivity mismatch (Figure 1.2) [4]. Furthermore, the spin polarization decays rapidly even just a few nanometers into the semiconductor.

Although ferromagnet/tunnel-barrier/semiconductor spin-LED structures have been grown to counter this problem, the spin injection efficiency of these devices is fairly low (~30 %) making them not viable for device applications [5-8].

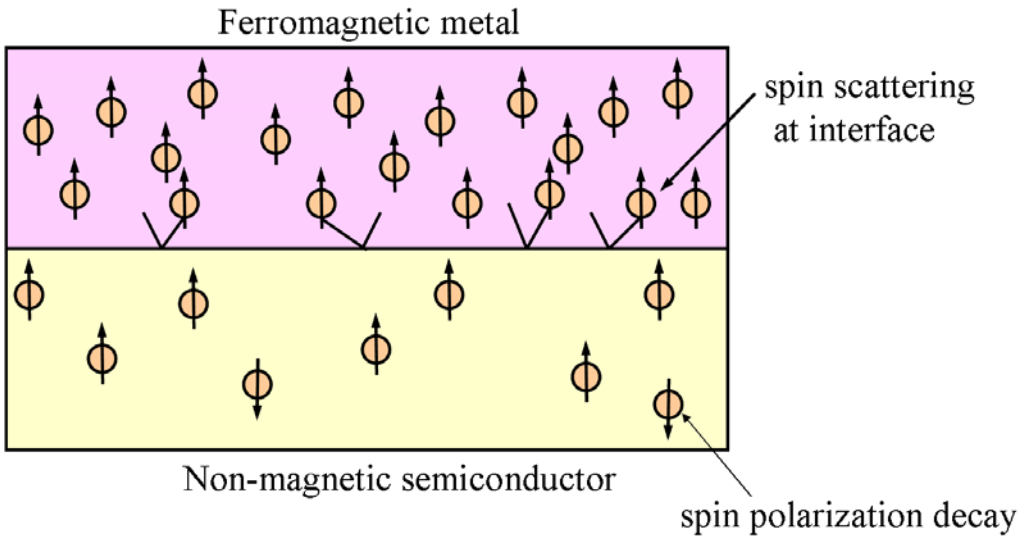

Figure 1.2: Spin injection from a ferromagnetic metal into a non-magnetic semiconductor.

A classical prototype for a spin based microelectronic device is the spin-field effect transistor (spin-FET), which was proposed by Datta and Das in 1989 (Figure 1.3) [9, 10]. In the Datta-Das device, a structure made from InAlAs and InGaAs provides a channel for two-dimensional electron transport between two ferromagnetic electrodes, one of which acts as an emitter and the other as a collector. This device allows for the injection of spin polarized current from the ferromagnetic emitter into the channel. The gate voltage applies an electric field that precesses the spin of the electrons through Rashba spin-orbit interactions. The electrons pass on to the collector if the spins are aligned and are blocked if they are antiparallel. The degree of spin precession is controlled by the gate voltage, which results in control over the spin alignment at the collector end and thus

controls the emitter to collector current, thereby realizing the basic operation of the transistor. Spin-FETs are able to turn off at lower voltages and provide for greater operation speeds. However, such a device has not yet been realized and may not be feasible due to the aforementioned problems of spin scattering between metals and semiconductors that result in low spin injection efficiencies.

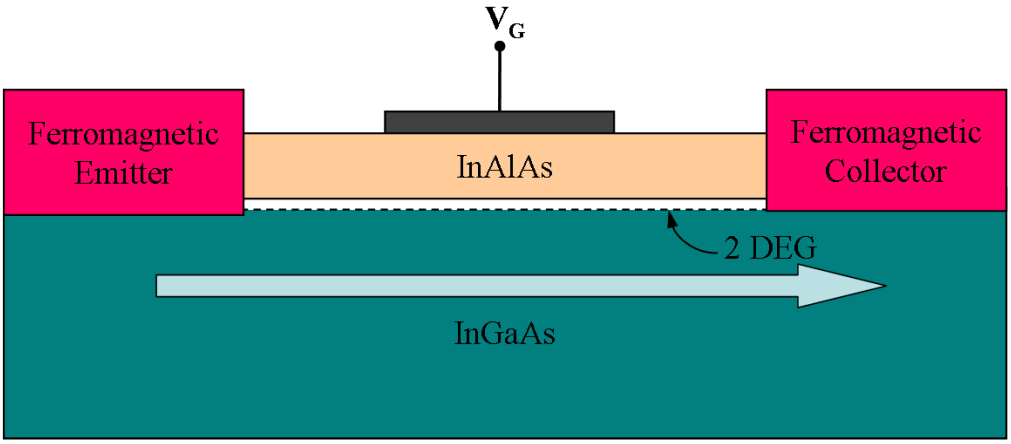

Figure 1.3: Schematic of the Datta-Das spin-FET [9].

1.2.2. Ferromagnetic Semiconductors

Popular semiconductors such as Si and GaAs do not contain magnetic ions and are non magnetic in nature. The Lande-g factor for these semiconductors is fairly small meaning that a large magnetic field would need to be applied to separate the energy levels of the two different spin orientations [11]. Ferromagnetism and semiconducting properties do coexist in magnetic semiconductors such as europiums, chalcogenides and semiconducting spinels. In 1960's, research was conducted on the growth of these compounds, however, these materials did not result in usable devices because of the difficulty in growing high quality thin films and heterostructures [12]. These materials

had Curie temperatures (T_C) in the range of 130-150 K, making them unfeasible for practical devices [11].

Thus, there exists a need for a new class of materials that is easy to fabricate, is compatible with existing growth and device technology and above all is ferromagnetic at room temperature. Dilute magnetic semiconductors are promising in this regard and are described next.

1.2.3. Dilute Magnetic Semiconductors

Non-magnetic semiconductors can be turned into magnetic semiconductors by doping them with magnetic ions such as transition metals (TM, e.g. Mn, Fe, Ni, Co, etc.) or rare earth elements (RE, e.g. Gd, Eu, Er, etc.) [13]. The TM and RE have unpaired spins that interact with the host semiconductor through exchange mechanisms and make the semiconductor magnetic [11]. Such semiconductors are called dilute magnetic semiconductors (DMS) as the concentration of the magnetic ions is generally less than 5 % (Figure 1.4).

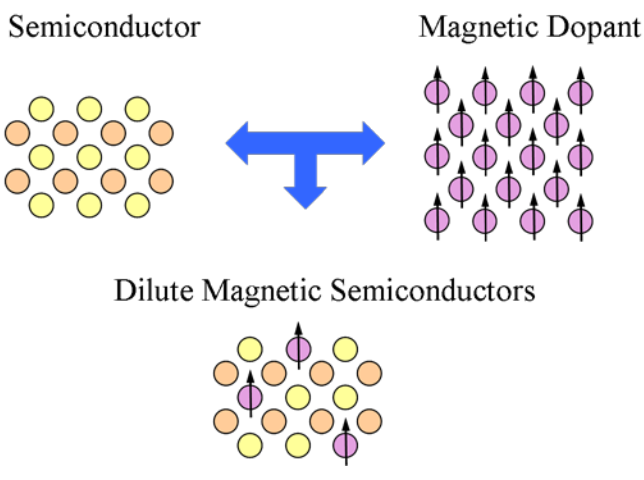

Figure 1.4: Schematic of developing a dilute magnetic semiconductor.

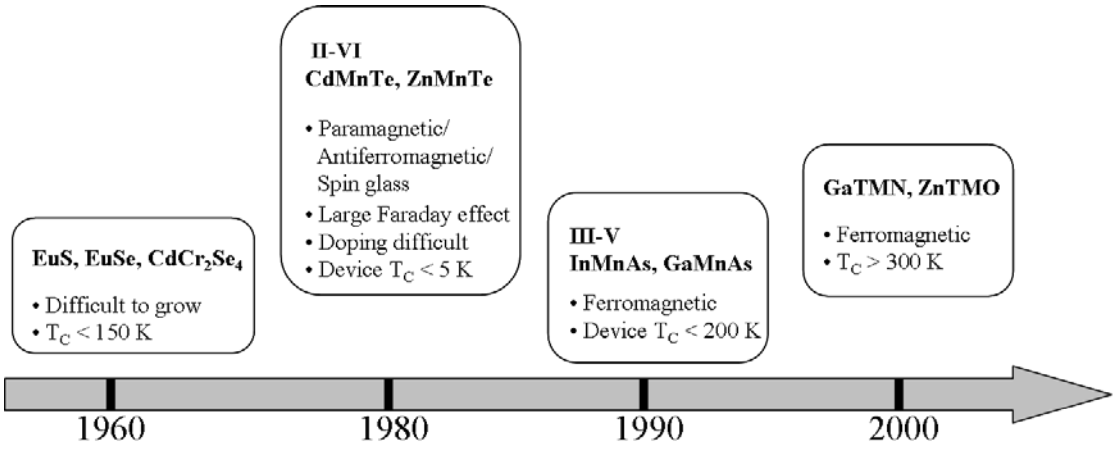

Figure 1.5: Timeline of spintronic material developments.

In the 1980's, significant research effort was applied to developing II-VI DMS such as CdMnTe and ZnMnS; however, these films were found to be paramagnetic, antiferromagnetic or exhibit spin glass behavior [12]. In the 1990's, the research efforts shifted to TM doping of InAs and GaAs, with GaMnAs being the most studied DMS [11]. Significant progress was made in the Arsenides and spin-LEDs were fabricated; however, this material system had a maximum T_C of 173 K making it unfeasible for practical applications [14]. Figure 1.5, displays the progress in spintronic material development over the years [12].

In 2000, theoretical studies by Dietl predicted the T_C for various p-type semiconductors doped with 5 % Mn and a hole concentration of 3.5 x 10^{20} cm^{-3} (Figure 1.6) [15]. It was shown that wide bandgap semiconductors such as GaN and ZnO should have T_C greater than RT due to their smaller lattice constants that allow for greater p-d hybridization and reduced spin-orbit coupling. Although ZnO is a promising candidate for spintronic devices, it is still difficult to obtain good quality ZnO material and p-doping of ZnO is challenging [16]. On the other hand, the GaN-based materials

already have a well established technology base for optoelectronic devices (primarily UV/blue LEDs and lasers) and electronic devices (high power FETs) into which the GaN-based DMS can be incorporated and hence this research will focus on TM and RE doping of GaN.

Since the theoretical prediction by Dietl, GaN has been doped with several TM such as chromium, manganese, and iron by various techniques such as ion implantation, molecular beam epitaxy (MBE), and metal organic chemical vapor deposition (MOCVD). These experiments have resulted in conflicting reports on the T_C of the materials and the mechanism behind the ferromagnetism. For example a wide range of T_C ranging from 10 K to 940 K have been reported for $Ga_{1-x}Mn_xN$ [16].

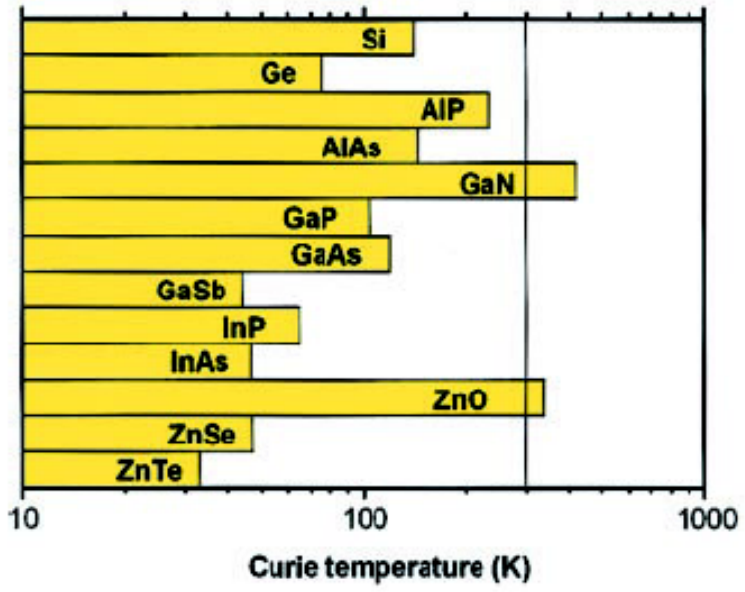

Figure 1.6: Schematic of calculated T_C for various p-type semiconductors doped with 5 % Mn and 3.5 x 10^{20} cm^{-3} holes [15].

Although, RT ferromagnetism has been seen in $Ga_{1-x}TM_xN$ the mechanism associated behind this observation is not clear, with groups reporting double exchange or

clusters as the most likely mechanisms [17, 18]. Furthermore, all the TM doped films obtained show that TM levels lie deep in the GaN bandgap and these films are insulating, which contradicts the original model put forward by Dietl [19, 20]. One of the main reasons behind these ambiguous observations is that different growth techniques have been applied to execute the TM doping in GaN, which has resulted in material of different quality with different structural and electronic defects within the material. One solution to clear the ambiguity is to use a consistent growth technique and to use a series of TMs within the same system to see how the magnetic properties are being changed by increasing and decreasing the number of unpaired electrons that participate in the magnetic interaction with the host semiconductor. This will also allow for investigation of the effect of the TM impurity level on the material and magnetic properties of the semiconductors and provide insight into the magnetic mechanisms that are present in this system.

To this end, this thesis will employ MOCVD growth technique as it is used to produce high quality commercial grade epitaxial films and allows for easy control over the growth process and live in-situ monitoring. Manganese has the highest number of unpaired spins and is, therefore, extremely promising for a high T_C DMS. Chromium and iron will be studied as well to understand the effect of having one less or one more unpaired spin in the d-orbital respectively. Additionally, the most promising TM dopant will be used to develop a spin-LED to obtain a better understanding of the DMS in a device environment and to test its spin transport and lifetime properties

An alternative route to realizing a DMS is to use RE elements that have unpaired 4f electrons. The 4f RE elements can have larger magnetic moments as compared to 3d TMs

as the 4f orbitals are localized and the direct coupling between the 4f ions is weak [21]. For creating a DMS using RE, gadolinium (Gd: $4f^7$, $5d^1$ $6s^2$) is most attractive as it is the only RE ion that has both unfilled d and f orbital that can participate in magnetic coupling through intra-ion 4f-5d exchange interaction followed by inter-ion 5d-5d coupling mediated by charge carriers. Several experiments have been performed to develop ferromagnetic $Ga_{1-x}Gd_xN$ by ion implantation and molecular beam epitaxy (MBE). The most promising report has been on MBE grown $Ga_{1-x}Gd_xN$ films which showed a large magnetic moment of ~4000 μ_B/Gd (as opposed to its atomic moment of 8 μ_B/Gd) for low Gd doping levels of 10^{15} cm^{-3}. These films also had above RT ferromagnetism [22]. Till date, there is not a robust theory to explain the giant magnetic moment observed in these materials, but a phenomenological model has been proposed, which suggests that the long range spin polarization of the GaN matrix is caused by the strain field induced by the introduction of the Gd atom [22]. Despite this large magnetic moment there have been no MOCVD reports on Gd doping in GaN. Thus, this thesis will perform Gd doping of GaN by MOCVD with the aim of developing a high magnetic moment RT ferromagnetic semiconductor. Furthermore, the effects of n- and p-dopants will also be analyzed.

1.2.4. Dilute Magnetic Nanostructures

Quantum dots (QDs) are promising building blocks for quantum computation, spin-based quantum operations and other spintronic applications as the carrier localization allows for more TM interactions, higher T_C, and higher spin relaxation times. Furthermore, the confinement offered by QDs also protects them from thermal perturbations, which make them more suitable for high temperature operations [23].

Dilute magnetic nanostructures (DMNS) are analogous to quantum dots and provide carrier confinement in all three directions [24]. This confinement allows for enhanced magnetic ion interaction, increased thermal stability, and also provide for long spin relaxation times [25]. Dilute magnetic quantum dots (DMQDs) offer the possibility to control band splitting by adjusting the size of the QDs. These QDs can be modified to result in large g factors thereby increasing the degree of spin polarization [2]. The growth of GaN-based nanostructures is still in the development stage and has yet to be optimized. This thesis will also focus on optimizing the growth of GaN-based nanostructures, which will then be doped with TM dopants to develop DMNS. This will enable us to see if the magnetic properties scale with size and if size has an impact on the magnetization mechanism.

1.3. Conclusion

To conclude the overall objective of this thesis is to develop a magnetic semiconductor that retains its ferromagnetic properties at room temperature and can be potentially used to create spintronic devices. Furthermore, this research aims at determining the mechanism associated with origin of ferromagnetism and aims to exercise control over its magnetic properties through n- and p-dopants.

CHAPTER 2

BACKGROUND: GaN, MAGNETISM, AND EXCHANGE PARAMETERS

2.1. Introduction

To obtain a better understanding of ferromagnetism in GaN, it is imperative to understand the basic properties of GaN, the origin of magnetism, and the different exchange mechanisms that make semiconductors ferromagnetic. This chapter will begin with discussing the aforementioned topics and begins with a discussion of the basics of GaN.

2.2. The Nitrides

The III-Nitrides have direct bandgaps with energies ranging from 0.7 eV for InN to 3.4 eV for GaN and up to 6.2 eV for AlN (Figure 2.1) [26]. These compounds are chemically and physically stable compound and thus possess high thermal conductivity and high electron saturation velocity. Due to these properties the III-Nitrides have found applications in light emitting diodes (LEDs), laser diodes, UV-detectors, and high temperature electronic devices such as high electron mobility transistors (HEMT). Furthermore, it is possible to form alloys of Al and In with GaN, allowing the production of emitters of different wavelengths.

Extensive research has been carried out on the Nitrides since 1907 but the lack of a suitable substrate made it difficult to grow high quality material. It was the advancement of growth technologies [27] and the novel concept of using a buffer layer (developed in

1986) to grow the Nitrides on lattice mismatched substrates that finally made good quality growth possible [28, 29]. Furthermore, GaN films are intrinsically n-type due to defects and so it is difficult to p-dope these materials. The development of p-type GaN (produced by thermal annealing, which un-passivated the holes) was another major breakthrough in the developments of the Nitrides [30, 31]. The growth and co-doping details are described in Chapter 3 of this thesis.

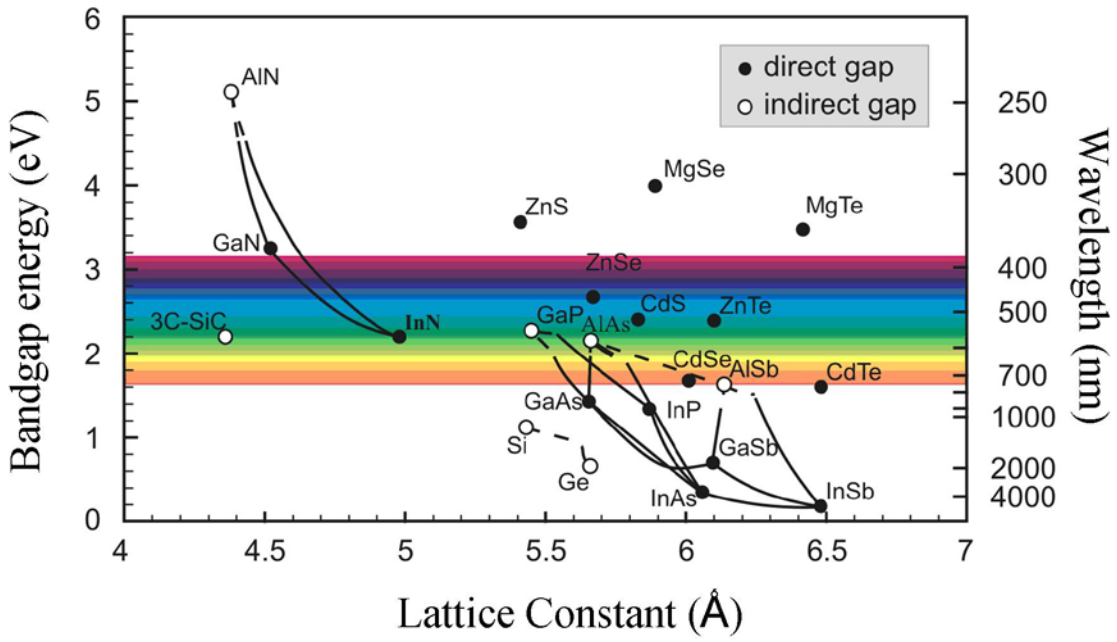

Figure 2.1: Bandgap energy vs. lattice constant for different semiconductors [26].

In 1993, Nakamura et al. were the first to demonstrate a GaN-based blue light emitting diode. They employed MOCVD growth technique to grow p-GaN/n-InGaN/n-GaN double-heterostructure, resulting in light emission at 440 nm with an output power of 125 μW, external quantum efficiency of 0.22 % and a forward current of 20 mA at room temperature. The fabrication of a successful LED, a major breakthrough, provided great impetus to this research area and by 1996 the number of publications in the area

was 100 times higher. Research continues in this area, focusing on the development of more efficient LED's, laser diodes, UV-detectors, solar cells, and spintronic devices. GaN is the most widely studied III-Nitride and promising for RT ferromagnetism. A discussion of its material properties is presented next.

2.2.1. Material Properties of GaN

The III-Nitrides crystallize both in wurtzite and zinc blende structure, but the wurtzite structure is more stable and thus more common [32]. These semiconductors are tetrahedrally coordinated and hence each atomic site has four nearest neighbors. The Bravais lattice of the wurtzite structure is hexagonal and the axis perpendicular to the hexagons is taken to be the c-axis (this is the film growth direction) [33]. The most common growth direction for these semiconductors is (0001) and the wurtzite structure consists of alternating Ga and N pairs stacked in an ABABAB sequence. The wurtzite structure has a $P6_3mc$ space group. The III-Nitrides have a strong ionic character due to the difference in electronegativity of the group III elements and Nitride. The group III-Nitrides lack an inversion plane perpendicular to the c-axis, and hence the crystals surfaces have either a group III element (Al, Ga, or In) polarity (0001) or a N-polarity (000-1) (Figure 2.2). The group III-Nitrides are non-centrosymmetric and thus they are piezoelectric and undergo spontaneous polarization. This results in band bending of the quantum well structure grown by these materials, and has an impact on the electroluminescence wavelength. The spontaneous polarization and piezoelectric effect reduces the number of electron-hole pair recombinations and as a result reduce the efficiency of the device. This intrinsic effect is very useful: charge accumulation occurs

at the AlGaN/GaN interfaces, which is favorable for electronic devices [34]. The material properties are summarized in Table 2.1.

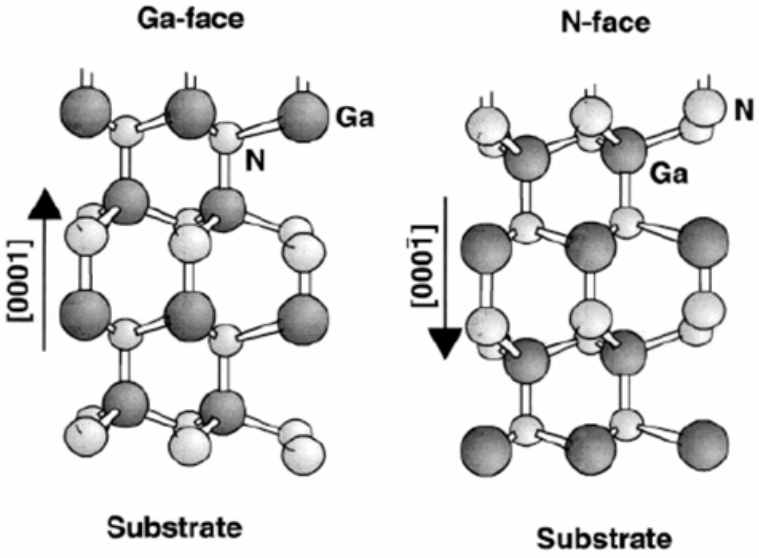

Figure 2.2: Schematic of the different polarities of wurtzite GaN [34].

Table 2.1: Summary of material properties of wurtzite III-Nitrides [32, 33].

Material Property	GaN	AlN	InN
Band-gap energy (300K) [eV]	3.39	6.2	0.7
Lattice constant, a [Å]	3.189	3.112	3.548
Lattice constant, c [Å]	5.185	4.982	5.70
Thermal expansion ($\Delta a/a$) [10^{-6}/K]	5.59	4.2	4
Thermal expansion ($\Delta c/c$) [10^{-6}/K]	3.17	5.3	3
Thermal conductivity (κ) W/cm.K]	1.3	2	0.8
Index of refraction	2.33	2.15	2.80-3.05
Static dielectric constant (ε_0)	8.9	8.5	15
High-ω dielectric constant (ε_∞)	5.35	4.8	8.4
Density [gcm^{-1}]	6.15	3.23	6.81
Electron effective mass (m_e)	$0.20m_0$	$0.40m_0$	$0.11m_0$
Therm. Cond. [$Wcm^{-1}K^{-1}$]	1.3	2.9	1.76
Melting temp. [^oC]	>2000	3000	1100

2.2.2. Band Structure and Allowed Optical Transitions

The conduction point at (Γ_7) has s-character. The top of the valence band is split into three by the crystal field and the spin-orbit coupling into A (Γ_9), B(Γ_7), and C(Γ_7) excitons [33].

As mentioned earlier GaN is a direct bandgap semiconductor with its conduction band minima and valence band maxima centered at Γ point K = 0. The conduction band at Γ_7 has an s-character [33]. The top of the valence band (p-character) is split into three by the crystal field and spin-orbital coupling. The holes and excitons associated with them are denoted as A (Γ_9), B (Γ_7), and C (Γ_7). The A, B and C are designated as heavy hole, light hole, and crystal field splitting respectively. The experimental crystal field splitting has an energy of 22 meV while the spin-orbit splitting energy is 12 meV. The band structure centered at K= 0 for wurtzite GaN is shown in Figure 2.3a. The breaking symmetry diagram with the allowed optical transitions is shown in Figure 2.3b. The influence of the subsequent interactions: spin-orbit (SO), crystal-field (CF), and the magnetic-field (B||c) are shown in the figure from left to right. The six degenerate valence band and two degenerate conduction band states in GaN can clearly be seen. The total angular momentum of the resulting states is given on the right side. The arrows represent the allowed transitions of the optically active excitons [35].

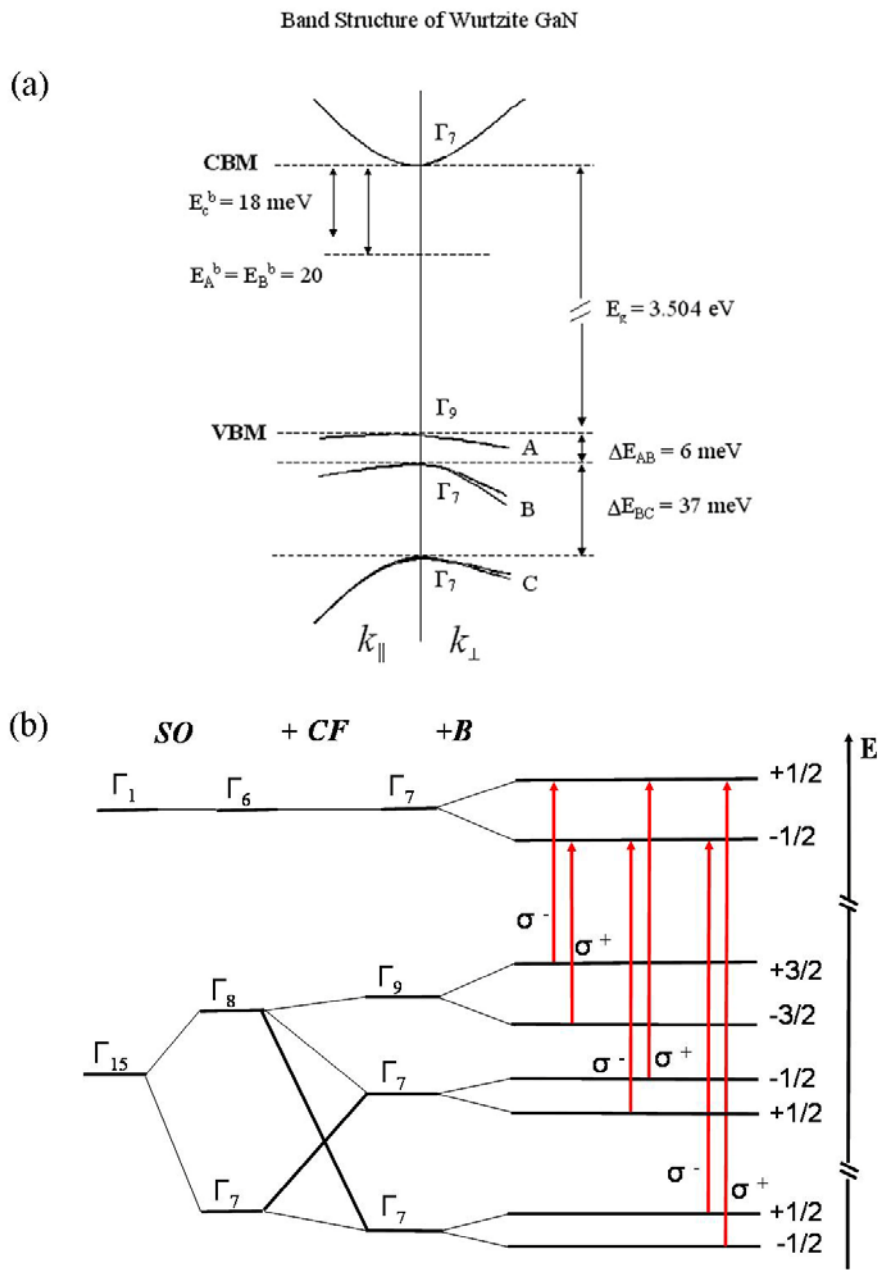

Figure 2.3: (a) Schematic of wurtzite band structure, (b) allowed optical transition in GaN [33, 35].

2.3. Origin of Magnetism

Magnetic fields are created by the movement of charge through space. In atoms, it is the movement of electrons that produce the magnetic fields. The strength of the magnetic

field produced is known as magnetic moment (μ). Magnetic moments are associated with both the spin (s) and orbital (l) angular momentum of each electron. The magnetic moment of an individual electron is the Bohr magneton given by Equation (2.1).

$$\mu_b = \frac{eh}{2\pi m_e} \qquad \text{Equation (2.1)}$$

where

e is the charge of the electron;

h is the Planck constant, and

m_e is the mass of an electron.

The Pauli exclusion principle states that no two electron within an atom can have the same set of quantum numbers. A direct consequence of this is that paired electrons must have opposite spins. Hunds rule states that before any two electrons occupy an orbital in a subshell, other orbitals in the same subshell must first each contain one electron. Also, the electrons filling a subshell will have parallel spin before the shell starts filling up with the opposite spin electrons. This means that the net magnetic moment of a filled electron shell is zero, and thus only partially filled orbitals can contribute towards a net magnetic moment.

The exchange energy removes the degeneracy of the spin-up and spin-down half bands (Figure 2.4) [36], creating an imbalance of spins and thereby allowing for a net magnetic moment. The larger the exchange energy the greater is the energy difference between the two half bands. As can be seen in the figure, electrons fill up the band by occupying the lowest energy states available. In cases of a smaller exchange energy

(Figure 2.4a), there will be some degeneracy of the energy of the available spin states. Typically, this will result in a non integral number of magnetic moments per atom. Where there is a large exchange energy (Figure 2.4b), complete separation between the half-bands will result in an integral number of magnetic moments per atom.

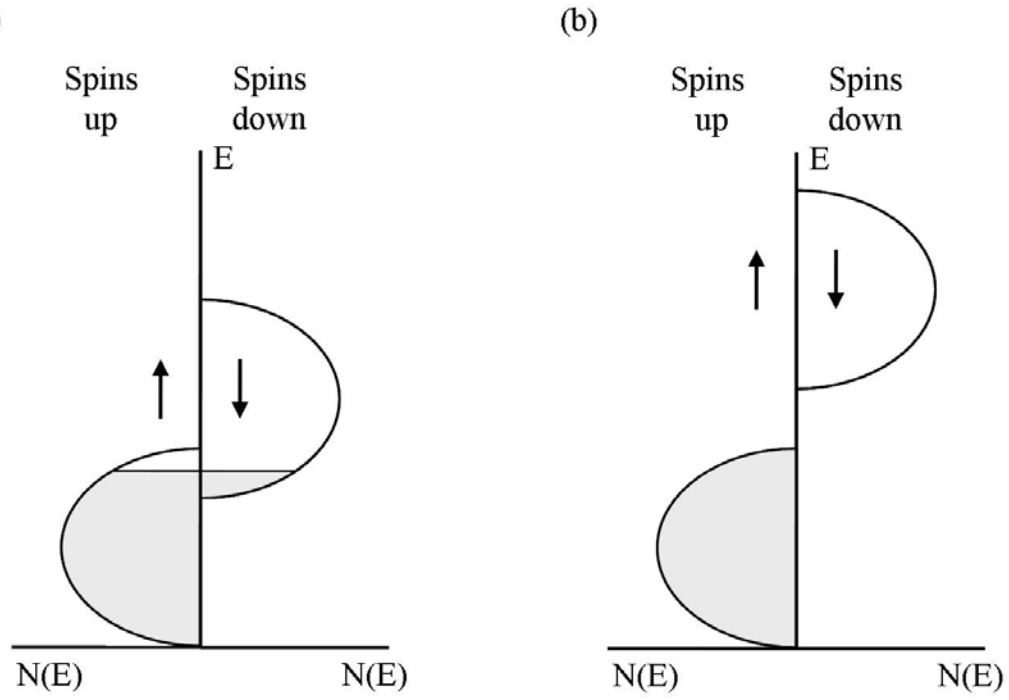

Figure 2.4: Schematic of density of states showing exchange splitting of the spin-up and spin-down half bands for (a) small exchange splitting, (b) larger exchange splitting [36].

In solids the overall magnetic moment consists almost entirely of that contributed by electron spin. This phenomenon is called the quenching of the orbital moment. It occurs because the electron orbitals are fixed in the crystal lattice, and cannot change their orientation when a magnetic field is applied. In practice it will be sufficient to regard the magnetic moment of solids as being due to the spin only. Thus, most of the time the terms spin and magnetic moment can be used interchangeably. However, it should be noted that in rare earth atoms and ions the orbital moment is not quenched, even in

crystalline solids. This is due to the 4f electrons being more effectively shielded by the outer electrons than the 3d electrons are in transition metals [36].

When a material consisting of several atoms is subjected to an applied magnetic field (H), the net magnetic moment per unit volume of the material is defines as the magnetization (M). The response of a material upon application of a magnetic field is known as magnetic induction or magnetic flux density (B). Inside a magnetic material, the relationship between B and H due to the magnetization is given by Equation (2.2).

$$B = \mu_o (H+M) \qquad \text{Equation (2.2)}$$

One of the most important properties of magnetic materials is susceptibility (χ) which is the degree of magnetization induced in a material per unit applied magnetic field. It is given by Equation (2.3).

$$\chi = \frac{M}{H} \qquad \text{Equation (2.3)}$$

2.3.1. Classes of Materials

Materials are divided into different classes of magnetism based on how the atoms interact collectively. These classes are discussed in this section and depicted schematically in Figure 2.5 [36].

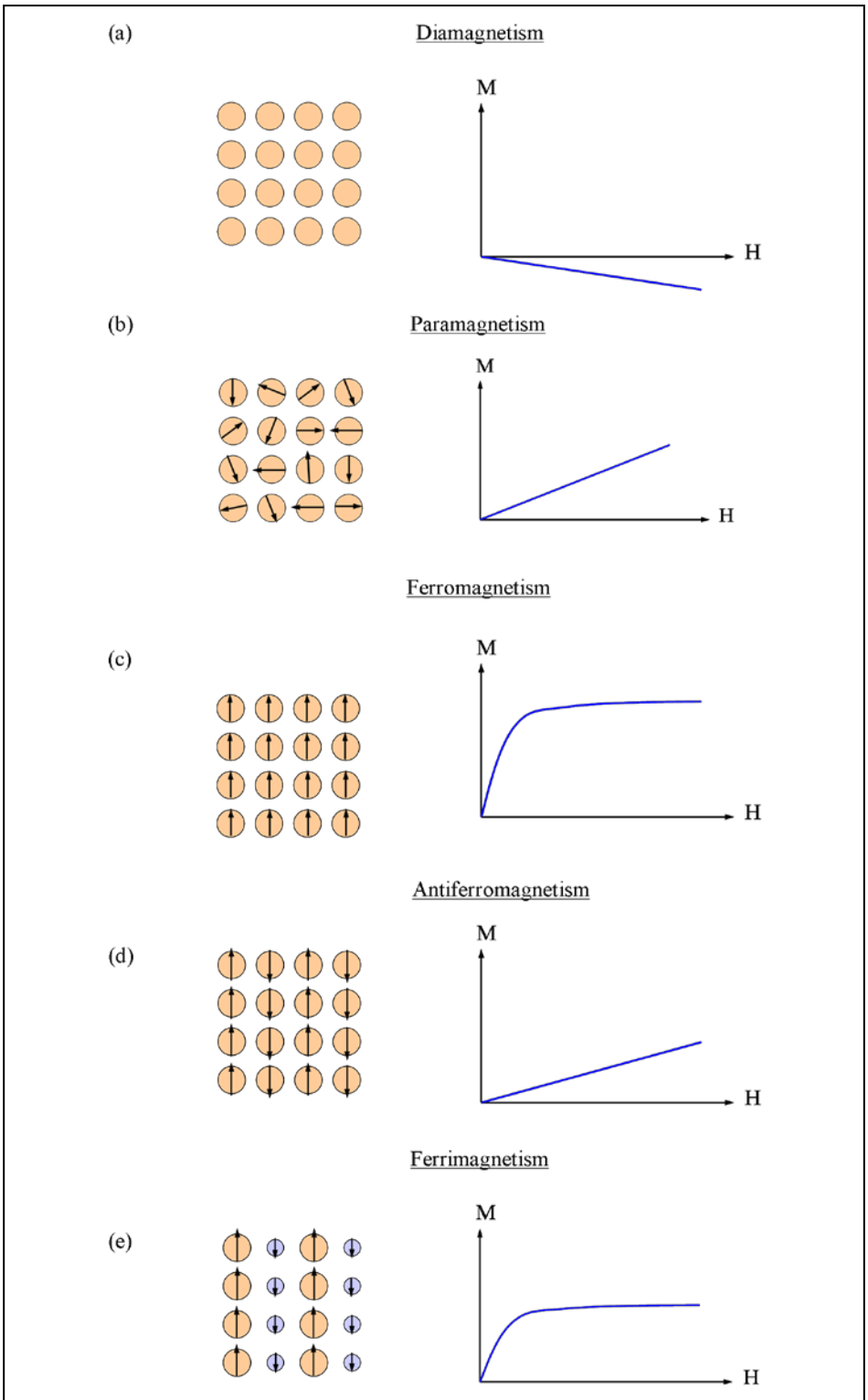

Figure 2.5: Schematic representation of the atomic spins and M vs. H curves for (a) diamagnetism, (b) paramagnetism, (c) ferromagnetism, (d) antiferromagnetism, and (e) ferrimagnetism [36, 37].

2.3.1.1. Diamagnetism

In this class of materials the magnetic response is opposite in direction to the applied magnetic field. Such materials have no unpaired electrons and therefore no net internal magnetic moment. Diamagnetic films have a negative magnetic susceptibility (χ), which can be understood in terms of Lenz's law: an applied external magnetic field induces a magnetic moment that is antiparallel to the external field [37]. The diamagnetic signal is independent of temperature and in M vs. H plots is seen as a line with a negative slope (Figure 2.5a).

2.3.1.2. Paramagnetism

Paramagnetism generally occurs in atoms or molecules with an odd number of electrons, leading to the electrons having a net spin. In isolation, the net magnetization is zero as all the spins are randomly aligned and so tend to cancel each other out. However, in the presence of an external magnetic field the spins align with the direction of the magnetic field, resulting in a net magnetic moment in the direction of the applied field [36, 37].

The susceptibility for paramagnetic materials is given by Curies-Weiss law shown in Equation (2.4).

$$\chi = \frac{N\mu_0 m^2}{3K_B T} \qquad \text{Equation (2.4)}$$

where μ_o is the permeability of a vacuum,

N is number of magnetic dipoles (m) per unit volume,

K_B is Boltzmann's constant, and T is temperature.

This law only holds for materials which have low magnetization strengths. Paramagnetic materials have a small positive magnetic susceptibility usually in the range of 10^{-5}–10^{-4}. The M vs. H plot is a straight line with a positive slope (Figure 2.5b). The magnetization decreases with temperature; the increased thermal agitations prevent alignment of the magnetic domains.

The above describes the most common form of paramagnetism, but it should be noted that some variants exist, including Pauli and Van-Vleck paramagnetism. Pauli paramagnetism is mostly seen in metals with large electron concentrations. Van-Vleck paramagnetism occurs in materials that have an even number of unpaired electrons. Unlike other forms of paramagnetism, the susceptibility in Van-Vleck materials is temperature independent.

2.3.1.3. Ferromagnetism

Ferromagnetic materials have unpaired electrons and thus have a net magnetic moment [36, 37]. When an external field is applied to materials of this class, the electron spins line up in the same direction as that of the applied magnetic field. These spins remain aligned even after the magnetic field is removed (Figure 2.5c). The alignment is retained despite the effect of KT. The electron spins interact with one another through an energetically favorable exchange mechanism. These interactions may occur through itinerant electrons, nearest neighbor exchange or other exchange mechanism that will be described in more detail later.

Most ferromagnetic materials contain magnetic domains which consists of atoms (10^{12}-10^{15}) aligned in the same direction. This is conceptually similar to the presence of a single crystal within a polycrystalline material. The magnetic moment lies along a

specific crystalline zone axis, referred to as the easy axis, which is the result of coupling between the electron spin and the angular momentum of the orbit. It is due to the easy axis that the magnetic moment is anisotropic to the magnetization from an external applied magnetic field. When the direction of the applied magnetic field is not along the easy axis, the applied magnetic field has to overcome the energy barrier and has to pull all the magnetic moments away from the easy axis and point them towards the field direction This energy barrier is know as the magneto crystalline anisotropy E_a and it is the atomic origin of hysteresis behavior in magnetic materials (described in the next sub-section).

Iron, nickel, and cobalt are examples of ferromagnetic materials. Ferromagnetism is strongly temperature dependent, and the magnetization of a ferromagnetic material is inversely related to temperature. The maximum temperature at which a ferromagnetic material retains its magnetization is knows as the Curie temperature (T_C). Above T_C, the spins randomize due to thermal energy and the material becomes paramagnetic with the susceptibility obeying the Curie-Weiss law (Equation 2.4). Thus, the saturation magnetization goes to zero at the Curie temperature.

2.3.1.3.1. Hysteresis

Ferromagnetic materials have the property that they retain a memory of an applied field once it is removed. This behavior is called hysteresis, and a plot of the variation of magnetization with magnetic field reveals the hysteresis loop. This occurs due to the presence of magnetic domains. Hysteresis is a very important property and is extremely useful for making magnetic memory devices. The hysteresis loop is measured by measuring the magnetization (M) of a ferromagnetic material while the applied force (H)

is changed (Figure 2.6) [38]. A ferromagnetic material that has never been previously magnetized will follow the dashed line as H is increased. At point “a” almost all of the magnetic domains are aligned. This point is known as the saturation magnetization as the application of an additional magnetization force will produce very little increase in magnetization strength. As H is reduced to zero, the curve will move from point “a” to point “b”. It is apparent that at point “b” the material possesses magnetization even though the applied field is zero. This point indicates the remanence or level of residual magnetism in the material. (i.e. some of the magnetic domains are aligned while others have lost their alignment). As the magnetic field is further reduced, the curve moves to point “c”, where the magnetization is now zero (the resultant magnetization is zero in the material as all the domains are flipped). This point is called the coercivity. The force required to reduce the residual magnetization to zero in the material is called the coercive force or coercivity of the material.

As the applied magnetic field is increased in the negative direction, the material will become magnetically saturated but in the opposite direction (point “d”). Reducing the field to zero brings the curve to point “e” which results in a residual magnetism with a similar magnitude as point “b”. Increasing the applied magnetic field again in the positive direction will return M to zero. The curve does not return to the origin of the graph as some force is required to remove the residual magnetism. The curve then moves to point “f” and back to the saturation point resulting in the completion of the loop. M vs. H plots have been used in this study to analyze the magnetic properties of dilute magnetic semiconductors DMS.

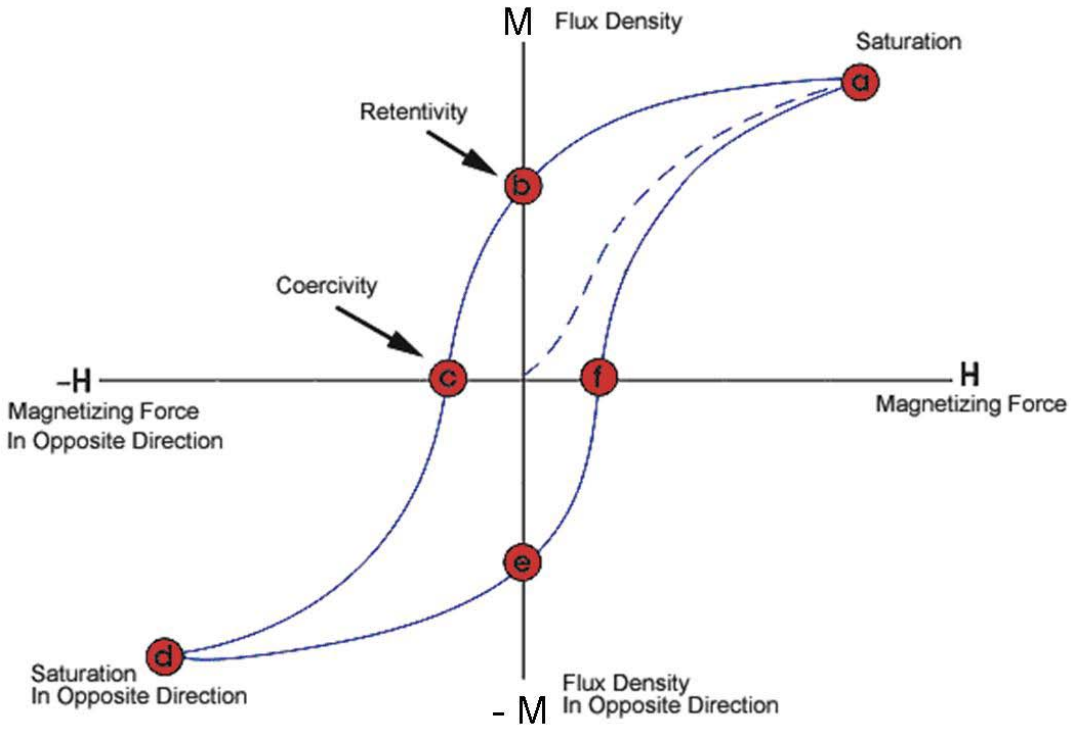

Figure 2.6: Hysteresis curve for a ferromagnetic material [38].

2.3.1.4. Antiferromagnetism

The materials in this class have mixed parallel and antiparallel magnetic moments that cancel each other out, resulting in a zero net magnetization (Figure 2.5d) [37]. Antiferromagnetism (AFM) is normally seen in transition metal oxides such as NiO and CoO. The temperature above which antiferromagnetic order ceases to exist is called the Néel temperature (T_N). Above T_N, antiferromagnetic materials behave like ferromagnets with its susceptibility exhibiting Curie-Weiss behavior but with a negative intercept in negative exchange interactions.

2.3.1.5. Ferrimagnetism

This type of magnetism is similar to ferromagnetism and is seen in ferrites and garnets. In this type of magnetism the interaction between nearest neighbors is antiferromagnetic, however these materials have unequal magnetic moments and hence a resultant net magnetic signal is obtained (Figure 2.5e) [37]. Such materials generally consist of two different elements or ions (Fe^{2+} and Fe^{3+}) and their ferromagnetic sublattices have unequal magnetic moment. This type of magnetism is usually mediated by superexchange or indirect exchange interactions (described later). Ferrimagnetism is therefore similar to ferromagnetism. It exhibits all the characteristics of ferromagnetic behavior: spontaneous magnetization, Curie temperatures, hysteresis, and remanence. However, ferro- and ferri-magnets have very different magnetic ordering.

2.3.1.6. Superparamagnetism

Superparamagnetism occurs in materials that are composed of small crystallites (analogous to nanoparticles range from 1-10 nm in size) that are so small that they can randomly flip direction due to thermal fluctuations [39]. As a result the material is not magnetic, except in the case of an external applied magnetic field and thus behave more like a paramagnetic material. In these materials the magnetic moment of the entire crystallite tends to align with the magnetic field. The energy required to change the direction of magnetization of a crystallite is called the crystalline anisotropy energy (E_a) and depends both on the material properties and the crystallite size (Equation 2.5).

Thus $E_a = KV$ Equation (2.5)

where

E_a is the magnetocrystalline anisotropy energy,

K is the effective anisotropic energy density, and

V is the volume of the particle.

As the crystallite size decreases, so does the crystalline anisotropy energy, resulting in a decrease in the temperature at which the material becomes superparamagnetic. With a decrease in particle size to a point below a critical diameter, E_a becomes comparable to the thermal activation energy K_BT (where K_B is the Boltzmann constant, and T is temperature) [39]. Due to the small anisotropy energy barrier the magnetization direction of the nanoparticles can be easily moved away from the easy axis by thermal activation energy or the applied magnetic field. If the thermal activation is sufficient to overcome E_a then the magnetic moment may point in any direction and behave like paramagnetic atoms. Thus magnetic order still exists in the nanoparticles but each particle behaves like a paramagnetic atom with a large moment, this behavior is known as superparamagnetism. Instead of aligning in a certain direction, the magnetization direction of the nanoparticles rapidly fluctuates. The temperature at which thermal activation energy overcomes the magnetic anisotropy barrier of small particles is known as blocking temperature (T_b), given by Equation (2.6).

$$T_b = \frac{KV}{k_b \ln\left(\tau_{\exp} / \tau_O\right)} \qquad \text{Equation (2.6)}$$

where

V is the particle volume,

K is the anisotropy constant,

τ_{exp} is the measurement time (usually 100 seconds), and

τ_o is the lifetime due to the natural gyromagnetic frequency of the particles.

Thus typically the term ln (t_{exp}/t_o) is 25.

The critical variables affecting T_b are K, the anisotropy constant, and V the volume of the magnetic particle.

At $T < T_B$, the moments of some of the particles are blocked: they do not possess sufficient magnetic energy to overcome the energy barriers in the timescale of the experiment. The energy barriers in the vicinity of H = 0 cannot be overcome without an increase in the thermal energy or an external magnetic field. For $T > T_b$, the thermal energy is high enough to overcome the coupling forces and randomize the spins and hence the magnetic signal reduces. Since there is no longer any magnetic order, the internal magnetic field no longer exists and the material exhibits paramagnetic behavior. If the material is non-homogeneous, a mixture of ferromagnetic and paramagnetic clusters of atoms exists at the same temperature.

2.4. Exchange Mechanisms

When semiconductors are doped with magnetic ions, exchange mechanisms exist between the magnetic ion and the host semiconductor. These exchange interactions eventually determine the overall magnetic properties. Exchange mechanisms can be divided into two main categories, namely direct and indirect. These interactions are described in the following subsection.

2.4.1. Direct Exchange

Direct exchange interaction occurs between neighboring magnetic atoms that have overlapping wave functions [37]. The exchange interaction (J) between these atoms arises from the Coulombic interaction between electrons. Electrons with parallel spins are kept apart due to the Pauli exclusion principle, which leads to a decrease in Coulombic repulsion. Thus, there is a difference in the exchange energy between parallel and antiparallel couplings in the exchange energy. If J is positive then the spins are parallel and point in the same direction; however, if the exchange interaction is negative then the spins are anti-parallel. Typically, the magnetic orbitals of the atoms do not possess sufficient overlap to develop ferromagnetism through direct exchange, and usually indirect exchange mechanisms are more significant in making semiconductors magnetic [40].

2.4.2. Indirect Exchange Interactions

Several indirect exchange mechanisms have been developed to explain magnetism in transition metal (TM) and rare earth (RE) doped semiconductors. The three main classical indirect exchange mechanisms are RKKY, double exchange, and superexchange. In recent years based on the observations of ferromagnetism in II-VI and III-V DMS several other indirect exchange mechanisms have been developed. This discussion begins with the explanation of the classical indirect exchange models.

2.4.2.1. RKKY - Carrier Mediated Exchange

RKKY is an indirect exchange mechanism named after its discoverers: Ruderman, Kittel, Kasuya, and Yosida [41-43]. This mechanism allows for the coupling of magnetic moments through Coulomb exchanges via band electrons over relatively large distances.

This theory was originally formulated to explain ferromagnetism in metals, and is an efficient mechanism when a high concentration of free carriers are present (Figure 2.7a). The original RKKY studies showed that the spin polarization of the conduction electrons oscillate in sign (Firedel oscillations) as a function of the distance from localized moments. The coupling may be ferromagnetic or antiferromagnetic depending on the separation of the interacting atoms. This mechanism has been used to explain the ferromagnetic mechanism for 4f electrons which are localized. In 4f metals, there is an indirect exchange mechanism between the outer 5d electrons which partly overlap with the 4f shell.

RKKY or carrier mediated exchange has been found to be the ferromagnetism mechanism in $Ga_xMn_{1-x}As$. This mechanism occurs because Mn is an acceptor in GaAs and introduces a hole in to $Ga_xMn_{1-x}As$, contributing a localized spin [44, 45]. The carrier-mediated exchange theory predicts a T_C that is dependent on the localized spin concentration as well as carrier concentration in these materials. However, the position of the TM defect levels is midgap and does not generate any free carriers to support this exchange mechanism [20]. Overall, the carrier mediated exchange mechanism is interesting as it allows the opportunity to alter magnetic properties by altering hole concentration.

2.4.2.2. Double Exchange Mechanism

Double exchange is a term that was coined by Clarence Zener and this mechanism involves the coupling of magnetic ions in different charge states by the hopping of an electron from one ion to another through interacting with the p-orbital (Figure 2.7b) [46]. Spin flips are not allowed in this model and it is energetically favorable if both the ions

have a similar magnetic structure. This mechanism explains magnetism in spinel magnetite, manganites, and Mn perovskites. This model has been used to describe the ferromagnetism in $In_{1-x}Mn_xAs$ [47]. In GaN, the TM *d* states split into a triply degenerate t_{2g} and a doubly degenerate e_g level (Figure 2.7b). In GaN the calculated levels sit at 1.44 and 0.22 eV (respectively) above the valence band maximum (VBM). The majority of t_{2g} levels have one electron in the case of Cr, two electrons in the case of Mn, and three in the case of Fe.

2.4.2.3. Superexchange

Another exchange interaction that is found in these materials is the coupling of nearest neighbor transition metals through a shared cation, known as superexchange (Figure 2.7c). The mechanism was first pointed out by Kramers in 1934 and then developed in detail by Anderson in 1950 [48, 49]. It results from the virtual hopping of carriers between the completely filled p-orbitals of anions and the d orbitals of the magnetic TM cations. In order for electrons from both adjacent atoms to occupy the same p-level, they must be opposite in spin, a result of Pauli exclusion principle considerations. This leads to an antiferromagnetic coupling of nearest-neighbor cations through a shared anion. This mechanism is of importance in ionic solids such as transition metal oxides and fluorides, where the bonding orbitals are formed by 3d electrons in the TM atoms and the 2p valence electors of the diamagnetic oxygen or fluorine atoms. Superexchange is also present in the Nitrides, though the strength of the exchange integral is roughly one order of magnitude less than in the oxide-based materials [50].

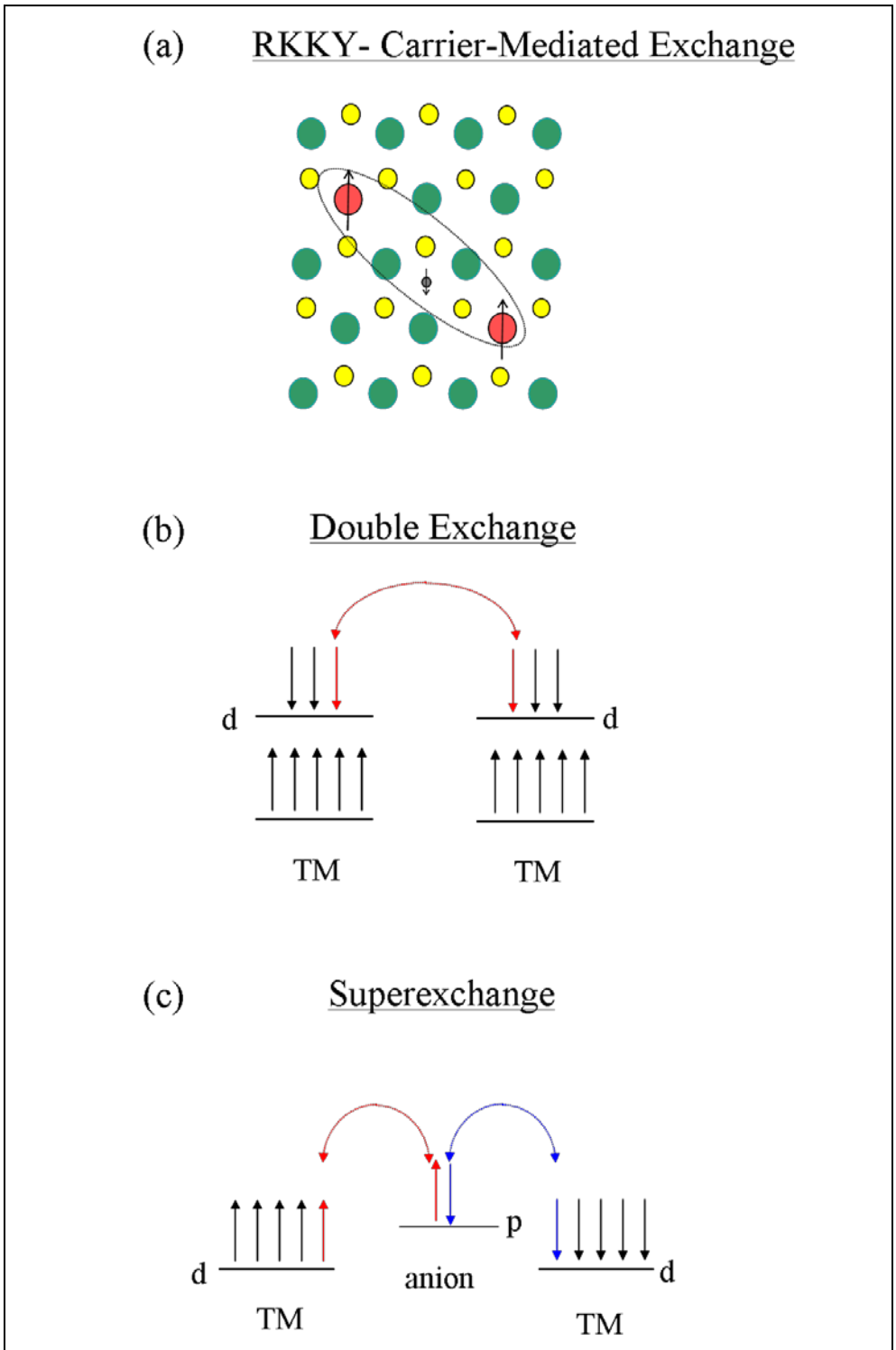

Figure 2.7: Classical indirect exchange mechanisms: (a) carrier mediated ferromagnetism, (b) double exchange, (c) superexchange in semiconductors.

2.4.2.4. Spin-Dependent Coupling Mechanism

Before proceeding further, it should be noted that there are two main spin-dependent coupling mechanisms in magnetic semiconductors that control the magneto-optical phenomenon. The first is the coupling between the conduction-band electrons (s-character) and localized spins (d-character) this is denoted by $N_0\alpha$. The other main mechanism is hole exchange coupling: coupling between the valence band holes (p-character) and localized spins (d-character), denoted by $N_0\beta$. This generally increases with decreasing lattice constant [51]. In the tetrahedrally coordinated DMS, if the TM (d orbitals) or RE (d or f orbitals) ions substitute the host cation the resultant electronic structure will be affected by hybridization of the d or f orbitals of the magnetic ion and the p or s orbitals of the neighboring atoms. In RE ions both the d and f states can participate in spin-coupling, but the f-states are more localized and thus their coupling is expected to be weak.

2.4.3. Additional Exchange Mechanisms

In addition to the classical direct and indirect mechanism, additional exchange mechanisms have been proposed to explain the observation of dilute magnetic semiconductors in DMS. These additional exchange mechanisms are described below.

2.4.3.1. Bound Magnetic Polarons

In magnetic semiconductors the magnetic moments are polarized to form sizeable magnetic moments at the vicinity of the donor/acceptor impurities. These are known as bound magnetic polarons (Figure 2.8) [52]. Decreasing temperatures result in an increase in the polaron interaction distance, leading to overlap between neighboring polarons and so allowing them to interact through the magnetic imputers, forming correlated polaron

clusters. A ferromagnetic transition occurs when the size of such clusters is equal to the size of the samples. Although the direct interaction between the localized carriers is antiferromagnetic, the interaction between the bound magnetic polarons can be ferromagnetic for large concentrations of magnetic impurities. This model has been used to describe the magnetism in low carrier density systems such as electronic oxides.

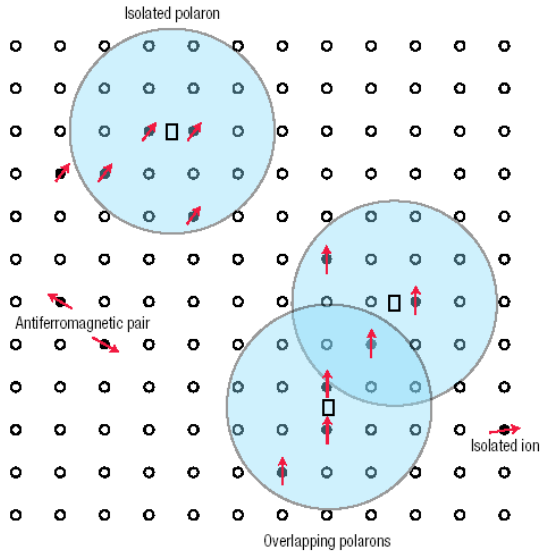

Figure 2.8: Schematic of bound magnetic polarons interactions [52].

2.4.3.2. Donor Impurity Band Exchange

A donor impurity band exchange model, proposed by Venkatesan, Coey et al., suggests that defect centers mediate ferromagnetism and are responsible for the magnetization seen in TM doped ZnO [52, 53]. Three scenarios for TM doping in ZnO were evaluated in this model (Figure 2.9). In the first scenario of a light 3d element (e.g. TM = Ti), the 3d spin-up states lie high in the 2p (O) and 4s (Zn) gap, overlapping the spin split donor impurity band. For the next element (TM = Mn) there is no overlap with the 3d level and the exchange is weak, and towards the end of the series (TM = Co) the

3d down states overlap with the impurity band which then has the opposite spin splitting for the same occupancy. High T_C are found when the unoccupied 3d states overlap the impurity band. The origin of the donor impurity band has been attributed to oxygen vacancies (F centers) in ZnO and it has been proposed that this model can be used to explain ferromagnetism in GaN, which can be caused by the d^0 centers. The higher magnetization that is seen in ZnO at the interfaces is due to the defects that are present in the region. Thus in order for long range magnetization to occur it is essential to have high carrier concentration and a large number of vacancies. Once the donor concentration increases significantly, the donors merge with the conduction band and then RKKY exchange mechanism begin to dominate.

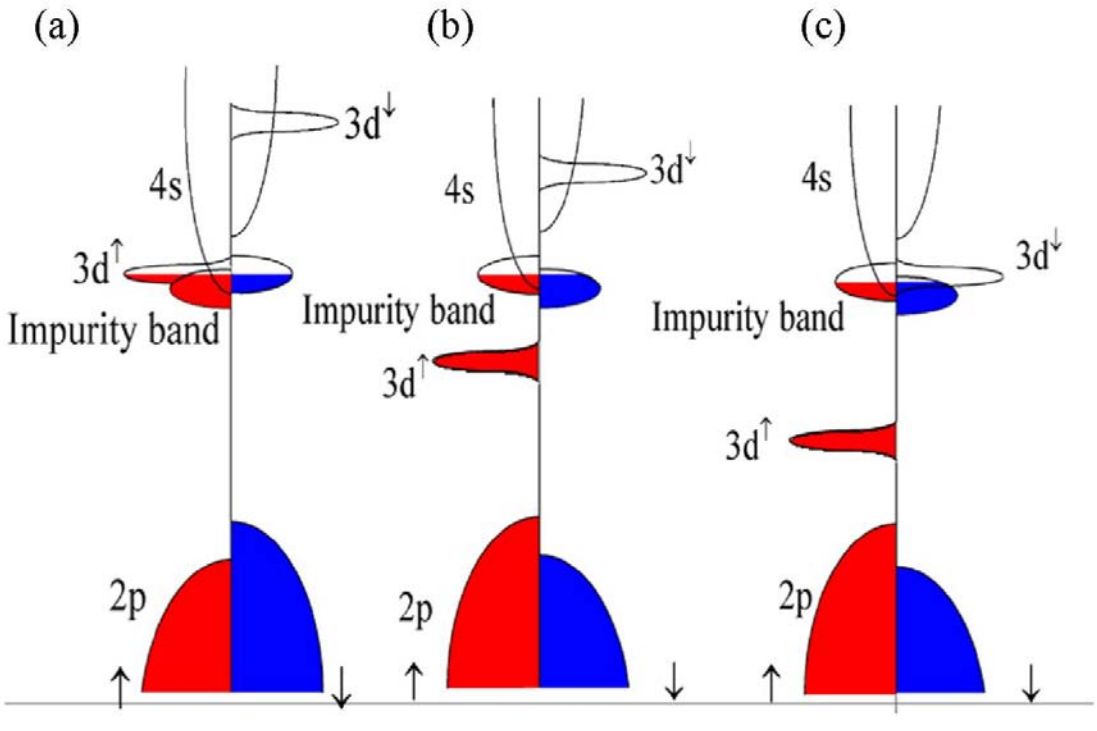

Figure 2.9: Schematic density of states for (a) TM = Ti, (b) TM = Mn, and (c) TM = Co. The Fermi level lies in a spin split donor impurity band [52, 53].

2.4.3.3. Indirect Exchange: Litvinov and Dugaev Model

The Litvinov and Dugaev model is used to explain ferromagnetism in both degenerate and non degenerate films. This model proposes an indirect exchange mechanism in which virtual electrons transition from the magnetic impurity acceptor level to the valence band [54]. This model applies to semiconductors in which there is a low concentration of magnetic ions and in which magnetic dopants do not introduce any free carriers. In this model the T_C depends on p-d exchange interactions and the energy between the TM impurity level and the band electron levels. This model has been applied to explain the ferromagnetism in $Ga_{1-x}Mn_xAS$ and $Ga_{1-x}Mn_xN$ films.

2.5. Theoretical Models

Based on the experimental results for the II-VI semiconductors and III-Arsenides semiconductors several theoretical models have been developed to elucidate the magnetism in these DMS, and many of these have then been extrapolated to GaN. The theoretical models relevant to this study are discussed next.

2.5.1. Zener Mean Field Model: Dietl

The Zener Mean field model has been proposed by Dietl et al. and has been used to determine the T_C of various zinc-blende semiconductors [15]. This model is based on the Zener and RKKY interaction models and takes into account the anisotropy associated with RKKY exchange which is associated with the spin-orbit coupling. This model evaluates ferromagnetic interactions mediating through holes introduced by TM doping (shallow acceptors). It was found that T_C is determined by a competition between the ferromagnetic and antiferromagnetic interactions. The T_C values calculated by the mean field model for different materials were performed using Equations (2.7) and (2.8).

$T_C = T_{FM} - T_{AFM}$ Equation (2.7)

$$T_c(x) = A_F(xeff/0.05)(\beta N_0[eV])^2[\frac{N_0(GaAs)}{N_0}]T_F - T_{AF}(x)$$ Equation (2.8)

where AF is the Fermi liquid parameter,

x_{eff} is the effective spin concentration,

β is the p, d exchange integral,

N_0 is the concentration of cation sites,

T_F is the FM ordering temperature, and

T_{AF} is the AFM ordering temperature.

A TM concentration of 5 % was used in this study along with a hole concentration of 3.5 x 10^{20} cm^{-3}. This model agrees well with the experimental results for p-$Ga_{1-x}Mn_xAs$ and $Zn_{1-x}Mn_xTe$ [44, 45].

T_C depends on the TM doping concentration and hole concentration and is higher for lighter elements. The spin-orbit coupling in the valence band is crucial for determining the T_C and direction of the easy axis.

Based on this model, GaN and ZnO are predicted to have a T_C higher than room temperature as they have smaller lattice constants and allow for greater p-d hybridization and reduced spin-orbit coupling. One of the challenging theories is that the solubility limit of TM is low in GaN and so it is challenging to obtain 5 % TM doping. Furthermore, p-doping in GaN is extremely challenging and hole concentrations on the order of 10^{20} cm^{-3} may not be feasible. It is this theory that has spearheaded the research in TM doped GaN and ZnO.

2.5.2. Impurity Band Model

Sato and Katayama-Yoshida et al. performed ab initio calculations on GaN doped with 5 % of various TM [18]. Their model shows that the $Ga_{1-x}Mn_xAs$ exhibits a spin-splitting of the density of states in the valence band, while GaN possess a spin-split density of states in the middle of the bandgap. Therefore, TM in GaN forms deep levels and does not generate free carriers [20]. It was shown that for half filled (or less) d shells such as in Mn, Cr, and V the ferromagnetic state is stable in GaN. For high Mn concentration the spin glass state is favored (Figure 2.10). Additionally, it was found that Fe, Co, and Ni doping are stable in the spin glass state in GaN. Furthermore, first principle calculations show that TM forms an impurity band and the ferromagnetism in the Nitrides is stabilized by a double exchange mechanism and broadening of the impurity band [47, 55]. Mean field approximations predicted a high T_C of 500 K and 350 K for 5 % Cr and Mn doped GaN respectively [55]. The double exchange mechanism in this system favors short range interaction between nearest neighbors. For a high T_C, the model requires a large concentration of TM (~ > 20 %) [56]. Further Monte Carlo simulations revealed that the T_C of Mn doped GaN is on the order of tens of Kelvin and so RT ferromagnetism is not feasible. This suggests that the mean field approximation overestimates the T_C significantly. It has been suggested that any RT ferromagnetism found experimentally is due to the presence of MnN clusters or secondary phases [57].

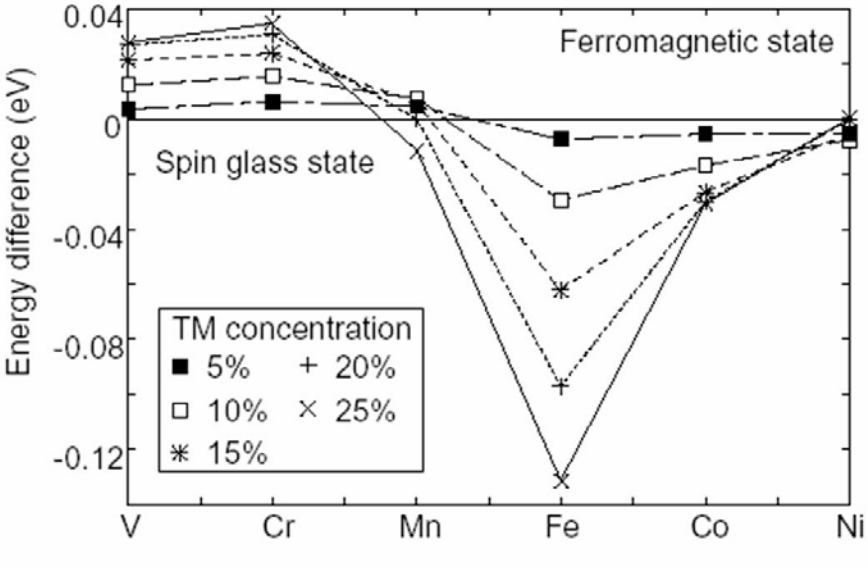

Figure 2.10: Stability of ferromagnetism in TM doped GaN [57].

2.5.3. Clusters

Local spin density calculations have been performed by van Schilfgaarde and Myrasov for 1-5 % TM doping in III-V semiconductors [58]. Their calculations show that the TM occupy deep levels in the host semiconductor. Furthermore, their calculations show that there is a strong driving force that favors the clustering of the TM atoms and that whether this clustering actually occurs is ultimately decided by the growth kinetics. The model considers magnetic interactions based on number of nearest neighbors (NN) and next nearest neighbors (NNN) present and the distances between them. Exchange interaction calculations show that Cr and Mn clusters are ferromagnetic and that Fe clusters result in antiferromagnetic interactions. Thus these interactions are a function of the d band filling. Initially increasing the TM concentration will result in an increase in the number of TM pairs and thus an increase in T_C, however, at really high concentrations the TM pairs are no longer separated and the contribution per pair starts to

decrease resulting in a decrease in T_C. First principle calculations by Das et al. show that TM cluster around N atoms and the TM-N interaction is AFM, while the TM-TM interaction is FM [59]. Thus the ferromagnetic interaction in DMS is an indirect exchange mechanism mediated by N atoms. It has been suggest that the high T_C observed experimentally is due to the presence of these ferromagnetic clusters.

2.5.4. Spinodal Decomposition

Furthermore, recent theoretical models by Dietl suggest that spinodal decomposition occurs in DMS and is responsible for the varying values of T_C reported for TM doped GaN [17]. Spinodal decomposition occurs when the TM doping concentration exceeds the solubility of the ion. The film then consists of regions of high and low TM concentrations, which results in magnetic nanocrystals being embedded in the semiconductor. As mentioned in the previous section, there is a strong driving force for the TM ions to cluster. The energy gained by bringing two Cr atoms together in GaN is 350 meV and for two Mn atoms is 300 meV. Spinodal decomposition does not necessarily result in a crystallographic phase and so can be hard to detect. It is not clear if these clusters are ferromagnetic, ferrimagnetic, or antiferromagnetic. Furthermore, at this point there is no model to predict whether these clusters should be metal or insulators. However, due the large TM concentration in the clusters, they tend to have high ordering temperatures. As mentioned earlier, the TM d-shells reside in the bandgap in the Nitrides. This property has been utilized to develop semi insulating materials as these midgap levels can trap carriers arising from impurities and defects in the materials. This trapping of carriers by the TM alters their charge state and impacts their Coulombic interactions. In materials with small carrier concentrations these interactions are not screened and so

Coulombic interactions can overcompensate the lowering of the free energy arising form the nearest neighbor bonding [60]. Thus co-doping of DMS with shallow acceptors or donors could provide an avenue for reducing or enhancing the TM aggregation. Furthermore, anti-surfactants can be used to enhance the aggregation of TM ions if desired. Similarly, ab initio electronic structure calculations by the Korringa–Kohn–Rostoker coherent potential approximations (KKR-CPA) method within the local-density approximation (LDA) by Katayama-Yoshida et al. have attributed the high T_C observed in Nitrides to spinodal decomposition [61]. For 30 % Cr doping, a T_C of 100 K is formed due to percolation network, while for 5 % Cr doping a high T_C of 700 K occurs due to a 3D Dairiseki-phase (clusters) caused by spinodal decomposition.

There are several theoretical models and exchange mechanism proposed for the ferromagnetism in DMS, with most of these models presenting conflicting arguments. These models are often revised or proven unlikely based on experimental observations. Pinning down which magnetic mechanism produces a particular experimental result is very challenging. Thorough growth and characterization studies are needed to obtain the real picture.

2.6. Background Literature for II-VI and III-Arsenide DMS

Non-magnetic semiconductors can be turned into magnetic semiconductors by doping them with 3d TM (e.g. Mn, Fe, Ni, Co, etc.) or 4f RE ions (e.g. Gd). The TM or RE replaces a fraction of the constituent atoms in these semiconductors. Such semiconductors are often called dilute magnetic semiconductors (DMS). Many developments have been made in this area since the 1980s with MBE growth of ferromagnetic II-VI and III-V compounds [12]. The developments in these materials and

devices are discussed in the following sections. The experimental background for the III-Nitrides is described in Chapter 4.

2.6.1. II-VI DMS

II-VI compounds such as CdTe and ZnS have been widely studied since the 1980s [12]. Here the valence of the cation matches common magnetic ions such as Mn, therefore, additional dopants must be incorporated to produce p- or n-type materials. TM have a higher solubility in II-VI semiconductors than in III-V since the TM is incorporated as TM^{2+} and the $4s^2$ electrons participate in the bonding [13]. The II-VI ferromagnetic compounds usually display paramagnetic, antiferromagnetic or spin glass behavior. However, heavily p-doped ZnMnTe and BeMnTe has shown to be ferromagnetic at very low temperatures [62, 63]. When an external field is applied and the temperature is low the II-VI semiconductors display a large Zeeman splitting, even at low Mn concentrations. For example, in $Zn_{0.9}Mn_{0.1}Se$ the splitting is 100 meV in the valence and 20 meV in the conduction band at 4.2 K with an applied field of 2 T. The II-VI DMS show large magneto-optical and Faraday effects at RT [12].

II-VI quantum dots doped with Mn have been studied quite extensively in recent years. As these quantum dots are doped with TM, one can consider them to be dilute magnetic nanostructures (DMNS). In DMNS, due to quantum confinement, strong spin interactions occur which allow for an increased T_C. In II-VI DMNS, the confinement leads to the formation of strong magnetic polarons that contain a substantial number of Mn ions [64, 65]. Magnetic circular dichroism (MCD) measurements on Mn doped ZnSe nanocrystals reveal an increase in the Zeeman effect by an order of magnitude as compared to bulk DMS for the same concentration [66]. A spin aligner LED has been

developed using II-VI bulk DMS and this is discussed in the spin-LED section of this chapter.

In recent years, significant efforts have been made towards the TM doping of ZnO, including theoretical studies by Dietl showing that p-doped ZnO with 5 % Mn concentration should result in RT ferromagnetism [15]. Several TM dopants have been tried (Mn, Co, V, and Ni) along with various growth techniques, including PLD, ion implantation and MOCVD [16]. However, the results concerning the existence of ferromagnetism have been rather controversial. While some groups have reported ferromagnetism in (Zn,TM)O systems with T_C ranging from 30 to 550 K [67-73], others have reported observations of antiferromagnetic and spin glass behavior [74-76]. Furthermore, secondary phases such as ferromagnetic $(Zn,Mn)Mn_2O_4$ precipitates have also been reported in these films [77]. The distribution of TM elements in the host ZnO is also an important issue to be addressed. Mn has a high solubility in ZnO and up to 35 % Mn doping has been obtained by PLD [78]. These films did not exhibit any FM. However, 5 % vanadium doping in ZnO has shown RT ferromagnetism with a T_C of 350 K and revealed n-type conductivity [73]. The insulating films in this study were not ferromagnetic. Furthermore, spin-coated nickel doped ZnO nanocrystalline thin films prepared using high-quality colloidal DMS quantum dots as solution precursors showed ferromagnetism with a T_C of 350 K [79]. On the other hand nickel doped ZnO films with concentration up to 25 % showed ferromagnetism up to 2 K and superparamagnetic behavior beyond 30 K [72]. Additionally, it is hard to obtain high quality ZnO material and p-doping of this material is also a challenge. To summarize, TM doping in ZnO is not

completely understood and several material issues need to be resolved before this material system can be successfully applied to spintronics.

2.6.2. III-Arsenide DMS

Later in the 1990s, attention was focused on making III-V semiconductors ferromagnetic by doping them with magnetic ions. These III-V semiconductors - such as GaAs and GaN - are widely used for high speed electronic, and optoelectronic devices. The introduction of magnetic ions into these established semiconductors would pave the way for novel devices which integrate magnetic, electrical, and optical functionalities [12]. The most widely studied of the III-V DMS compounds is $Ga_{1-x}Mn_xAs$, which exhibits a close coupling between carrier concentration and T_C. The main challenge for TM doping in the Arsenides is that the TMs have a very low solubility limit (~0.1 %) and so it is hard to fabricate homogeneous films. Molecular beam epitaxy (non equilibrium) techniques have been successfully used to grow these films at the low temperature of 250 °C (as opposed to regular growth temperatures of 600 °C) to allow for TM incorporation of up to 10 % [11]. LT techniques limit the thermal energy to support secondary phase formation while still maintaining crystalline film growth. Studies show that Mn occupies the cation site and in addition to introducing magnetic moments it also results in the addition of holes. Thus, $Ga_{1-x}Mn_xAs$ is a p-type material (with hole concentration on the order of 10^{20} cm^{-3}) due to the shallow nature of the Mn acceptor (Mn lies 110 meV above the valence band), so that spin-polarization can be observed even in the absence of an applied field [45]. These hole carriers are thought to mediate the long range ferromagnetic interaction between isolated Mn centers. Thus the ferromagnetism observed in $Ga_{1-x}Mn_xAs$ is attributed to an RKKY mechanism (i.e. carrier mediated

exchange). It was shown that beyond 6 % the T_C begins to drop, with a maximum T_C of 160 K reported for these films [80]. This has been attributed to a metal-insulator transition due to donors (such as Mn interstitials) that begin to compensate for the holes. It has been stated that in the films closer to the insulator side, the localization length is smaller than the sample size (millimeters), but it is still large in comparison to the length scale of magnetic interactions (nanometers) and thus, the RKKY-like interaction can still be in effect in the insulating samples [11]. Post-growth annealing in a nitrogen atmosphere for 90 minutes at 250 °C can be done to drive out the donor defects, which results in an increase in T_C [81].

High growth temperatures reduce the donor impurities that occur in the semiconductor, but as the growth temperature increases, MnAs cluster formation is favored. Thus, a trade off has to be made and low growth temperatures are used. Similar studies have been carried out for $In_{1-x}Mn_xAs$ (x = 0-18 %) with a maximum T_C of 60 K for x = 7 % [82, 83].

$Ga_{1-x}Mn_xAs$, has been shown to be effective at providing a spin injection layer in optically based devices. However, the T_C of these systems is limited to less than 200 K [14, 16].

2.7. Spin-LEDs

As this research is focused on GaN-based optoelectronic devices, the main emphasis of this work will be on developing a RT DMS for spin-LED devices. To this end, the detection of spin injection and the spin-LEDs based on II-VI and III-V DMS and DMNS are discussed next.

2.7.1. Detecting Spin Injection

Before proceeding to the discussion of the spin-LEDs based on II-VI and III-Arsenide semiconductors it is important to understand how spin injection is detected in devices. A traditional way to determine the injection of spin polarized electrons into a semiconductor is by using two ferromagnetic contacts on the semiconductor and measuring the difference in resistance for parallel and anti-parallel magnetic alignment of contacts. However, this technique is not suitable for devices with low spin polarization.

In semiconductors the photoexcited spin-polarized electrons and holes exist for a time 't' before they recombine. If the recombination time is greater than the spin relaxation time then the luminescence will be polarized. If spin polarized current is injected into LEDs and the polarization efficiency of the emitted light is measured, it is possible to determine the spin injection efficiency. Thus spin-LEDs provide a convenient way to study spin dynamics in heterostructures.

In GaAs, the conduction band (s-character) is two-fold spin degenerate, whereas the valence band (p-character) is four-fold degenerate (heavy- and light-hole spin). In Zinc Blende semiconductors such as GaAs, the selection rules for radiative recombination of electrons and holes are spin selective (Figure 2.11) [84, 85]. Four possible recombination methods exist, two of which include a heavy hole and the other two being light hole states. The resulting optical polarization of the photons depends on the spin polarization of the electrons. An electron with spin +1/2 is allowed to recombine with a light hole with spin -1/2 or a heavy hole with spin +3/2, resulting in a photon with circular polarization of σ^- for light hole and σ^+ for the heavy hole. The signs for spin-down electrons (-1/2) causes the signs of the polarization to be reversed. The probability of a

heavy hole process is three times as large as for a light process. Thus the luminescence emitted by a spin polarized electron recombining with unpolarized holes will be circularly polarized.

The degree of circular polarization (P_{circ}) is given by Equation (2.9)

$$P_{circ} = \frac{\sigma^+ - \sigma^-}{\sigma^+ - \sigma -} = \frac{(3n\uparrow + n\downarrow) - (3n\downarrow - n\uparrow)}{(3n\uparrow + n\downarrow) - (3n\downarrow + n\uparrow)} = \frac{1}{2}\frac{n\uparrow - n\downarrow}{n\uparrow + n\downarrow} = \frac{1}{2}P_{spin} \qquad \text{Equation (2.9)}$$

where σ^+ is the heavy hole transition,

σ^- is the light hole transition,

$n\uparrow$ and $n\downarrow$ are the occupation of the spin levels, and

P_{spin} is spin polarization.

Equation (2.9) connects the circular polarization of the emitted electroluminescence with the current density polarization degree which is given by Equation (2.10)

$$P_j = \frac{j\uparrow - j\downarrow}{j\uparrow + j\downarrow} \qquad \text{Equation (2.10)}$$

where J is the current density of the spin-polarized electrons.

For the case of non degenerate light and heavy holes, the degree of optical polarization and spin polarization will be equal and has a maximum value of 0.5. In a quantum well the HH and LH bands are separated in energy by the quantum confinement. The band splitting is typically several meV even in shallow QWs, and is larger than the thermal energy at low temperature (0.36 meV at 4.2 K) resulting in the higher energy states not being occupied. Thus only the heavy holes participate in the recombination

energy and based on Equation (2.6) a maximum value of 1 is attainable for P_{circ}, yielding a maximum spin injection efficiency of 100 %.

Often times in research papers, a P_{circ} of 0.5 is used as an guideline for 100 % spin injection efficiency. Thus, the degree of polarization of the light is proportional to the degree of polarization of the injected carriers and also to the amount of depolarization due to scattering at the interface and during the diffusion into the quantum well.

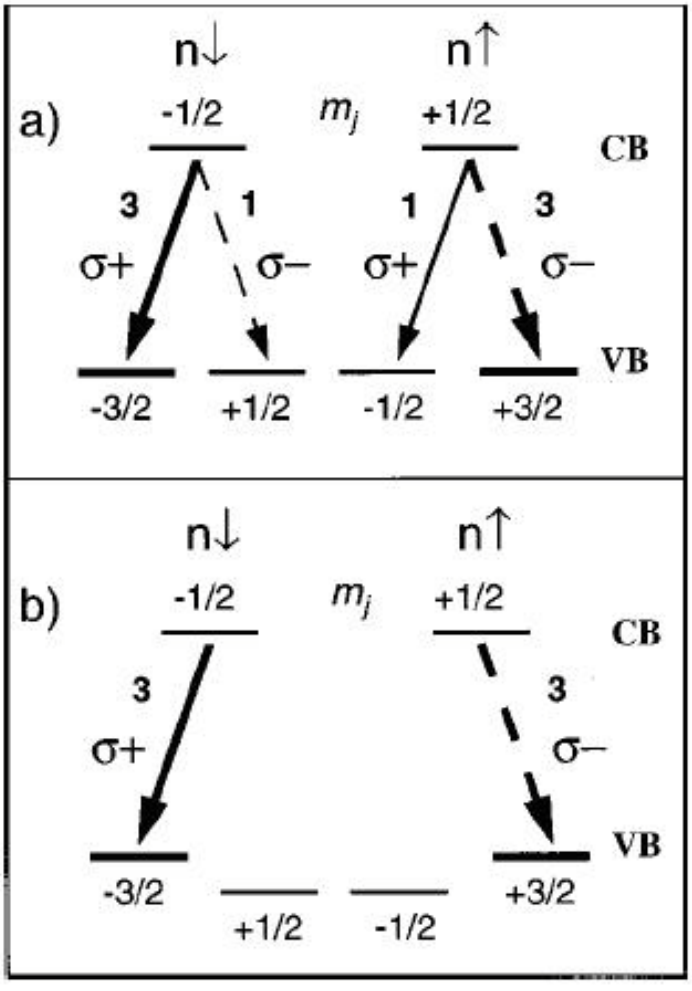

Figure 2.11: Schematic of the selection rules for interband transitions between m_j sub-levels for circularly polarized light [84, 85].

2.7.2. p-$Ga_{1-x}Mn_xAs$ Spin-LED

Ohno et al. demonstrated the first successful spin injection in materials using a ferromagnetic semiconductor as a spin injector (Figure 2.12) [86]. Spin polarized holes were injected from the 300 nm thick $Ga_{0.955}Mn_{0.045}N$ (Mn in GaN introduces holes and thus makes it p-type) under forward-bias into the $In_{0.13}Ga_{0.87}As$ QW and recombined with unpolarized electrons from the 500 nm thick n-GaAs (N_D = 2.3 x 10^{18} cm^{-3}) substrate. Ferromagnetic hysteresis curves were observed for temperatures up to 52 K but above this temperature GaMnAs became paramagnetic.

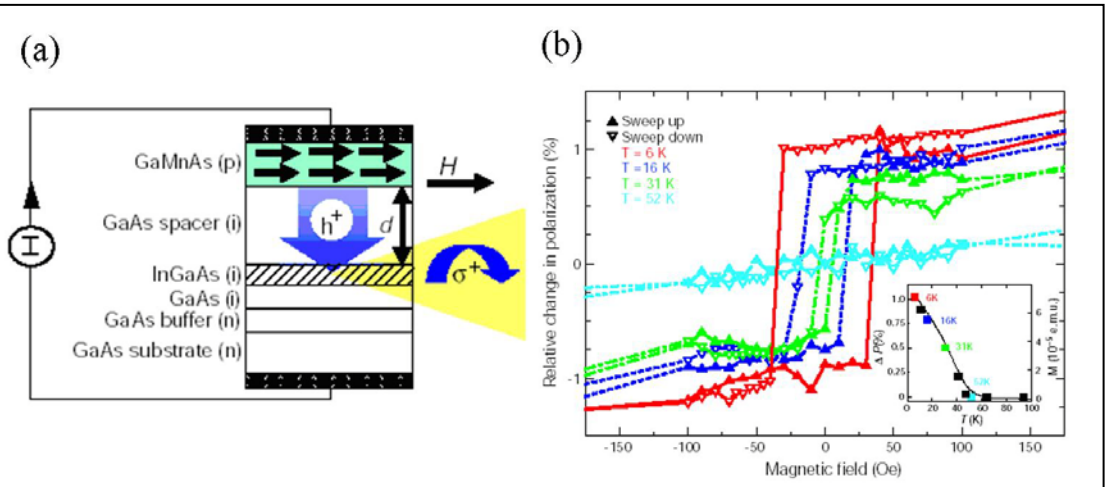

Figure 2.12: (a) Schematic of spin LED based on GaMnAs spin injector, (b) spin polarization efficiency as a function of applied field; inset shows the temperature dependence of the remanent polarization as a function of temperature for no applied field [86].

2.7.3. n-type $Be_xMn_yZn_{1-x-y}Se$ Spin Aligner LED

Quartneary n-type $Zn_{0.94}Mn_{0.06}Se$ and n-type $Be_{0.07}Mn_{0.03}Zn_{0.9}Se$ have been used to make a spin aligned LED on a GaAs-based heterostructure (Figure 2.13) [84, 85]. Spin-injection of electrons rather than holes is advantageous because of the reduced spin-orbit coupling in the conduction band, decreasing spin decoherence. In undoped or n-type

ZnSe the manganese spins are coupled antiferromagnetically. However, at low Mn-concentrations the sp-d exchange interaction leads to a giant g-factor, which results in a giant Zeeman splitting of band-edge-related states. On the application of an external magnetic field, the electrons passing through $Be_xMn_yZn_{1-x-y}Se$ will become spin-polarized. The polarization degree of the injected electrons will depend on the thickness of the semi-magnetic layer d_{SM}. The distance between the $Be_xMn_yZn_{1-x-y}Se$ layer and the GaAs layer is 100 nm to reduce the dephasing and scattering of the injected carriers' spin. Thus, these electric devices are driven by spin polarized currents. The holes are injected from the bottom p-GaAs substrate and pass through p-$Al_{0.03}Ga_{0.97}As$. Recombination of the polarized electrons and unpolarized holes takes place in the i-GaAs layer and ideally circularly polarized light is produced. Circular polarization of 43 % at 2.5 K and electron spin polarization of 86 % (neglecting effect of QW confinement) was reported for these structures. However, the T_C of these devices was around 4.2 K rendering them unfeasible for practical device operation.

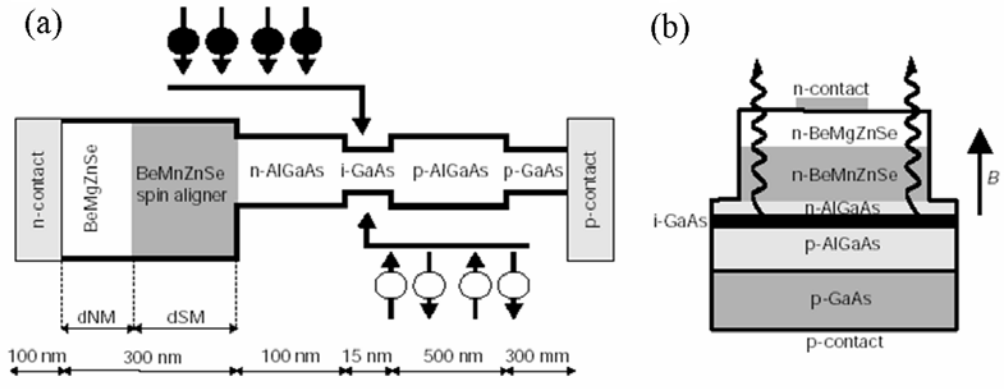

Figure 2.13: (a) Schematic of the band structure of the II-VI and III-V based spin aligner LED, (b) side view of the spin aligner LED [84].

2.7.4. GaAs Quantum Dot Spin-LED

MBE growth of the $In_{0.4}Ga_{0.6}As/GaAs$ quantum-dot surface-LED has been carried out in which 400 nm $p^{+}Ga_{0.974}Mn_{0.026}As$ was used as the spin injector layer (Figure 2.14). Spin polarized holes from this ferromagnetic layer combine with the unpolarized electrons from the n-GaAs layer in the quantum dots to produces circularly polarized light. For GaAs the spin diffusion lengths for holes are considerably smaller than electrons, and this ferromagnetic layer has to be placed as close as possible to the recombination region. This device emits at 1.27 eV and its peak optical polarization efficiency of 18 % is obtained at 5.1 K. The spin injection efficiency is estimated to be 36 % in the presence of a 0.1 T applied magnetic field [25]. Furthermore, magnetization measurements reveal that the device had a T_C of 44 K. Quantum dots are a favorable recombination medium as the spin relaxation in quantum dots is longer than in quantum wells and the ground state transition energy of the InGaAs/GaAS QD is considerably smaller than the bandgap of GaAs thus making field induced dichroism effects negligible.

InMnAs DMQDs have been grown by MBE and used for spin injection into an $In_{0.4}Ga_{0.6}As$ QD active region (Figure 2.14) [87, 88]. Electron energy loss spectroscopy measurements confirmed that the individual dots contained Mn atoms. However, the Mn composition in the dots is not uniform. Atomic force microscopy measurements show that the base length and height of the dots are 35–37 and 13–15 nm, respectively; the dot density is 3×10^{9} cm^{-2}. Initially a 5 kOe magnetic field was applied to align the DMQDs. Hysteresis measurements on the InMnAs QD/GaAs barrier levels reveal a T_C, of 350 K, however, the magnetization is fairly small and is of the order of 10^{-5} emu/cm^3. Furthermore, it is not clear if this T_C is due to the Mn within the QDs or due to secondary

phases such as MnAs (318 K) and MnGa (340 K), which have above RT T_C's. The magnetic field was then removed and spin injection was verified by the emission of circularly polarized light. This emission was observed up to temperatures of 160 K, with a maximum degree of circular polarization of 5.8 %, measured at 28 K, thereby providing the evidence of spin injection and an operational device [88]. However, these GaAs DMQDs have not led to a device that is operational at RT, meaning that further efforts are required to develop another material that can realize feasible spintronic devices. The effects of strain, quantum confinement, non-uniformity of TM concentration and disorder are of significance when analyzing the magnetic properties of DMQDs. It has been suggested that the high temperature ferromagnetism in DMQDs is due to carrier confinement within a QD that strengths the hole localization and subsequently enhances the thermal stability of the magnetic polarons.

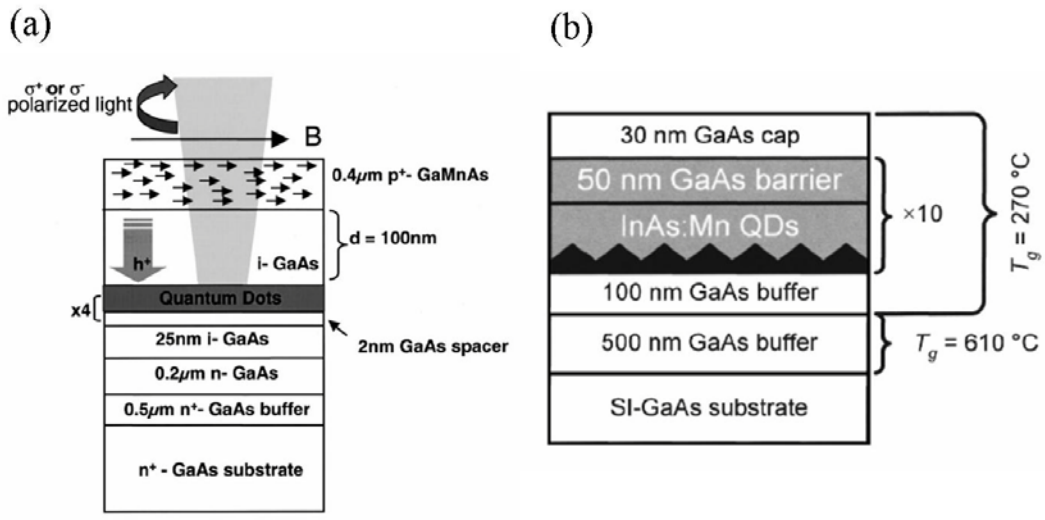

Figure 2.14: Schematic of (a) p-$Ga_{0.974}Mn_{0.026}As$ spin LED with active region consisting of $In_{0.4}Ga_{0.6}As$ quantum dots, (b) spin LED consisting of InAs: Mn quantum dots [87, 88].

2.8. Conclusions

Significant progress has been made in developing II-VI and III-DMS and spin-LEDs. Despite these efforts, to date there is no DMS that is magnetic at RT. The theoretical mode proposed by Dietl suggests that RT ferromagnetism is possible for GaN and ZnO semiconductors that are doped with a high concentration of Mn ions and have high hole concentrations. GaN is attractive as it already has an established optoelectronic base and magnetic developments made in this material can be more easily integrated as compared to developments in ZnO. The theoretical models that have been used to predict magnetic behavior in GaN-based DMS often present conflicting results and do not concur with experimental observations. This thesis will focus on executing systematic and thorough growth and characterization experiments, with the aim of developing a RT DMS in which the effect of TM or RE doping on the material, optical, and magnetic properties are well understood.

CHAPTER 3

MOCVD GROWTH AND CHARACTERIZATION: EXPERIMENTAL SETUP

3.1. Introduction

III-Nitride thin films have been produced by numerous techniques, such as ion implantation, molecular beam epitaxy (MBE), and metal organic chemical vapor deposition (MOCVD). Among these, MOCVD is the growth technique most widely used in industry to produce high quality epitaxial films for III-V devices, such as light emitting diodes (LEDs), photo-detectors, laser diodes, and solar cells. MOCVD is a non-equilibrium growth technique that relies on chemical reactions between metal organic sources and hydrides to deposit thin films onto a substrate. Didchenko et al. published the first reports on the growth of III-V compounds from metal-organics and hydride sources in 1960 [89]. The term MOCVD was coined by Manasevit et al. towards the end of 1960s, when they developed single-crystal GaAs films by using pyrolitic reactions between triethylgallium and arsine in an open tube cold walled reactor [90, 91]. This growth technique has proven to be ideal for large scale growth and allows for growth of atomically abrupt thin films with high purity and uniformity. This research used MOCVD to achieve transition metal and rare earth doping of GaN as this allowed for the creation of high quality thin films which could be integrated into existing III-Nitride devices. Described below are the details of the MOCVD growth process.

MOCVD consists of two main growth processes: thermodynamics and kinetics [92]. Thermodynamics determines the driving force for the overall growth process and

thermodynamic calculations can predict the maximum growth rate attainable, the solid composition of the system (in terms of the vapor phase partial pressure), the substrate temperature during growth, and dopant incorporation. Too large a driving force during growth causes surface roughening and too small leads to slow growth rates [93]. Thermodynamics determines the state of a system over a long duration of time.

As MOCVD is a non-equilibrium process, kinetics determines the rate of the chemical reactions that occur homogenously in the gas phase and heterogeneously at the growth interface [93]. Surface kinetics takes into account the adsorption of reactants, surface diffusion, surface reaction at steps or kinks, and desorption of gas products. Another important parameter is mass transport, which takes into account the gas velocities and temperature gradients in the vicinity of the hot susceptor which control the rate at which material is transported to the solid/vapor phase [93, 94]. Hydrodynamics and diffusion are important components of mass transport.

The MOCVD growth process consists of the following steps:

(1) Precursor transport from the chamber inlet to the wafer proximity.

(2) Reaction of gases to form daughter molecules.

(3) Transport of these reactants to the surface of the substrate.

(4) Surface reactions.

(5) Desorption of gaseous by-products from the reactor.

(6) Transport of by products through exhaust.

The above steps are represented schematically in Figure 3.1 [92].

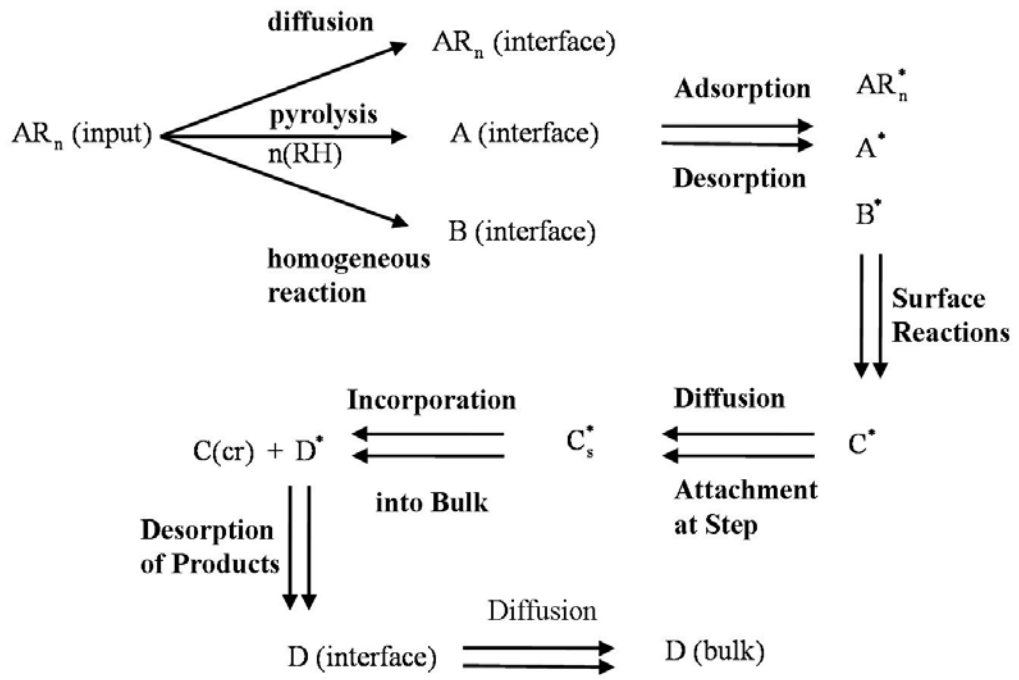

Figure 3.1: Schematic representation of the steps in the MOCVD growth process [92].

3.2. MOCVD Reactor

This study employed a commercial rotating disk reactor with a short vertical jar configuration that was modified to allow experimentation with incorporation of transition metals (TM) and rare earth (RE) dopants. This reactor has a specially modified flow flange injection system with dual injector blocks to minimize pre-reactions of the Nitride and TM/RE precursors in the transport phase (Figure 3.2).

Additionally, this tool provides the flexibility of using either nitrogen or hydrogen as the carrier gas. Purifiers have been installed to ensure that the carrier gasses are at high purity when they enter the reactor. This reactor is capable of reaching growth temperatures of up to 1200 ºC and can hold three 2” wafers at a time.

(a)

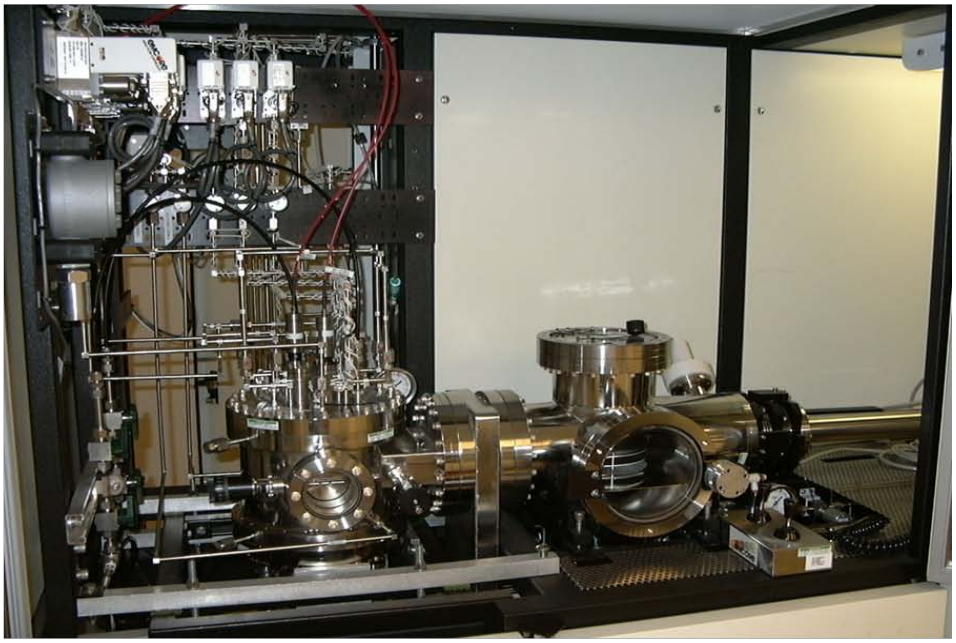

(b)

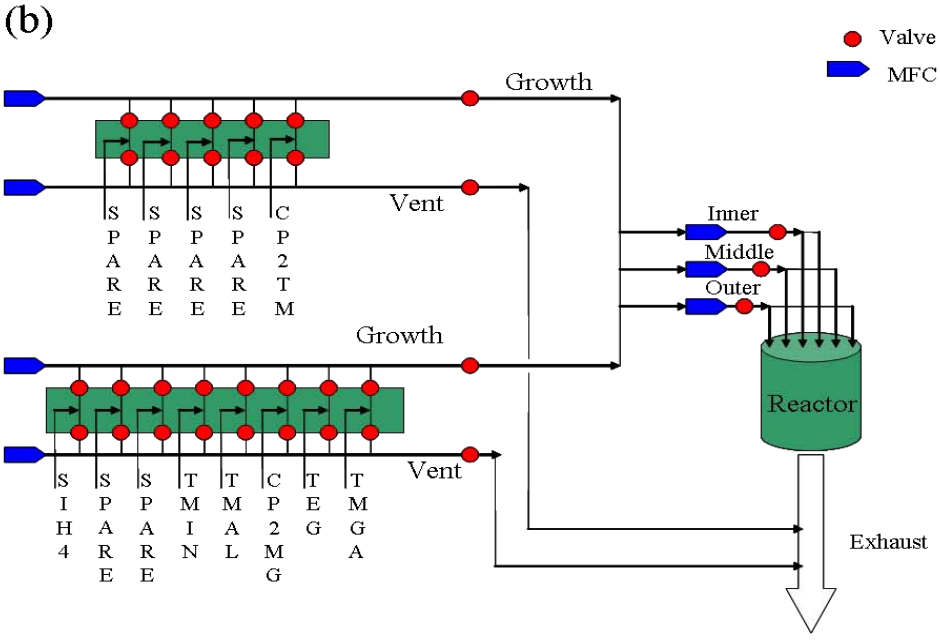

Figure 3.2: (a) Photograph of the MOCVD growth system used in this study, (b) gas flow schematic of the growth tool.

3.3. Precursor Selection

High purity precursor selection is critical for successful MOCVD growth. For the growth of III-Nitrides, it is desired that the ideal precursor be volatile and have minimal silicon and oxygen impurities as they make GaN n-type [32, 95]. An important parameter in precursor selection is the vapor pressure (V.P.) as it determines the concentration of the source dopant and the growth rate. The V.P. is given by Equation 3.1.

$$\log_{10}(P) = A - \frac{B}{T} \qquad \text{Equation (3.1)}$$

where P is the pressure in Torr,

T is the absolute temperature in degrees Kelvin, and

A and B are the vapor pressure coefficients.

The commonly used Nitride precursors are listed in Table 3.1 on the next page.

Ammonia is the precursor used for the nitrogen supply as it is readily available, cheaper, and less toxic as compared to other group V hydrides. Silane and Magnesium are the commonly used n- and p-dopants respectively for III-Nitrides. The precursors are kept in a thermal bath containing a coolant or oil and are maintained at a particular temperature to ensure that they enter the chamber in gaseous state.

The gas lines connecting the precursors to the reactor are heated to ensure that the sources do not cool on their way to the chamber and deposit in the gas lines. All the gas flows are regulated by mass flow controllers. In this study due to the low V.P. of the TM and RE precursors, high bath temperatures had to be used to ensure that the precursors entered the chamber in the gaseous state.

Table 3.1: Commonly used precursors for III-Nitride growth.

Metal Organic	Chemical Formula	A	B	V.P.
Group III precursor				
Trimethyl Gallium (TMGa)	$(C_3H_3)_3Ga$	8.495	1825	64.5 Torr @ 0 °C
Triethyl Gallium (TEGa)	$(C_2H_5)_3Ga$	9.165	2530	3.4 Torr at 20 °C
Trimethyl Indium (TMIn)	$(CH_3)_3In$	9.735	2830	1.2 Torr at 20 °C
Trimethyl Aluminium (TMAl)	$(CH_3)_3Al$	10.475	2780	9.7 Torr @ 20 °C
Group V precursor				
Ammonia	NH_3	-	-	P= 128.8 at 21 °C
n- and p-dopants				
Silane	SiH_4	-	-	P = 1250 PSIG @ 20 °C
Bis(cyclopentadienyl) Magnesium (Cp_2Mg)	$(C_5H_5)_2Mg$	10.56	3556	0.05 Torr at 25 °C
TM and RE dopants				
Bis(cyclopentadienyl)Manganese (Cp_2Mn)	$(C_5H_5)_2Mn$	-	-	0.01 Torr at 27 °C
Bis(cyclopentadienyl)Iron (Cp_2Fe)	$(C_5H_5)_2$ Fe	-	-	0.03 Torr at 40 °C
Bis(cyclopentadienyl)Chromium (Cp_2Cr)	$(C_5H_5)_2$ Cr	-	-	Expect < 0.01 Torr at 25 °C
Tris(2,2,6,6 – tetramethyl 3,5 heptanedionato) Gadolinium $(TMHD)_3Gd$	$(OCC(CH_3)_3$ $CHCOC(CH_3)_3)_3Gd$	-	-	~0.15 Torr at 140 °C

The chemical reaction that occurs during growth in the MOCVD chamber can be generalized by Equation 3.2.

$$R_3M(g) + EH_3(g) \rightarrow ME(s) + 3RH(g) \qquad \text{Equation (3.2)}$$

where R is the alkyl radical, M is a Group III element, and E is a Group V element. Here R_3M acts as a Lewis acid and EH_3 as a Lewis base [96]. With regards to the growth of GaN, the above equation translates into Equation 3.3.

$$(CH_3)_3Ga + NH_3 \rightarrow GaN + 3CH_4 \qquad \text{Equation (3.3)}$$

3.4. Substrates for Growth

The production of bulk GaN requires very high pressures (10 kbar) and high temperatures (~1600 °C), making it very difficult and expensive to obtain high quality material [32]. Because of this GaN is generally grown epitaxially on foreign substrates. The ideal substrate would have a lattice constant and thermal expansion coefficient close to GaN. The two most common substrate materials for GaN growth are sapphire and SiC. Sapphire is most commonly used due its low cost, good crystal quality, optical transparency, and its chemical stability at high temperatures. GaN is usually grown on the sapphire c-plane (0001) and has a lattice mismatch of ~15 % [97]. There is a 30° rotation of the (0001) III-Nitride plane with respect to the sapphire (0001) without which the lattice mismatch would be ~30 % [97]. 6H-SiC substrates have a basal plane lattice mismatch of 3.5 % with GaN and a more closely matched thermal expansion coefficient (Table 3.2). Previously it was difficult to obtain smooth SiC substrates, and while this problem has been overcome, these substrates are still more expensive than sapphire and thus are not as extensively used [32]. In this study, all growths were carried out on sapphire substrates.

Table 3.2: Lattice constants and thermal expansion coefficients for GaN and commonly used substrates [32].

Material	Lattice Constant *a* (Å)	Lattice parameter *c* (Å)	Thermal Expansion coefficients (K^{-1})
GaN	3.189	5.185	$\alpha_a = 5.59 \times 10^{-6}$ $\alpha_c = 3.17 \times 10^{-6}$
Al_2O_3 c-plane	4.758	12.991	$\alpha_a = 7.5 \times 10^{-6}$ $\alpha_c = 8.5 \times 10^{-6}$
6H-SiC	3.08	15.12	$\alpha_a = 4.2 \times 10^{-6}$ $\alpha_c = 4.7 \times 10^{-6}$

3.5. GaN Growth

GaN is a wide bandgap semiconductor that has found numerous applications in optoelectronic devices such as blue LEDs, laser diodes, and UV-detectors [32]. Due to the significant lattice mismatch between GaN and sapphire, it has been difficult to grow smooth, high quality GaN films. GaN growth attempts by chemical vapor deposition and sputtering processes began in the 1970s but without much success as the films obtained were rough and had high background concentrations [98, 99]. In 1983, Yoshida et al. deposited an AlN buffer layer on sapphire substrates which resulted in enhanced GaN nucleation and improved film quality [100]. This technique served as a basis for the MOCVD growth conducted by Amano et al. that used a low temperature AlN buffer layer which was crystallized prior to GaN growth. The 50 nm thick AlN layer was grown at ~600 °C on a sapphire substrate prior to GaN growth at ~1000 °C. This two step process resulted in GaN films with reduced threading dislocations and improved electrical and optical properties [28]. This technique was adopted by Nakamura in 1991, who used a GaN buffer layer for the growth of epitaxial GaN which was successfully

employed to grow blue LED structures [29, 101]. The GaN growth in this study is based on a GaN buffer layer and the entire growth processes is described below.

3.5.1. Substrate Pre-Treatment

Initially the substrate was heated to 1000 °C in hydrogen atmosphere for about 5 minutes, to reorganize and improve the growth surface. Next, the substrate underwent a nitridation step, which entailed exposure to ammonia for approximately 3 minutes. This step has been shown to be extremely important as it improves the surface quality for two dimensional GaN growth, reduces the defect density, enhances the electron mobility, and reduces the yellow luminescence in subsequently grown films [102, 103].

3.5.2. Buffer Layer Growth

As mentioned above, a buffer layer is critical to obtain good quality smooth GaN epitaxial films. During this step the substrate was cooled to 500-550 °C and a low temperature GaN buffer layer was deposited for approximately 3 minutes. At this low temperature, due to the low interfacial energy between GaN and the substrate, a high density of nucleation centers (island formation) that have the same orientation as the substrate are obtained [104].

During the early stages of the nuclei growth, these islands expand and coalesce to form lateral growth. The optimum thickness of the GaN buffer layers were determined to be around 200-250 Å, as at this thickness the buffer layer is mirror-like and enhances lateral growth.

3.5.3. Buffer Layer Recrystallization

The crystal structure of a low temperature GaN buffer is amorphous and disordered. Thus, a recrystallization step (also known as anneal step) was applied after the buffer growth. In this step the temperature was ramped up to 1000 °C in an ammonia ambient to convert the amorphous GaN to crystalline GaN.

3.5.4. Rough GaN Growth

As the temperature is ramped up to the GaN growth temperature of ~1015 °C, the nucleation centers formed during the low temperature buffer growth begin to increase in size (ripen) and also increase in roughness, and hence this layer is known as the rough GaN growth layer.

3.5.5. Recovery GaN Growth

As the high temperature growth further continues, the ripened nucleation centers begin to coalesce and the GaN growth transfers from a 3-D to a 2-D film. This step is marked by an increase in the in-situ reflectivity signal and is hence marked as the recovery stage.

3.5.6. Main GaN Growth

Finally, the 2 μm thick GaN layer is grown at ~1050 °C with high a V/III ratio in the range of 2000-3000 to ensure the presence of sufficient nitrogen. GaN is usually grown at high temperature as ammonia cracks most efficiently at temperatures greater than 800 °C. Additionally, the high growth temperature reduces the incorporation of impurities that enhance yellow luminescence. This layer is typically grown at a growth rate of ~2 μm/hr.

It is essential to grow in the optimal growth regime as the material stoichiometry and material properties are affected significantly.

Figure 3.3 displays the different steps in the GaN growth process and the corresponding in-situ reflectivity curve.

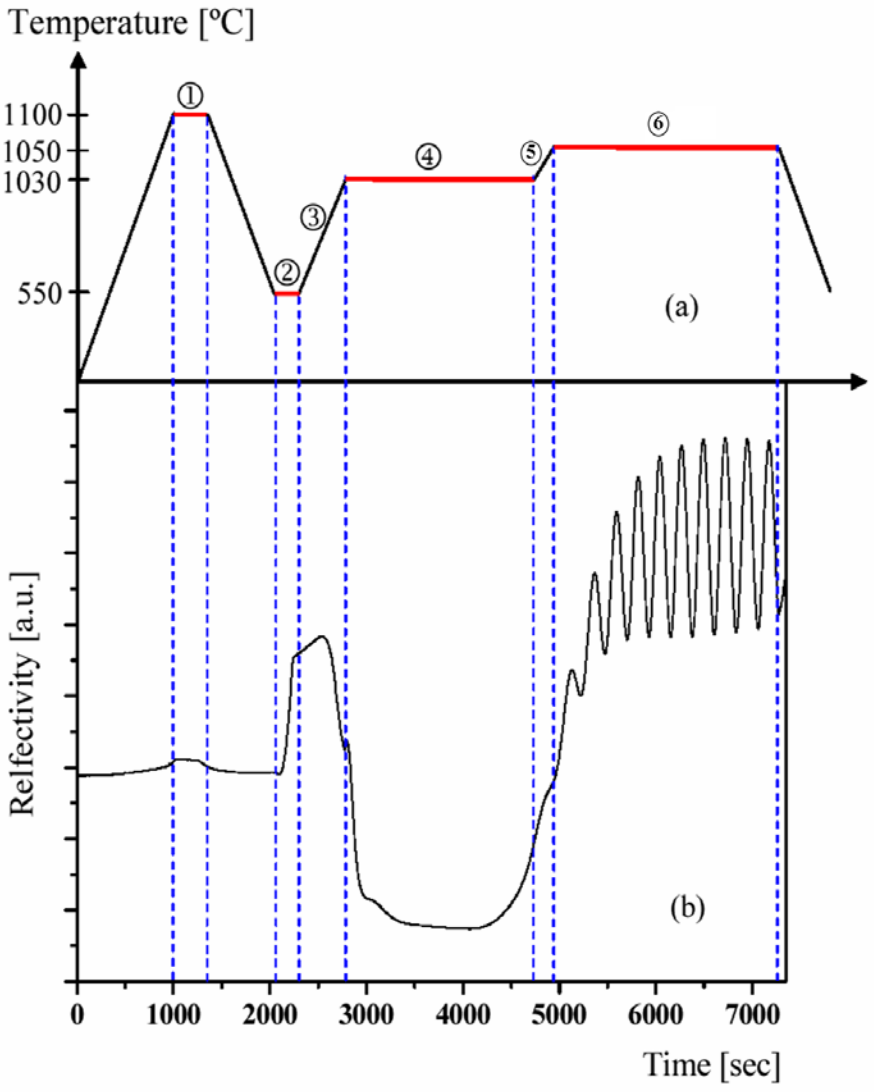

Figure 3.3: (a) Schematic of GaN growth process, (b) in-situ reflectometry curve for GaN growth, where (1) substrate pre-treatment, (2) buffer layer growth, (3) buffer layer recrystallization, (4) rough GaN growth, (5) GaN recovery, and (6) GaN growth.

3.6. In-situ Characterization

Epitaxial growth is a critical step in the manufacturing of III-V-based optoelectronic and electronic devices as it determines material quality which is a significant indicator of device performance. Thus, it is critical to have the capability to monitor and control the growth process in real time. In-situ optical reflectometry is an important real time monitoring technique that is commonly used and provides an avenue to significantly improve the productivity of MOCVD systems. This technique provides real time information regarding the growth rate, layer thickness, and surface roughness during epitaxy.

This measurement technique uses a broadband light source that is passed through a narrow bandpass filter to select a particular wavelength of light that is then focused onto the sample in the reactor though an optical fiber, and the reflectance is detected by a photo diode. In this study, the wavelength was set to 600 nm.

The fraction of the incident light that is reflected is called reflectance (R), and is given by Equation 3.4 [105].

$$R = \frac{I_{reflected}}{I_{incident}} = (n-1)^2 + \frac{k^2}{(n+1)^2} + k^2 \qquad \text{Equation (3.4)}$$

where I is the light intensity,

n is the refractive index of the material, and

k is the extinction index.

The reflectance depends on the wavelength of the incoming light and changes with the layer composition and substrate temperature. As the layer is growing, the intensity of

light reflected at the substrate and thin film interface is measured at a single wavelength as a function of time. If the growing layer is partially transparent at the wavelength of the incoming light, an intensity modulation can be observed. The period of this modulation is used to measure the thickness and growth rate of the layer. Only a part of the incoming light is reflected at the surface while the rest passes into the semiconductor layer (Figure 3.4) [105]. This transmitted beam will undergo a similar process where a part of the beam is reflected and the rest is transmitted. The resulting intensity of the reflected light is due to the superposition of all reflected beams. Fabry-Pérot oscillations are obtained due to constructive or destructive interference between the beams which have different phases.

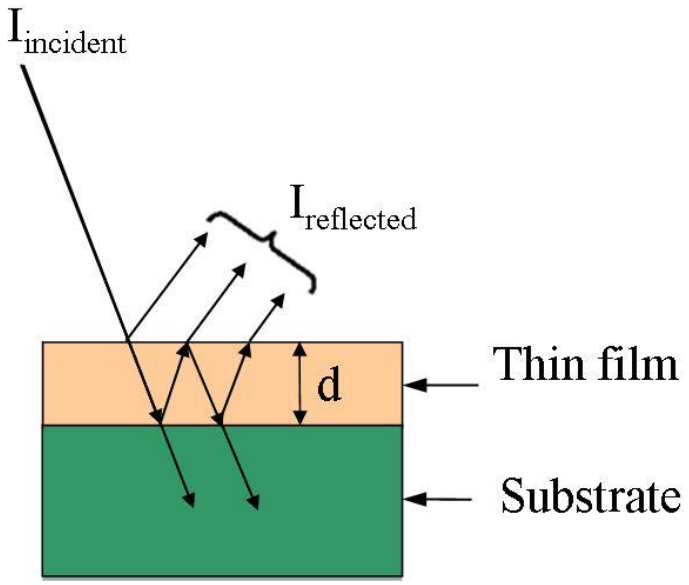

Figure 3.4: Schematic depicting the principle of in-situ reflectometry measurements for epitaxial growth [105].

The intensity of the reflected light depends on the thickness of the growing layer, the refractive index of the material, and the wavelength of the light. Constructive interference

occurs if the path difference between the beams is equal to an even integer multiple of the half wavelength as shown in Equation 3.5 [105].

$$2nd = m\lambda \qquad \text{Equation (3.5)}$$

where n is the refractive index,

d is the thickness of the layer,

m is the even number, and

λ is the wavelength.

For destructive interference the path difference is equal to an odd integer multiple of the half wavelength (Equation 3.6).

$$2nd = (m + \frac{1}{2})\lambda \qquad \text{Equation (3.6)}$$

The layer thickness (d) can thus be determined by measuring the intensity-transient of the reflected light. The growth rate (G.R.) can be determined by taking the ratio of the thickness and the growth time (t), as shown in Equation 3.7.

$$G.R. = \frac{d}{t} \qquad \text{Equation (3.7)}$$

For maximum reflectance:

$$(G.R) * t = \frac{m\lambda}{2n} \qquad \text{Equation (3.8)}$$

and for minimum reflectance:

$$(G.R) * t = (m + \frac{1}{2})\frac{\lambda}{2n} \qquad \text{Equation (3.9)}$$

Growth parameters greatly influence the, intensity, shape and period of the reflectance curve. Overall in-situ reflectometry curves provide great insight into real time growth and is an indispensable tool for epitaxy.

3.7. Ex-situ Characterization

Once a material was grown, in-depth ex-situ characterization was performed to determine the structural, optical, electrical, and magnetic properties of the films. Ex-situ characterization provides insight into the ideal growth conditions required to obtain a good film quality.

3.7.1. Structural Characterization

Due to the lack of a lattice matched substrate, several defects and dislocations occur during growth. It is imperative to carry out detailed structural characterization to ensure that the film grown is of good crystalline quality, strain free, and has a smooth surface morphology.

3.7.1.1. X-ray Diffraction

X-ray diffraction (XRD) is a non destructive technique used to determine the crystal structure, chemical composition, and the physical properties of bulk materials and thin films [94]. In this study, a Philips X'pert materials research diffractometer-pro 4-circle analyzer was used with a monochromatized CuKα (with λ = 1. 54Å) as the X-ray source. The collimated X-ray (K_0) is then projected onto a sample at an angle of θ. The sample is generally a three dimensional crystal which consists of planes of atoms separated by a distance d (Figure 3.5). The interaction of the incident beam with the sample results in constructive interference if it satisfies Bragg's law as shown in Equation (3.10).

$$n\lambda = 2d\sin\theta$$ Equation (3.10)

where n is the diffraction order as an integer,

λ is the X-ray wavelength,

d is the spacing between adjacent crystallographic planes, and

θ is the incident angle.

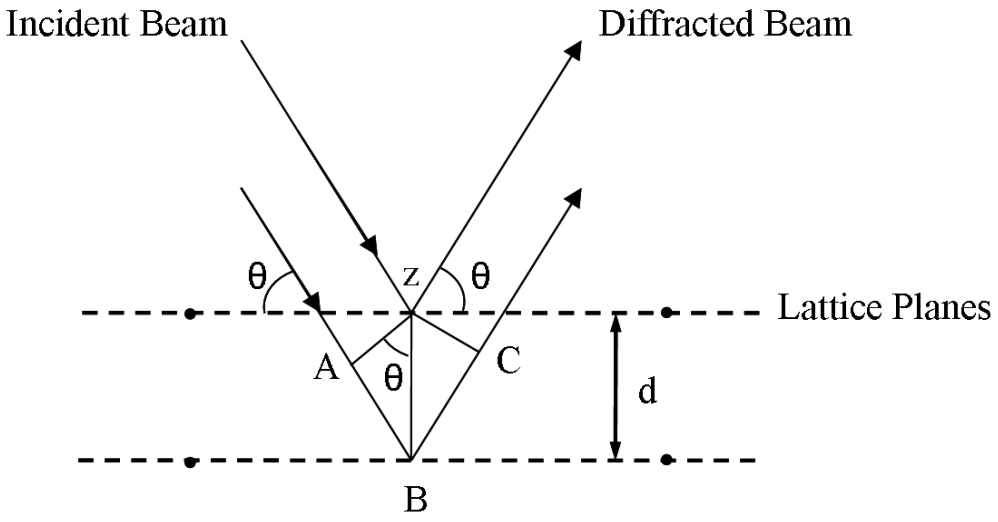

Figure 3.5: Schematic of X-ray diffraction as per Braggs law.

The diffracted X-rays are then detected. Scanning the sample through a range of 2θ angles and plotting the angular position with respect to the intensities of the resultant diffracted X-ray beam produces a pattern that is characteristic of the sample.

In epitaxial films such as GaN, there is one family of planes that is parallel to the growth axis. Other XRD measurement techniques such as rocking curve scans, reciprocal space maps, superlattice peaks, and X-ray reflectivity are often used to characterize such films in order to determine the lattice parameters, the chemical composition, and the film quality. A commonly employed rocking technique is the ω scan. In this measurement

technique, the detector is kept at fixed angle while the sample is rocked/rotated around the axis perpendicular to the diffraction plane, which in turn varies the incidence angle. The full width half maximum (FWHM) of the rocking curves is proportional to the dislocation density and hence this measurement is useful to determine the material quality [94]. Furthermore, the FWHM of the rocking curves conducted of on off-axis planes (i.e. 102) can be used to determine the crystal quality as these peaks are more sensitive to threading dislocations. In this study, the on axis (002) FWHM for the 2 μm GaN films is 250 arcsec, while the FWHM for the off axis scan is 350 arcsec for (102) off axis.

Another common measurement technique is the ω-2θ scan. In this measurement technique, the detector rotates at an angle twice that of the sample, thus the diffraction angle is equal to the angle of the incident beam. The angular spread of the diffracted beam is not measured; therefore, the diffraction peaks are narrower and do not overlap as much as in the ω scan. This measurement provides information about lattice mismatch between the film and the substrate, and therefore, is indicative of strain and stress in the epitaxial layer.

3.7.1.2. Raman Scattering

Raman scattering is a structural diagnostic technique based on the inelastic scattering of light by molecules and crystals. In this measurement, light of a known frequency and polarization is focused on the sample being measured. This light then undergoes scattering and the scattered light's frequency and polarization is analyzed. Raman scattered light is frequency-shifted with respect to the excitation frequency, but the magnitude of the shift is independent of the excitation frequency. This "Raman shift" is therefore an intrinsic property of the sample. The inelastic exchange occurs because the

incident photons either lose or gain energy from the material under examination. These photons scatter due to their interaction with lattice vibrations (phonons). The inelastic scattering is a result of a frequency shift of the scattered photon to longer wavelengths (Stokes shift: emitted photon has less energy than incident photon) or shorter wavelengths (anti-Stokes shift: emitted photon has greater energy than incident photon). In general, only a small fraction of the incident photons (1 in 10^6-10^7) undergo inelastic scattering. A typical Raman spectrum consists of the scattered light intensity plotted versus the wavenumber. Raman spectroscopy can be used to measure the strain and stress in a material, as the phonon frequencies depend on the chemical bonding and atomic structure.

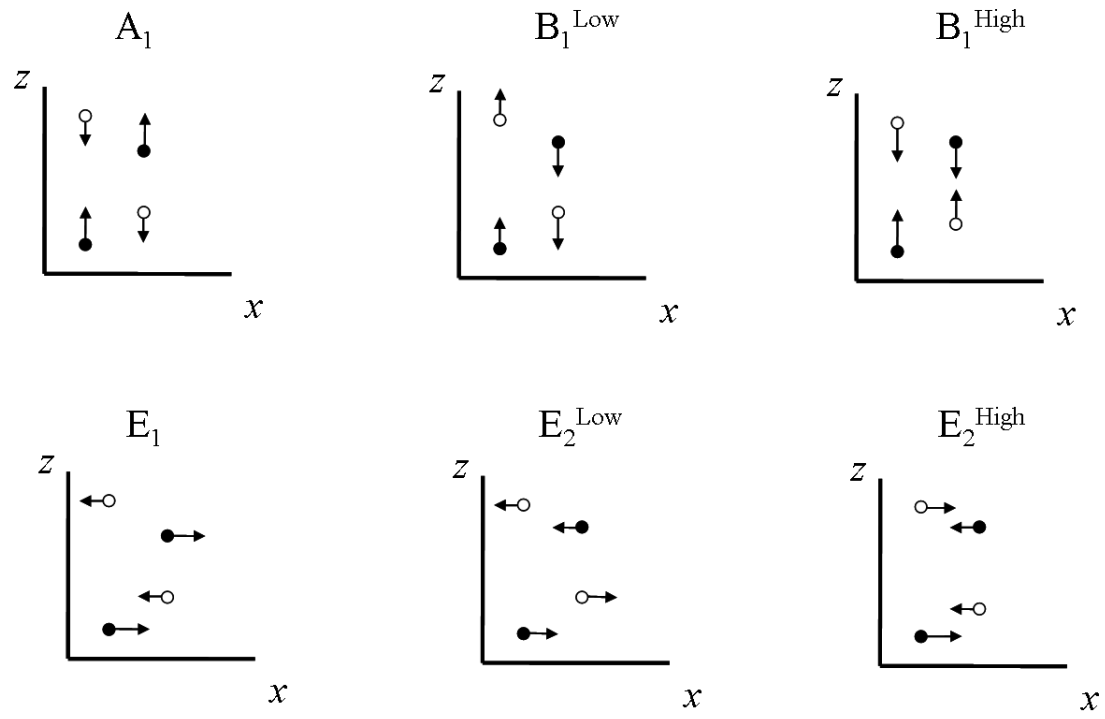

Figure 3.6: Schematic of the atomic displacements for long range phonons in wurtzite GaN [106].

Porto notation is the notation used for identifying the direction and polarization of the incident and scattered light. This notation is represented in the following form a(b,c)d, where a is the direction of the incident beam, b the polarization direction of the incident beam, c is the polarization direction of the scattered beam, and d is the direction of the scattered light. Figure 3.6 shows the optical vibrations for wurtzite GaN and their direction.

The A_1 and B_1 modes are atomic displacements along the *c*-axis, while the E_1 and E_2 are atomic displacements perpendicular to the *c*-axis. The two E_2 modes are Raman active, the A_1 and E_1 modes are both Raman and infrared (IR) active, and the two B_1 modes are neither Raman nor IR active (silent modes). The low and high superscript denote low and high frequencies [106]. Table 3.3 shows the configuration of the allowed Raman modes in wurtzite GaN: TO and LO are the transverse optical and longitudinal optical phonons, respectively.

Table 3.3: Raman configurations of allowed modes in hexagonal Nitrides [106].

$x(yy)^{-}x$	$x(zz)^{-}x$	$x(z,y)^{-}x$	x(y, z)y	x(y,y)z	z(y,x)z	$z(y, y)^{-}z$
$A_1(TO)$, E_2	$A_1(TO)$	$E_1(TO)$	$E_1(TO)$, $E_1(LO)$	E_2	E_2	$A_1(LO)$, E_2

Table 3.4 shows the values of the phonon frequencies observed for bulk GaN at room temperature (RT).

Table 3.4: Active Raman phonon frequencies (cm^{-1}) for bulk GaN at RT [106].

Material/Modes	E_2 (low)	$A_1(TO)$	$E_1(TO)$	E_2 (high)	$A_1(LO)$	$E_1(LO)$
GaN	144	532	559	567	734	741

In this study, a Renishaw micro-Raman system with a 488 nm excitation source was used to perform the Raman measurements.

3.7.1.3. Atomic Force Microscopy

Atomic Force Microscopy (AFM) is a high resolution scanning probe microscopy technique that can be used to image organic and inorganic surfaces with near atomic resolution. In 1986, Gerd Binnig, Christoph Gerber, and Calvin Quate developed the AFM to measure non conducting surfaces. The cantilever used in this original measurement consisted of a diamond shard glued onto a strip of gold foil. This tip was placed in direct contact with the surface, and was rastered over the surface. The Van der Waals forces between the tip and the sample cause the cantilever to deflect as per Hooks law, shown below in Equation (3.11). It is this deflection that is used to determine the topography. In modern AFM systems the cantilever assembly is typically fabricated from Si or Si_3N_4 and can have a tip radius as low as 10 nm and spring constants ranging from 0.1-50 N/m.

$$F = kx \qquad \text{Equation (3.11)}$$

where k is the characteristic spring constant (N/m), and x is the cantilever deflection (nm).

In this study a Park Systems XEI 100 AFM system was used to determine the sample topography and sample roughness. This tool has an acoustic enclosure for damping out noise and is capable of maximum scan sizes of 45 μm^2. The sample under test is placed on a stage that can be moved in the x and y direction. The cantilever-tip assembly is mounted onto a piezoelectric crystal that moves in the z directions. This system contains

an active feedback mechanism that enables the piezoelectric z scanners to maintain the tip at a constant force or height as the tip is scanned over the sample.

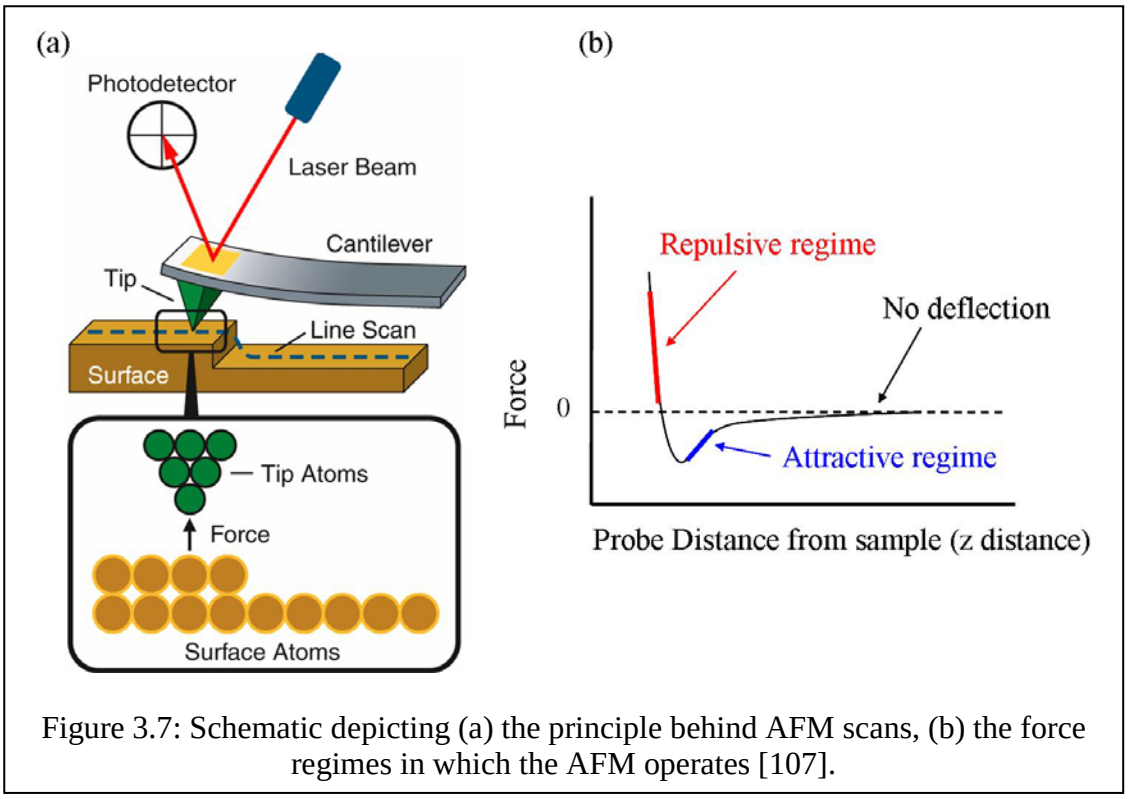

Figure 3.7: Schematic depicting (a) the principle behind AFM scans, (b) the force regimes in which the AFM operates [107].

This AFM uses an optical detection system in which a laser diode is focused onto the backside of a reflective cantilever to which the tip is attached. As the tip scans over the contours of the sample, the reflected laser beam is focused onto a photodiode that converts this signal into a voltage that is used by the piezoelectric scanner to maintain the cantilever at constant force or height (Figure 3.7a) [107].

This AFM is equipped with two main operating modes: contact mode and non-contact mode. In contact mode measurements, the tip is in contact with the sample surface. The short range repulsive forces (~10^{-9} N) between the tip and the sample cause the cantilever to deflect, the force between the cantilever and the sample is kept constant by the feedback loop. The cantilever displacement provides information on the sample

height and the surface topography is obtained by plotting the sample with respect to horizontal tip position.

In non-contact mode, the cantilever is made to vibrate at very small amplitudes and at a fixed frequency that is close to the cantilever resonant frequency (~100-400 kHz). As the tip is scanned approximately 50-150 Å above the sample surface the long range attractive Van der Waals forces (~10^{-12} N) between the tip and the sample cause the amplitude and phase of the cantilever vibration to change. These changes are monitored by the feedback loop and the scanner responds to maintain a constant tip-to-sample distance. It is this change of the scanner with respect to position that is used to obtain the sample topography (Figure 3.7b). In this study, contact mode was used to analyze the 2D thin films and non contact mode was used to scan the rough surface of QD films.

3.7.1.4. Secondary Ion Mass Spectrometry

To determine the concentration of the transition metal dopants, a secondary ion mass spectrometer (SIMS) was used. In this measurement technique an ion gun releases ionized particles that are bombarded onto the sample at a high energy (~1-30 keV), resulting in the emission of secondary ions (sputtered particles). These secondary ions are detected by a mass spectrometer, which identifies the elements by comparing their mass to charge ratio (m/e) to a calibration sample. In this work, SIMS measurements were conducted using an Atomika Instruments Ion Microprobe A-DIDA 3000. An oxygen or cesium beam is commonly used as the sputtering source for electropositive and electronegative elements respectively as they result in high ion yield. Depth profiles can be determined as well by measuring the secondary ion count rate as a function of time.

3.7.1.5. Energy Dispersive X-ray Spectroscopy

Energy dispersive X-ray spectroscopy (EDS) was used to determine the TM and RE doping concentration. This measurement is a chemical microanalysis technique performed in conjunction with a scanning electron microscope (SEM). In this measurement technique, the sample is bombarded with the electron beam of the SEM, and electrons are ejected from the atoms on the sample surface. This resulting vacancy is filled by an electron from a higher shell and an X-ray is emitted to balance the energy deference between the two states. EDS identifies the elements in the sample by using this X-ray energy, which is characteristic to a particular element. The EDS X-ray detector measures the intensity of emitted X-rays versus their energy. A spectrum of the energy versus relative counts of the detected X-rays is obtained and evaluated for qualitative and quantitative determinations of the elements present in the sampled volume. In this study a LEO 1530 thermally-assisted field emission SEM system was used. This tool has an operating voltage in the range of 200 V-30 kV, and has a resolution of up to 1 nm at 20 kV.

3.7.2. Optical Characterization

GaN is a direct bandgap semiconductor that is commonly used to manufacture opto-electronic devices such as LEDs and lasers, thus it is crucial to analyze the optical properties of the GaN films before they are incorporated into device structures. The optical characterization techniques used in this study are described below.

3.7.2.1. Photoluminescence Measurements

Photoluminescence is an important non-destructive technique that can be used to determine the material bandgap, impurity and defect levels and the material quality.

Photoluminescence is defined as light emission that is caused by irradiation of a material by a separate light source. In this measurement a material (usually a direct bandgap semiconductor) is typically excited by a light source that has photon energy greater than the semiconductor bandgap energy. This photo-excitation causes electrons within the material to move into permissible excited states. When these electrons return to their equilibrium states, the excess energy can be released in the form of light emission, which is known as a radiative process. The energy of the emitted light (photoluminescence) relates to the difference in energy between the excited and equilibrium states involved in the transition. The quantity of the emitted light is related to the relative contribution of the radiative process. The permissible electron states involved in radiative recombination can be: band-to-band, donor-to-valence band, conduction band-to-acceptor, donor-acceptor transition, and transition within a localized lumine [108]. A schematic of these cases is shown in Figure 3.8. Non-radiative recombination can occur via an intermediate state. Shallow levels, near the bandedge, participate in radiative recombination, but temperature must be low to discourage thermal activation of non-radiative traps.

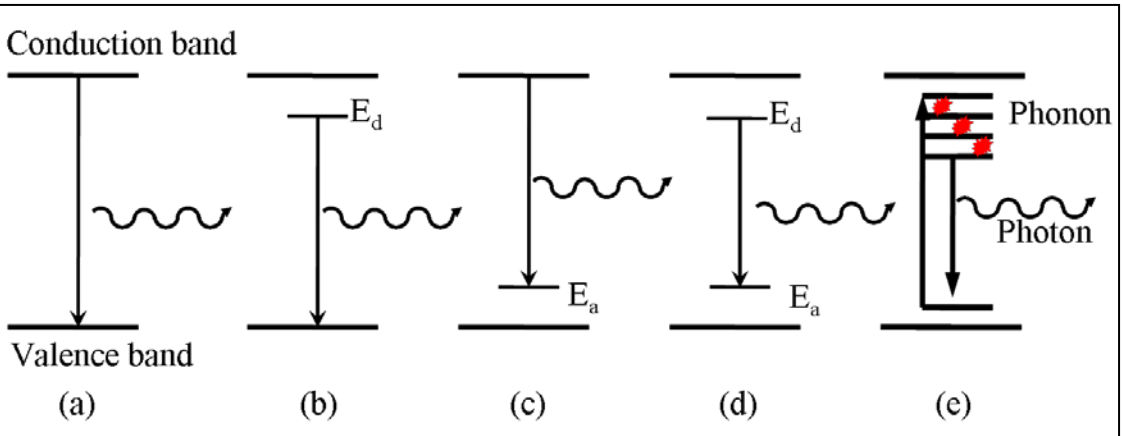

Figure 3.8: Schematic of possible optical transitions that can be observed by photoluminescence (a) band-band, (b) donor level-valence band, (c) conduction band-acceptor level, (d) donor-acceptor transition, (e) transition within localized lumine [108].

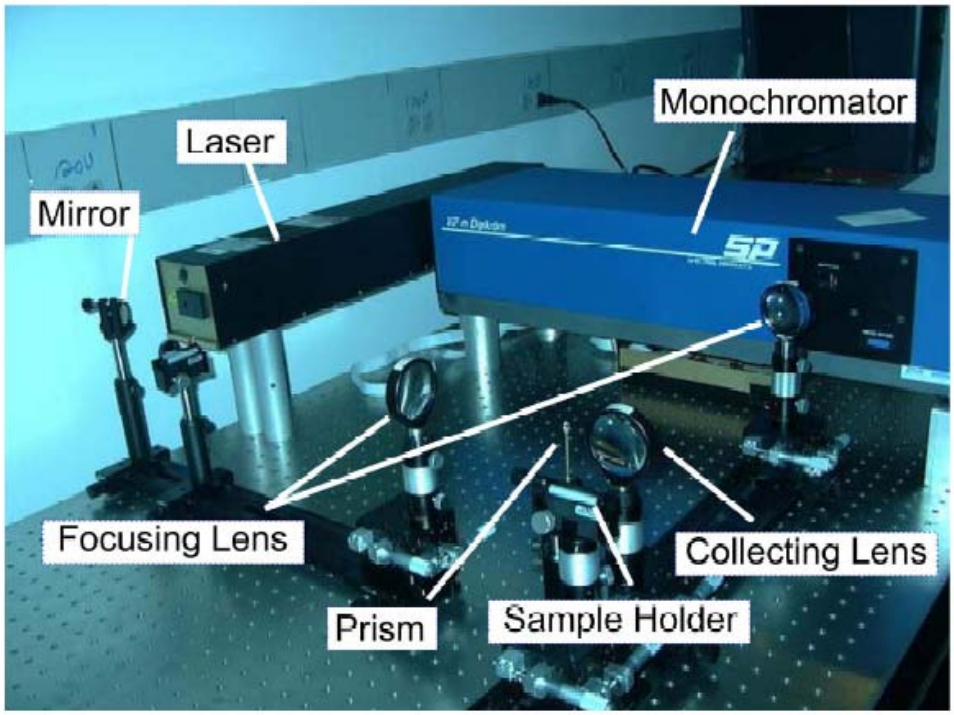

Figure 3.9: PL setup used for this research.

The PL setup used in the study is shown in Figure 3.9. This study employed two laser excitation sources, namely a He-Cd 325 nm laser and a Ne-Cu 248 nm laser system. The laser is focused onto a sample through a focusing lens and prism. The light emitted from the sample is directed through a collecting lens and then focused onto a monochromator and finally detected using either a CCD camera or photomultiplier tube.

3.7.2.2. Optical Transmission

Optical transmission measurements were performed in this study to determine the internal transitions (i.e. d-d transitions) that occur in the TM and RE dopants. In this measurement technique a broadband light is focused onto the sample; the transmitted light is then passed through a monochromator and detected by a photomultiplier tube. A Varian–Cary 300 UV-VIS spectrometer was used for transmission measurements in the UV-visible range.

3.7.3. Electrical Characterization

Before a film is incorporated into a device structure electrical characterization measurements are carried out to ensure that the film is conductive and can be incorporated into devices. This consists primarily of Hall effect measurement. The Hall effect measurement setup used in this work is described below.

3.7.3.1. Hall Measurements

Hall measurement is a fast and simple technique that is used to determine carrier density, electrical resistivity, and the mobility of carriers in semiconductors. The underlying principle behind the Hall effect is the Lorentz force, which is the force experienced by a charged particle moving in a direction perpendicular to a magnetic field. This force is perpendicular to both the particles velocity and the magnetic field and is given by Equation (3.12).

$$F = q(E + v \times B) \qquad \text{Equation (3.12)}$$

where q is the charge of particle,

E is the electric field,

v is the carrier velocity, and

B is the magnetic field.

For Hall effect measurement a magnetic field is applied to a conductor perpendicular to the direction of current flow in the conductor. This produces an electric field which is perpendicular to the magnetic field and the current (Figure 3.10) [94].

For constant current flow in the presence of a magnetic field, the carriers will be subjected to a Lorentz force and drift away from the direction of the current flow resulting in the excess charge on one side of the sample. This excess charge is the origin of the Hall voltage (V_H).

For an *n*-type material, the sheet carrier concentration (n_s) can be obtained by measuring the Hall voltage and is given by Equation (3.13).

$$n_s = \frac{IB}{q|V_H|} \qquad \text{Equation (3.13)}$$

where I is the current,

B is the magnetic field, and

q (1.602×10^{-19} C) is the elementary charge.

The carrier type is determined by the sign of the V_H.

The sheet resistance (R_S) and the mobility (μ) can then be determined by Equation 3.14.

$$\mu = \frac{|V_H|}{R_s IB} = \frac{1}{(qn_s R_s)} \qquad \text{Equation (3.14)}$$

In this research, an Ecopia EKS Hall effect measurement system with a 0.51 T magnet was used to perform the measurements. All samples were measured using Van der Pauw geometry with Ohmic contacts made using an indium alloy.

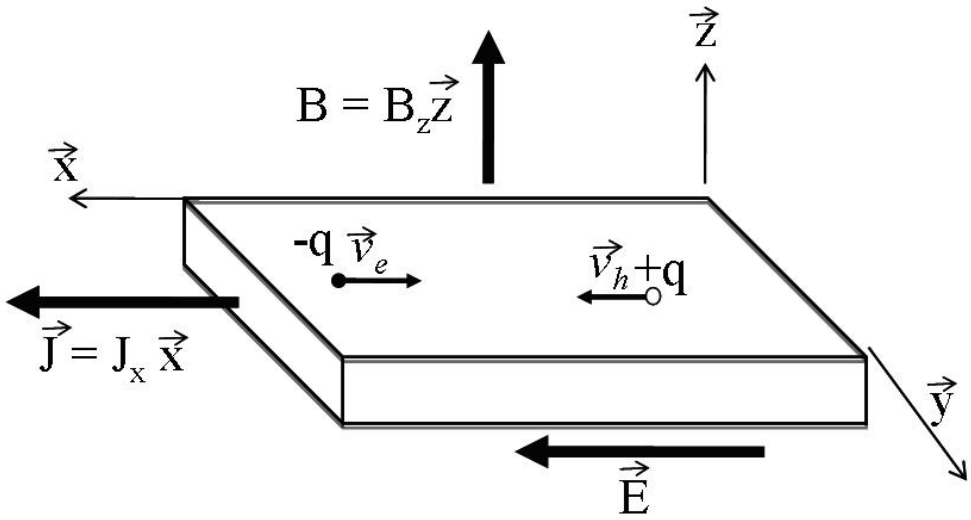

Figure 3.10: Schematic of the Hall measurement setup with a uniform electric field applied in the x direction with the magnetic field applied perpendicular to the electric field [94].

3.7.4. Magnetic Characterization

As this study is focused on developing a RT ferromagnetic semiconductor, it is essential to perform magnetization studies on the TM and RE doped GaN films. The magnetic characterization techniques used in this study are described below.

3.7.4.1. Vibrating Sample Magnetometry

Vibrating sample magnetometry (VSM) was invented by Simon Foner in 1956 and is now widely used for measuring magnetic properties of materials. This measurement technique is based on Faraday's law of induction, which states that an electromotive force (e.m.f) is induced in an inductor by a changing magnetic field. This electric field can be measured and provides information on the changing magnetic field. A VSM is used to measure the magnetic behavior of magnetic materials.

In this measurement technique, a sample is mounted on a rod and placed in between the coils of an electromagnet. If the sample is magnetic, the magnetic domains will be

aligned in the presence of a magnetic field. The sample is then vibrated at a known low frequency. This vibration causes the magnetic field to alternate with respect to the sample, resulting in an electric field in the pick-up coils. The resulting current will be directly proportional to the magnetization of the sample, and the greater the magnetization, the greater the induced current.

In this work, measurements were performed using a Lakeshore 7404 vibrating sample magnetometer, with the magnetic field applied both parallel and perpendicular to the plane of the thin film. Although VSM is not as sensitive as a superconducting quantum interference device (discussed in the next section), it is comparatively a faster and cheaper technique to measure the magnetization.

3.7.4.2. SQUID

A superconducting quantum interference device (SQUID) is the most sensitive device used for detecting magnetic flux. This device can also be used to detect small magnetic fields, current, voltage, inductance, and magnetic susceptibility. The DC SQUID is commonly used and consists of two superconductors separated by thin insulating layers to form two parallel Josephson junctions. The central element of a SQUID is a ring of superconducting material through which a constant biasing current is fed. The sample under test is placed on a rod and moved using a step motor through a pair of induction coils in the presence of a superconducting magnet. As the sample passes through, the magnetic moment of the sample induces an electric current in the coils. These current changes are indicative of the changes in the magnetic flux. The SQUID functions as a linear current-voltage converter, thus the variations in the current result in corresponding variations of the SQUID voltage, which is proportional to the change in

magnetic flux (Figure 3.11) [109]. The SQUID response is the voltage plotted as a function of the sample position and is fitted to yield the sample magnetization.

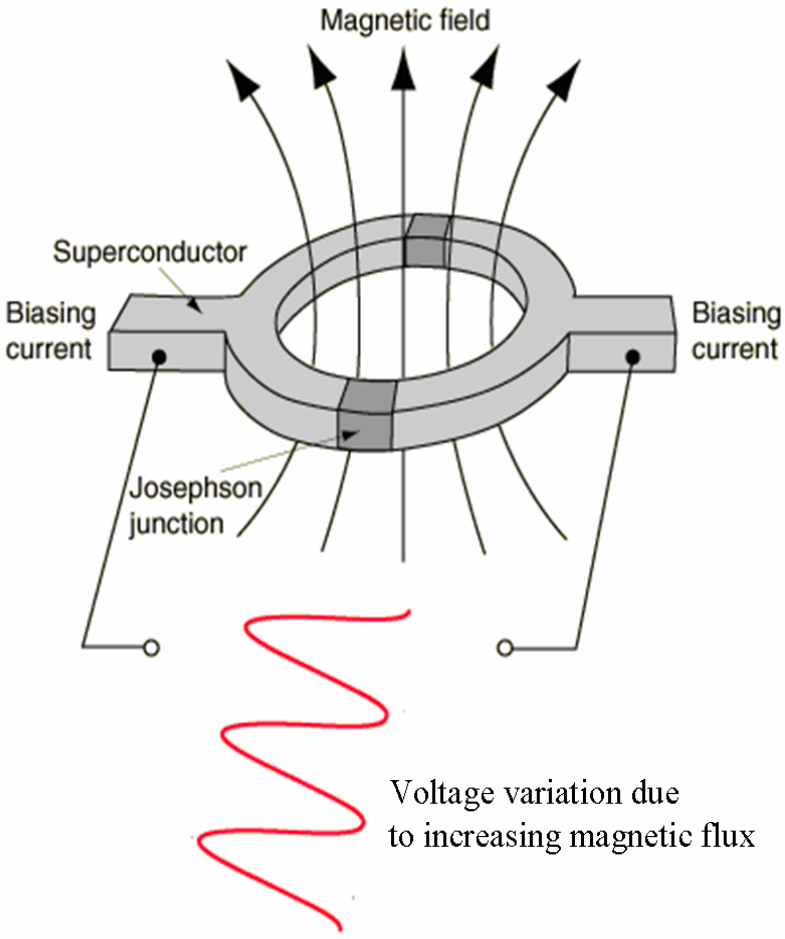

Figure 3.11: Schematic of a SQUID measurement system [109].

In addition to measuring the magnetization as a function of the applied field at a constant temperature, the magnetization of the sample can also be measured as a function of temperature under a constant applied field. The commonly used temperature measurements are the zero-field cooled (ZFC) and the field cooled (FC) measurements. ZFC measurements are done by cooling the sample from RT to a low temperature (LT) with the magnetic field set to zero. A magnetic field is applied and the magnetic moment is measured as the temperature is increased to desired level.

In the FC measurements the sample is cooled to the lowest point in the presence of a magnetic field and the magnetic moment is measured as the temperature is increased. ZFC/FC measurements are good to determine the Curie temperature of the sample and to determine the temperature range over which the magnetization is reversible.

A Quantum Design MPMS-5S SQUID magnetometer was used for these measurements. The magnetization measurements were conducted by varying the applied field from -5 T to +5 T. The ZFC/FC measurements were conducted from 5 K to 400 K under an applied field of 100 G. The background signal (arising from the sapphire substrate) for the transition metal and rare earth doped GaN was found to be diamagnetic and was subtracted from the magnetization data reported here.

3.8. Device Fabrication

After the individual films grown are analyzed and their material quality is verified suitable for devices, an LED structure is grown as shown in Figure 3.12. The active layer consists of 5 multi quantum wells which are made up of InGaN wells and GaN barriers. The steps to fabricate the device structure grown are described below**.**

3.8.1. p-type Activation

The first step in the fabrication of GaN LEDs is to activate the Mg acceptors that are passivated by hydrogen atoms. This is accomplished by utilizing a rapid thermal annealer (RTA), which uses infrared lamps to rapidly heat a sample for short periods. Other applications for RTAs include annealing contacts and ion implantation samples. This work utilized an AET addax RX RTP. This RTP can heat samples up to 1100 °C in 20

seconds. The p-type activation in this research involves annealing in an N_2 atmosphere at 800 °C for 4 minutes.

3.8.2. Photolithography

Photolithography is the process of transferring a pattern from a mask onto a wafer. The photolithography process relevant to this study is described below.

3.8.2.1. Wafer Cleaning

After the MOCVD growth of a GaN-based LED the wafer is cleaned with organic solvents to remove any surface impurities. This consists of rinsing the sample with acetone followed by a methanol and then by deionized water. The wafer is then dried using a nitrogen gun leaving it ready for photoresist coating.

3.8.2.2. Metal Deposition – Current Spreading Contact

The p-GaN resistance is a few orders of magnitude higher than the n-GaN layer, so a current spreading layer is deposited on top of the p-GaN layer to ensure that current spreads to regions not covered by the top electrode. This current spreading layer acts as an Ohmic contact and should be transparent to the emitted light so as not to negatively impact efficiency. An electron beam evaporator is used to deposit this current spreading layer which consists of 5 nm of Ni (adhesion layer) followed by 5 nm of Au. In this research a CVC e-beam evaporator was used for metal deposition. In this deposition technique a high energy electron beam is focused on the center of a crucible that contains the metal to be evaporated. This energy causes the metal to melt and evaporate onto the sample which is placed face down above the crucible. The chamber is pumped down to a

pressure of 5 x 10^{-7} Torr to increase the mean free path of the evaporated particles. The deposition rates range from 2 to 5 Å/second.

3.8.2.3. Current Spreading Contact Annealing

The current spreading contact is annealed in an RTA at 500 °C in atmosphere for 2 minutes. This causes the formation of a NiO layer at the inference and facilitates an Ohmic contact to the p-GaN surface.

3.8.2.4. Mesa Pattern Transfer

Next photolithography is used to transfer the mesa pattern onto the wafer, which defines the outline for each LED. Two coats of the positive photoresist AZ5214 are spun onto the sample at 2500 RPM for 30 seconds. The wafer then undergoes a soft bake which entails heating a wafer on a hotplate at 100 °C for 1.5 minutes. The soft bake drives away the solvent from the resist and makes it more photosensitive. A mask aligner is used to align the mesa mask with the wafer being patterned. Ultraviolet light having an energy of 60 mJ/cm^2 is exposed through the mask pattern onto the photoresist on the sample. The exposed areas of the resist undergo a chemical change when exposed to light. The sample then undergoes a post-exposure bake at 115 °C for 2.5 minutes; this causes cross linkage of the PR in the exposed regions. This is followed by a flood exposure of UV light (no mask is used) at 180 mJ/cm^2 which causes the unexposed photoresist area to undergo a chemical reaction which makes it more soluble in the developer. Finally the pattern is obtained by placing it in a developer solution of 5:1 H_2O:AZ 400 K for 1 minute.

3.8.3. Mesa Etch

Before the LED mesas can be defined by etching, the devices are dipped in potassium iodide to etch away any metal that is not covered by the photoresist. The sample is then cured by baking in an oven for 30 minutes at 120 °C. A Plasma-Therm inductively coupled plasma (ICP) etcher is used to etch the GaN films. ICP etching uses radio frequency induced plasma consisting of Cl_2-Ar gas to generate free ions which are accelerated towards the surface to be etched. Chemical reactions occur between chlorine and gallium, and the surface is etched away. The sample is removed from the chamber, and its depth profile is measured to confirm the etch depth. After this, it is cleaned and is ready for the next processing step.

3.8.4. n-GaN Contact

The pattern transfer for the n-GaN bonding pad is performed next. This procedure begins with the same photolithography step mentioned prior to the mesa etch, except only a single coat of photoresist is used, and the spin speed is increased to 3500 rpm. The metal deposition begins with 10 nm of titanium acting as an adhesion layer, followed by 50 nm of aluminum, 10 nm of titanium, and finally 200 nm of gold. A thick layer of gold is deposited so that the sample can be wire bonded if needed. After metal deposition, a lift off process is performed by dipping the wafer in acetone to remove the metal from the regions that were covered by the photoresist.

3.8.5. p-GaN Contact

Finally, the p-contact is deposited. This procedure is similar to the n-GaN contact, except the layers used are 50 nm of nickel and 200 nm of gold. The GaN-based LED structure is shown in Figure 3.12 along with a photograph of a fabricated LED.

3.9. Device Testing

Upon completion of device fabrication the LEDs can be electrically tested. The two types of testing performed on for devices are I-V and electroluminescence (EL). The I-V measurements in this study are performed by connecting the LEDs to a Keithley source-meter, which sweeps a voltage source over a defined range while measuring the current supplied to the device. These results are recorded by Keithley's LabTracer software. The GaN-based LEDs in this research had a typical forward voltage of 3.5 V at 20 mA.

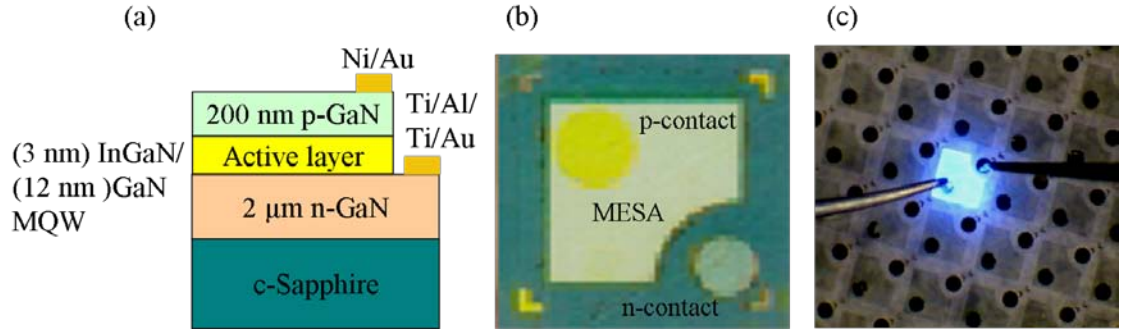

Figure 3.12: (a) Schematic of GaN-based LED structure, (b) schematic of overlay of contact masks, (c) photograph of electroluminescent measurement of fabricated LED.

The electroluminescence measurements are performed by connecting the LEDs to a power supply to pass a current through the device that causes the recombination of electrons and holes in the active region and thereby results in light emission (Figure 3.12c). As this work involves measuring the spectrum of a spin-LED, the electroluminescence measurements are conducted in the presence of a magnetic field, and the emitted light is passed through a collecting lens onto a quarter wave plate followed by a linear polarizer that is oriented at +45 or -45 degrees with respect to the optical axis. This light is then passed into a monochromator followed by a PMT. The difference in

intensity for the two orientations of the linear polarizer is an indicator if the light emitted is more left or right circularly polarized or linear.

3.10. Conclusions

This chapter provides the basic principle behind the growth technique and characterization techniques used in this study, and provides a foundation for understanding the results presented in later chapters.

CHAPTER 4

DEVELOPMENT OF A DILUTE MAGNETIC SEMICONDUCTOR BY TRANSITION METAL DOPING OF GaN

4.1. Introduction

The most common way to create a dilute magnetic semiconductor (DMS) is by transition metal (TM) doping of the host semiconductor [11]. TMs have valence electrons in the 4s shell and partially filled 3d orbitals. The unpaired spins in the 3d orbitals are responsible for the magnetic behavior. The TMs generally replaces the cation site in the GaN host lattice (i.e. Ga in the GaN host lattice), and depending on the Fermi level, are generally incorporated as either TM^{3+} or TM^{2+} [16]. This substitution results in a strong hybridization of the 3d orbitals of the TM ions and the p orbitals of the host anions. It is crucial that they have a Curie temperature (T_C) equal to or higher than room temperature, i.e. the DMS should retain its magnetic properties at room temperature to be viable for spintronic device applications.

Investigations of TM in GaN were first motivated by the theoretical findings of Dietl el al. [15] that suggested that room temperature (RT) ferromagnetism exists in GaN when 5 % Mn is introduced into p-type material. This is due to the strong p-d hybridization that results from the small lattice size of GaN and the small spin-orbit dephasing interaction. Since then several experimental and theoretical studies have been carried out on TM doped GaN, with the Mn doping of GaN being the most widely studied [16]. These studies have resulted in conflicting observations and a wide range of values for T_C (from 10-940 K) have been reported for Mn doped GaN [110-112]. Furthermore, there is no

consensus on the mechanism behind the observed ferromagnetism in these materials. A reason for the varying observations is that different growth techniques result in the TM being incorporated differently. The ferromagnetism mechanism behind TM doped GaN can be better understood by using a consistent growth technique to study a series of different TM's within the same system. This will show how the magnetic properties are changed by increasing and decreasing the number of unpaired electrons that interact magnetically with the host semiconductor (Figure 4.1) [16, 19, 20, 58, 113-116]

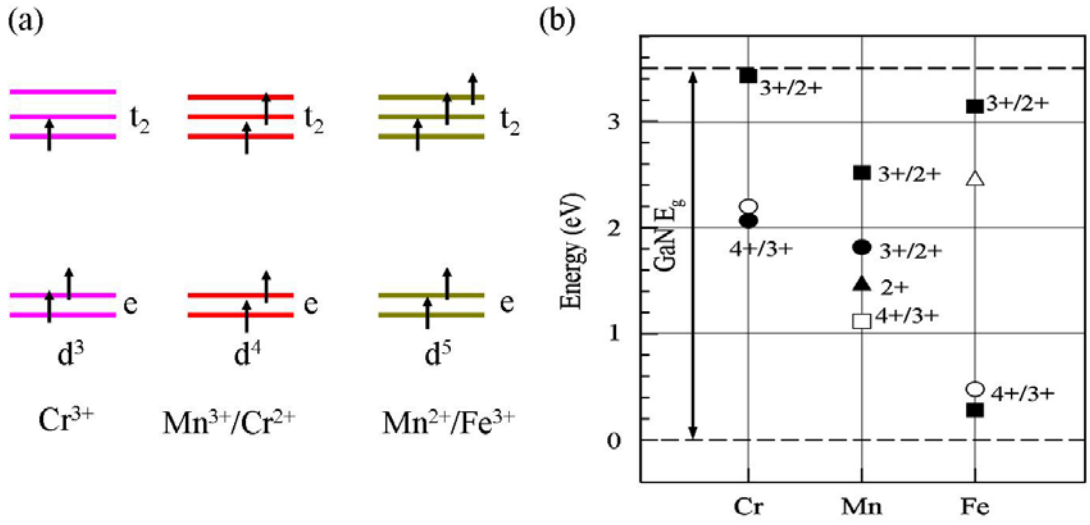

Figure 4.1: (a) Schematic of the electronic configuration of the TM ions, (b) charge transfer levels within the GaN bandgap for the TM used in this study (adapted from Liu et al. [16], where the data represented as (■) are from Gerstmann et al. [113], (▲) from Mahadevan et al. [20,114], (●) from Graf et al. [19], (△) from Baur et al. [115], (○) from van Schilfgaarde et al. [58], and (□) from Han et al. [116].

Moreover, the investigation of several different transition metals enables the concurrent variation of a number of other parameters of interest in the various materials systems. In particular, the location of the acceptor level in III-V semiconductors is an important parameter (Figure 4.1), as it influences the interaction of the magnetic center and band carriers (electrons or holes) in the carrier mediated model or the polaronic radii

and percolation threshold in a bound magnetic polaron model. The degenerate doping levels of the TM ions induce the formation of impurity bands and act as a pinning level for the Fermi energy. The location of this pinning level influences the defect formation (Ga vacancy (V_{Ga}) or Ga interstitial (Ga_i) in GaN) which in turn influence the material's overall properties [117]. Figure 4.1 shows the relative electronic configuration of Cr, Mn, and Fe in the high spin configuration within a tetrahedral crystal field environment. As the electronic configuration progresses from d^3 to d^5, in addition to the unpaired magnetization going from $3\mu_B$ to $5\mu_B$, the impurity band levels go from one-third to completely filled, which should have a strong impact on the magnetic behavior. The relative position of the $TM^{2+/3+}$ acceptor level within the bandgap is also shown; the Mn level resides lower than either the Cr or Fe levels due to the large correlation energy for Mn^{2+} in the d^5 configuration driving the acceptor level towards the valence band [118, 119]. At these energy levels the formation of nitrogen vacancies is energetically more favorable [117], which could have a large effect on the nano-scale atomic ordering. In addition, some theoretical investigations have examined the role of various transition metals on the magnetic ordering within the system [18]. Comparing the observed properties with those predicted by first principle calculations can also provide some insight into the effectiveness of correlating the model with observed behavior.

Furthermore, if cluster formation or secondary phases are the main driver behind the magnetism then by analyzing the T_C of the magnetic semiconductor the configuration of the clusters or secondary phases formed can be determined [58]. For example, Mn_4N is ferromagnetic with a T_C of 743 K, while Fe_3N has a T_C of 548 K [110, 120].

To this end, this research focused on the TM doping of GaN with Cr, Mn, and Fe with the aim of developing a RT DMS and of obtaining a better understanding of the mechanism associated with the observed ferromagnetism.

4.2. Background: Literature Survey

Before proceeding with the experimental findings of this research, a synopsis of the background literature for the TM dopants in GaN investigated in this study is presented below.

4.2.1. Experimental Studies of $Ga_{1-x}Cr_xN$

Cr doped GaN is an attractive material as it has been found that the background carrier concentration of the Nitrides will cause the Cr_{Ga} and Cr_{Al} t_2 defect level (which sits at ~2 eV above the valence band) to be pushed from a 1/3 filling to a 1/2 filling [121]. The inter-atomic exchange is maximized for a 1/2 filled level as per the Zener double exchange model. First principle calculations have shown the coupling between Cr atoms in GaN to be ferromagnetic with a magnetic moment per atom of 2.69 μ_B in bulk GaN and 4 μ_B in clusters [16]. Single crystals of $Ga_{1-x}Cr_xN$ with a T_C of 280 K have been demonstrated by use of a sodium flux method [122]. In these films the carrier density in the crystal is about 9 x 10^{18} cm^{-3} (n-type), and the mobility is about 150 cm^2/Vs. Ion implantation of GaN with Cr have been carried out at doses of 10^{15} to 5 x 10^{16} cm^{-2} [123]. Magnetization experiments revealed room temperature magnetization, but no mechanism has yet been attributed to this observation. Furthermore, optical measurements have revealed a broad yellow luminescence along with a peak at 2.4 eV, which has been attributed to a conduction band-Cr acceptor level transition

$Ga_{1-x}Cr_xN$ thin films grown by molecular beam epitaxy (MBE) were deemed to be very encouraging. MBE has been used to grow $Ga_{1-x}Cr_xN$ (x = 1.5 %) on sapphire substrates with a higher T_C of 400 K [124]. Magnetization measurements revealed that the coercivity is about 90 Oe at 300 K. The spontaneous magnetic moment per Cr atom was determined to be 2.6 μ_B. Optical studies conducted at 10 K on MBE grown $Ga_{1-x}Cr_xN$ (x = 0.5 to 1.5 %) show the presence of a sharp excitonic peak at 3.36 eV, a blue luminescence band centered in the range of 2.79-2.91 eV, and an increase in the yellow luminescence band. The blue luminescence is caused by Cr doping and is attributed to a donor-acceptor pair transition, where the donor is the deep-acceptor related center Cr_{Ga}, and the acceptor is the shallow compensating vacancy complex, Cr_{Ga}-V_N [125].

Of particular interest have been MBE reports of Cr doping of GaN (3 % Cr) and AlN (7 % Cr) on SiC substrates. These epitaxial films were reported to have a T_C as high as 900 K [126]. The coercive field for $Ga_{0.98}Cr_{0.02}N$ is 100 Oe at 325 K and decreases to 60 Oe at 800 K. On the other hand, it was reported that for 7 % Cr doped AlN, the coercive field is 120 Oe at 300 K and 70 Oe at 800 K. The saturation magnetization moment for 3 % Cr doped GaN was determined to be 1.8 μ_B, implying that 60 % of the Cr is magnetically active. Similarly, the maximum saturation magnetization moment for 7 % Cr doped AlN was found to be 0.6 μ_B, suggesting that 20 % of the Cr is magnetically active. No ferromagnetic secondary phases were seen from X-ray diffraction (XRD), transmission electron microscopy (TEM), and electron energy loss spectroscopy (EELS). Trace amounts of CrN were seen in $Ga_{1-x}Cr_xN$, but this phase is deemed to be antiferromagnetic.

Electrical measurements of $Ga_{1-x}Cr_xN$ grown on sapphire substrates revealed that the resistance followed the Equation 4.1 as follows:

$$R = R_0\left[\frac{T_0}{T}\right]^{1/2} \qquad \text{Equation (4.1)}$$

where R is the resistance, and T is the temperature.

This is characteristic of variable range hopping between localized states with a Coulomb gap as per Mott's law. Theoretically and experimentally, Cr is shown to form a near midgap deep level in the Nitrides [58, 127]. The d levels are exchange split, and the crystal field causes a three-fold degenerate t_2 and a doubly degenerate e level, with the e level being ~1 eV below the t_2. For Cr, the majority of the t_2 levels are 1/3 filled, leading to a magnetic moment of 3 μ_B. Reports by Newman et al. state that the observed conduction is due to the variable range hopping of spin-polarized electrons in the Cr impurity band, and the ferromagnetism in Cr-doped GaN and AlN is due to the double exchange mechanism within the partially filled Cr t_2 band [121]. The electron carrier density and Hall mobility at 300 K for $Ga_{0.96}Cr_{0.04}N$ grown on sapphire substrates were measured to be 1.4 x 10^{20} cm^{-3} and 0.06 cm^2/Vs for magnetic fields up to 5 T. The extremely low mobility is related to the observed hopping conductivity. The Cr-AlN films grown on sapphire substrates were found to be quite resistive, with a resistivity greater than 10^3 Ω cm [126].

Recently, metal organic chemical vapor deposition (MOCVD) grown $Ga_{1-x}Cr_xN$ has been reported to show a hysteresis curve at a low temperature of 5 K [128]. However it is reported that these films were grown under non-optimal conditions and the origin of the low magnetization signal observed is still undetermined.

Overall experimental results to date point to double exchange being the mechanism for ferromagnetism in $Ga_{1-x}Cr_xN$ and this magnetization is expected to be enhanced by Si doping as an extra electron is added to the t_2 level. These observations will be tested by the experiments in this study.

4.2.2. Experimental Studies of $Ga_{1-x}Mn_xN$

Mn is the most widely studied TM dopant as it has the highest number of unpaired spins. Furthermore, the success of introducing Mn into GaAs to achieve hole mediated ferromagnetism has provided an impetus to the area of spintronics [86].

Various growth techniques such as ammonothermal growth [129], ion implantation [130], post-growth diffusion [131], MBE [110], and MOCVD [132] have been applied with the objective of developing single phase $Ga_{1-x}Mn_xN$ that exhibits ferromagnetism at room temperature.

An ammonothermal method has been used to produce microcrystalline $Ga_{1-x}Mn_xN$ samples with Mn content up to x = 0.005 [129]. This technique resulted in the presence of non-uniform crystallites, and XRD showed the characteristic diffraction lines for hexagonal GaN phase mixed with a small contribution from a Mn_3N_2 phase. Raman spectra exhibited peaks that could be associated with Mn-induced lattice disorder. Electron spin resonance (ESR) and magnetization measurements showed that the material was paramagnetic indicating that Mn is predominantly present in the Mn^{2+} charge state.

$Ga_{1-x}Mn_xN$ films were later produced by ion implantation of MOCVD grown p-GaN films with high doses (1×10^{15}-5×10^{16} cm^{-2} to produce Mn concentrations from 0.1-5 %) of Mn^+ ions at ~350 °C and annealed at 700-1000 °C [130]. At low doses (< 3 %

Mn), the $Ga_{1-x}Mn_xN$ is paramagnetic with a large number of lattice defects. At high doses (> 3 % Mn) platelet like structures of $Ga_{1-x}Mn_xN$ are formed which have been attributed to the observed ferromagnetic behavior in the samples up to ~250 K.

$Ga_{1-x}Mn_xN$ has also been produced by post-growth doping of GaN using solid state diffusion of Mn [131]. This resulted in samples that had a background concentration of 1-2 % Mn away from the surface where diffusion took place. Mn-doped GaN with T_C in the range of 228–370 K were obtained and structural characterization by XRD suggested that the ferromagnetic properties are not a result of secondary magnetic phases. These Mn-doped GaN films have ferromagnetic behavior with hysteresis curves showing a coercivity of 100–500 Oe. All the techniques discussed above produced highly non-uniform materials that were difficult to measure because the data obtained was always some average of the properties of the crystallites and of the layer.

Given the low solubility limit of the transition metals in a GaN matrix, non-equilibrium growth techniques such as MBE and MOCVD are preferred. These techniques result in a more uniform layer and allow for easier integration of these materials into devices. A number of groups have reported the growth of $Ga_{1-x}Mn_xN$ using various modifications of MBE with differing levels of success.

One of the first reports of the thin film growth of $Ga_{1-x}Mn_xN$ was by Overberg et al. who employed a gas source MBE to grow the DMS [110]. Auger electron spectroscopy showed that 7 % Mn could be incorporated in a single phase as determined by XRD. The ferromagnetic $Ga_{1-x}Mn_xN$ had a T_C between 10 and 25 K. Recently, a similar T_C has been reported for plasma-assisted MBE (PAMBE) growth study [133]. Another low temperature MBE report (400-650 °C) with 2 % Mn incorporation resulted in

paramagnetic films which were highly resistive [134]. Structural characterizations of MBE growths have shown the formation of a $GaMn_3N$ phase and a Mn_4N phase at Mn concentrations greater than 1.7 % and 17 % respectively [135, 136]. The highest T_C has been reported by MBE grown $Ga_{1-x}Mn_xN$ with 3 % Mn by Sasaki et al. [112]. They claim to have produced wurtzite $Ga_{1-x}Mn_xN$ films showing ferromagnetic behavior well above room temperature with a T_C of 940 K which far exceeds that measured by other groups or suggested by theoretical models. They acknowledge the coexistence of ferromagnetic and paramagnetic phases in their films.

The contributions towards the growth of MOCVD have been made mainly by the research conducted in this study and by Reed et al. [132, 137]. As the experimental findings of the two studies were done at similar times, the experimental results from this study will be discussed in the results portions of this chapter with comparisons being made to the observations of Reed et al.

Overall, a wide range of T_C values have been reported for $Ga_{1-x}Mn_xN$, with temperatures ranging from 8 K to 940 K. Furthermore, there is still no consensus on the mechanism behind the ferromagnetism in the Nitrides. This can be party attributed to the different growth techniques used resulting in materials of different quality and with different structural and electronic defects. The use of a consistent growth technique, i.e., MOCVD has been used to help clarify the ferromagnetism mechanism.

4.2.3. Experimental Results for $Ga_{1-x}Fe_xN$

Doping GaN with Fe has been of interest for a longer period than Mn. Fe has been doped into GaN layers by MOCVD to develop semi-insulating GaN films for high electron mobility transistors as early as 2002 [138, 139]. First principle calculations have

predicted that Fe^{3+} in GaN has a d^5 configuration and very low density of states. Thus, it should exist in the spin glass state that is stabilized by antiferromagnetic superexchange interactions [140]. Despite these predictions, magnetization measurements conducted on $Ga_{1-x}Fe_xN$ grown by ion implantation, MBE, and MOCVD have resulted in a magnetic signal [140]. The significant experimental and magnetization results reported in literature for $Ga_{1-x}Fe_xN$ are summarized below.

MOCVD grown p-GaN (3×10^{17} cm^{-3}) has been doped with 3 % Fe by ion implantation and displayed hysteresis up to 250 K with no evidence of secondary phases [141]. A similar study has shown a transition from overall paramagnetic behavior at 5 % doping to RT ferromagnetic behavior at 10 % doping of Fe into p-GaN by ion implantation [142, 143]. MBE techniques have been used to dope GaN with Fe (10^{19} cm^{-3}) resulting in ferromagnetic properties up to 100 K. X-ray absorption fine structure data shows that the Fe substitutes the Ga site in GaN [144]. X-ray absorption near edge structure spectra indicate that the observed magnetization is due to the change in the Fe electronic state in response to the strong hybridization between Fe 3d and N 2p states [145]. Another MBE study with 5×10^{21} cm^{-3} concentration in GaN shows superparamagnetic behavior which has been attributed to the formation of nano-scale Fe or FeN crystallites in the epilayer [146]. Hexagonal $Ga_{1-x}Fe_xN$ microcrystals with 0.5 % Fe molar concentration have been grown by the ammonothermal method. Magnetization measurements revealed the presence of both paramagnetic (Van-Vleck type-paramagnetism arising from Fe^{2+}) and ferromagnetic phases [147].

Recent efforts have focused on producing $Ga_{1-x}Fe_xN$ at lattice concentrations suitable for spintronics, and there have been reports of MOCVD grown material that exhibit room

temperature ferromagnetism [148, 149]. It was determined that Fe has a 0.4 % solubility in GaN and beyond this limit spinodal decomposition occurs. Furthermore EPR measurements revealed that both the Fe^{3+} (d^5 configuration: responsible for Curie-type paramagnetism) and Fe^{2+} (d^4 configuration: responsible for Van-Vleck-type paramagnetism) charge states are present in the material. It was shown that for Fe doping values greater than 4 %, the ferromagnetism increases significantly and exceeds the paramagnetic contribution. The ferromagnetic response in these films has been attributed to the presence of coherent nanocrystals (presumably Fe_xN), which have been observed by TEM and energy dispersive X-ray spectroscopy (EDS) [149].

4.3. Experimental Method

This study carried out TM (where TM = Cr, Mn, and Fe) doping under optimized GaN growth conditions to grow 0.5 µm thick $Ga_{1-x}TM_xN$ on MOCVD grown undoped GaN templates on sapphire substrates as shown in Figure 4.2. The doping concentrations ranged from Mn: 0-1.5 %, Fe: 0-1 %, and Cr: 0-3 %. In this study bis(cyclopentadienyl)TM precursors were used. To be certain that the source did not interfere in the magnetic observations for the different TM dopants, the same alkyl radical was used for all three sources. A major challenge with TM doping in MOCVD is that the precursors obtained have low volatility. Thus, to ensure that the precursors entered the chamber in gas phase the bath temperature for the sources was maintained at 45 ˚C. SIMS measurements were performed to determine the actual concentration of Mn in the sample. EDS was used to determine the actual Fe and Cr concentration of the films grown. The growth rate was kept low (0.2-0.9 µm/hr) to allow enough time for adatom

diffusion and to prevent clustering. The reflectivity data for $Ga_{1-x}TM_xN$ thin films is shown in Figure 4.2c.

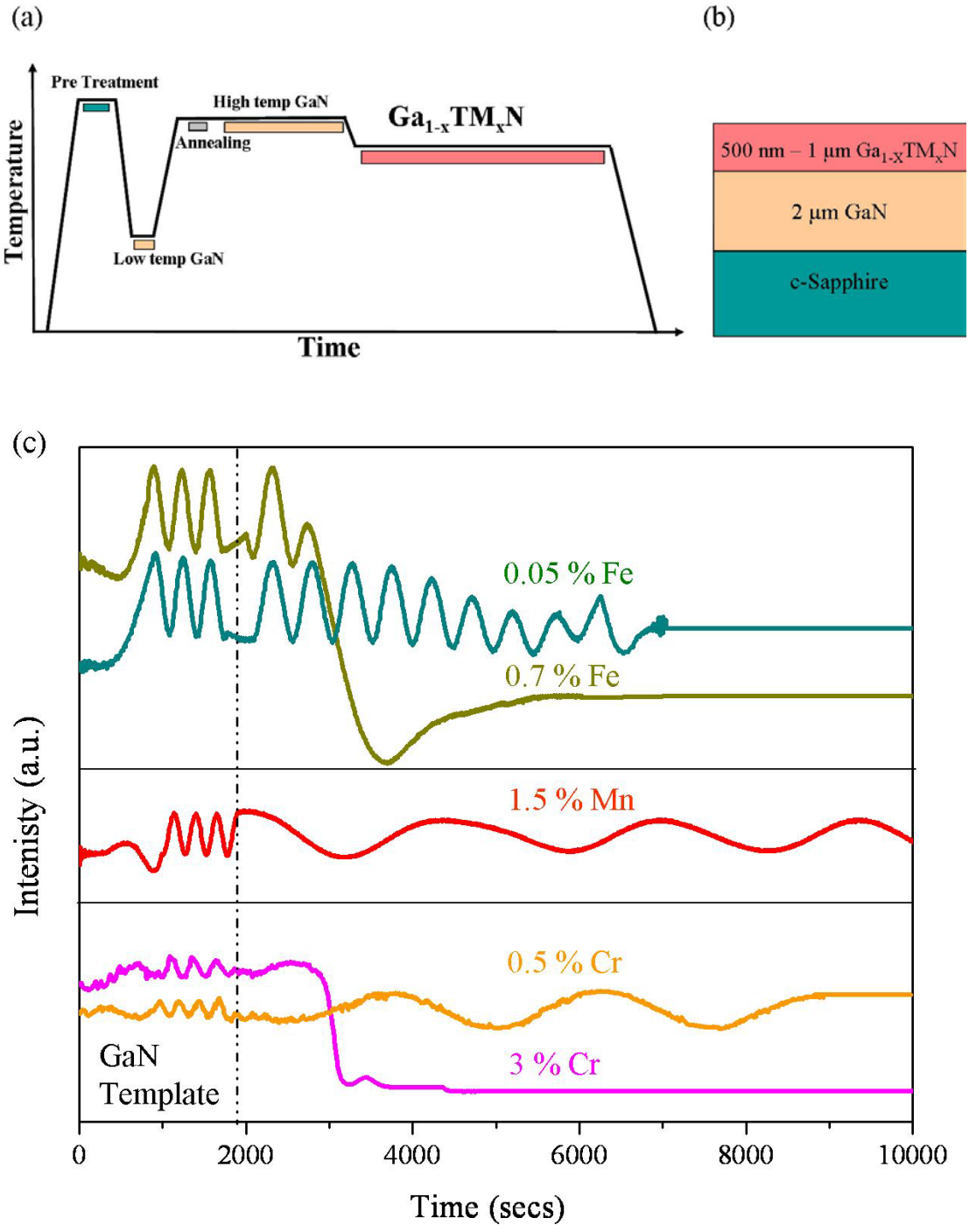

Figure 4.2: (a) Growth profile for $Ga_{1-x}TM_xN$ on sapphire, (b) schematic of the final structure grown, (c) in-situ optical reflectometry curve for $Ga_{1-x}TM_xN$ (after dotted line) grown on GaN templates (before dotted line).

It can be seen that fairly good oscillations were obtained for up to 1.5 % Mn doped GaN. However, increasing the Fe and Cr doping levels beyond 0.5 % results in significant degradation of the reflectometry signal after a few nanometers of growth indicating significant surface roughening.

Silane and magnesium doping of these optimized $Ga_{1-x}TM_xN$ films were also carried out to determine the effect of n- and p-dopants on this material system. The next section presents a detailed analysis of the material properties of the films grown.

4.4 Characterization Results of the DMS

Material characterization is critical to obtain a better understanding of how the dopants affect the properties of the host semiconductor. The characterization results and analysis are described below.

4.4.1. Structural Properties of $Ga_{1-x}TM_xN$

The MOCVD grown $Ga_{0.98}Mn_{0.02}N$ films are specular in nature and have a reddish tint that increases with thickness and Mn concentration. This red tint is attributed to an internal d-d transitions in Mn. The Fe and Cr films tend to be milky in appearance and at concentrations > 1 % the film quality deteriorates rapidly. High resolution X-ray diffraction (HR-XRD) measurements were done to determine the crystalline quality of the material. The ω-2θ scans for $Ga_{1-x}TM_xN$ for the 0002 reflections are shown in Figure 4.3. No significant deviation from the GaN peak was observed in these films. This implies that there is no significant strain present in the materials. A slight shift towards smaller c lattice constant is seen for the Cr and Fe doped GaN. A similar observation was made by Liu et al. for 3 % Cr doped GaN and the decrease in lattice constant was

attributed to the introduction of point defects [126]. Furthermore, no additional peaks were observed in the TM doped GaN films indicating that no macroscopic secondary phases are present.

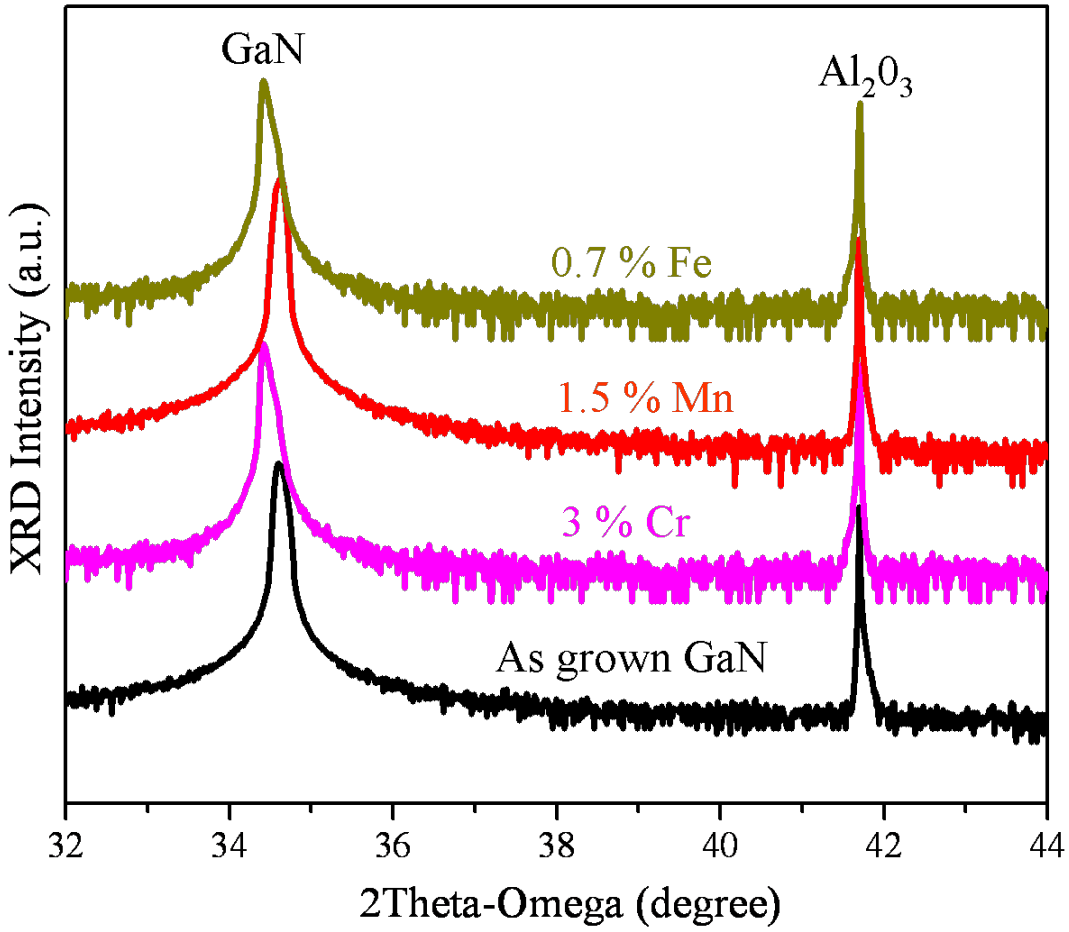

Figure 4.3: HR-XRD showing no secondary phases resulting from TM doping of GaN.

The presence of small ferromagnetic clusters or additional phases cannot be eliminated as embedded nanocrystallites or an orientation along non c-axis directions would not be measurable under the design configuration.

Surface morphology studies performed by atomic force microscopy (AFM) on $Ga_{1-x}TM_xN$ reveal that there is little change in the morphology of the layer at low doping levels (Figure 4.4). However, Fe and Cr doping of GaN causes an increased surface

roughness with root mean square surface roughness of 28.4 nm and 172.16 nm for 0.9 % Fe and 1 % Cr respectively. The surface morphology results support the degradation seen in the in-situ reflectometry curves in Figure 4.2c. With increased concentrations, the Fe and Cr doped GaN samples show poor nucleation and more of an island like growth. The Mn doped samples maintain a smooth surface morphology with a root mean square roughness (RMS) of 3.3 nm, which is similar to undoped GaN despite the high doping concentration of 1.5 %. The 1.5 % Mn doped GaN films were annealed at 700 °C for 30 minutes to ensure that the films could withstand an activation step which has to be generally applied to the p-doped GaN films. No significant change in surface morphology was seen at these elevated temperatures. Furthermore, XRD measurements on the annealed $Ga_{0.985}Mn_{0.015}N$ Mn did not show the presence of any secondary phases or any shift in the GaN peak position.

Based on the AFM images and the in-situ reflectometry curves, it is apparent that the solubility of the TM ions in the GaN host lattice is fairly low. The solubility limit of Mn is higher than for Cr and Fe as it is possible to obtain smooth surfaces for 2 % Mn doping, whereas the GaN films doped with Cr and Fe are limited to 0.7 % Cr and 0.3 % Fe doping respectively. The low solubility limit presents a challenge for obtaining a uniform dilute magnetic semiconductor, as cluster formation is more favorable under these conditions.

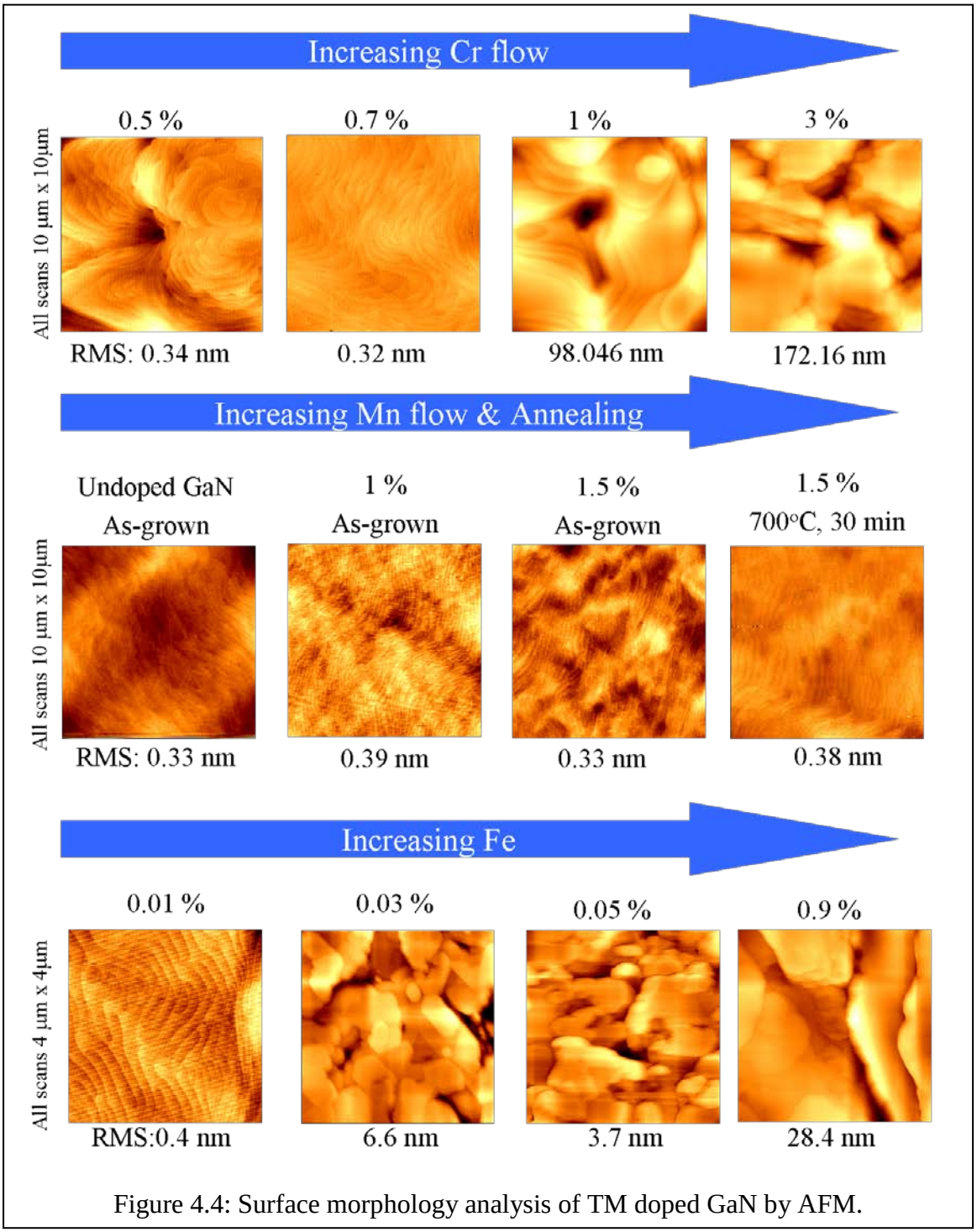

Figure 4.4: Surface morphology analysis of TM doped GaN by AFM.

Raman spectroscopy studies were performed at RT in z(..)-z configuration to examine the effect of TM incorporation on the vibrational modes of the GaN lattice. Figure 4.5 shows the Raman spectra for an as-grown GaN epilayer along with GaN doped with 3 % Cr, 1.5 % Mn, and 0.7 % Fe. The most prominent feature in all of these scans is the E_2(high) and A_1(LO) modes at 569 cm^{-1} and 735 cm^{-1} respectively. These observations indicate that there is no significant strain introduced by TM doping as no shift is observed in the dominant peaks. Furthermore, the high intensity of the E_2(high) peak indicates that there is no significant degradation of the crystalline quality. Additionally, the presence of the A_1(LO) mode (which is similar to GaN in both intensity and full width half maximum (FWHM)) indicates that are no free carriers introduced by TM doping, providing further confirmation that carrier induced ferromagnetism is unlikely in these materials.

Furthermore, for both the Mn and Fe samples there is an additional mode at 710 cm^{-1} which appears as a shoulder to the A_1(LO) mode. With increasing doping concentration of the TM, this mode increases in intensity. This mode has previously been reported in other Raman studies of TM doped GaN and is attributed to a structurally induced disorder mode [150]. In addition to the allowed c-plane GaN Raman modes, in the Cr and Fe doped samples scans there appears an additional A_1(TO) and E_1(TO) mode. The appearance of this mode is indicative of an imperfect crystal and is consistent with the in-situ reflectometry and surface morphology results [151].

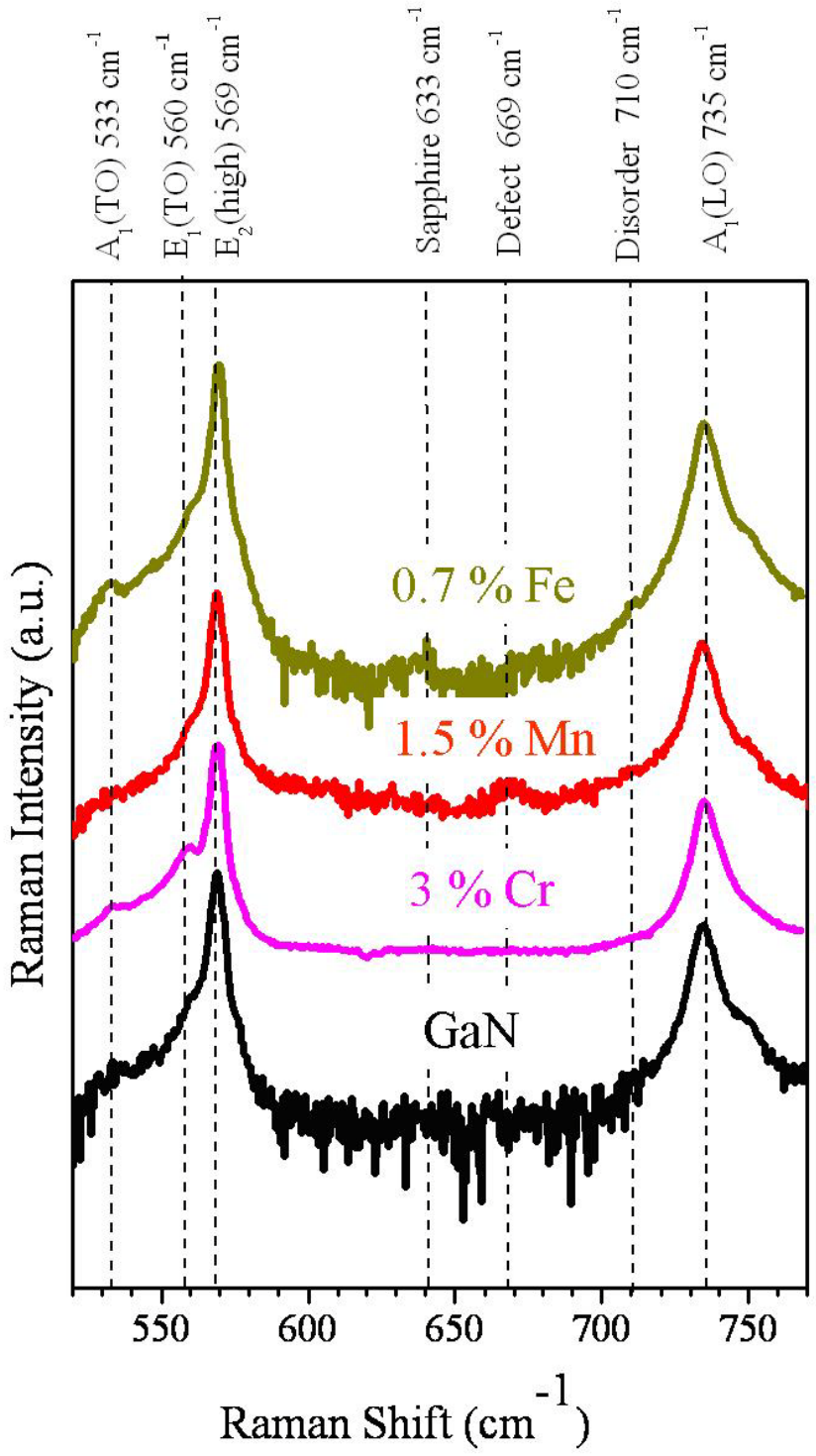

Figure 4.5: Raman spectrum for TM doped GaN reveals strain free films.

A zoomed-in Raman spectrum (conducted with a 532 nm sources) showing the effect of Cr concentration and Si doping is presented in Figure 4.6. It can be seen that as the Cr or Si concentration increases the intensity of the E_1(TO) mode at 560 cm^{-1} reduces (Figure 4.6a). Additionally a red shift is observed in the E_2(high) upon increased Si doping indicating the possibility of strain. With regards to the A_1(LO) mode, upon Si doping a blue shift is observed and the intensity of this mode decreases and broadens, which is to be expected as free carriers are introduced (Figure 4.6b). This may be promising as with Si doped Cr has the same electronic configuration as Mn^{3+}.

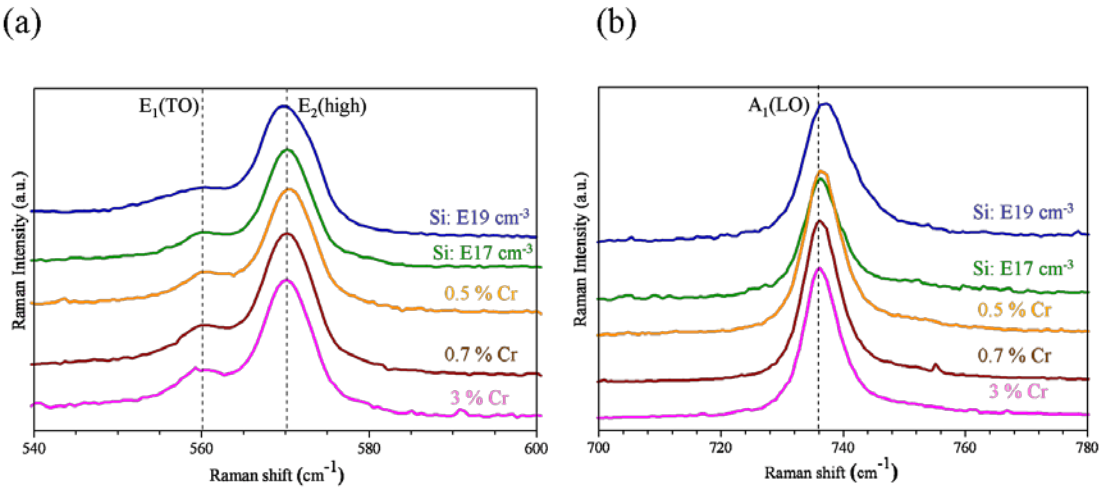

Figure 4.6: Zoomed in view of the (a) E_2(high) and (b) A_1(LO) modes for varying Cr and Si concentrations in GaN.

Mn doping during MOCVD growth of GaN caused the appearance of modes at 669 cm^{-1} and a shoulder at 664 cm^{-1} which are attributed to nitrogen vacancies [151, 152]. The $Ga_{0.985}Mn_{0.015}N$ films were doped with Si (10^{20} cm^{-3}) to test this hypothesis as Si is known to cause a reduction in the nitrogen vacancies in GaN [117]. Raman spectra of two $Ga_{0.985}Mn_{0.015}N$ epilayers are shown in Figure 4.7. The intensity of the 669 cm^{-1} mode increases with increasing Mn concentration, though the line width does not change.

Furthermore, it is apparent that upon Si doping the intensity of the 669 cm^{-1} mode is strongly reduced providing confirmation for the aforementioned hypothesis.

Overall, Raman measurements confirm that all the TM doped GaN films grown in this study are strain free.

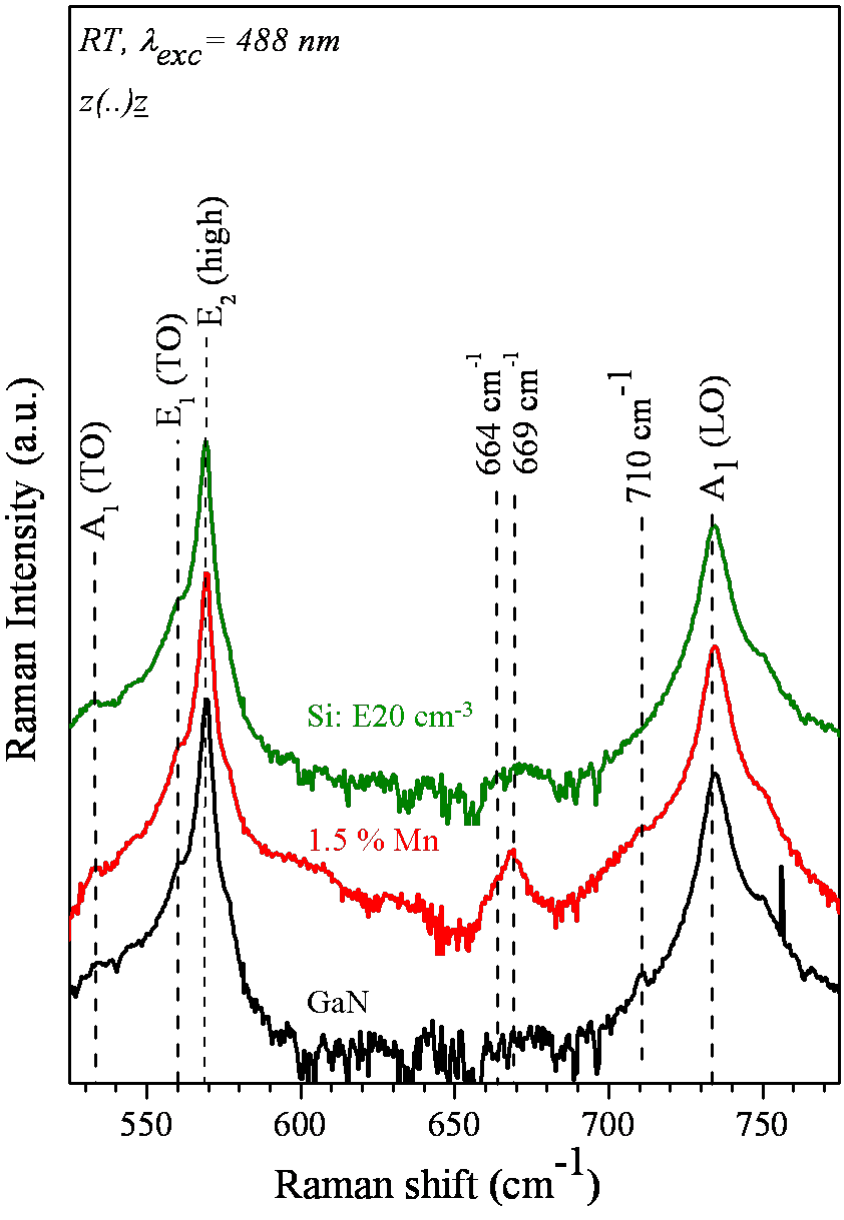

Figure 4.7: Effect of Si doping on the Raman spectra of $Ga_{0.985}Mn_{0.015}N$.

4.4.2 Optical Properties of $Ga_{1-x}TM_xN$

If $Ga_{1-x}TM_xN$ is to be used for opto-electronic spintronic applications, it is imperative that the optical properties of the semiconductor be retained. Photoluminescence (PL) studies were performed at room temperature to obtain a better understanding of the effects of TM doping on the optical properties of GaN. The detailed optical analysis for the $Ga_{1-x}TM_xN$ films is presented below.

4.4.2.1. Optical Properties of $Ga_{1-x}Cr_xN$

RT PL studies reveal that increasing the Cr concentration from 0.5 % to 3 % dampens the bandedge emission, with the emission completely disappearing when co-doped with 3 % Cr (Figure 4.8).

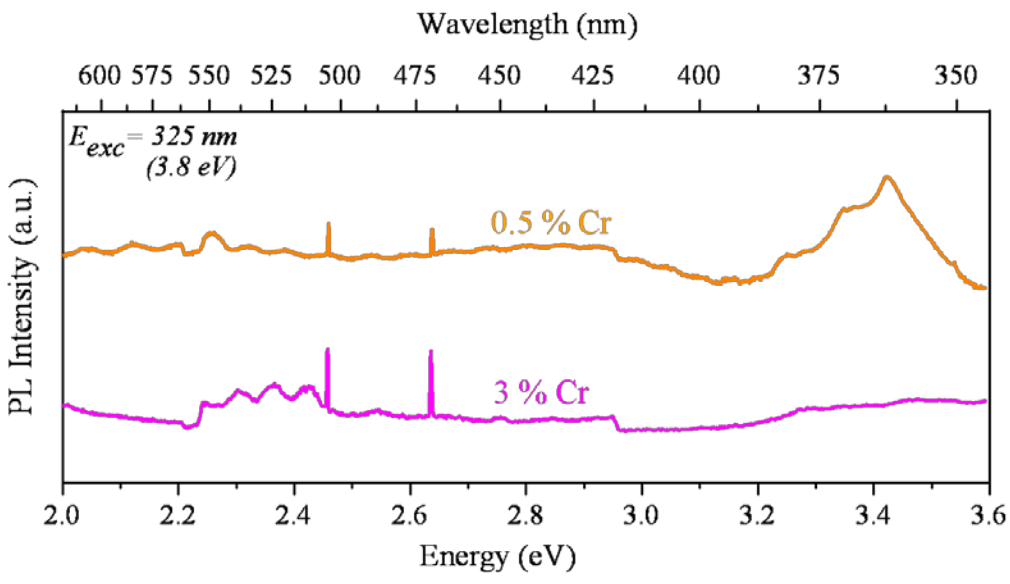

Figure 4.8: Effect of Cr doping on the optical properties of GaN as observed by PL measurements at RT.

The optical results for high Cr concentrations support the reflectometry and surface morphology results which suggest that the material quality deteriorates with increased Cr flow. PL measurements for Si and Mg doped $Ga_{0.995}Cr_{0.005}N$ films revealed similar

features to co-doped GaN which is not surprising given the low Cr concentration used in the co-doped films.

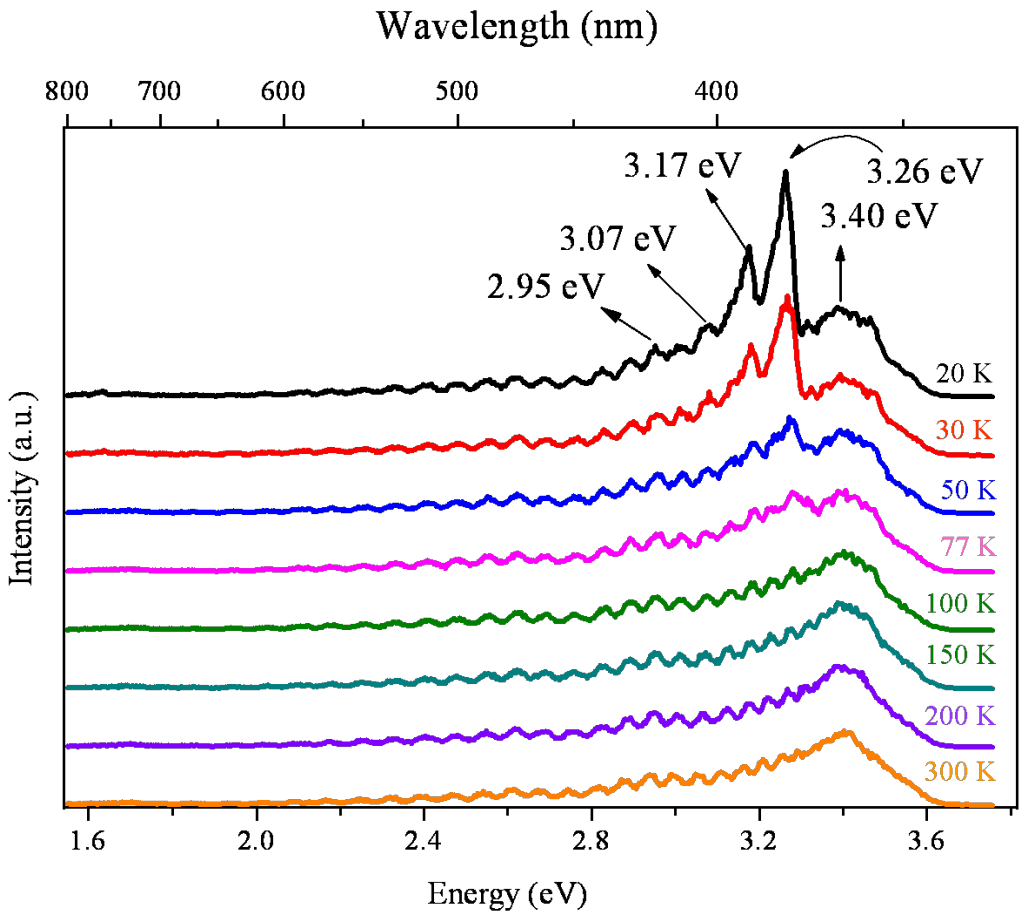

Figure 4.9: Synchrotron radiation measurements on $Ga_{0.995}Cr_{0.005}N$ as a function of temperature.

To obtain an in-depth understanding synchrotron radiation (SR) deep UV (150-300 nm) excitation photoluminescence (PL) measurements were conducted on GaN doped with 0.5 % Cr over a temperature range of 20-300 K (Figure 4.9). The GaN exciton recombination peak at 3.40 eV is observed along with a series of peaks at 3.26 eV, 3.17 eV, 3.07 eV, and 2.95 eV respectively. These shoulder peaks become more prominent at temperatures below 77 K [125]. For Si doped samples, the GaN exciton line at 3.40 eV became weaker and broader, indicating that the crystalline perfection became

poorer. In addition, the neighboring peaks are shifted and the peaks that appear at 3.26, 3.17, 3.07, and 2.95 eV are shifted upon Si doping to 3.27, 3.19, 3.09, and 2.98 eV respectively. These shoulder peaks are characteristic of donor-acceptor pairs (DAP) transitions that have also been observed in MBE grown $Ga_{0.985}Cr_{0.015}N$ films [125]. These DAP peaks are attributed to a transition between nitrogen vacancy and chromium.

4.4.2.2. Optical Properties of $Ga_{1-x}Mn_xN$

In addition to GaN peak, a blue emission band was found to dominate the PL spectrum of the samples with a Mn concentration > 0.5 % resulting in two distinct peaks at 3 eV and 2.86 eV (Figure 4.10) [132].

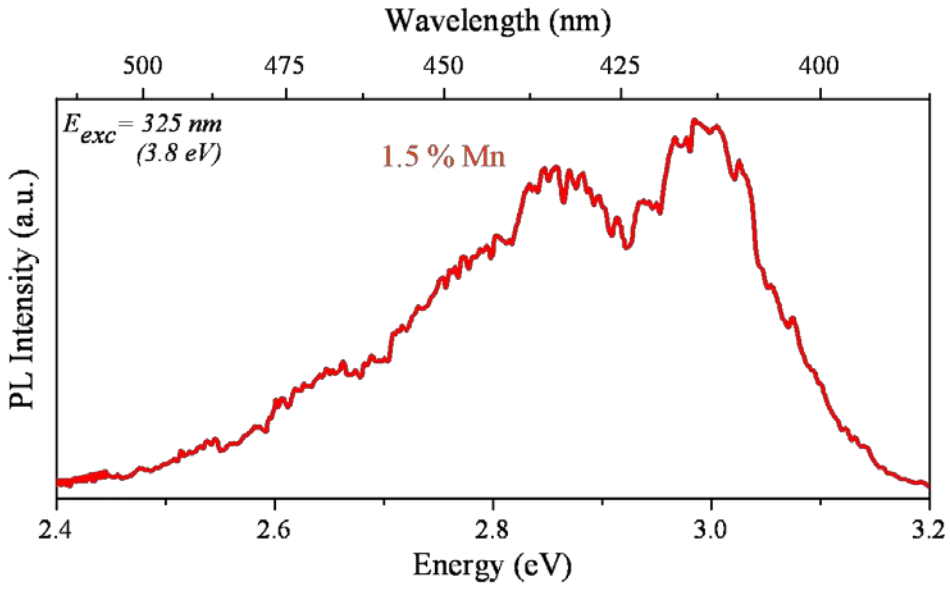

Figure 4.10: Zoomed in optical spectra for $Ga_{0.985}Mn_{0.015}N$ as observed by PL measurements at RT.

This blue band appears in GaN upon compensation of acceptors by doping induced defect states as well as by the incorporation of hydrogen on interstitial sites [153]. Similar observations have been made in MBE grown $Ga_{1-x}Mn_xN$ and ion-implanted material

which have attributed these peaks to transitions from conduction band electrons to Mn-related states and from shallow donor (e.g., N vacancy) to Mn acceptor states [154, 155]. The blue band does not appear in films that are doped with less than 0.5 % Mn concentration, annealed films or samples co-doped with Si. Instead a pronounced yellow band appears which is attributed to intrinsic gallium defects [153]. With regards to Mn films with concentrations less than 0.5 %, the observed behavior is attributed to the lower amount of Mn ions available to substitute on lattice sites, decreasing the number of Ga vacancies. In the other two cases, intrinsic and extrinsic shallow donor states are introduced resulting in the compensation of Mn^{3+} acceptors. An even stronger compensation of Mn acceptors is seen for Si co-doped films.

Optical transmission measurements were carried out to determine the acceptor level position of the Mn ion. The incorporation of Mn into GaN layers during MOCVD growth leads to a broad absorption band: a spectrally diffuse line around 1.5 eV (FWHM of 150 meV), as shown in Figure 4.11. The FWHM and intensity increased with increasing Mn concentration. The observed absorption band is attributed to the Mn^{3+} transitions from the e state to the partially filled t_2 levels of the 5d state [18]. The absence of an absorption band around 1.5 eV in the $Ga_{1-x}Mn_xN$ layer co-doped with silicon indicates sensitivity of the e to t_2 transitions to the position of the Fermi level. Si doping converts the Mn^{3+} to Mn^{2+} and shifts the Fermi level towards the conduction band.

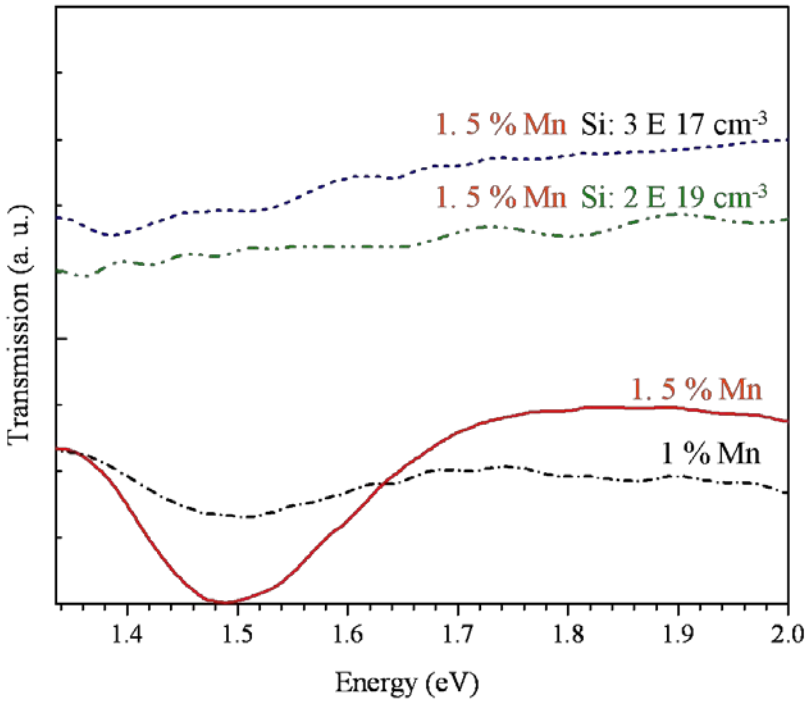

Figure 4.11: Transmission measurements conducted on as-grown and Si co-doped $Ga_{0.985}Mn_{0.015}N$ at RT showing an absorption band at 1.5 eV.

No absorption features were detected further into the infrared spectral range (down to 0.5 eV). This suggests that the location of the Fermi level in the broad absorption band of the investigated samples is around 1.8 eV above the top of the valence band, and even closer to the conduction band than for the Si co-doped sample [19]. Thus, Mn is a deep acceptor and the original theoretical predictions of the possibility of carried mediated ferromagnetism in the Nitrides are not supported [15]. The absorption data points more towards Mn forming a broad impurity band favoring a double exchange model. LT transmissions measurements were conducted at 2 K and revealed a characteristic internal forbidden d-d transition of the Mn^{3+} zero phonon line at 1.41 eV [19, 156, 157]. The sharpness of this line is contrary to the predicted broad impurity-band like behavior.

Similar observations have been made in MBE-grown $Ga_{1-x}Mn_xN$ [156, 158]. It is quite clear from the optical transmission measurements that Mn is a deep acceptor in GaN.

4.4.2.3. Optical Properties of $Ga_{1-x}Fe_xN$

In addition to the GaN bandedge emission at 3.4 eV, the RT PL spectrum in Figure 4.12 shows a broad blue band luminescence peak centered at 2.8 eV. The broad nature of this band suggests that this band is a defect related band. The transition at 2.8 eV can be possibly attributed to a DAP transition between a Fe acceptor and a donor defect [143].

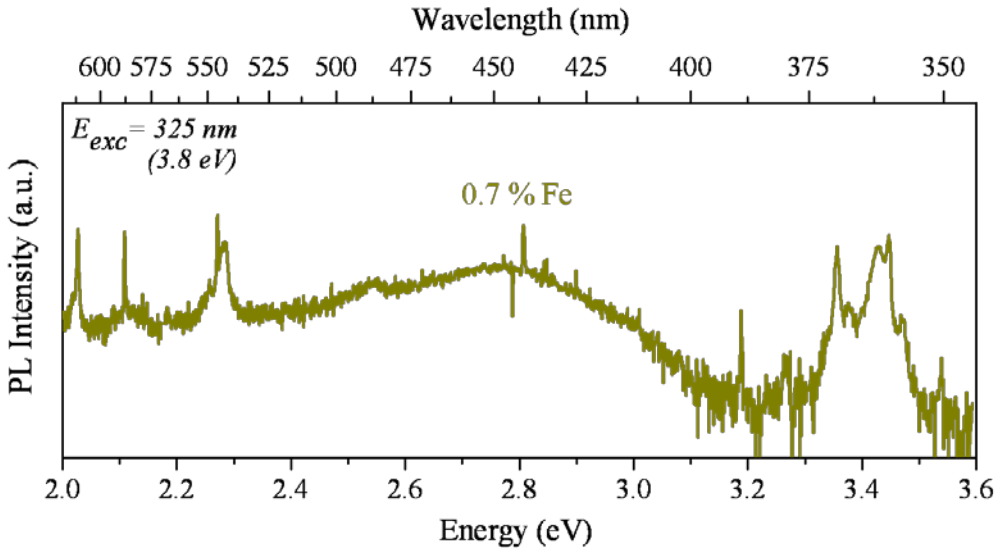

Figure 4.12: RT PL for GaN doped with 0.7 % Fe.

With regards to the GaN band-edge emission two peaks are seen, namely a peak at 3.44 eV and an additional shoulder peak at 3.425 eV. This could be caused by the variation in the Fe composition in the sample or by the diminished structural quality of the $Ga_{1-x}Fe_xN$ films.

4.4.3. Electrical Properties of $Ga_{1-x}TM_xN$

Van der Pauw Hall measurements were used to analyze the carrier type and concentration in these materials. The GaN doped with Mn and Cr was measured to be n-type, in accordance with literature reports [110, 159]. Doping the films n- or p-type did not result in any change of the carrier concentration. The carrier concentration for these films was measured to be around 10^{16} cm^{-3}, which is approximately the background carrier concentration of GaN. The underlying GaN buffer on which the $Ga_{1-x}TM_xN$ films are grown provide a conduction pathway during hall measurements and impacts the carrier concentration measured by Hall.

To test for the validity of the Hall measurements $Ga_{1-x}Mn_xN$ films were grown from the substrate up with Mn in the template layers. The films were found to be too resistive for Hall measurements and the contact resistance increased by several orders of magnitude, consistent with theoretical predictions and other observation of Mn as a deep impurity level. Thus, all of the measured n-type behavior is due to parallel conduction through the GaN buffer.

As mentioned earlier Fe doping reduces the electronic concentration and results in semi-insulating GaN films. The films obtained in this study were too resistive to conduct Hall measurements and this resistivity increased as the Fe concentration was increased.

The electrical measurements are consistent with the literature reports that suggest TM's are deep acceptors in the Nitrides and that they do not create any free carriers [16]. Thus, carrier mediated ferromagnetism is unlikely.

4.4.4. Magnetic Properties of $Ga_{1-x}TM_xN$

An ideal DMS should retain its ferromagnetic properties at RT and ideally the magnetic properties should be controllable through the TM concentration and n- and p-carrier doping. The RT magnetization measured by superconducting quantum interference device (SQUID) for $Ga_{1-x}TM_xN$ is presented below.

4.4.4.1. Magnetic Properties of $Ga_{1-x}Cr_xN$

The effects of Cr concentration on the magnetization at RT were analyzed by SQUID measurements, the results of which are shown in Figure 4.13a. The magnetization strength increases from approximately 3 emu/cm^3 for the 0.5 % Cr to 4 emu/cm^3 for 0.7 % Cr and then to 7 emu/cm^3 for 3 % Cr. Low temperature SQUID measurements were performed at 5 K on these films, but there is no significant difference in the magnetization data. These results are similar to the magnetization results reported for MBE grown films which attribute the observed ferromagnetism to a double exchange mechanism [121].

Based on the double exchange mechanism, co-doping the $Ga_{1-x}Cr_xN$ films with Si should cause an extra electron to be added to the t_2 level of Cr and enhance the magnetic moment of each Cr atom. Co-doping studies with Si and Mg were carried out on the GaN films doped with 0.5 % Cr. The RT magnetization results are presented in Figure 4.13b. Contrary to expectations, it is seen that Si doping causes a reduction in the magnetization and makes the film diamagnetic.

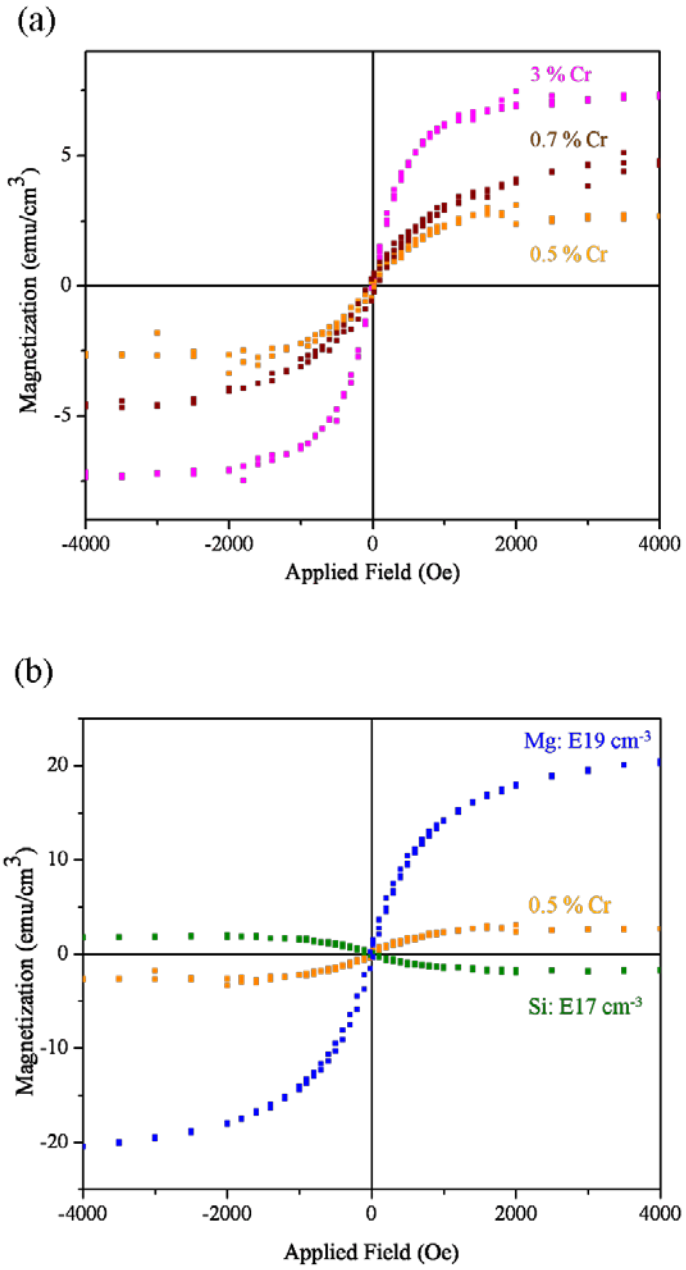

Figure 4.13: RT magnetization data from SQUID for $Ga_{1-x}Cr_xN$: (a) effect of varying Cr concentration, (b) effect of co-dopants on magnetization.

Furthermore, it would be expected that with Mg doping the magnetization would reduce as the t_2 band will be empty, but this does not occur; rather, the magnetization is further increased. Carrier mediated magnetization is unlikely as Cr is a deep acceptor

(impurity level of 2 eV) and no free carriers exist. In addition, the double exchange seems unlikely. First principle theoretical calculations propose that a percolation limit of 20 % is necessary to facilitate nearest neighbor interactions [61]. The origins of these magnetic properties are explored in section 4.5.

4.4.4.2. Magnetic Properties of $Ga_{1-x}Mn_xN$

Magnetization measurements by SQUID revealed ferromagnetic hysteresis for the as-grown $Ga_{1-x}Mn_xN$ films at 300 K (Figure 4.14). Magnetization strength of 12 emu/cm^3 is obtained for the 1 % Mn doping, which is enhanced to 16 emu/cm^3 when the Mn concentration is increased to 1.5 %. The magnetic moment for these films can be calculated using the following equation:

$$M = N \mu \qquad \text{Equation (4.2)}$$

where M is the saturation magnetization,

N is the number of Mn atoms per unit volume, and

μ is the magnetic magneton per Mn atom.

A magnetic moment of 2.9 μ_B/Mn is obtained for 1 % Mn doping and 1.2 μ_B/Mn for the 1.5 % Mn doped film. This indicates that approximately 60 % (for 1 % Mn) and 30 % (for 1.5 %) of the Mn atoms were active in the matrix. These results indicate that Mn_4N clusters are not present, since these have a magnetic moment of 17 μ_B/Mn atom [160].

The strength of this magnetization depends on the thickness of the sample and on the film growth rate, with stronger magnetization in general being exhibited for films with slower growth rates. As seen in Figure 4.14, upon annealing the magnetization of the sample drops significantly to 4 emu/cm^3. There is still some area remaining in the

hysteresis loop observed for this sample, indicating that the ferromagnetic phase is not completely lost or that there may be a small contribution from local areas of the alloy that were either unaffected by the anneal or consist of ferromagnetic second phases. A similar behavior for the magnetism is seen in Si doped $Ga_{1-x}Mn_xN$ (Figure 4.14). The magnetic moment decreases with increasing Si doping concentration and is nearly zero at Si concentrations greater than $10^{19}cm^{-3}$.

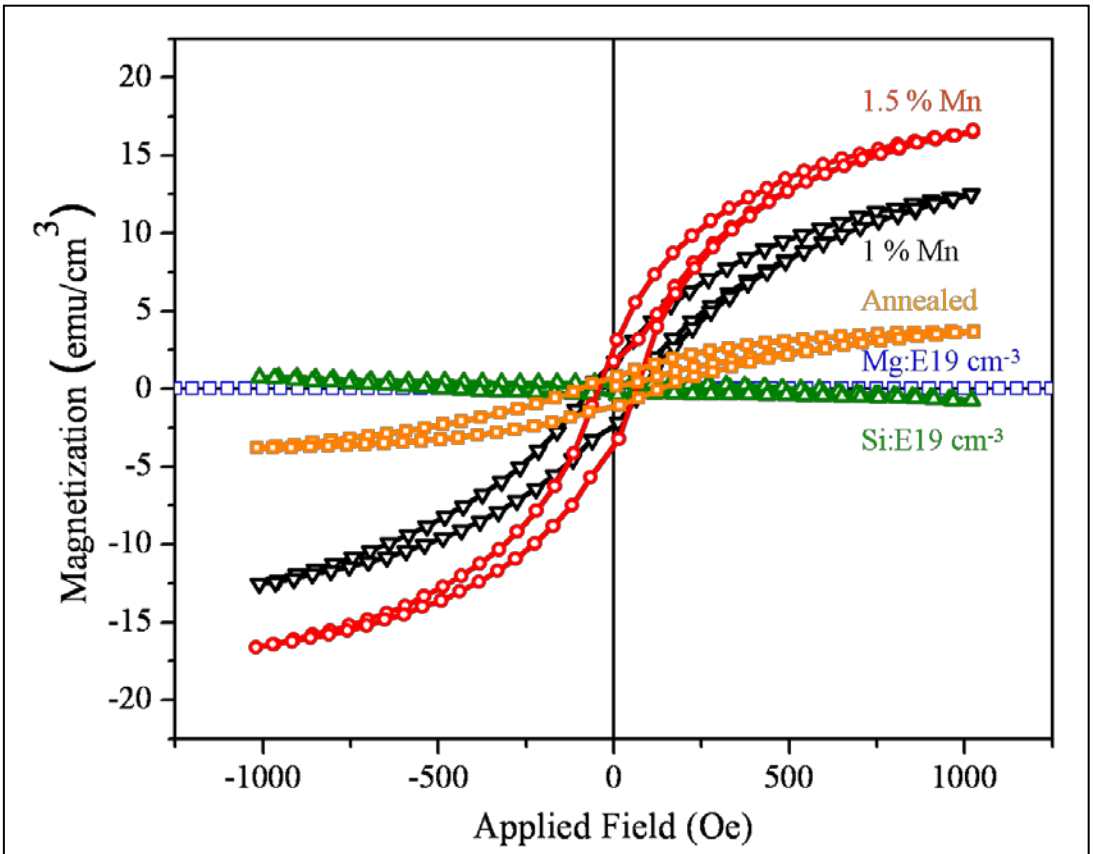

Figure 4.14: RT magnetization results for as-grown, n-, and p-doped $Ga_{1-x}Mn_xN$.

As mentioned earlier the optical absorption measurements revealed that Mn is incorporated into GaN as Mn^{3+}, and is converted to Mn^{2+} upon Si-doping. These results have been confirmed with electron paramagnetic resonance (EPR) measurements, which reveal that Mn is in the Mn^{2+} state in both the annealed and Si doped $Ga_{1-x}Mn_xN$ films.

MOCVD experiments conducted by Reed et al. showed similar magnetization results for the n-$Ga_{1-x}Mn_xN$ films [137].

The p-doping of $Ga_{0.985}Mn_{0.015}N$ with Mg concentrations of $10^{19}cm^{-3}$ results in the significantly reduced magnetization and the films show a diamagnetic signal (Figure 4.14). Similar magnetization results were obtained for p-doped $Ga_{1-x}Mn_xN$ by Reed et al. who suggest that the Mg acceptor states absorb the electrons from the Mn impurity band and as the Mg acceptor level is 1.2 eV below the Mn impurity band, they are unable to participate in the Mn-Mn exchange interactions [137]. Furthermore, this group reports that under non-optimal growth conditions, Mg doping (10^{19} cm^{-3}) can result in enhanced ferromagnetism as it increases the number of Mn ions contributing to the magnetism [137]. In this scenario, Mg is acting as an anti-surfactant and promoting Mn clusters. Thus competition exists between Mg and TM as they have similar material chemistry (Cp_2Mg and Cp_2TM), and the Mg ions can occupy the TM sites and promote TM clustering [161]. Thus, the theory proposed by Dietl that carrier mediated ferromagnetism is possible in p-$Ga_{1-x}Mn_xN$ is not viable. Overall, although Mn has the highest number of unpaired electrons, it is not possible to enhance the magnetic properties of this DMS through n- and p-dopants.

Overall the magnetization results for the $Ga_{1-x}Mn_xN$ films fit best with the double exchange model of ferromagnetism. In the as-grown $Ga_{1-x}Mn_xN$ films, Mn is incorporated as Mn^{3+} (d^4) and the electrons can hop between the partly filled t_2 levels of the TM ion thereby supporting a double exchange mechanism that is responsible for the stabilization of the ferromagnetic phase in the material. The Si doping increases the Fermi level by introducing donor states near the conduction band and results in the filling

of the t_2 band with the donor electrons, thereby converting the Mn^{3+} (d^4) to the Mn^{2+} (d^5) configuration and thus eliminating the hopping pathway necessary for the double exchange interactions. It is believed that when the sample is annealed, vacancies and other shallow donor defects are introduced that disrupt the hopping pathway necessary for the double exchange mechanism and hence the ferromagnetism is reduced.

4.4.4.3. Magnetic Properties of $Ga_{1-x}Fe_xN$

SQUID magnetometry of 0.7 % Fe doped films is shown in Figure 4.15. The magnetization strength is significantly reduced as compared to the Mn and Cr doped films with the magnetization strength being 1 emu/cm^{-3}.

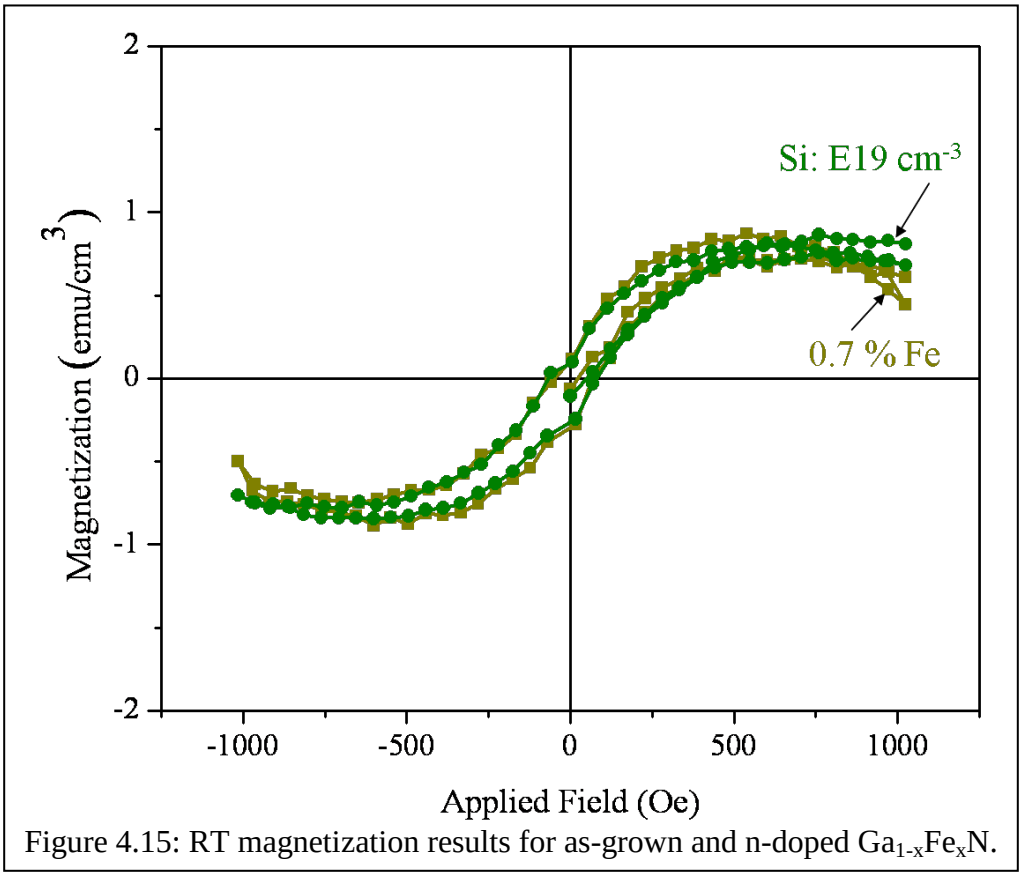

Figure 4.15: RT magnetization results for as-grown and n-doped $Ga_{1-x}Fe_xN$.

Upon Si doping no change is observed in the magnetization strength. Si doping converts the Fe^{3+} state to the Fe^{2+}, and should result in Van-Vleck paramagnetism, as reported for MBE grown $Ga_{1-x}Fe_xN$ films [149]. The average concentration of magnetic ions is far below the percolation limit for the nearest-neighbor coupling, and at the same time the free-carrier density is too low to mediate an efficient long-range exchange interaction. Thus it is unlikely that the magnetism arises from a double exchange mechanism. The MBE study points to a non-uniform distribution of the TM ions in the GaN host lattice and ferromagnetic clusters are responsible for the observed ferromagnetism.

4.5. Investigation of Ferromagnetic Mechanism

Zero field cooled (ZFC) and field cooled (FC) measurements were conducted to enable a better understanding of the ferromagnetism mechanism. The ZFC and FC measurements were performed in the presence of an applied field of 200 Oe for $Ga_{1-x}Cr_xN$ at several different Cr concentrations. The results are shown in Figure 4.16a, and reveal a pronounced splitting for all tested concentrations of Cr in GaN.

Further ZFC/FC investigations were carried out on the co-doped $Ga_{1-x}Cr_xN$ films (Figure 4.16). From the ZFC and FC figures it is apparent that the Si-$Ga_{1-x}Cr_xN$ is magnetically inactive. Si co-doping of $Ga_{1-x}Cr_xN$ converts the Cr^{3+} to the Cr^{2+}, which has been associated with Van-Vleck-type paramagnetism (magnetization that does not vary with temperature) in II-VI semiconductors [162]. On the other hand the Mg doped films show a pronounced splitting (larger than the $Ga_{1-x}Cr_xN$ films), indicating that magnetic clusters exist in the material and are enhanced by Mg doping. These measurements point towards the fact that the enhanced magnetization is due to magnetic clusters that are

occurring in the material rather than the formation of a dilute magnetic semiconductor. As mentioned this is consistent with the reports on unoptimized p-$Ga_{1-x}Mn_xN$ films in which Mg facilitates the increase in Mn concentration and thereby enhances the magnetization by as much as four times [137, 161]

This markedly different behavior, namely the increasing ZFC-FC difference on lowering temperature indicates the presence of clusters whose response is determined by thermally activated processes across some energy barriers. This behavior is characteristic of anisotropic magnetic clusters below its blocking temperature.

The blocking temperature (T_b) of a magnetic cluster is given by Equation (4.3):

$$T_b = \frac{KV}{k_b \ln\left(\tau_{\exp} / \tau_O\right)} \qquad \text{Equation (4.3)}$$

where

V is the particle volume,

K is the anisotropy constant,

τ_{exp} is the measurement time (usually 100 seconds), and

τ_o is the lifetime due to the natural gyromagnetic frequency of the particles.

The critical variables that affect T_b are K and V. At $T < T_b$, the moments of some of the particles are blocked and do not possess sufficient magnetic energy barriers within the time scale of the experiment. For $T > T_b$, the thermal energy is high enough to randomize the spin and hence the magnetic signal reduces. Thus, below T_b superparamagnetic behavior is seen. The magnetic anisotropy term together with volume of the particles,

could lead to blocking temperatures well above room temperature and result in the observation of magnetic hysteresis in films below the blocking temperature.

Thus, the Cr doping in GaN, undergoes spinodal decomposition (i.e. segregates into regions of varying TM concentration) above the solubility limit to create magnetic clusters. The size distribution of these clusters results in a distribution of T_b and thus the T_b recorded is a mean value for all the magnetic clusters present. Energy density calculations show that Cr distribution in GaN is not random or homogeneous but that it is energetically favorable for the Cr atoms to be embedded as clusters, and it is likely that the clusters formed will be of varying sizes and configurations [163]. The cluster formation is enhanced both by increasing the TM concentration and also by high growth temperatures. These allow for enhanced TM cluster interactions and for enhanced TM mobility respectively. Density function calculations have shown that Cr atoms may cluster around N to form Cr_2N and Cr_3N nano-clusters, which have been found to be ferromagnetic with magnetic moments of 9 μ_B and 13 μ_B respectively [164]. The p-doping causes an increase in magnetization and a pronounced splitting in the ZFC and FC measurements is consistent with the theoretical studies that state that doping with shallow acceptors enhances carrier screening and leads to nanocrystal aggregation [17].

Spinodal decomposition is limited in $Ga_{1-x}Mn_xAs$ as it is grown at low temperatures and phase segregation is kinetically limited. Furthermore, Mn is a shallow acceptor and, due to its large Bohr radius, the holes reside in the valence band which in turn makes the Mn negatively charged, reducing the clustering and making it possible to deposit homogenous films beyond the solubility limit [17, 58].

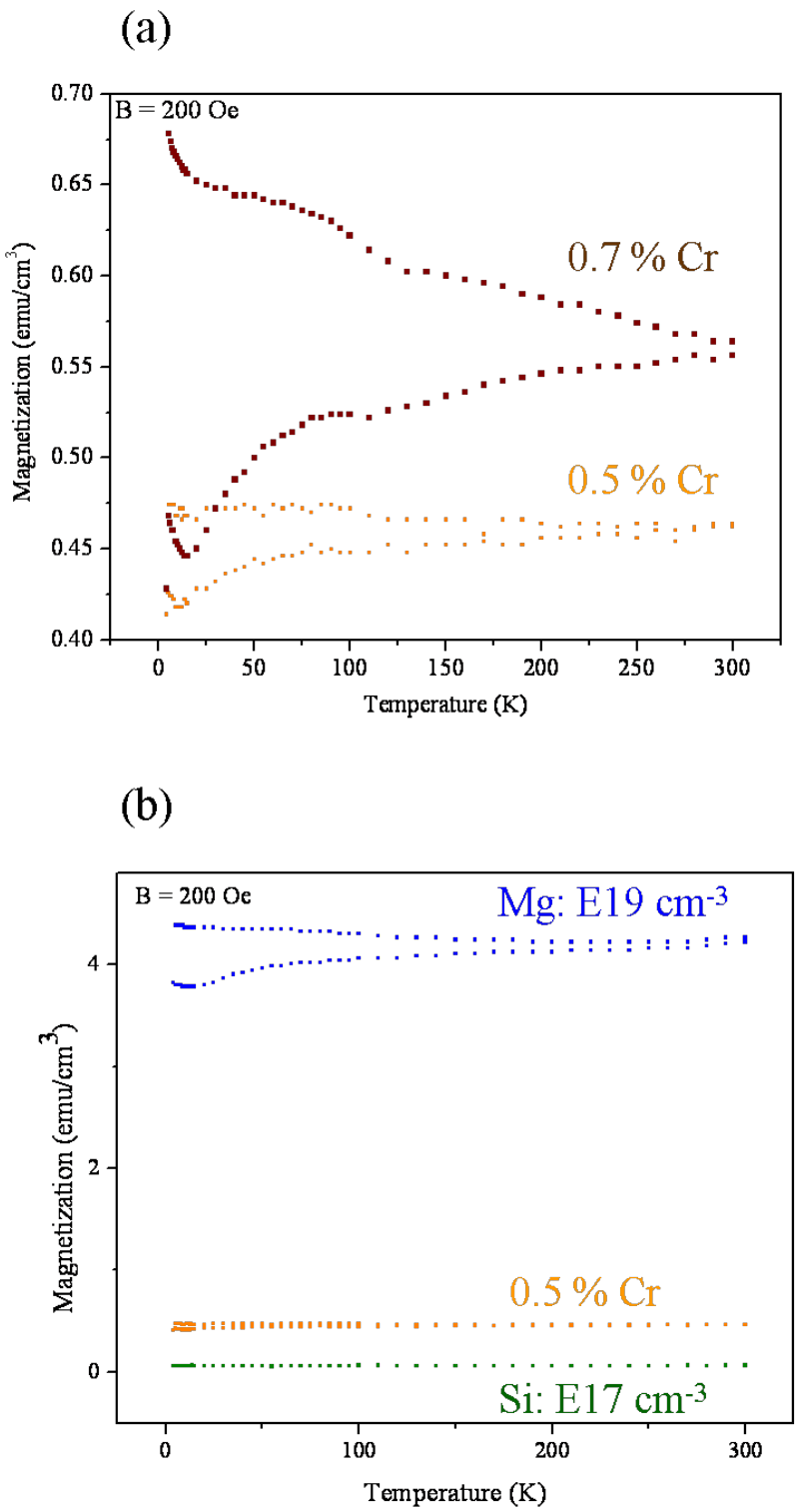

Figure 4.16: ZFC (bottom curve for each case) and FC measurements (top curve for each case) for (a) as-grown, (b) n-and p-doped $Ga_{0.995}Cr_{0.005}N$ under an applied field of 200 Oe.

ZFC/FC investigations on the 1.5 % and 0.7 % Mn and Fe doped GaN did not show a pronounced splitting (Figure 4.17a). Detailed investigation were carried out on the Si doped $Ga_{0.985}Mn_{0.015}N$ and reveal a pronounced superparamagnetic splitting that can be observed in the ZFC/FC curves with increasing silane molar flow rate (Figure 4.17b). This is reminiscent of the results associated with the superparamagnetic splitting of a distribution of magnetic nanoparticles of varying sizes. This observation can be understood by looking at the role of Si on both the charge state of the manganese ions and the expected behavior of a group of magnetic nanoparticles of varying sizes.

Silicon has two effects on the growth of $Ga_{1-x}Mn_xN$ by MOCVD. The first is that Si doping results in the reduction of the Mn valence state from Mn^{3+} to Mn^{2+} which facilitates spinodal decomposition through Coulombic interactions. The second is that silicon on the GaN growth surface increases the local surface energy, and acts as a nucleation site for islands [165]. This results in an overall decrease in the volume of the nanoparticles, which in turn results in reduced blocking temperature, and hence a more pronounced splitting in the ZFC/FC magnetization curves.

A similar behavior may be expected for Fe doped GaN films. The growth rate for the Fe doped films was 0.9 μm/hr whereas the growth rate for the Cr and Mn doped films in this study was 0.25 μm/hr and 0.4 μm/hr respectively. This allows for shorter diffusion distances and fewer Fe-Fe interactions.

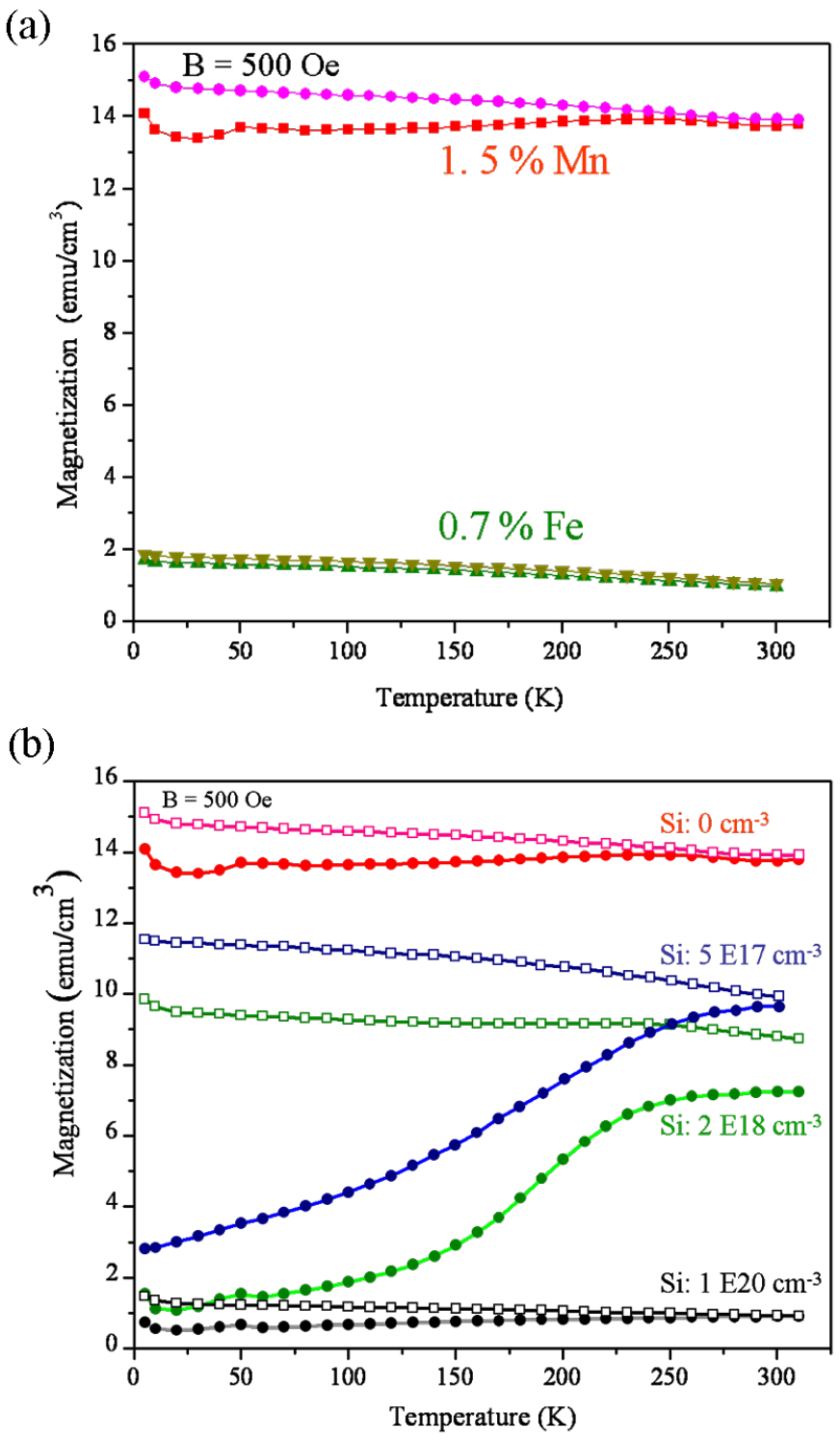

Figure 4.17: (a) ZFC (bottom curve for each case) and FC (top curve for each case) measurements for as-grown $Ga_{1-x}Mn_xN$ and $Ga_{1-x}Fe_xN$, (b) effect of different Si doping levels on the magnetic properties of $Ga_{1-x}Mn_xN$ (x = 1.5 %).

The observation of the appearance of the superparamagnetic phase and the optical observation of the conversion of Mn^{3+} ions to Mn^{2+} is consistent with the recent predictions of charged controlled phase separation in these semiconductor alloys [166]. Similarly, magnetization reports by Bonanni et al. suggest the room temperature ferromagnetism observed in their $Ga_{1-x}Fe_xN$ samples is attributable to the presence of Fe rich nanocrystals formed by spinodal decomposition and have performed EDS measurements that show the Fe concentration is large within these nanoclusters [149]. It is not essential that spinodal decomposition result in the precipitation of another crystallographic phase that can be easily detected by XRD [167]. Overall, the experimental results in this study along with theoretical predictions support the fact that ferromagnetism in $Ga_{1-x}TM_xN$ is mediated through magnetic clusters that are promoted through spinodal decomposition and Coulombic interactions rather than the double exchange mechanism previously reported.

4.6. Devices

The development of a spintronic device that functions at RT has been a quest for a decade now. In this regard, RT spin light emitting diode (spin-LED) are interesting to pursue as they are comparatively easy to fabricate. The analysis of the polarization of the light emission from these LEDs can provide insight into the spin injection efficiency, transport, and spin lifetimes. Ion implantation of p-GaN with Mn have been carried out to develop a spin-LED [168]. Such a device should allow the modulation of the polarization of the light emitted by the spin-LED by the application of an external magnetic field. However, it was found that the high resistance of the implanted region and high density of deep recombination centers significantly decrease the electroluminescence (EL)

efficiency, and increase the forward voltage (V_f) from ~4 V to ~8 V. No reports on the polarization analysis were made in this study.

MBE-growth of $Ga_{1-x}Mn_xN$ (x = 3 %) films which show RT ferromagnetism has been reported by several groups [169]. Due to the n-type conductivity of these layers it was necessary to grow inverted LED structures with an n-type contact layer [170, 171]. However, such a structure is difficult to fabricate and has a higher series resistance due to the lower lateral conductivity of p-GaN compared to n-GaN. It has also been shown that it is more difficult to attain a high quality of the GaN/InGaN multi-quantum well (MQW) active region when growing on a very heavily Mg-doped p-GaN layer. Further, $Ga_{1-x}Mn_xN$ is highly resistive and results in poor ohmic contact formation. It is essential to ensure that the annealing temperature of the ferromagnetic layers does not destroy the ferromagnetism.

In this study, LED structures were grown with the aim of using the $Ga_{1-x}Mn_xN$ as a spin aligner layer. In this device unpolarized holes are made to pass through the ferromagnetic $Ga_{1-x}Mn_xN$ layer with the aim of aligning the holes to make them spin polarized. These spin polarized holes should then recombine with the unpolarized electrons to produce circularly polarized light. The polarization of this light will provide insight into the spin injection efficiency of this LED structure.

To this end, a thin 100 nm $Ga_{0.985}Mn_{0.015}N$ layer was inserted into a regular LED structure right before the p-GaN layer was grown (Figure 4.18a). The active structure consisted of 5 multi-quantum well structures consisting of $In_xGa_{1-x}N$ wells (with x = ~12 %) and GaN barriers. Magnetization measurements were conducted on this device, showing that the $Ga_{0.985}Mn_{0.015}N$ retains its magnetization despite its reduced thickness in

the device structure. However, upon annealing to activate the p-type carriers, the magnetization is significantly reduced, but is still ferromagnetic. A reference LED was grown which is basically a regular GaN-based LED without the ferromagnetic $Ga_{1-x}Mn_xN$ layer.

I-V measurements were conducted on both the spin-LED outlined above and on a reference LED. It was found that the spin-LED had a higher turn on voltage (V_f) of 6.5 V, compared with 3.5 V for the reference LED when both were biased at 20 mA (Figure 4.18b). This increase in turn on voltage is not surprising as Mn is a deep acceptor in GaN which results in increased resistivity of the ferromagnetic film and thus of the overall device.

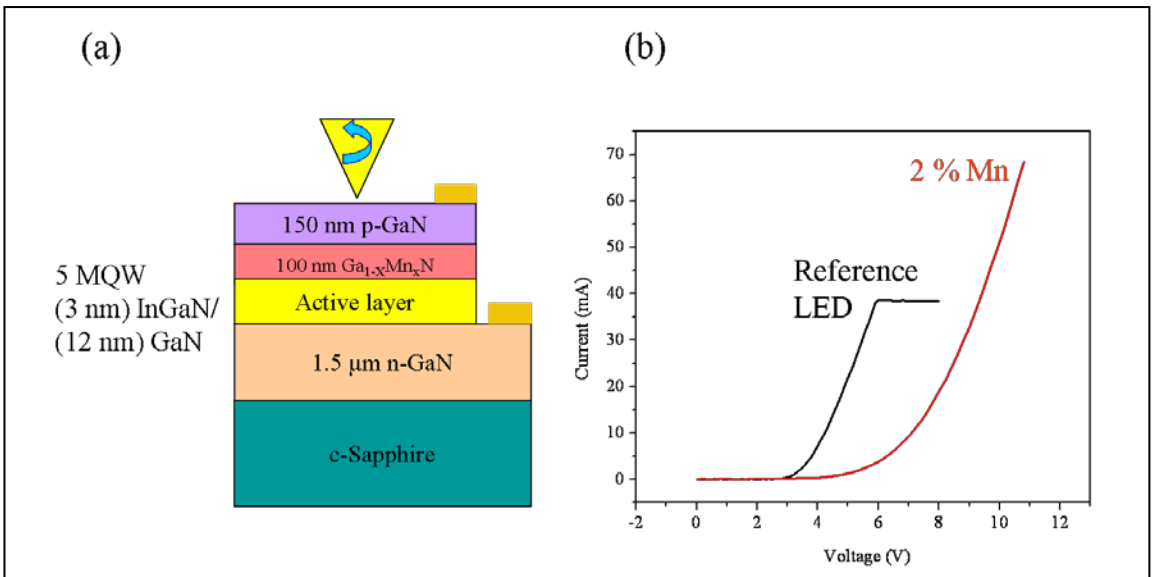

Figure 4.18: (a) Schematic of the spin LED structure using a spin aligner layer, (b) I-V curves for the spin LED in comparison to a reference LED.

EL measurements showed a broad peak with maxima at 448 nm and 456 nm. The two peaks result from fluctuations in the indium composition, which in turn arise from the spinodal decomposition of indium in the Nitrides. This is caused by strain induced

piezoelectric effects that result from the growth conditions. RT EL measurements were performed in the presence of a magnetic field, but no difference was found in the light emissions at polarizations of both left and right polarization of the light as the magnetic field strength was increased (Figure 4.19).

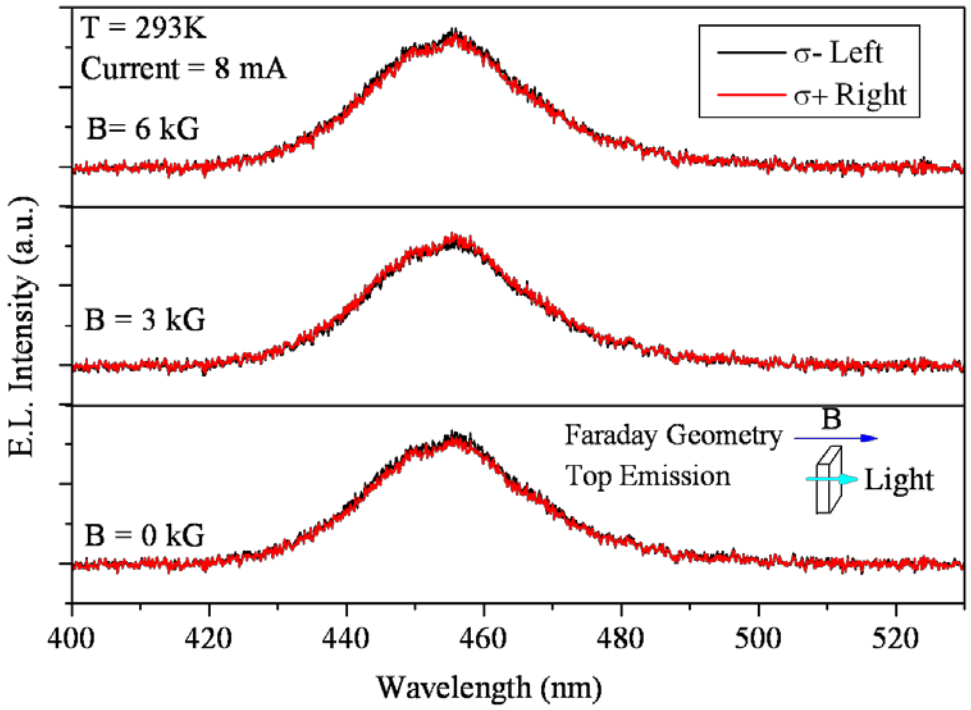

Figure 4.19: RT electroluminescence for a spin-LED for varying magnetic fields.

Very similar results to those found here have been reported in the literature: both Polyakov et al. and Buyanova et al. report electroluminescence peaking at 450 nm with a V_f of 15 V [170, 171]. No polarization of light emission at room temperature was observed in applied magnetic fields ranging from 0 to 5 T in either of their EL and PL measurements. It was determined that, independent of the spin polarization of the $Ga_{1-x}Mn_xN$ (x = 3 %) layer, the fast spin relaxation in the $In_{1-x}Ga_xN$ (x = 40 %) MQW will itself destroy any spin polarization of injected carriers leading to the vanishing spin injection efficiency of the spin-LED. It was stated that the observed fast spin relaxation in

the $In_{1-x}Ga_xN$ MQW is likely to be caused by breaking of symmetry and the resultant mixing of the spin states. This in turn is caused by strong compositional non-uniformity, strain, and a built-in electric field in $In_{1-x}Ga_xN$, as well as strong spin scattering by defects.

Thus, an effective spin detector that will be sensitive to injected spin polarization, (e.g., by increasing the hh–lh energy separation) or looking at alternate recombination schemes is needed. It has been suggested that it is difficult to create polarized carriers with high indium composition due to large Stokes shift (up to 200 meV) in the MQWs [172]. However, another study has suggested that high indium composition results in phase separation causing the formation of quantum dots (QDs) [173]. The carrier localization in these QDs suppresses the scattering process, which decreases the spin flip rate, thereby increasing the spin life time. At this time, the effect of indium composition in the InGaN MQW on spin relaxation time is unclear and further study is needed to clarify this.

A great challenge to the use of TM doped GaN in spintronic devices is the reduction in magnetization upon annealing (a crucial step in LED processing). Moreover, as the ferromagnetism is caused by cluster formation it will be essential to exercise control over their magnetic properties through the use of growth and co-doping methods to ensure their utility in device structures.

4.7. Conclusions

Transition metal doping of GaN has been successfully carried out by MOCVD in order to fabricate a RT DMS. The TMs employed in this study were Cr (0-3 %), Mn (0-1.5 %) and Fe (0-0.9 %), with the aim of analyzing the effect of the number of unpaired

spins and of the TM acceptor level's impact on the ferromagnetism in the DMS. Structural characterization revealed single phase and strain free $Ga_{1-x}TM_xN$ films. Surface morphology measurements by AFM revealed that for Cr and Fe doping a transition from 2D to 3D growth occurs at low concentrations of 1 % and 0.03 % respectively. On the other hand, 1.5 % Mn doping in GaN can be executed without any significant roughening. Optical and absorption measurements reveal that the TM's are indeed deep acceptors in the GaN lattice and are unlikely to result in the free carriers that could result in carrier mediated ferromagnetism. Attempts were made to perform hall measurements on these films, but they were highly resistive and semi-insulating in nature. Room temperature magnetization measurements were obtained for all the $Ga_{1-x}TM_xN$ films. It was found that Si doping significantly reduced the magnetization of the Mn and Cr doped GaN films. Magnesium doping of $Ga_{1-x}Cr_xN$ resulted in an enhanced magnetization providing hope for the use of it as a TM for producing a DMS. Detailed ZFC and FC measurements revealed that for all the ferromagnetic as-grown or co-doped $Ga_{1-x}TM_xN$ a pronounced splitting is seen between the two ZFC and FC curves, indicating that magnetic clusters are present in the material. Spinodal decomposition and Coulombic interactions were found to be the driving force behind the formation of these anisotropic magnetic clusters, which is in agreement with the recent theoretical predictions for DMS based on TMs [17]. Overall, this work has shown the systematic effect of different TM dopants and co-dopants on magnetizations and helped elucidate the much debated ferromagnetism mechanism in these materials. Figure 4.20 provides a summary of the dopants used and the respective magnetization strengths obtained at RT.

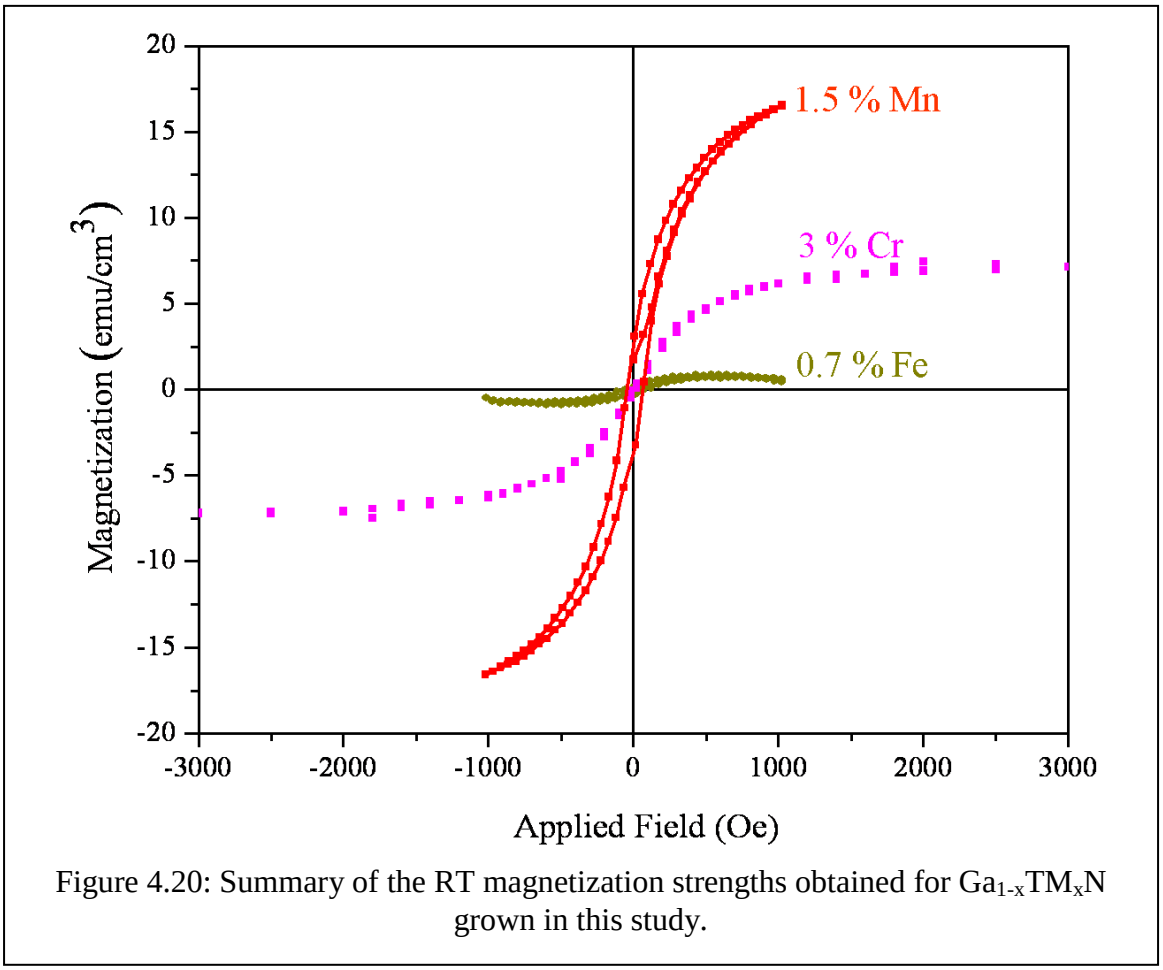

Figure 4.20: Summary of the RT magnetization strengths obtained for $Ga_{1-x}TM_xN$ grown in this study.

CHAPTER 5

RARE EARTH DOPING OF GaN

5.1. Introduction

Rare earth (RE) elements are promising alternatives to transition metals (TMs) for use in developing a dilute magnetic semiconductor (DMS) for spintronic applications. RE elements have unpaired electrons in the 4f orbitals and thus have a higher net magnetic moment as compared to TM ions. The 4f orbitals are localized and the direct coupling between the 4f ions is weak [21]. There have been several attempts of using RE elements for optoelectronic applications, as their various internal f-shell electronic transitions vary in energy from infrared to visible [174, 175].

In crystalline materials the rare earths usually exist in a 3+ charge state though occasionally as 2+ [174]. RE ions generally substitute the Ga lattice site in GaN (Figure 5.1) [174]. Wurtzite GaN has a strong ionic bonding character and the lack of inversion symmetry results in the production of strong ligand fields that increase the probability of 4f-4f transitions that are forbidden by Laporte selections rules in the isolated ion [175]. When introduced into a semiconductor, the RE radiative transitions display intense intra 4f luminescence and the electron-phonon coupling is weak due to the shielding provided by the $5s^2$ and $5p^6$ electrons. It is due to this shielding that the RE electronic levels are more influenced by spin-orbit coupling than by the crystal field [176]. The solubility of RE in GaN is much higher as compared to Si and other narrow bandgap semiconductors, optically active erbium concentrations ranging from 3 to 5 % have been reported in GaN [177]. Over the past few years significant effort has been

made in doping GaN with RE dopants such as Eu and Er as well as Tm to develop red, green and blue electroluminescent devices [174].

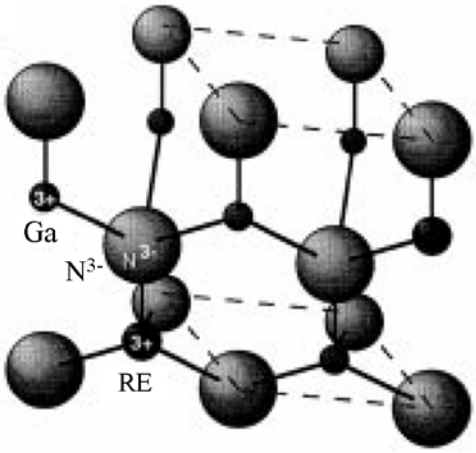

Figure 5.1: Schematic depicting the RE incorporation in GaN [174].

With regards to using a RE to create a DMS, gadolinium (Gd: $4f^7\ 5d^1\ 6s^2$) is most attractive as it is the only RE ion that has both unfilled d and f orbitals. This enables magnetic coupling through intra-ion 4f-5d exchange interaction followed by charge carrier mediated inter-ion 5d-5d coupling. Because of this, several studies have been performed with the goal of developing ferromagnetic $Ga_{1-x}Gd_xN$ using ion implantation and molecular beam epitaxy (MBE). A synopsis of these studies is presented in the background section of this chapter. This chapter presents the first reported growth study of $Ga_{1-x}Gd_xN$ thin films produced by metal organic chemical vapor deposition (MOCVD). MOCVD is the epitaxial growth technique most commonly used for commercial production of high quality layered structures for semiconductor devices. This chapter presents the growth technique and characterization results for developing room

temperature (RT) ferromagnetic $Ga_{1-x}Gd_xN$ films with potential to be used to create spintronic devices.

5.2. Background: Literature Survey

5.2.1. Experimental Reports on $Ga_{1-x}Gd_xN$

The first reports on epitaxial $Ga_{1-x}Gd_xN$ layers were made by Teraguchi et al. who used RF-plasma-assisted MBE to grow the epitaxial layers on the (0001) Si-face of a SiC substrate [178]. They grew 250 nm of $Ga_{0.94}Gd_{0.06}N$ that displayed ferromagnetic behavior with T_C higher than 400 K, which is greater than the T_C of Gd metal (T_C = 292.5 K) and the T_C of rock salt structure GdN (T_C = 58 K) [179-181]. Their optical characterization at RT yielded an emission peak at 370 nm, which is slightly red shifted than the band gap luminescence of GaN (363 nm) indicating that the bandgap of GaN shrinks when Gd atoms are incorporated. An emission peak centered around 645 nm was also observed and was believed to be related to Gd^{3+} based on results from Eu doped GaN [178].

A separate study on GaN bulk crystals doped with Gd by Lipinska et al. shows that Gd doping introduces some new features in optical characterization results [182]. Low temperature photoluminescence (PL) measurements performed at 4.2 K revealed luminescent peaks at 3.3 eV (= 370 nm) in addition to the GaN band gap. Contrary to the assignment by Teraguchi et al., Lipinska et al. attribute these additional peaks to a transition from the $Gd^{3+}(4f^7)$ excited level $^6P_{7/2}$ to its ground state $^8S_{7/2}$. Additional peaks are also seen at 1.6-1.8 eV and have been attributed to Gd^{3+} transitions. These are believed to be due to transitions between $^6G_{7/2}$ to ^6P_J (J = 7/2, 5/2, 3/2) states [182].

In a study by Dhar et al. lightly doped (< 10^{16} cm^{-3}) $Ga_{1-x}Gd_xN$ were grown by MBE on SiC substrates. This epitaxial film appeared to be a single phase material and exhibited a very large ferromagnetic moment (~4000 μ_B/Gd as opposed to its atomic moment of 8 μ_B/Gd atom (Figure 5.2) [22].

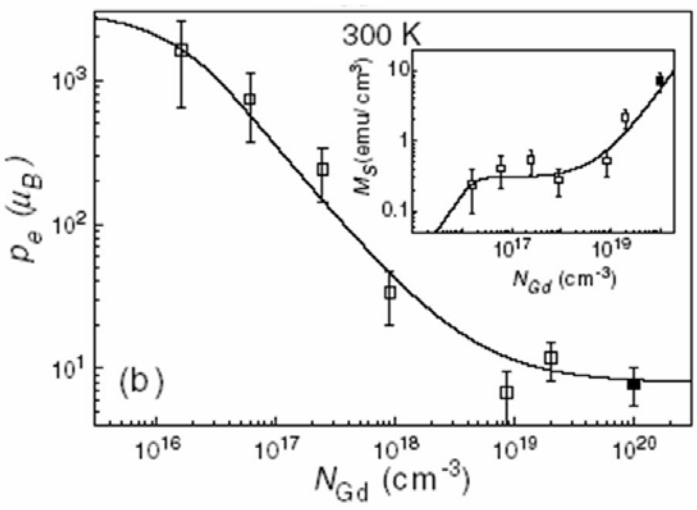

Figure 5.2: Magnetic moment per Gd atom as a function of Gd doping in MBE experiments by Dhar et al. [22].

Based on the convergence of the field cooled (FC) and zero field cooled (ZFC) curves, the T_C was reported to be 360 K. The $Ga_{1-x}Gd_xN$ films obtained were found to be highly resistive with a resistivity of 1 MΩ-cm. There is no robust theory to explain the giant magnetic moment observed in these materials, but a phenomenological model has been proposed which suggests that the long range spin polarization of the GaN matrix is caused by the strain field induced by the introduction of the Gd atom [22]. This is based on the reasoning that because Gd has a larger atomic size than Ga, it is possible that Gd substitution of Ga in GaN produces a large strain field around it. Dhar et al. suggest that due to the large piezoelectric coefficient of GaN along the c axis, a strain field generates a potential dip around each Gd atom. These potential minima trap the carriers locally, and

if there is a spin-splitting in the band structure, the localized carriers become spin polarized [22]. It is the observation of the high magnetic moment by Dhar et al. that has provided impetus to the study of Gd doping in GaN.

MBE reports have been made by Hite et al. for $Ga_{1-x}Gd_xN$ grown at 700 ˚C on sapphire substrates [183]. Their results show that doping of GaN with 10^{17} Gd atoms/cm^{-3} makes the host semiconductor ferromagnetic at RT and also highly resistive. This report showed that doping with Si can improve the conductivity, but the magnetization measurements did not show any significant impact of Si on saturation magnetization.

Recently, $Ga_{1-x}Gd_xN$ thin films with Gd concentration as high as 12.5 % were obtained by MBE (growth temperature < 300 ˚C) on sapphire substrates by Zhou et al. [184]. X-ray diffraction (XRD) results showed no obvious secondary phase, and the films displayed room temperature ferromagnetism. This MBE study showed that $Ga_{1-x}Gd_xN$ films grown at 700 ˚C with Gd concentrations greater than 7.8 % result in the formation of secondary phases such as GdN, which results in the reduction of the net magnetization per unit volume as GdN has a T_C of 58 K. Extended X-ray absorption fine structure measurements showed that the Gd atoms were primarily incorporated on Ga site. The MBE grown $Ga_{1-x}Gd_xN$ (x = 12.5 %) displayed a saturation magnetization of 320 emu/cm^3 resulting in a magnetic moment of 6.4 μ_B/Gd atom. The saturation magnetization was enhanced by 6 times upon Si doping of $Ga_{1-x}Gd_xN$ (x = 8.9 %) resulting in an increase in saturation magnetization from 137 emu/cm^3 to 1046 emu/cm^3 [184]. Zhou et al. attribute the magnetization in $Ga_{1-x}Gd_xN$ films to nitrogen vacancies, which can be enhanced by doping with donors.

5.2.2. Theoretical Models Presented in Literature

$Ga_{1-x}Gd_xN$ is promising as it has the potential to be doped with donors (acceptors) with a concentration exceeding that of Gd to generate spin-polarized electrons (holes) in the conduction band (valence band), which could be applied to spintronic devices [185, 186].

Till date, there is no consistency in the mechanism proposed for the observed magnetism in $Ga_{1-x}Gd_xN$ thin films. The first reports on ferromagnetic $Ga_{0.94}Gd_{0.06}N$ by Teraguchi et al. attributed the magnetism to the Ruderman-Kittel-Kasuya-Yosida (RKKY)-type interaction via the spin-polarized valence band of GaN [187]. Dhar et al. attributed the large magnetic moment observed to the long range spin of the GaN matrix by Gd atoms [188]. On the other hand MBE reports by Zhou et al. predict that electrons introduced by Si doping or defects (nitrogen vacancies) help to stabilize the ferromagnetic phase in $Ga_{1-x}Gd_xN$ films as they offer electrons that couple between the Gd f and host s states [189].

Dalpian and Wei have performed ab initio band structure calculations and determined the density of states (DOS) for zinc blende $Ga_{1-x}Gd_xN$ for x = 6.25 % (Figure 5.3) [186]. Their calculations show that the coupling between Gd atoms in zinc blende $Ga_{1-x}Gd_xN$ is antiferromagnetic as the spin-splitting in the ferromagnetic phase does not result in energy gain as compared to the unsplit antiferromagnetic phase. The antiferromagnetic phase is stabilized through superexchange interactions between the Gd 4f and N p states. The theoretical calculations show that the addition of electrons can stabilize the ferromagnetic phase as the s-f coupling results in a negative spin exchange splitting (ΔE_{FM-AFM}) [186]. Dalpian and Wei predict that both holes and electrons will

result in ferromagnetic interaction in $Ga_{1-x}Gd_xN$ but the electrons are more efficient in stabilizing the ferromagnetic phase and should result in larger magnetic moments.

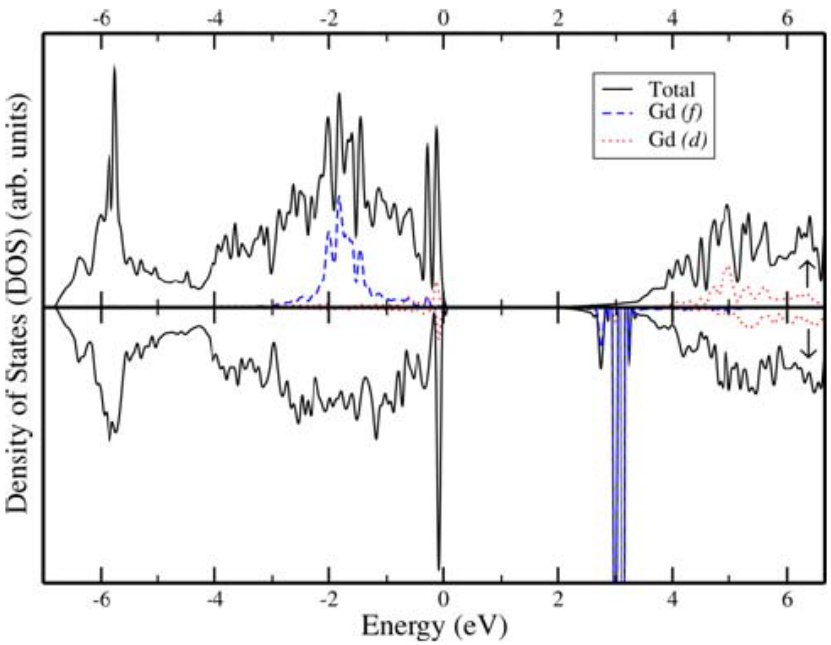

Figure 5.3: Density of states for zinc blende $Ga_{1-x}Gd_xN$ (x = 6.25 %) [186].

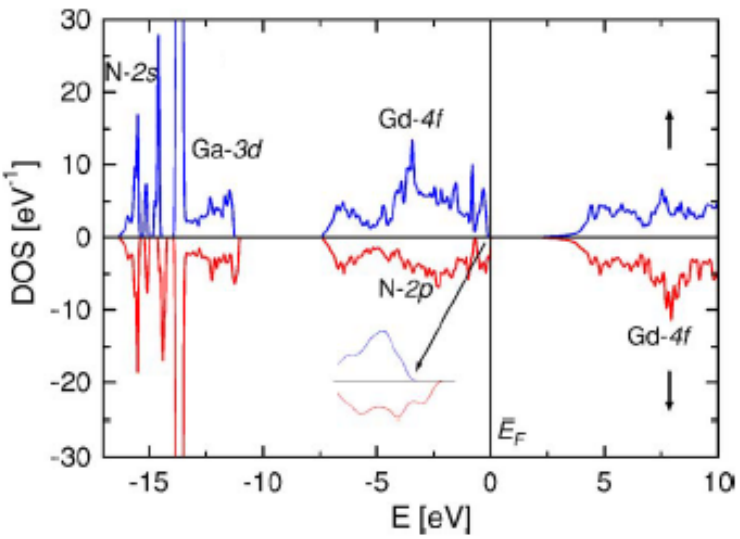

Figure 5.4: Electronic structure of wurtzite $Ga_{1-x}Gd_xN$ (x = 12.5 %) [190].

Recently, first principle calculations based on spin density functional theory have resulted in the electronic structure for wurtzite $Ga_{1-x}Gd_xN$ (x = 12.5 %) shown in

Figure 5.4 [190, 191]. In this model, the 7.4 eV broad valence band is of N 2p character and the conduction band is predominantly formed by the 4s Ga electrons. According to Hejtmanek et al. the 4f orbitals spin-up band is positioned -3.5 eV below the valence band maximum and the spin-down states are 6 eV above the conduction band minimum [190]. The substitution of Ga by Gd is isovalent and thus no electrons or holes are created. Their findings suggest that ferromagnetism in $Ga_{1-x}Gd_xN$ is caused by the Ruderman-Kittel-Kasuya-Yosida (RKKY) exchange mechanism and is mediated through itinerant carriers that occur due to excitation from an impurity band to the conduction band or due to an impurity band in the degenerate semiconductor [192]. Unlike TM doped GaN, which exhibits metallic or semi-metallic states the $Ga_{1-x}Gd_xN$ system is always a semiconductor with the bandgap gradually decreasing with an increase in Gd concentration [21]. First principle calculations by Zhong et al. show that the Fermi level is always located at the maximum position of the valence band for different Gd concentrations (x ranging from 0.03 to 0.25) [21].

Several theoretical analyses have been performed to determine the validity of the long range polarization of the GaN lattice by Gd atoms [21, 186, 192] . These calculations show that the net spin exchange splitting in the valence band or conduction band for RE doped GaN is smaller than that of TM doped, as the f-s, f-p, and f-d couplings in GaN are weaker than that of the d-s, d-d, and d-p hybridization in $Ga_{1-x}TM_xN$. Thus more Gd atoms enhance the magnetic coupling through N atoms, and these N atoms are visibly polarized in the presence of Gd atoms, but this polarization is too small to result in the large magnetic moment of 4000 μ_B/Gd atom [21, 185].

Unlike other DMS, Gd in GaN has both partially filled 5d and 4f electrons that can contribute to the magnetic moment of Gd, thus it is imperative to analyze the effect of both of these orbitals on the ferromagnetism.

Spin density functional theory calculations have been performed by Liu et al. to determine the magnetism mechanism in $Ga_{1-x}Gd_xN$ [192]. Their findings suggest that the 4f orbitals are too far apart from the VBM and CBM, and their coupling with free carriers should be weak. Thus, they explored the impact of the Gd 5d electrons. The five-fold degenerate 5d orbitals of Gd are split by the tetrahedral field of the GaN lattice into two e_g and three t_{2g} states. The lowest conduction band of GaN is mainly s-like in character and has very little d character and thus the s-d coupling is expected to be weak as long as the Gd local environment has T_d symmetry. In wurtzite samples, defects and the hexagonal symmetry can result in s-d coupling. On the other hand, relatively flat Gd 5d orbitals with t_{2g} symmetry occur around the p-like valence band maxima (VBM) of GaN. As the Gd 5d t_{2g} have the same symmetry as the GaN VBM at the zone center, the p-d hybridization is very strong as observed in Mn doped GaAs. The energy difference between the ferromagnetic and antiferromagnetic configurations was found to be zero for the structure used in this model; suggesting that $Ga_{1-x}Gd_xN$ should be paramagnetic unless defects exist that stabilize the ferromagnetism. Due to the larger atomic radius of Gd as compared to Ga it is expected that a large density of vacancies exist that could be responsible for the observed ferromagnetism [191, 193].

The two possible scenarios are nitrogen vacancies and gallium vacancies. Nitrogen vacancies (V_N) introduce three conduction electrons to the system and cause the Fermi level to shift well above the VBM. As the local symmetry now allows s-d coupling, the

lowest conduction band will contain significant d-character and thus have a significant density of states (DOS) occurring at the Fermi level. The energy difference $\Delta E=E_{FM}-E_{AFM}$ for $Gd_{Ga}-V_n$ complex is 3.9 meV/Gd atom and implies that s-d coupling is rather weak. The ΔE_{FM-AFM} for the wurtzite structure is on the order of -0.7 meV/Gd atom. Liu et al. state that the n-type carriers cannot be responsible for the large magnetic moment of 4000/Gd atom observed by Dhar et al. [22].

In the case of gallium vacancy (V_{Ga}), the missing Ga atom contributes three holes, and the d-band DOS near the Fermi level shows noticeable difference between the spin-up and spin-down states (Figure 5.5). The calculated energy difference $\Delta E=E_{FM}-E_{AFM}$ by Liu et al., is -697.1 meV/Gd atom [192]. Their calculations show that a strong FM p-d exchange coupling exists that is 180 times stronger than s-d coupling.

The p-d exchange is so strong that three unoccupied spin-down valence bands from GaN matrix are pushed above the VBM of the spin-up states resulting in the magnetic moment of the Gd d electron being spread over the p bonding orbital. The calculated ΔE_{FM-AFM} is -326.1 meV/Gd atom for the super-cell unit for a Ga vacancy. The FM p-d exchange in $Ga_{1-x}Gd_xN$ (for both wurtzite and zinc blende) is over 2 orders of magnitude stronger than the s-d exchange, which implies that holes are more effective than electrons in contributing to the ferromagnetism [192].

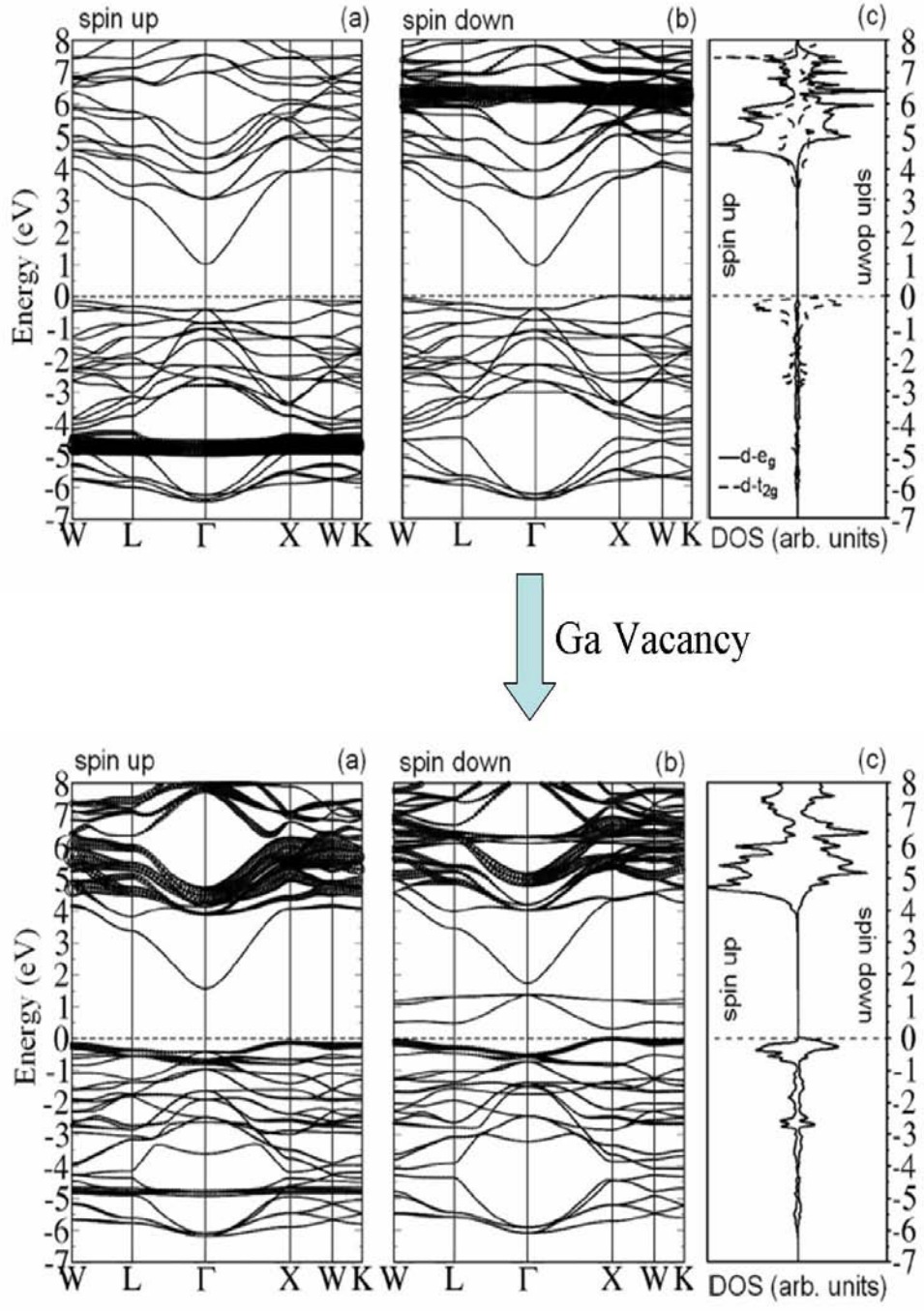

Figure 5.5: Band structure for (a) spin up, (b) spin down, and (c) d-orbital DOS for $Ga_{1-x}Gd_xN$ in the FM configuration. Top figure (without Ga vacancy) and bottom figure (with Ga vacancy) [192].

Theoretical studies by Gohda et al. suggest that the 5d electrons participate in nitrogen bonding and do not contribute to the magnetic moment. Their findings reveal that Gd incorporation causes Ga vacancies and the formation of defect complexes between Ga and Gd atoms are energetically favorable and result in ferromagnetic interactions (Figure 5.6) [191]. In the absence of V_{Ga}, the magnetic moment comes from the 4f electrons (7 μ_B), and for each V_{Ga} the magnetic moment increases monotonically by $3\mu_B$. Overall, this report suggests that the large magnetism observed is due to V_{Ga} that introduce holes above the VBM and implies that holes are responsible for the large magnetization.

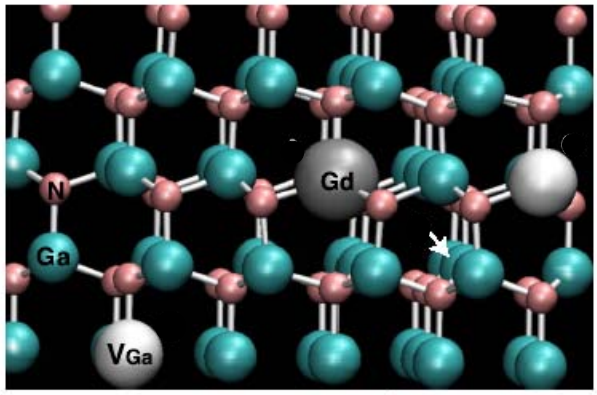

Figure 5.6: Atomic structure of GaGdN with the incorporation of Ga vacancy [191].

It must be pointed out that all theoretical models reported till date have been developed to explain the experimental observation of the large magnetic moment of 4000 μ_B/Gd ion in the $Ga_{1-x}Gd_xN$ films grown by Dhar et al. [185]. Recent theoretical predictions point to the fact that in wurtzite GaN holes result in greater exchange interactions and larger magnetization strengths as compared to electrons, but this has yet to be demonstrated experimentally [191, 192].

5.3. Experimental Method

This study carried out Gd doping under optimized GaN growth conditions to grow 0.5 μm thick $Ga_{1-x}Gd_xN$ on undoped GaN templates which were grown on sapphire substrates by MOCVD as shown in Figure 5.7. The challenges with Gd doping in MOCVD are that the precursors obtained have low volatility and vapor pressure curves are often not readily available from vendors. In this study Tris(2,2,6,6 - tetramethyl 3,5 heptanedionato) gadolinium was the Gd precursor used, and the bath temperature for the source was raised to 145 ˚C to ensure that the source entered the chamber in vapor phase. The growth rate was maintained at approximately 0.25 μm/hr to allow time for adatom diffusion and to prevent clustering. The theoretical doping concentration ranged from 0.5-24 %, it must be noted that these concentrations were calculated using the molar flow values of the precursor as follows:

$$\text{Gd \%} = \frac{[(\text{TMHD})_3 Gd]}{[TMGa)] + [(TMHD)_3 Gd]} \qquad \text{Equation (5.1)}$$

The reflectivity data for $Ga_{0.98}Gd_{0.02}N$ thin films is shown in Figure 5.7. It can be observed that fairly good oscillations were obtained indicating no significant material quality deterioration or surface roughening. Silicon and magnesium doping of these optimized $Ga_{0.98}Gd_{0.02}N$ films were also carried out to determine the effects of n- and p-type dopants on this material system.

Energy dispersive X-ray spectroscopy (EDS) was used to determine the actual Gd concentration of the films grown. These measurement results yielded a concentration of 0-4 % for the $Ga_{1-x}Gd_xN$ films. The next section presents a detailed analysis on the material properties of the films grown.

(a)

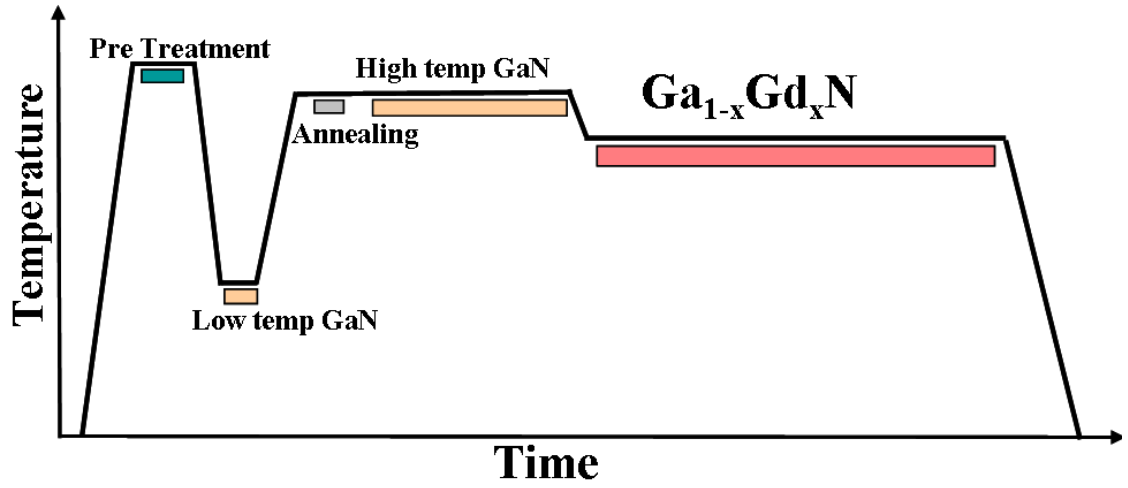

(b)

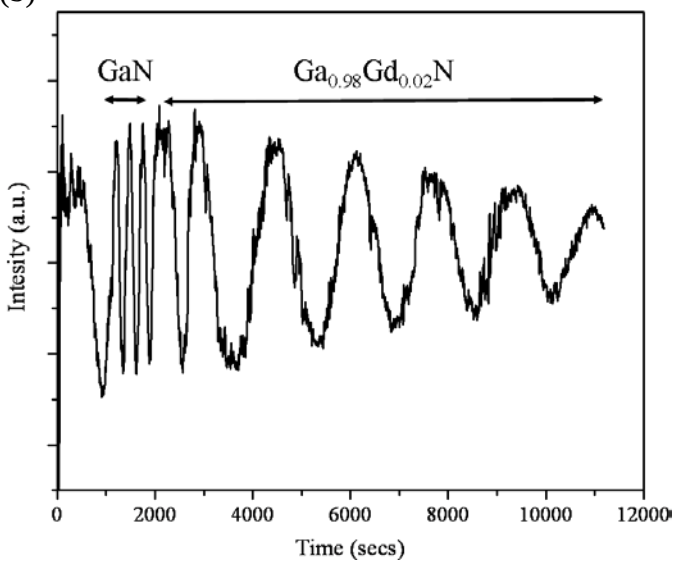

(c)

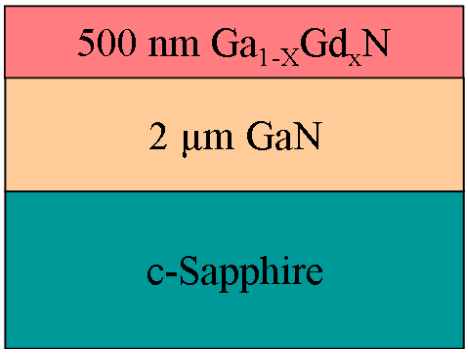

Figure 5.7: (a) Growth profile for $Ga_{1-x}Gd_xN$ on sapphire, (b) in-situ optical reflectometry curve for $Ga_{0.98}Ga_{0.02}N$ grown on GaN templates at a growth rate of ~0.25 µm/hr, (c) schematic of the final structure grown.

5.4. Material Analysis and Discussion

In-depth characterization was carried out to obtain a better understanding of the structural, optical, magnetic and electrical properties of the materials. The findings and discussion are presented below.

5.4.1. Structural Characterization

High resolution X-ray diffraction (HR-XRD) measurements were carried out to determine the quality of the thin films grown. Two main diffraction peaks were observed: a wurtzite GaN (0002) peak at 34.5° and a sapphire peak at ~42°. Additionally, a sample holder peak was detected at 38° (Figure 5.8). The diffraction curves also did not show the presence of any gross secondary phases. Neither the GdN (111) diffraction peak at 30.960° nor the GdN (200) diffraction peak at 35.2° were detected in this study [184, 194]. HR-XRD 2θ-ω plots did not show any shift or broadening of the GaN (0002) diffraction peak (Figure 5.8). It must be pointed out that GaN doped with 4 % Gd showed a similar XRD spectrum as 2 % Gd in GaN with no shift in peaks or additional phases. The Gd atom has a large atomic radius of 2.5 Å as compared with that of Ga (1.8 Å) and nitrogen (0.75 Å) and thus it would be expected that due to strain a XRD shift should be observed. The RE-N bonds are generally more polar than the Ga-N bond due to electronegativity differences (Pauling's electronegativity for RE is 1.1-1.25 versus Ga 1.8), and this helps to compensate for the RE-Ga size mismatch [174]. Similar observations were made for MBE grown $Ga_{1-x}Gd_xN$ with Gd concentration as high as 12.5 % that show no shift or new phases in the GaN XRD peaks [22, 184]. Additionally, it should be pointed out that the p-$Ga_{0.98}Gd_{0.02}N$ films were annealed at 800 °C for 4 minutes in a nitrogen atmosphere to activate the acceptors. Despite this annealing

treatment no secondary phases were observed. As apparent from the discussions in Chapter 4, HR-XRD is not sensitive enough to detect nano-clusters that may form during growth.

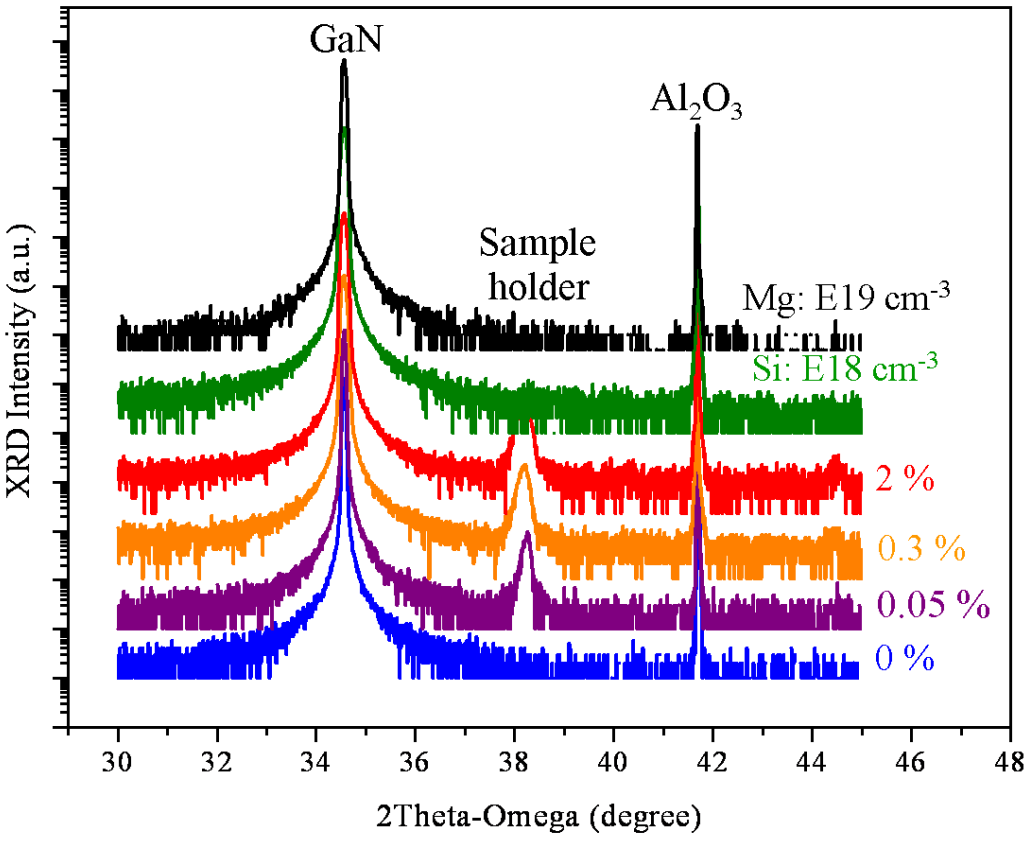

Figure 5.8: XRD curves for $Ga_{1-x}Gd_xN$ of varying concentration (x = 0-2 %). The Si and Mg doped diffraction curves are for 2 % Gd in GaN.

Raman measurements were performed on the $Ga_{1-x}Gd_xN$ films to determine the crystal quality and detect the presence of strain in these thin films (Figure 5.9). These measurements were performed in an unpolarized back-scattering geometry denoted as z(..)-z. The high intensities of the GaN E_2(high) peak at 569 cm^{-1} and A_1(LO) peak at 733 cm^{-1} visible in the Raman spectrum confirm the good structural quality of the doped films despite the larger size of the Gd atom and the high Gd concentration (10^{20} cm^{-3}). The e_g mode of the sapphire substrate is also observed at 750 cm^{-1} [195]. Furthermore, the

forbidden A_1(T0) mode at 531 cm^{-1} and the E_1(TO) mode at 560 cm^{-1} were also observed indicating imperfections in the GaN crystal.

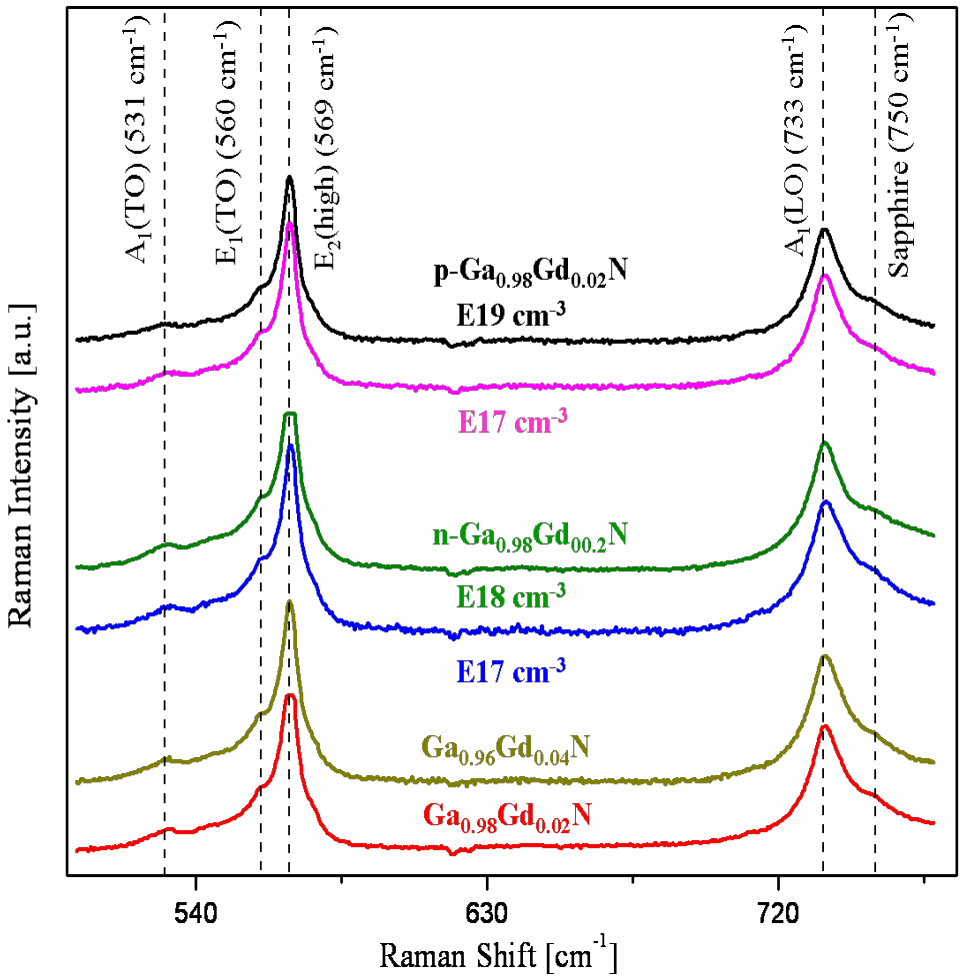

Figure 5.9: Strain analysis of $Ga_{1-x}Gd_xN$ by Raman spectroscopy as a function of Gd concentration and Si and Mg co-doping.

No reduction, broadening, or shift towards high frequency is observed for the A_1(LO) peak upon Gd co-doping, indicating that there is no significant increase in carrier concentration [196]. Further, no local vibration modes (LVM), disorder-activated modes, or vacancy related defects were observed upon Gd doping as in TM doped GaN [151, 152]. In 2 % Eu doped GaN, LVM have been observed at 535 cm^{-1} which increase with the doping concentration [151], but this effect was not observed for Gd doped GaN in this

study. The Si and Mg (annealed and unannealed) co-doped $Ga_{1-x}Gd_xN$ samples showed a similar spectrum as $Ga_{1-x}Gd_xN$, indicating no stress or strain is induced upon co-doping.

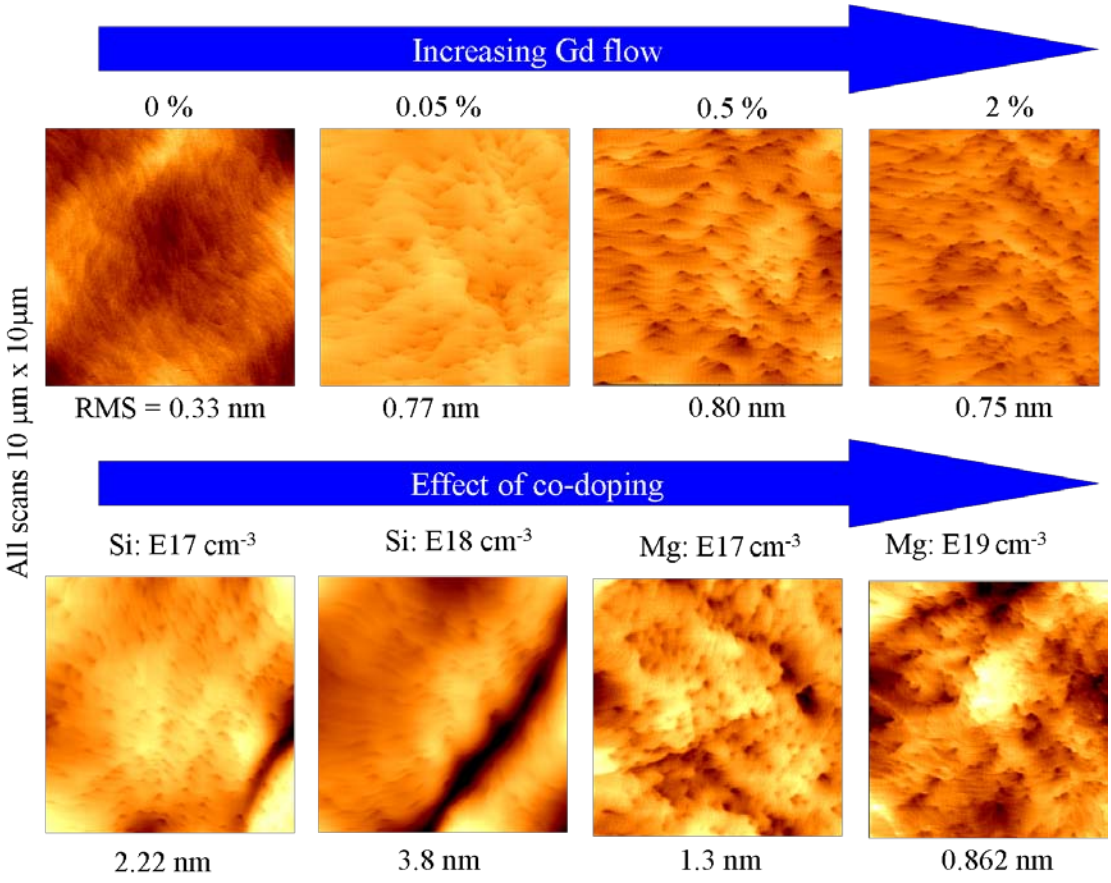

Figure 5.10: AFM images showing the effect of increasing Gd concentration and Si and Mg doping on the surface morphology of GaN.

AFM images display a step flow pattern for $Ga_{1-x}Gd_xN$ films, which is a characteristic of the MOCVD step flow growth mode (Figure 5.10). The images do not reveal a significant change in surface morphology as the Gd concentration is changed from 0.05 to 2 % and the films yield an RMS surface roughness of 0.75 nm for 2 % Gd. The surface roughness increases slightly upon Si and Mg co-doping to 3.8 nm and 0.862 nm, respectively. An increased surface roughness is expected with the introduction of Si, as it acts as an anti-surfactant for GaN [197]. Furthermore, upon annealing, no

significant change in surface morphology was observed in the AFM images for p-$Ga_{0.98}Gd_{0.02}N$ films. Overall, structural characterization revealed single phase, strain free films with a smooth surface for Gd doped GaN.

5.4.2. Optical Measurements

RT and low temperature (LT) PL measurements were performed on the epitaxial $Ga_{1-x}Gd_xN$ layers to determine the optical quality of the material.

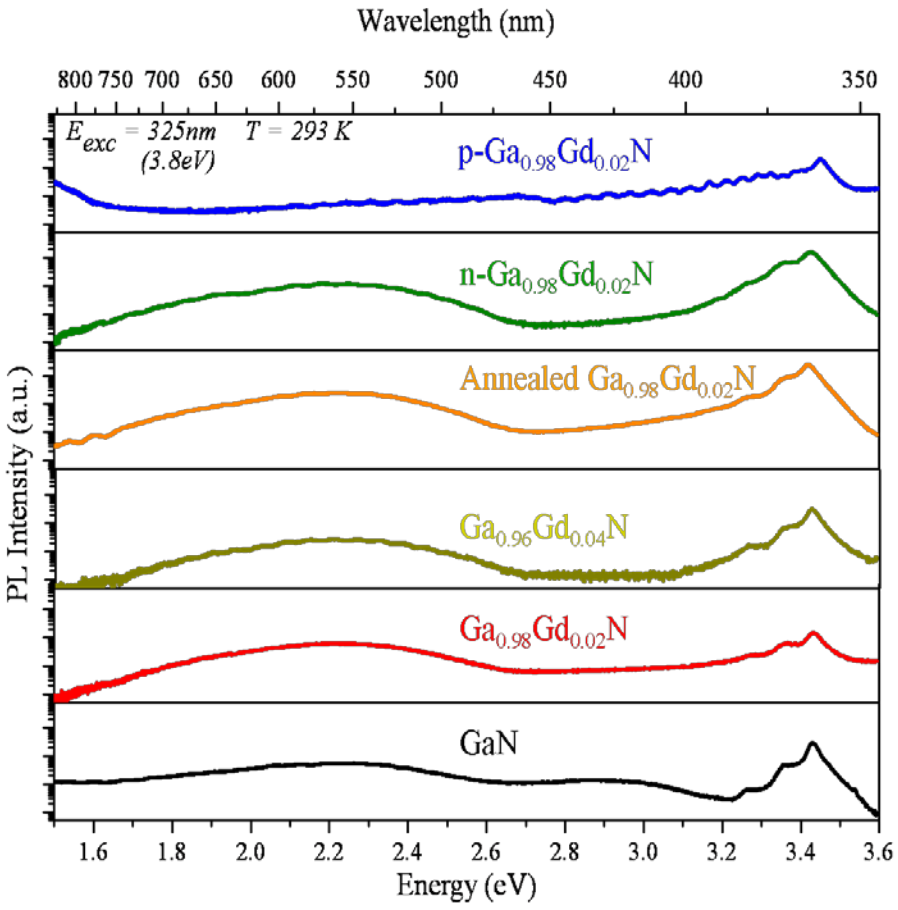

Figure 5.11: Room temperature PL for $Ga_{0.98}Gd_{0.02}N$ as-grown, annealed, n-, and p-doped as compared with GaN.

PL was excited using a HeCd gas laser with a wavelength of 325 nm. A long-pass filter was used for PL measurements beyond 600 nm to remove second order diffraction

of the laser and GaN bandedge emission. These measurements show the presence of the GaN bandedge emission at 3.42 eV indicating that the Gd doping does not degrade the optical quality of the material (Figure 5.11).

No significant enhancement of the yellow luminescence band was observed by Gd doping, which further confirms that the defect density was not increased. Furthermore, in comparison to undoped GaN, the blue luminescence is quenched for the Gd doped GaN films. This band is usually attributed to a gallium vacancy (V_{Ga}) located at 0.8 eV above the valence band and oxygen donor (O_N) impurity located at 0.25 eV below the conduction band minimum [153].

LT PL measurements were carried out on $Ga_{0.98}Gd_{0.02}N$ to further probe into the optical quality of the material (Figure 5.12). It was observed that below 100 K additional peaks at 3.0-3.3 eV and at 1.78 eV appear. In the range of 3.0-3.3 eV, four distinct peaks are observed: 3.0 eV, 3.09 eV, 3.18 eV, and 3.27 eV. The intensity and peak positions do not vary significantly as the temperature is varied from 8.5 to 100 K. This peak position matches the previously reported satellite peaks in LT measurements of GaN that have been attributed to donor-acceptor pair (DAP) transitions [198]. Thus the peak at 3.27 eV is the zero phonon line (ZPL) and the peaks at 3.18, 3.09, and 3.0 eV are the LO phonon replicas of the shallow donor to acceptor transition. The DAP observed here are attributed to transitions between donors such as nitrogen vacancies or oxygen donors and Gd ions.

It has been suggested earlier that these peaks can be attributed to the internal transition associated with Gd^{3+} that occur between the first excited state $^6P_{7/2}$ and the ground state of $^8S_{7/2}$ [182, 199]. However, this internal transition value is usually at 3.95 eV and it is hard to justify the large deviation. These DAP are also present in Mg

doped $Ga_{0.98}Gd_{0.02}N$ films but are harder to resolve due to the dominance of the DAP transitions in the spectrum that normally occur in p-GaN. At high temperatures the DAP transitions give way to electron-acceptor transitions, which are seen as a bump in the low energy side of the GaN bandedge room temperature spectrum [200]. The experimental results suggest that Gd doping enhances the DAP transition in GaN and may possibly results in the creation of acceptors.

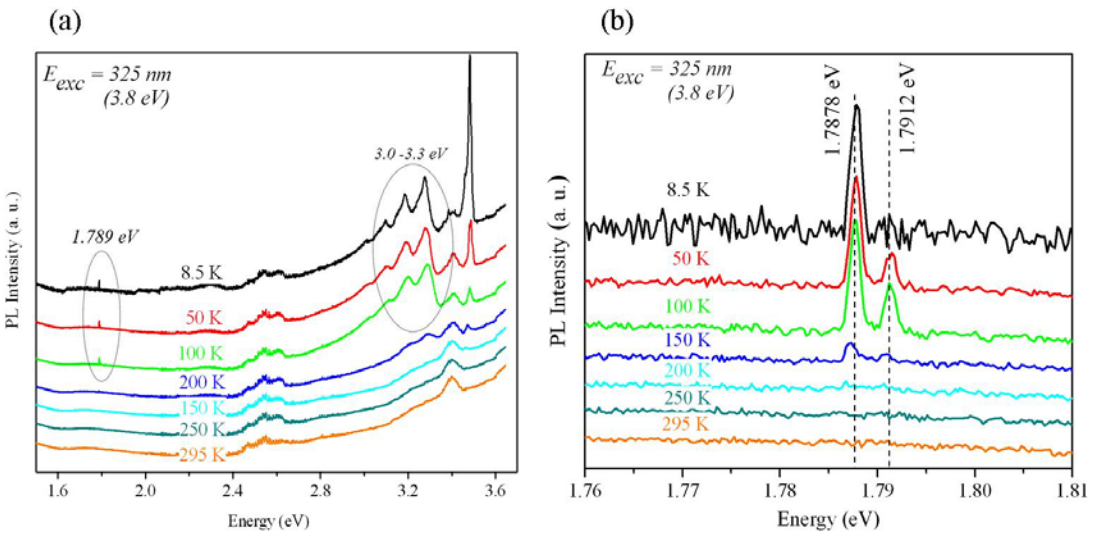

Figure 5.12: Temperature dependent PL spectrum for $Ga_{0.98}Gd_{0.02}N$: (a) wide scan, (b) narrow spectrum to analyze the low energy doublet.

Detailed LT measurements at 1.78 eV revealed the presence of a doublet peak which is separated by approximately 3.4 meV and has a full width half maximum of (FWHM) less than 40 μeV. This transition becomes apparent at temperatures below 150 K and the doublet peak intensity increases with decreasing temperature till about 10 K where only a single peak is observed. This is because as the temperature is reduced Boltzmann statistics dictates that electrons do not have sufficient energy to occupy the higher sub-bands and hence this transition is not observed.

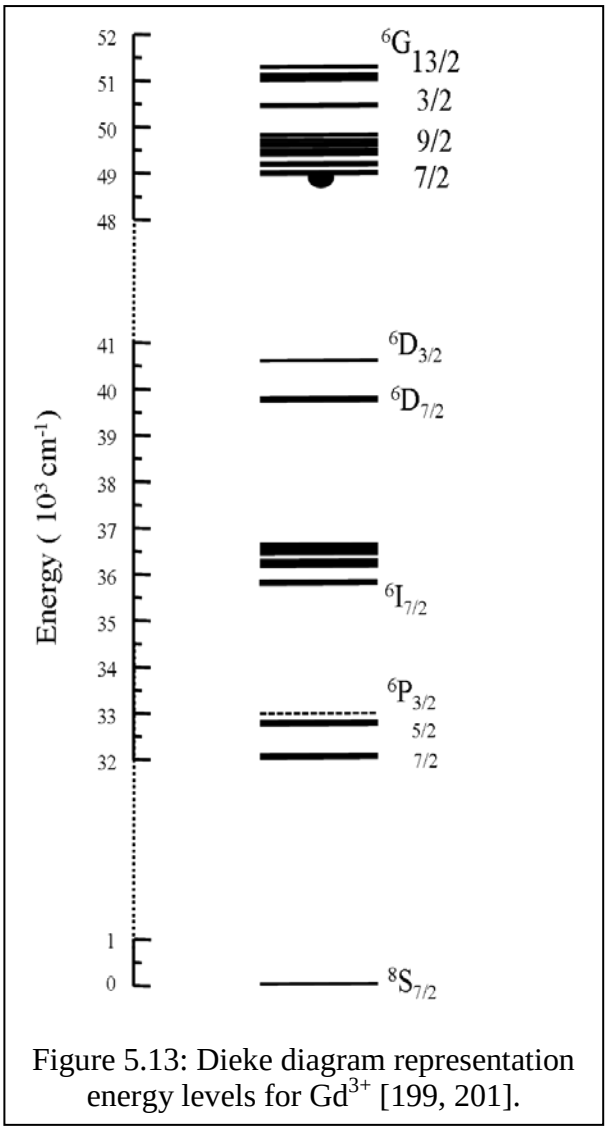

Figure 5.13: Dieke diagram representation energy levels for Gd^{3+} [199, 201].

Optical measurements conducted at 4 K by Lipinska et al. on bulk GaGdN grown by high pressure methods show the presence of a sharp peak at 1.78 eV with a linewidth of 5 meV [182]. They attribute this peak to an internal transition of Gd^{3+} between $^6G_{7/2}$ to ^6P levels. However as per the energy level Dieke diagram for the Gd^{3+} ion (Figure 5.13), the actual transition values for these levels is closer to 1.986 eV [199, 201].

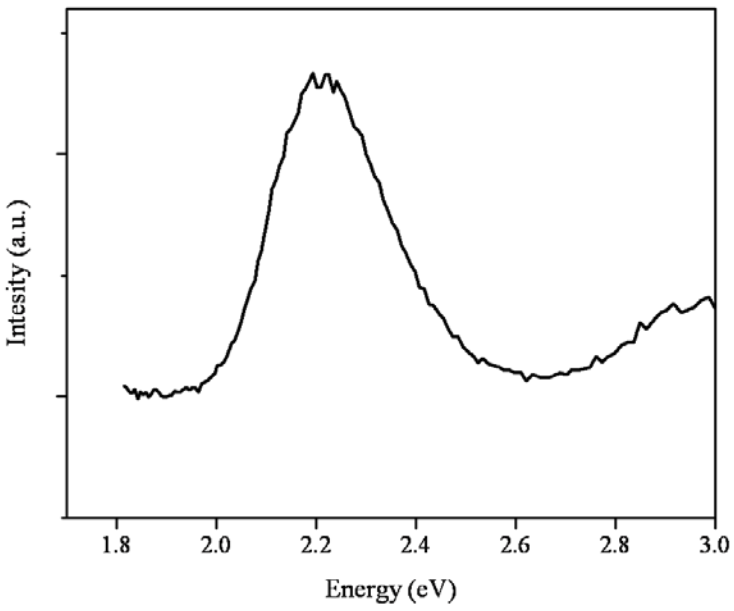

Figure 5.14: PLE spectrum taken at RT to observe the transitions that can excite the 1.78 eV peak.

Photoluminescence excitation (PLE) spectra were recorded at RT and LT to identify the energies that can excite the transition responsible for the 1.78 eV (Figure 5.14). These measurements were performed using a 250 W halogen-tungsten lamp in combination with a 275 mm double monochromator as a tunable light source. The detection unit consisted of a 300 mm double monochromator and a PMT with a GaAs photocathode. Lock-in technique was used for noise reduction. The PLE spectrum indicates that 2.2 eV and 2.99 eV can excite the emission observed at 1.78 eV.

Generally the RE ions incorporated can be excited by an energy transfer from electronic recombination within the host crystal to the 4f electrons. The subsequent radiative relaxation has been observed in the form of luminescence in the red and infrared for a range of RE ions (Figure 5.15) [174]. Such transitions have been observed for Eu (621 nm) and Er (537/ 558 nm) doped GaN.

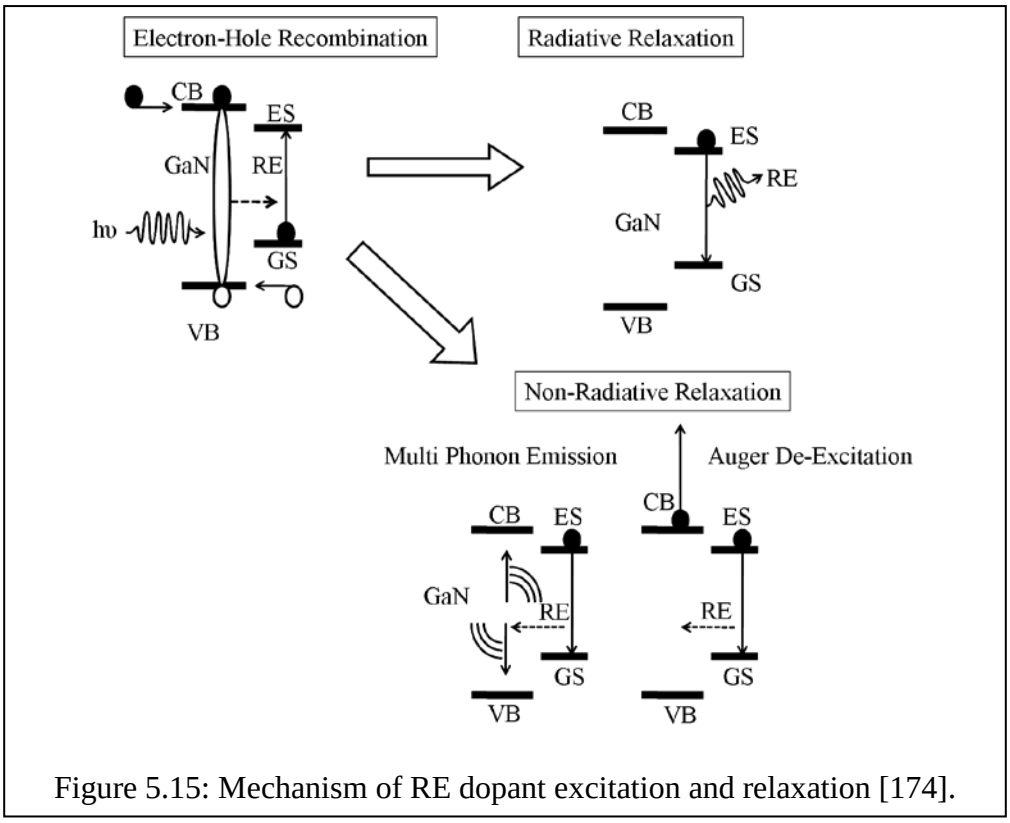

Figure 5.15: Mechanism of RE dopant excitation and relaxation [174].

Time resolved PL measurements on $Ga_{0.98}Gd_{0.02}N$ films were done at room temperature to determine the lifetime of the doublet transition (Figure 5.16). This measurement was conducted using a 473 nm laser excitation beam that was chopped at a frequency of 25 Hz and the temporal profiles were recorded using a Tectronics oscilloscope. The transition lifetimes were determined to be 3.53 ms (Figure 5.16) which is consistent with the lifetime of 3 ms presented for the 1.78 eV for the bulk GaGdN films [202]. A second indication that, Lipinska is reporting the same emission that is discussed here is a shoulder peak to right of the 1.78 eV that was seen in the bulk GaGdN films, which could be analogous to the doublet seen here.

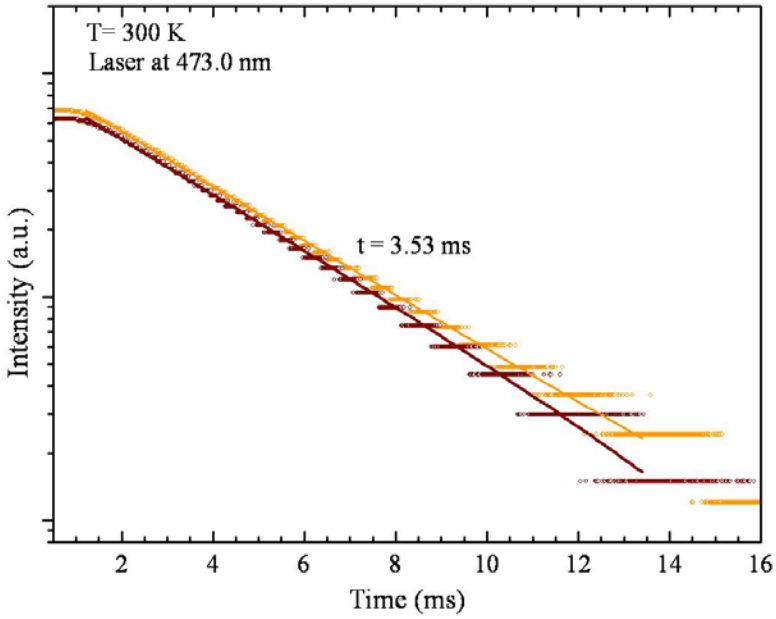

Figure 5.16: Time resolved PL for the $Ga_{1-x}Gd_xN$ doublet peak at 1.78 eV.

Upon probing further, it is determined that the 1.78 eV doublet seen in this study is due to the octahedrally coordinated Cr^{3+} impurities that are present in the sapphire substrate and is responsible for the ruby color in sapphire [203, 204]. It is ironic that the reports by Lipinska et al., on bulk GaGdN (not grown on any substrates) shows a peak at the exact same position. At this time, it can not be concluded that the doublet in the MOCVD films are primarily due to Gd and further investigations will have to be done on substrates that are free of transition metal impurities.

Till date the only optical report on epitaxially grown $Ga_{1-x}Gd_xN$ has been presented by Choi et al. on MBE grown $Ga_{0.94}Gd_{0.06}N$ films grown on SiC substrates [205]. RT optical measurements carried out by a 325 nm HeCd laser reveal a sharp line at 652 nm with a lifetime of 41 μs which is attributed to an internal transition of Gd^{2+}. However, this contradicts their X-ray photoelectron spectroscopy and X-ray absorption near edge structural characterization results that reveal Gd to be present in the Gd^{3+} state [206].

Furthermore, below 150 K a broad peak is observed at 505 nm in the MBE grown films, which is attributed to a dipole transition with lifetimes of 1 and 15 ns. Although the mechanism is not clear, two theories have been proposed by Choi et al. The first being a transition from 5d orbital to 4f orbital of the Gd ion and the second being due to a nitrogen vacancy adjoined to the Gd ion. This study used high Gd concentrations and the structural and optical characterization results present conflicting results. Additionally, RE doping in GaN results in 4f intra transitions with lifetimes on the order of 1 μs to 1 ms which does not support the nanosecond lifetimes reported by the MBE films [174]. Overall, till date, there are no conclusive reports on the optical properties of Gd doped GaN. It is possible that these low lifetime transitions are annihilated by defects in the semiconductor and are difficult to detect. Furthermore, care has to be taken to grow these films using substrates and precursors that do not have significant impurities that can interfere with the optical observations.

5.4.3. Magnetic Properties

RT magnetization data for $Ga_{1-x}Gd_xN$ were obtained by a vibrating sample magnetometer (VSM) as shown in Figure 5.17. It was observed that as the Gd concentration is increased (from 0 to 2 %), a transition from diamagnetism to ferromagnetism occurs; the saturation magnetization strength for ~2 % Gd is fairly strong with a value of 20 emu/cm^3. The superconducting quantum interference device (SQUID) measurements conducted at 5 K revealed exactly the same magnetization strength and a similar coercivity to RT measurements conducted by both the SQUID and VSM. SQUID measurements reveal that films with 4 % Gd although still ferromagnetic resulted in a significant drop in magnetization, with a maximum strength of 0.65 emu/cm^3.

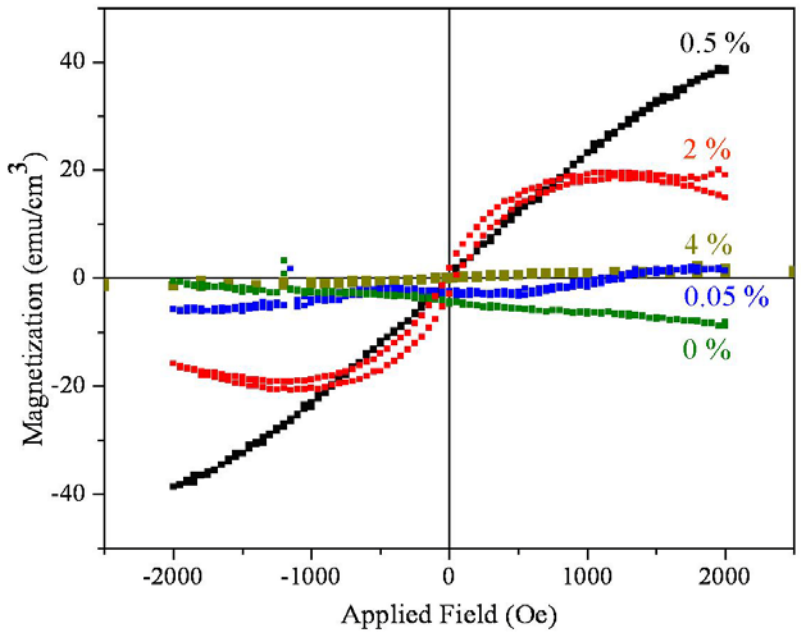

Figure 5.17: Room temperature magnetization data from VSM for $Ga_{1-x}Gd_xN$ thin films as a function of Gd concentration ranging from 0-4 %.

The 20 emu/cm^3 for $Ga_{0.98}Gd_{0.02}N$ results in a magnetic moment of 2.5 μ_B/Gd atom (calculated by Equation 5.2), which is approximately 33 % of the theoretical magnetic moment of a Gd atom (7.548 μ_B/Gd atom) [207].

$$M = N \mu \qquad \text{Equation (5.2)}$$

where M is the saturation magnetization,

N is the number of Gd atoms per unit volume, and

μ is the magnetic moment per Gd atom.

To be able to use DMS practically in semiconductor devices it is ideal that their magnetization properties be retained or enhanced upon n- and p-doping. To this end, magnetization studies have been conducted on Si and Mg co-doped $Ga_{0.98}Gd_{0.02}N$ films. A systematic increase in magnetization was observed as the Si concentration was varied

from 10^{16} cm^{-3} to 10^{18} cm^{-3}, with a maximum magnetization strength of 110 emu/cm^3, which is five times greater than the regular $Ga_{0.98}Gd_{0.02}N$ films (Figure 5.18). A similar trend has been observed for Si doping of $Ga_{1-x}Gd_xN$ in MBE grown films [183, 184].

It is apparent that the addition of donors enhances the magnetization and stabilizes the ferromagnetic phase in the material. These findings are in agreement with the theoretical predictions of Dalpian and Wei, which state that electrons stabilize the ferromagnetic phase in zinc blende $Ga_{1-x}Gd_xN$.

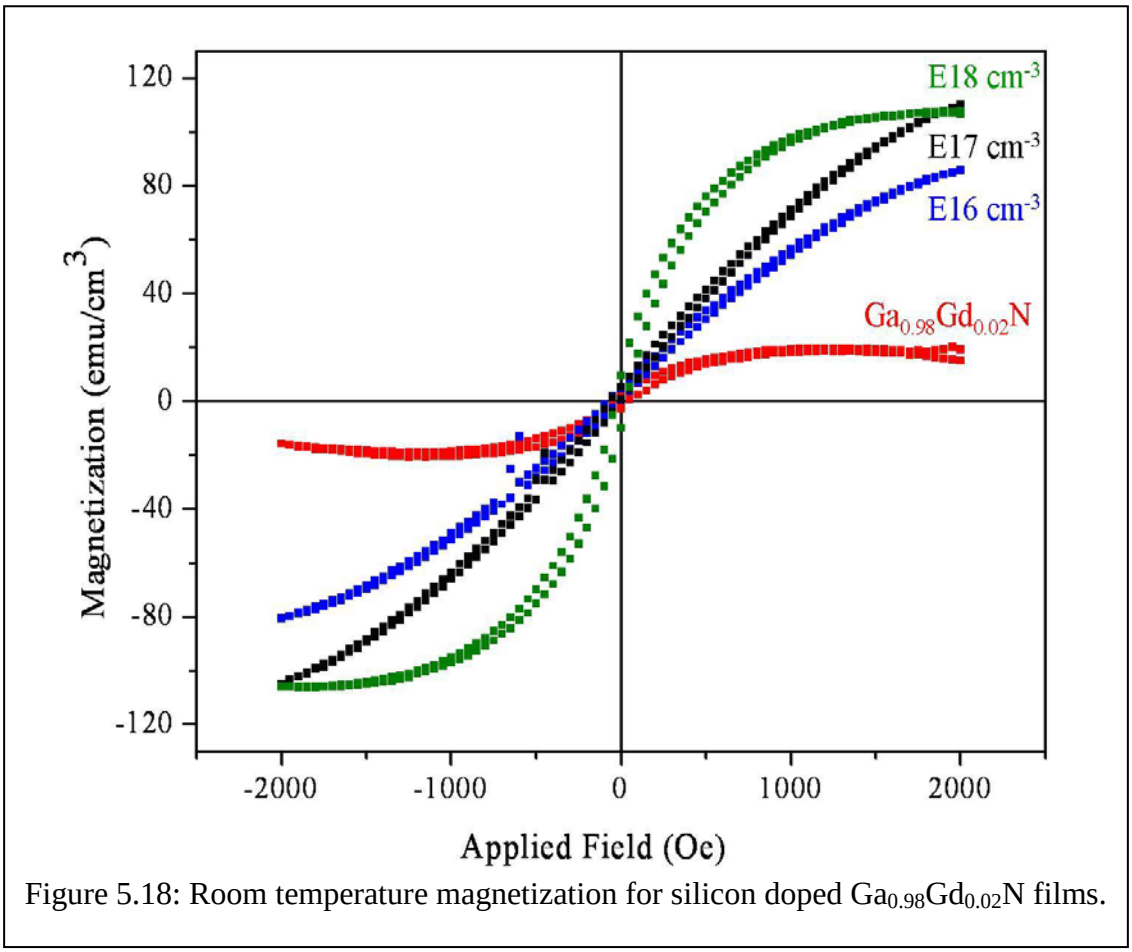

Figure 5.18: Room temperature magnetization for silicon doped $Ga_{0.98}Gd_{0.02}N$ films.

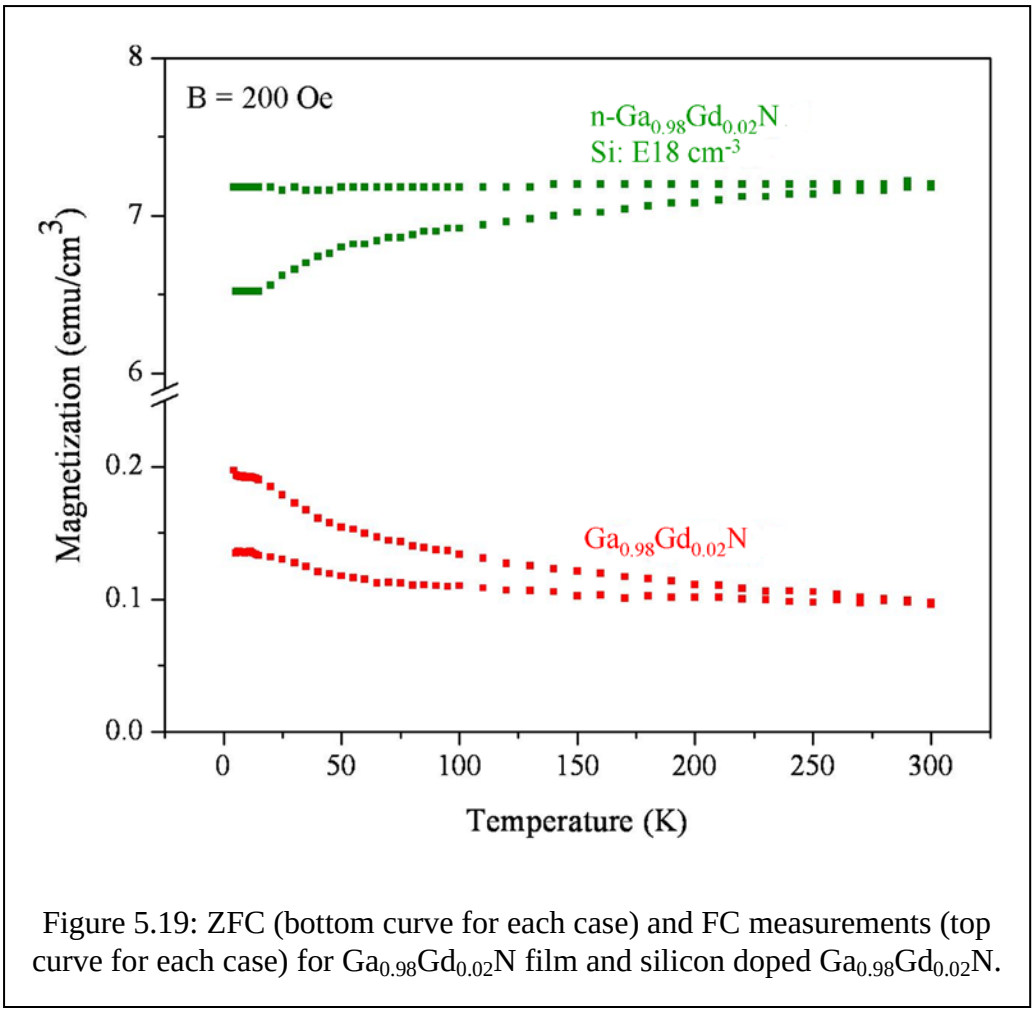

Figure 5.19: ZFC (bottom curve for each case) and FC measurements (top curve for each case) for $Ga_{0.98}Gd_{0.02}N$ film and silicon doped $Ga_{0.98}Gd_{0.02}N$.

Zero field cooled (ZFC) and field cooled (FC) measurements were performed at 200 Oe to obtain a deeper insight into the magnetic properties of the material. Figure 5.19 shows a small splitting between the ZFC and FC curves for Si-$Ga_{0.98}Gd_{0.02}N$ films. This splitting is much smaller as compared to TM doped GaN where the splitting ranged over 8 emu/cm^3 for $Ga_{0.985}Mn_{0.015}N$ doped with Si concentration of 10^{18} cm^{-3}. Furthermore, no pronounced closing of the curves is seen in the curves at low temperatures excluding the possibility of the presence of GdN clusters in the thin film [179]. It should be pointed out that the actual T_C could be higher than 300 K as the curves do not completely intersect at this point.

Till date there have been no reports of p-doping in $Ga_{1-x}Gd_xN$ by any growth technique. Room temperature magnetization data obtained by VSM is shown for p-$Ga_{0.98}Gd_{0.02}N$ films in Figure 5.20. Prior to Mg activation (carried out at 800 ˚C for 4 minutes in a N_2 atmosphere), a slight enhancement is seen upon Mg doping with 10^{17} cm^{-3}. However, after activation when all the Mg acceptors are broken away from the hydrogen atoms that passivate them, a massive increase is seen in the magnetization for Mg doping levels of 10^{17} cm^{-3} and 10^{19} cm^{-3}, with a maximum magnetization strength of 500 emu/cm^{-3} (25 times greater than the magnetization for $Ga_{0.98}Gd_{0.02}N$ film) obtained for 10^{19} cm^{-3}. These findings suggest that it is holes (acceptors) that result in higher magnetization than electrons (donors).

It is interesting to note that, in contrast to the $Ga_{1-x}TM_xN$ results, co-doping and p-type activation of $Ga_{1-x}Gd_xN$ enhances the magnetic signal [208]. Theoretical and experimental studies have indicated that carrier mediated ferromagnetism is possible in $Ga_{1-x}Gd_xN$ [183, 184, 186]. This study provides support for the theory that carriers enhance ferromagnetism in $Ga_{1-x}Gd_xN$ and provides a potential avenue for the realization of spintronic devices.

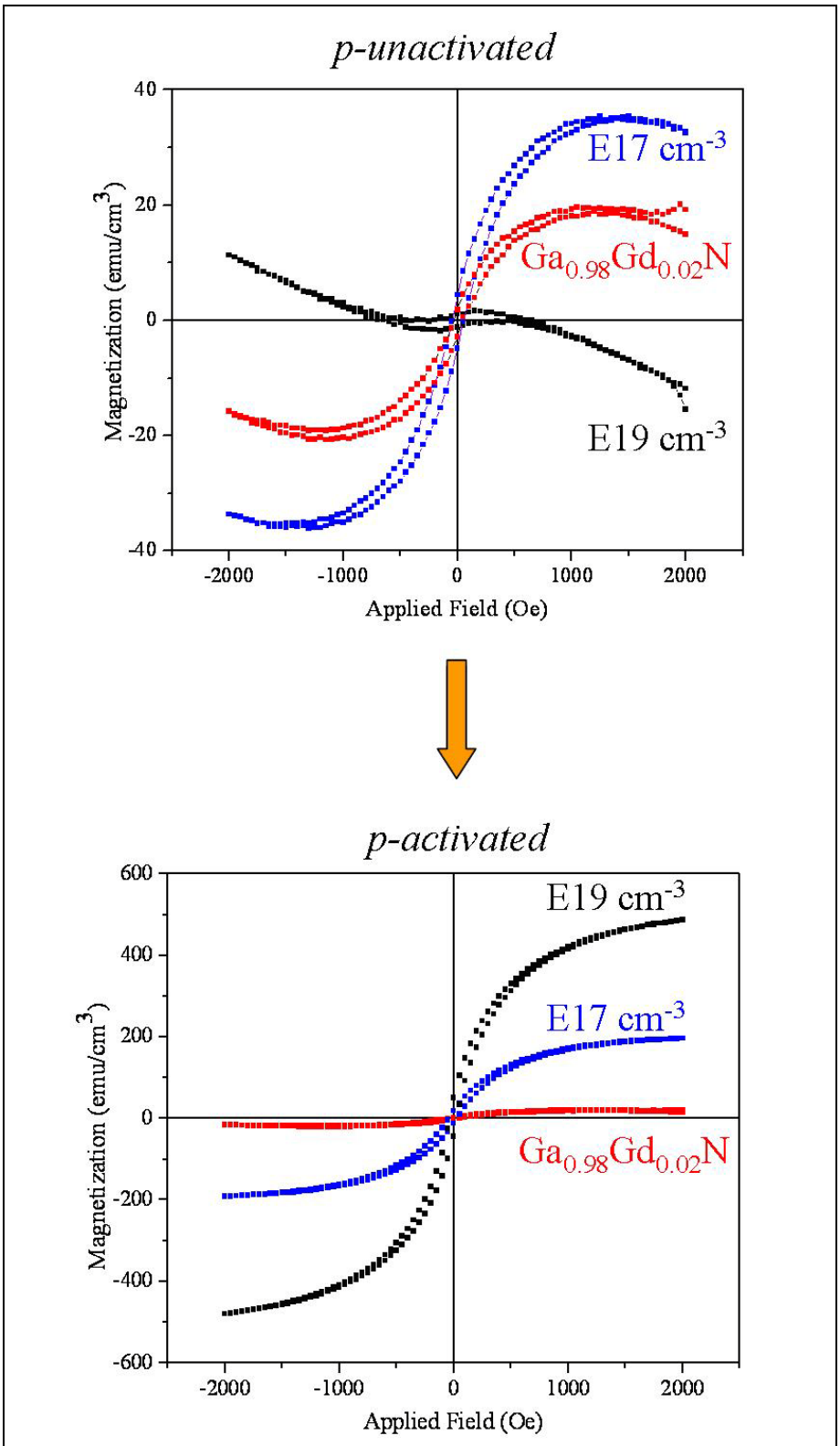

Figure 5.20: RT hysteresis curves for p-doped $Ga_{0.98}Gd_{0.02}N$ films and the effect of p-type activation on magnetization.

5.4.4. Electrical Properties

Magnetization measurements show that $Ga_{1-x}Gd_xN$ displays room temperature magnetization that can be enhanced by doping it either n- or p-type. This DMS could be useful for spintronic device applications provided that it is conducting. Till date most of the $Ga_{1-x}TM_xN$ films obtained are semi-insulating and thus do not pose much utility for device applications. The most promising $Ga_{1-x}Gd_xN$ films grown by Dhar et al., were found to be highly resistive and, hence, they ruled out free carrier mediated ferromagnetism [209]. MBE studies showed that $Ga_{1-x}Gd_xN$ films are highly resistive and the films become increasingly conductive upon Si doping [183]. The electrical properties were determined by conducting Hall effect measurements on the $Ga_{1-x}Gd_xN$ films, and n- and p-doped $Ga_{1-x}Gd_xN$ thin films, the Hall data obtained is shown in Table 5.1. To ensure that the underlying GaN template layer did not provide a conduction path, the GaN buffer was also doped with Gd. It is widely believed that Gd is incorporated as Gd^{3+} in GaN and is isovalent in this host semiconductor and should not result in any free carriers [174]. The Hall measurements reveal that Gd doping in GaN results in an increase of carriers and makes the semiconductor more n-type. This could be due to an increase in nitrogen vacancies or due to an increase in oxygen defect levels that both act as donors. The $Ga_{1-x}Gd_xN$ films are conducting and possess low resistance. This is the first report of conducting $Ga_{1-x}Gd_xN$ whose magnetization strengths can be enhanced by co-doping. These results are extremely promising as they provide an avenue to realize spintronic devices. Furthermore these conducting films indicate that Gd_2O_3 is not primarily formed during growths. This secondary phase is insulating and commonly used

as a dielectric [210, 211]. Figure 5.21 depicts the effect of carrier concentration on magnetization in $Ga_{1-x}Gd_xN$ films.

Table 5.1: Electrical properties as determined by Hall measurements for $Ga_{1-x}Gd_xN$ thin films.

Gd doping Concent. (%)	***Co-dopant Concent. (cm^{-3})***	***Carrier Concent. (cm^{-3})***	***Mobility (cm^2/Vs)***	***Resistivity (Ω-cm)***	***Sat. Magnet. (emu/cm^3)***	***Coercive Field (Oe)***
GaN						
-	-	E16-E17	300	0.09	-	-
$Ga_{1-x}Gd_xN$						
0 %	-	2.7 E17	145.4	0.15	-	-
0.5 %	-	4.59 E17	187	0.7	-	19
2 %	-	7.09 E17	195.3	0.03	20	35.46
4 %	-	2.5 E17	467	0.053	1	-
Si doped $Ga_{0.98}Gd_{0.02}N$						
2 %	E17	4.33 E17	392.7	0.037	110	29.165
2 %	E18	1.531 E18	288	0.014	110	36.636
Activated Mg doped $Ga_{0.98}Gd_{0.02}N$						
2 %	E17	7.19 E14	260	1.84	197	34.72
2 %	E19	5 E16	42	0.55	484	31.17

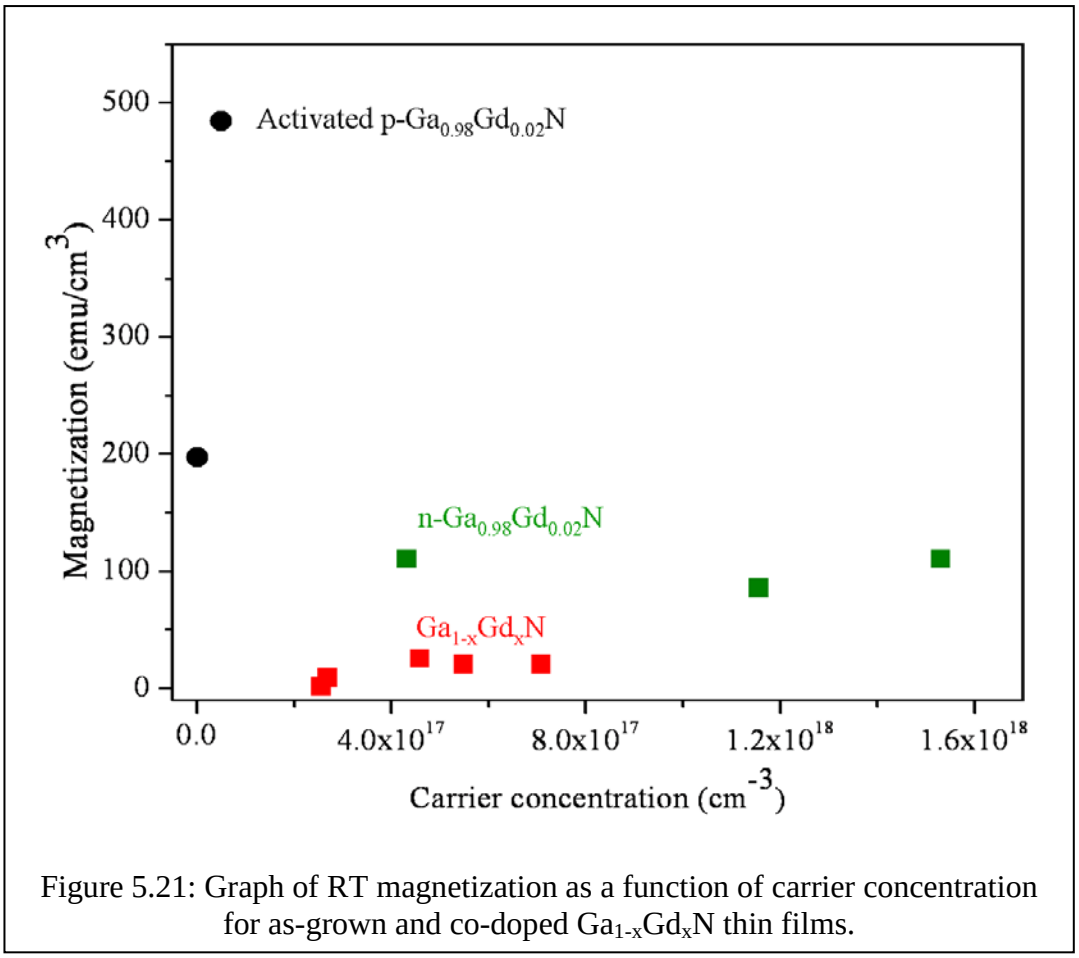

Figure 5.21: Graph of RT magnetization as a function of carrier concentration for as-grown and co-doped $Ga_{1-x}Gd_xN$ thin films.

5.5. Mechanism Associated with the Observed Magnetization

It is generally accepted that Gd in GaN occupies the cation site and is isovalent. As mentioned in section 5.2.2, the theoretical studies state that the Gd-Gd interactions in $Ga_{1-x}Gd_xN$ are antiferromagnetic and need the presence of impurities to mediate the ferromagnetism [186, 192]. Till date, all reports of Gd doped GaN have resulted in insulating films even though GaN is generally n-type with a carrier concentration of 10^{16} cm^{-3} arising due to the intrinsic defects (generally nitrogen vacancies). This observation has led experimentalist and theorist to believe that vacancies are generated during Gd doping that compensate for the intrinsic donors in the material and cause the films to become resistive. However, the experimental results in this study reveal

conductive films with n-type behavior. Thus it is proposed that the ferromagnetism in the films grown in this study is stabilized by donors resulting from either nitrogen vacancies or oxygen donors and not gallium vacancies as proposed by recent theoretical studies. This is further supported by recent report on MBE grown $Ga_{1-x}Gd_xN$ (x = 12. 5 %) film which show through X-ray absorption fine-structure (XAFS) the presence of a large number of nitrogen vacancies around Gd atoms.

Additionally, beyond 4 % the magnetization reduces significantly, this is because at high Gd concentrations the mean free path between the Gd ions decreases and the antiferromagnetic exchange interactions takes over and the ferromagnetic contribution decreases. This effect of a decrease in magnetization with high concentration has also been seen in films grown by ion implantation and MBE [185, 190]. Additionally, it is also feasible that at this higher concentration low T_C microscopic secondary phases, such as GdN, are being formed resulting in an overall reduction of the RT ferromagnetic signal. As seen in $Ga_{1-x}TM_xN$ films, microscopic secondary phases are not always easy to detect by structural characterization techniques such as XRD.

Intentionally doping the semiconductor with donors results in the magnetization being enhanced five-fold. This observation is attributed to the s-f coupling that is allowed in T_d GaN symmetry (unlike TM doped GaN where s-d coupling is not allowed or very weak in the presence of vacancies) and results in ferromagnetic exchange. This s-f coupling results in a negative exchange splitting of the conduction band minimum (ΔE_{FM-AFM}) and the added electrons occupy the spin-down CBM states and stabilize the ferromagnetic phase. It must be pointed out that the possibility of s-d coupling cannot be ruled out completely in the presence of extrinsic donors or intrinsic defects. A critical

deciding factor if s-d or s-f coupling is responsible for the ferromagnetic mechanism will depend on the actual location of the d and f levels in the GaN host semiconductor. Although there is still debate among theorist if s-d or s-f coupling is responsible for the magnetization it is quite apparent that the addition of donor does indeed enhance the magnetization of $Ga_{1-x}Gd_xN$ films and provides an avenue for controlling magnetization strength.

Additionally, electrical characterization by Hall measurements reveal that p-doping of $Ga_{1-x}Gd_xN$ does result in compensation of the n-type carriers and once the background donor's concentration is overcome the semiconductor turns p-type and the resulting magnetization is enhanced by 25 times. This large magnetization can be understood in the terms of p-d exchange coupling between the p-like GaN valence band and Gd 5 orbital. The addition of holes near the valence band results in a significant difference in the spin-up and spin-down states and results in the stabilization of the ferromagnetic phase [192]. The coupling with d orbitals results in magnetic moments larger than coupling with f orbitals and supports the hypothesis that p-d interactions are responsible for the enhanced magnetization.

The high magnetization strength of p-$Ga_{1-x}Gd_xN$ supporting the fact that p-d exchange interactions are much stronger than s-d or s-f coupling. This work resolves the debate between the theoretical models proposed by Dalpian and Wei, and by Liu et al. on whether holes or electron exchange interactions are more stronger in stabilizing ferromagnetism in $Ga_{1-x}Gd_xN$ [186, 192].

The overall mechanism for ferromagnetism in $Ga_{1-x}Gd_xN$ films can be attributed to RKKY indirect exchange interaction. This is because it is the presence of donors and

electrons that are responsible for the ferromagnetism observed in this semiconducting material.

The advantage of the $Ga_{1-x}Gd_xN$ films obtained in this work is that they are conducting and the magnetic and electrical properties can be controlled by n- and p-doping.

5.6. Devices

A simple device that can be used to provide a proof of concept for use of $Ga_{1-x}Gd_xN$ for spin injection and spin transport is a spin-LED. In this device spin polarized holes (electrons) and unpolarized electrons (holes) are injected from each electrical contact and recombine in a quantum well. Ideally the light emitted should be circularly polarized, $\sigma +$ (right circularly polarized light) or $\sigma -$ (left circularly polarized light) depending on the polarization of the injected carriers.

To this end, three main device structures have been grown in this study as shown in Figure 5.22. As both the n- and p-type $Ga_{1-x}Gd_xN$ are ferromagnetic and conducting, this study can invoke devices that utilize the spin injection of electrons and holes. The first two structures are a p-LED and a p-contact LED, which provide for the injection of spin polarized holes. Magnetization measurements on these two LED structures showed that the p-$Ga_{0.98}Gd_{0.02}N$ still retained a high magnetization despite the reduced thickness of 150 nm. The p-contact LED was grown to achieve a device that allowed for spin injection of holes with a reduced turn on voltage. The n-LED structures allowed for the injection of spin polarized electrons. This structure is important as spin injection of electrons is more efficient as they have higher mobility and spin lifetimes than holes [212]. Furthermore it

is easier to make contacts to n-GaN versus p-GaN. The active layer in this study consisted of InGaN quantum wells (QWs) and GaN barriers with indium concentrations of approximately 12 %. Typically five sets of multiple quantum wells (MQW) were used, though this number was reduced to three to study the impact of the wells on the polarization of the light emitted. A low indium concentration was maintained to ensure that the built-in strain caused by high indium concentration in the InGaN MQW did not impact the spin lifetimes.

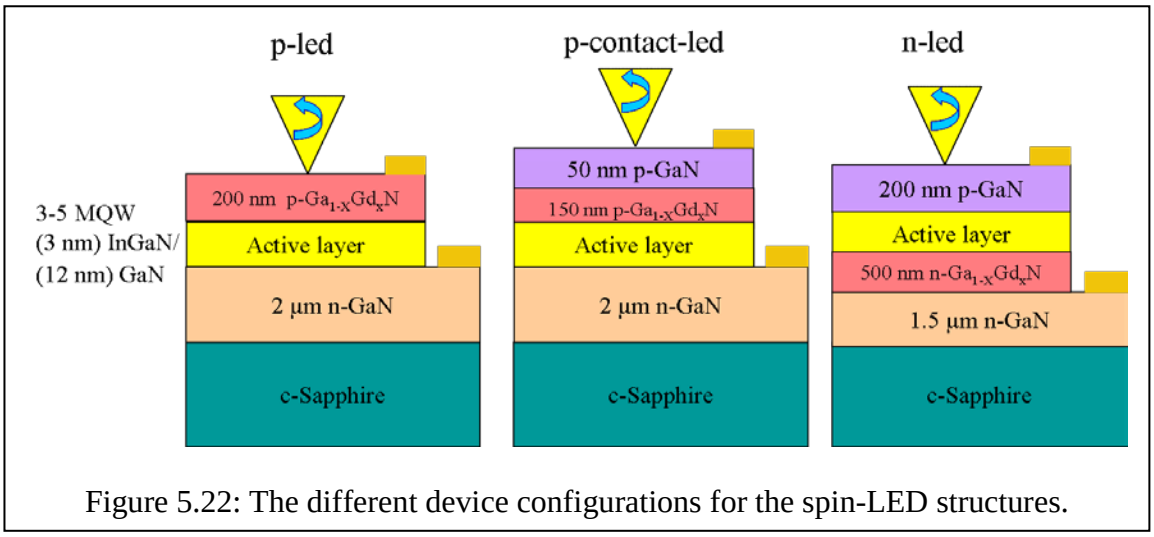

Figure 5.22: The different device configurations for the spin-LED structures.

I-V measurements conducted on these device structures revealed a low forward voltage (V_f) as compared to the TM doped GaN devices. The V_f were found to be 5 V, 7 V, and 8 V for the p-contact LED, n-LED, and p-LED respectively (Figure 5.23). The number of MQWs did not have an impact on the I-V measurements for each of the three structures.

Due to the strain caused by wurtzite InGaN MQW in GaN-based LEDs, these devices often show polarized light emission without any magnetic dopants and thus it is essential to use the polarization signal at 0 Gauss as a background signal. Furthermore, if

polarized light is emitted due to the spin polarized carriers then the circular polarized light intensity should respond to the applied magnetic field and is given by Equation 5.3.

$$P_{circ} = \frac{I(\sigma^+) - I(\sigma-)}{I(\sigma+) + I(\sigma-)} \qquad \text{Equation 5.3}$$

where $I(\sigma^+)$ and $I(\sigma^-)$ are the intensities of the right and left circularly polarized light respectively.

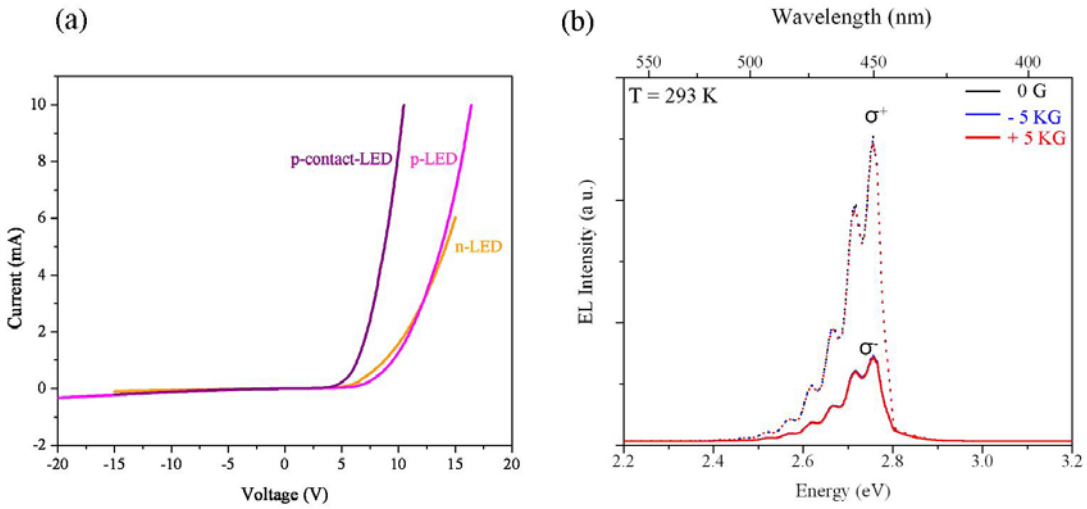

Figure 5.23: Device characterization for $Ga_{0.98}Gd_{0.02}N$ LEDs (a) I-V measurement for the three LED configuration, (b) RT polarization for the p-led configuration.

RT electroluminescence (EL) or photoluminescence measurements did not reveal any polarization in the Gd doped LED structures for any of the three configurations (RT EL shown in Figure 5.23). The difference in intensity between σ^+ (right circularly polarized light) and σ^- (left circularly polarized light) is a characteristic of GaN LEDs that arises due to the built in strain in the InGaN/GaN MQW [32]. The intensity of the emitted light does not vary with the application of magnetic field and is not indicative of polarization due to spin injection.

The observations here are similar to the EL results obtained for spin-LEDs based on $Ga_{1-x}Mn_xN$ in which the lack of polarized emission was attributed to the fast relaxation in the InGaN MQW, which is caused by breaking of symmetry and mixing of the spin states due to the strong compositional non uniformity, strain, built-in electric field in InGaN, and the strong spin scattering by defects.

It should be noted that this device study is an initial investigation and serves as a proof of concept that $Ga_{1-x}Gd_xN$ can be used in device structure without dampening the device performance

Furthermore, these LED structures could be grown on non polar substrates by using alternate planes of sapphire substrate which allow for enhanced spin injection efficiencies as C excitons can be utilized rather than B excitons. In polar substrates, a large overlap between the A and B excitions exists and this greatly limits the polarization efficiency. This device study has demonstrated that Gd doping of n- or p-GaN does not dampen the LED light emission or significantly enhance the turn on voltage. The $Ga_{1-x}Gd_xN$ DMS can survive in a device structure and upon optimization shows promise for spin injection and the possibility of spintronic device.

5.7. Conclusions

This research produced the first reports on MOCVD grown $Ga_{1-x}Gd_xN$ film with Gd concentration ranging from 0 to 4 %. Silicon and magnesium co-doping were successfully carried out to enable n- and p-doping of this semiconductor. Structural characterization revealed that the films obtained were single phase and did not show any strain despite the large size of the Gd atom. Gd doping did not alter the surface morphology of the films and rendered a surface roughness less than 1 nm.

Photoluminescence measurements using a HeCd laser at 325 nm revealed the films to be of excellent optical quality with the GaN bandedge clearly visible at room temperature. Low temperature optical measurements reveal the presence of donor acceptor pairs situated at 3.0-3.3 eV indicating transitions between donors such as nitrogen vacancies or oxygen donors and Gd ions.

High room temperature magnetization has been obtained for $Ga_{1-x}Gd_xN$ and it was demonstrated that this magnetization can be enhanced by n- and p-doping (Figure 5.24). The $Ga_{0.98}Gd_{0.02}N$ films displayed a saturation magnetization of 20 emu/cm^3 which amounted to 2.5 μ_B/Gd atom. Silicon and magnesium doping significantly enhanced the saturation magnetization with a maximum magnetization strength of 110 emu/cm^3 (Si:10^{18} cm^{-3}) and 500 emu/cm^3 (Mg:10^{19} cm^{-3}) respectively.

Furthermore, all the films obtained in this study are conductive and maintain good carrier mobility. The electrical properties of $Ga_{1-x}Gd_xN$ show n-type characteristics and as Gd is isovalent in GaN this implies that Gd doping results in the incorporation of donors such as nitrogen vacancies or oxygen. Magnesium can be introduced to facilitate p-type $Ga_{1-x}Gd_xN$ once the doping concentration surpasses the background donor concentration.

The magnetic interactions in $Ga_{1-x}Gd_xN$ are antiferromagnetic but are stabilized by the unintentional donors present in the material. At high Gd concentration (> 4 %) the mean free path between the Gd ions decreases and antiferromagnetic interactions begin to take over and the magnetization decreases. Silicon co-doping results in donor levels near the conduction band and results in ferromagnetic s-f (or s-d) coupling. Furthermore, the

introduction of holes causes p-d coupling, which has an extremely strong exchange interaction and results in films with significantly enhanced magnetization moments.

Ferromagnetism in $Ga_{1-x}Gd_xN$ can be stabilized by electrons and holes and is facilitated by the RKKY indirect exchange mechanism. This work has shown experimentally that holes result in greater exchange interaction and result in higher magnetization strengths as compared to electrons.

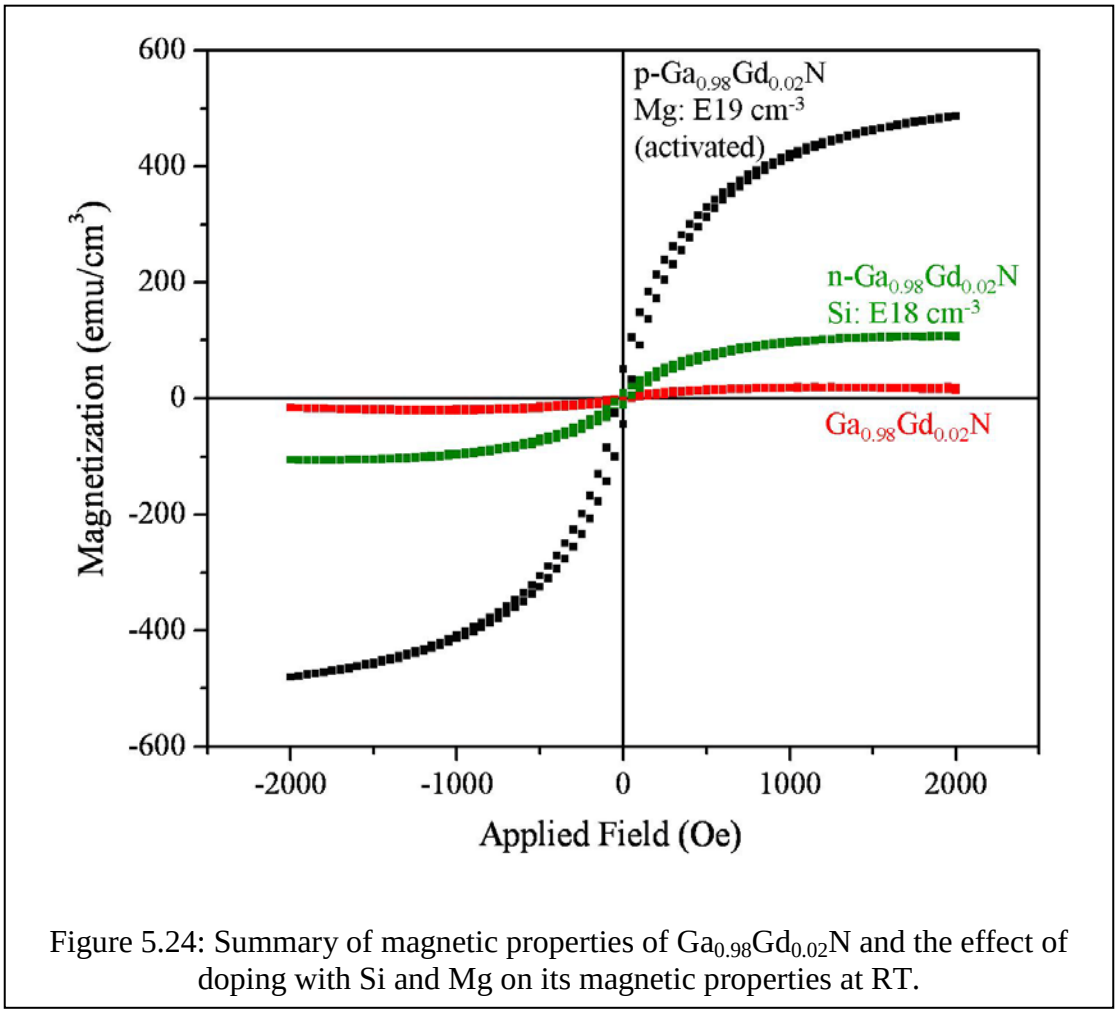

Figure 5.24: Summary of magnetic properties of $Ga_{0.98}Gd_{0.02}N$ and the effect of doping with Si and Mg on its magnetic properties at RT.

The n- and p-type $Ga_{1-x}Gd_xN$ layers were incorporated into LED structures to facilitate spin injection of polarized carriers. It is demonstrated that Gd doping of n- or p-type GaN does dampen the LED light emission or significantly enhance the turn on

voltage. RT electroluminescence and photoluminescence measurements did not show any spin induced polarization. This could be due to fast spin relaxation times caused by the InGaN MQW. Nevertheless, it is demonstrated that $Ga_{1-x}Gd_xN$ DMS can survive in a device structure and upon optimization offers promise for spin injection into semiconductors thereby realizing spintronic devices.

Overall, this study has resulted in the successful creation of a room temperature ferromagnetic semiconductor that is conductive and whose magnetic properties can be enhanced by n- and p-doping, thus providing a path towards realizing spintronic devices.

CHAPTER 6

MOCVD GROWTH AND TRANSITION METAL DOPING OF GaN NANOSTRUCTURES

6.1. Introduction

GaN-based semiconductors have been used for developing optoelectronic devices, such as, light emitting diodes (LEDs) and laser diodes [32, 213]. High dislocation densities are present in group III-Nitride heterostructures, which render it necessary to localize the carriers for light generation and prevent non-radiative transitions. Therefore, reducing the dislocation density and increasing the number of carrier localization sites may help to improve the efficiency of light emitting devices. One way to achieve this is by incorporating quantum dots (QDs) instead of the usual quantum wells in the active layer [24]. In semiconductor physics, QDs provide three-dimensional confinement of carriers while quantum wells only confine these sub-atomic particles to a planar region (Figure 6.1a). In QDs electrons are confined to length scales on the order of the electrons' de Broglie wavelength, and it is this confinement that leads to discrete quantized energy levels (Figure 6.1b) [24, 214]. Since the QD has discrete energy levels, much like an atom, they are sometimes called "artificial atoms". A unique property of QDs is their size-based photon emission wavelength. An increase in the size of the QDs results in a red shift, and a decrease in size results in blue shift. This property of tuning the wavelength of emission, coupled with the high wavelength yield, makes it attractive to incorporate QDs into semiconductor devices as has been demonstrated for quantum dot infrared photodetectors and lasers [215, 216]. Furthermore, the confinement of carriers

prevents them from migrating to non-radiative sites, thereby increasing the efficiency of optical devices.

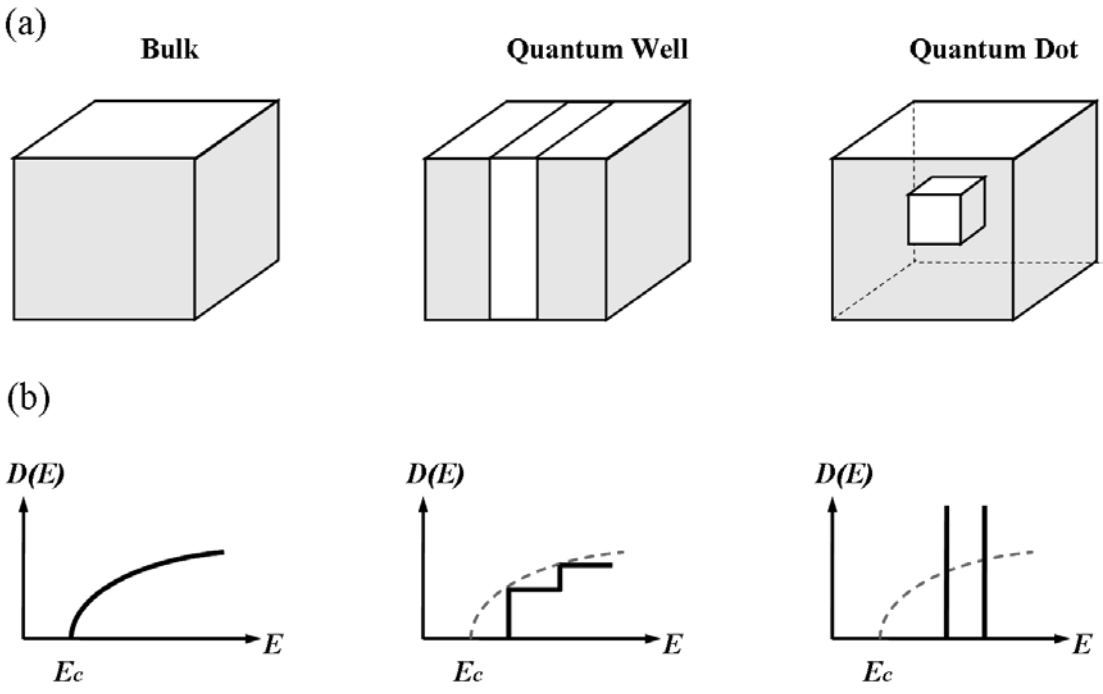

Figure 6.1: (a) Schematic morphology of bulk, quantum well and quantum dot structures, (b) density of states for the respective structures described in (a) [24].

QDs are a promising building block for quantum computation, spin-based quantum operations, and other spintronic applications as the carrier localization allows for more transition metal (TM) interactions, higher T_C, and higher spin relaxation times. Additionally, the confinement offered by QDs also protects them from thermal perturbations, which make them more suitable for high temperature operations [23]. Within the diluted magnetic semiconductors, the growth of quantum dots of $Ga_{1-x}Mn_xAs$ has already been reported [87] and demonstrated for use in spin filtered polarized light emitting diodes and lasers (Refer Chapter 2, section 2.7.4) [88]. In addition, an enhancement of the Curie temperatures in Arsenide-based dilute magnetic semiconductor

quantum dots has been reported [87], though there is still some controversy as to whether this is due to carrier localization within the quantum dot or through an assembly and clustering of MnAs within the dot. This research takes advantage of the aforementioned benefits of QDs for spintronic applications and as a result dilute magnetic nanostructures (DMNS) have been developed in this study. The DMNS were developed by TM doping of optimized GaN nanostructures. A comparison between the properties of dilute magnetic semiconductor at the thin films and nanostructure level provides insight into the effect of size and confinement on the magnetic properties of the material. Furthermore, this comparison allows for a better understanding of the ferromagnetic mechanism in the transition metal doped Nitrides.

To this end, this study initially focused on the development of the optimal growth parameters and material properties of GaN nanostructures on AlN buffer layers grown on sapphire substrates. This is because the MOCVD growth parameters for GaN nanostructure were not well established prior to this report and thus a systematic study had to be conducted to determine the ideal growth window. TM doping of the optimized GaN nanostructures was carried out next and has resulted in the first published reports on $Ga_{1-x}TM_xN$ nanostructures [217].

Before proceeding into the development of the nanostructures, it is important to have an understanding of the different growth mechanism that favor self-assembly of GaN nanostructures. To this end, discussion on the growth mechanisms is presented next.

6.2. Growth Mechanisms

Formation of nanostructures by self assembly is more desirable than lithographic techniques as it is cheaper, faster, and more convenient. This self assembly of

nanostructures mainly depends on the lattice mismatch between the substrate and the epilayers being grown. Generally three different growth modes are possible depending on the interface energy between the epilayer and the substrate and also the lattice mismatch. These modes are Frank-van der Merwe, Volmer-Weber, and Stranski-Krastanow-like growth modes and are described below and schematically shown in Figure 6.2. [218]

Frank-van der Merwe (F-vdM) mode represents a layer-by-layer 2D growth. This occurs in conditions where the epilayer and the substrate are lattice matched and the energy of the sum of the epilayer surface (σ_e) and interface energy (γ) is higher than substrate surface energy (σ_s).

Volmer-Weber (VM) growth mode occurs in films which have a significant lattice mismatch, resulting in island or 3D like growth. This occurs in systems where $\gamma+\sigma_e > \sigma_s$. These systems release strain by increasing the surface energy system, which is what leads to the island formation.

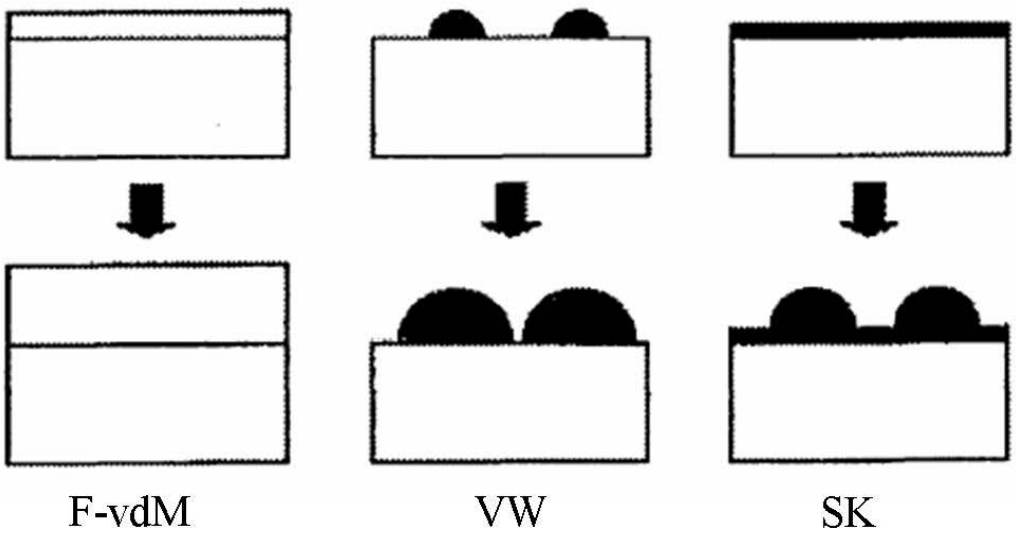

Figure 6.2: Schematic of the three different growth modes: Frank-van de Merwe (F-vdM), Volmer Weber, and Stranski-Krastanow [218].

For systems with a large lattice mismatch but small interface energy (γ), the first few monolayers deposited grow in a layer-by-layer fashion, i.e. 2D growth, and is referred to as the wetting layer. As the layer thickness increases, the strain energy increases; the strain is released by 3D island formation through elastic relaxation without any dislocations [218]. This growth technique is known as Stranski-Krastanow (SK)-like growth. The thickness at which a 2D growth transitions towards a 3D growth is known as its critical thickness. Another characteristic of SK-like growth is that eventually smaller islands are dissolved to form larger islands, which results in an overall reduction in the surface energy. This process is known as Ostwald ripening and is thermodynamically driven. The SK-like growth mode is mainly seen in films subjected to compressive strain which causes the atoms to coalesce, while in films with tensile strain 2D growth occurs and the strain energy is released through plastic relaxation and the creation of dislocations. However, it is possible to have a 2D to 3D transition in films with tensile strain if the lattice mismatch between the epilayer and substrate is large.

The growth of QDs by VM or SK-like growth mode is known as self assumed or self-organized growth. GaN QDs are usually grown on AlN buffer layers to provide lattice mismatch that can support 3D growth. Daruka et al. have developed an equilibrium phase diagram showing monolayer deposited, referred to as coverage (H), vs. lattice mismatch, referred to as misfit (ε), as shown in Figure 6.3 [219]. It is apparent that for the 2.5 % lattice mismatch between GaN and AlN the Stranski-Krastanow (SK)-like growth mode is not supported. In reality the growth mode does not depend only on the lattice mismatch between the epilayer and the substrate, but also on the growth conditions, such as substrate temperature and the flow rates of various sources.

Furthermore, this model is based on the assumption of equilibrium conditions, but GaN is normally grown by molecular beam epitaxy (MBE) or metal organic chemical vapor deposition (MOCVD), both of which have non-equilibrium growth conditions. Such methods can offer extreme growth conditions, allowing SK-like growth for GaN on AlN. The most prominent MBE and MOCVD literature reports on GaN nanostructure growth are presented next.

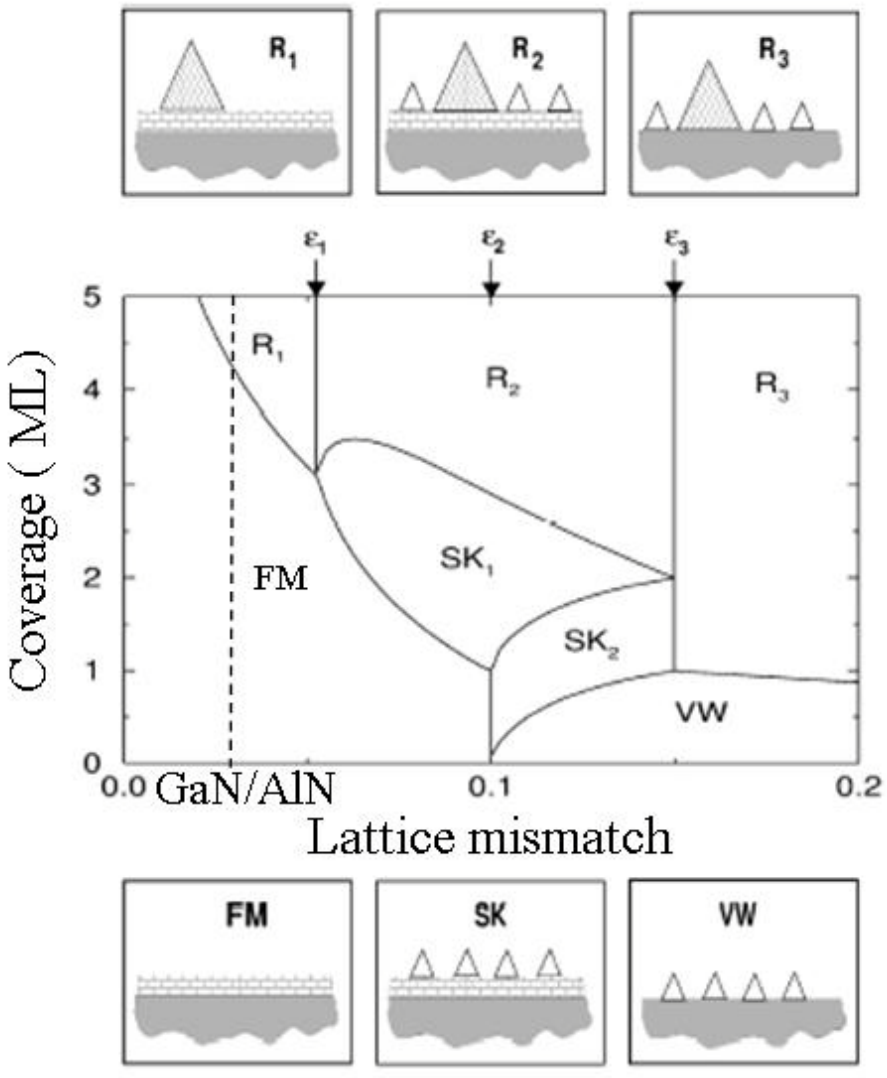

Figure 6.3: Equilibrium phase diagram of coverage vs. lattice mismatch for GaN/AlN system [219].

6.3. Literature Background of GaN Nanostructures on AlN Buffer Layers

MBE growths have been carried out for the growth of GaN QDs on AlN buffer layers on sapphire substrates [220-222]. In these films a 300 nm AlN buffer layer is deposited first. GaN is then deposited in the temperature range of 710-750 ^{o}C in a nitrogen rich environment. The 2D wetting layer is about 2 monolayers (ML) thick, upon which 3D islands in the shape of truncated hexagonal pyramids begin to form. Atomic force microscopy (AFM) revealed islands 10 nm wide and 2 nm in height with an island density of 10^{11} cm^{2}. The dot density saturates at a coverage of 2.8 ML, which suggests that kinetics limit the diffusion mean free path of the Ga adatoms on the growing surface and cause an increase in size of dots rather than enhanced nucleation. Furthermore, it was found that in this case excessive Ga inhibits 3D growth. Beyond 8 ML the dots begin to get larger again due to the reduced elastic strain of the dots. MBE growth has also been used to stack GaN QDs with alternating layers to form GaN QD/AlN superlattices. Stacking of QDs results in an increase in optical intensity as observed by photoluminescence. This implies that the photo-excited carriers can be injected into each layer of GaN QDs, leading to high-total QD density and intense photoluminescence (PL). However, the PL intensity is not proportional to the number of stacked layers and shows a saturation tendency [223].

It has been shown that for small dots (8 nm in diameter) a blue shift of nearly 0.3 eV from the GaN band gap is observed, with the PL peak centered at 3.75 eV, whereas for larger dots (17 nm in diameter) a red shift is observed to 2.95 eV [222]. Thus, by altering the dot size the output emission can be changed. This indicates the existence of a strong built-in electric field (several MV/cm) that can significantly modify the optical properties

of GaN QDs [224]. The PL decay time and emission wavelength increases with increasing size of the QDs, an effect caused by reduced oscillator strength resulting from a strong built-in electric field induced by both the piezoelectric field and the spontaneous polarization field in the GaN/AlN heterostructures [225].

MOCVD growth of GaN nanostructures on AlN has been carried out on SiC substrates [226]. First, a 110 nm thick AlN layer was grown on a (0001)-oriented 6H-SiC substrate at 1180 ^{o}C. The temperature was then reduced into the range of 960-990 ^{o}C to grow GaN with a V/III mole fraction below 30. After the growth of the GaN layer, the growth is interrupted for 3 seconds by a stream of NH_3 in order to facilitate QD formation. SK-like growth was observed with the initial critical thickness of GaN layer being 4 ML. By depositing over this critical thickness, 3D QDs were immediately formed on the 2D GaN layer, a characteristic of the SK growth mode. The density of the QDs increases as the GaN coverage becomes higher until it reaches saturation at 8 ML, after which Ostwald ripening occurs. The average diameter of the dots was 20 nm with a height of 2 nm with an island density of 10^{10} cm^{-2}.

Based on the MOCVD reports it is apparent that the formation of GaN QDs hangs on a delicate balance between the V/III ratio and the growth temperature and varies vastly depending on the growth system. Prior to this research there were no published reports on GaN QDs grown on AlN buffer layers on sapphire substrates by MOCVD. Sapphire substrates are attractive as they are cheaper than SiC and are used widely in the manufacturing of thin film GaN and GaN-based devices. Thus, for QDs to be integrated into existing devices, it is critical to develop the growth parameters for GaN on sapphire.

6.4. Experiment Setup

The formation of GaN nanostructures grown on AlN on sapphire substrates was studied as a function of growth temperature, growth rate, and V/III ratio (Figure 6.4). The nucleation studies were performed in a highly modified commercial GaN MOCVD tool with a vertical injection system with a short jar confined inlet designed to minimize precursor pre-reactions. Trimethylgallium and trimethylaluminum were used as group III sources. Ammonia was used as a group V source, and bis-cyclopentyldienyl manganese and bis-cyclopentyldienyl iron was used as the manganese and iron source respectively. In some samples silane was introduced as an anti-surfactant.

To obtain SK-like growth of GaN QDs it is important that the AlN buffer layer be smooth. In order to achieve high quality AlN buffer layers, a two step growth process was employed in which a 30 nm low temperature AlN interlayer was grown at 600 °C followed by a 0.3 μm-0.7 μm high temperature AlN layer grown at 1090 °C. A high growth temperature is employed for AlN growth as it has a high reaction energy [227]. Furthermore, a low growth pressure of 50 Torr is maintained so as to inhibit the parasitic reaction that occurs in the chamber prior to GaN growth [228]. Additionally, low growth pressures are beneficial as they enhance lateral growth [229]. A 1x1 μm^2 AFM scan on the optimized buffer layer revealed a surface roughness of 6 Å as shown in Figure 6.5.

A series of systematic nanostructure growth experiments were performed with temperatures between 800 and 1100 °C. In order to determine the optimum molar flows for the growth a wide range of V/III ratios were explored. These covered the range from the standard growth conditions for high quality GaN epilayers to the extremely low V/III

ratios (i.e. 3500-30 respectively) that are known to delay the transition from 2D to 3D growth.

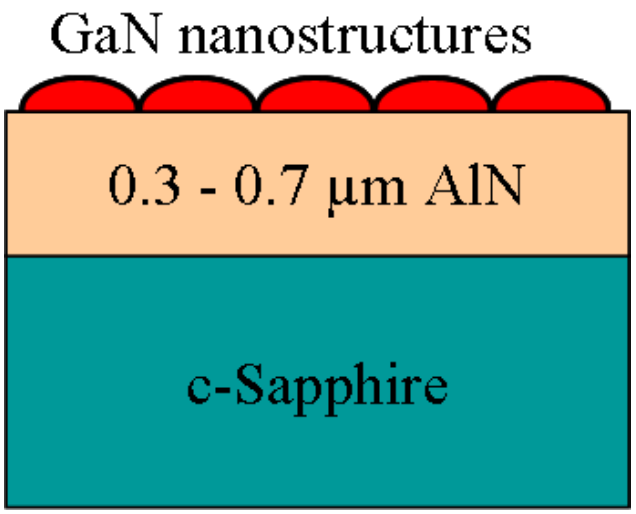

Figure 6.4: Cross-section view of GaN nanostructures growth.

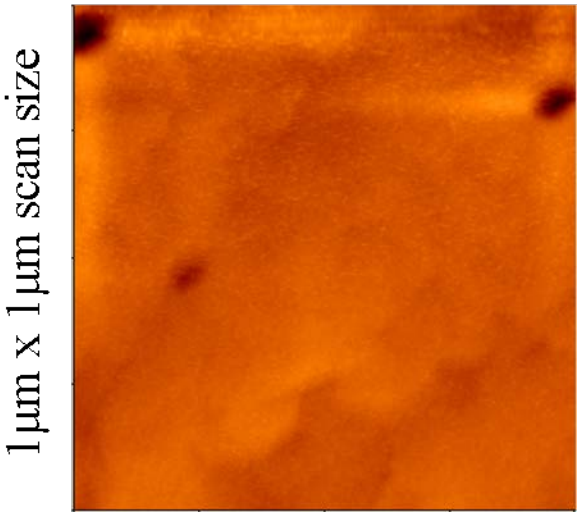

Figure 6.5: AFM image of optimized AlN buffer layer (1 µm x 1 µm).

Since the formation of GaN nanostructures is supported by a gallium bilayer, the influence of an anti-surfactant on the formation of nanostructures in MOCVD growth conditions was studied [197]. Silane flow of 5 μmoles/min was introduced prior to GaN deposition to increase the available nucleation sites that leads to 3D formation of GaN [165, 230].

6.5. Development of GaN Nanostructures

The growth parameters for GaN nanostructures vary significantly based on the growth technique used. Furthermore, within the same technique, the growth conditions vary significantly due to variations in substrate and reactor conditions. As a result, the growth parameters need to be developed and optimized. To this end the temperature, V/III ratio, and the amount of material deposited were varied to investigate the dimensions and density of the GaN nanostructures grown on AlN epitaxial layers on sapphire substrates.

6.5.1. Effect of Anti-Surfactant.

Prior to the growth of GaN, silane was flowed into the chamber to act as an anti-surfactant. Anti-surfactants reduce the surface free energy and create nucleation site for GaN nanostructure. Furthermore, the anti-surfactant reduces the kinetic energy of the adatoms allowing them to adhere to the nucleation site. Silicon as an anti-surfactant has been applied to MOCVD grown GaN nanostructures on $Al_{0.85}Ga_{0.15}N$ surfaces which were grown on SiC substrates [165]. Their findings suggest that the introduction of silane results in the formation of Si-N and that the GaN growth kinetics are modified on the surface, transitioning towards 3D growth.

In this study silane was flowed for 5 seconds with a molar flow of less than 5 µmoles prior to GaN deposition, in order to enhance nucleation in these experiments. Addition of silane results in an increase in nanostructures density from 10^9 cm^{-2} to 10^{10} cm^{-2} as shown in the AFM images in Figure 6.6. Despite the anti-surfactant, the diameters of the GaN nanostructures are still rather large and have to be reduced through optimization of other growth parameters.

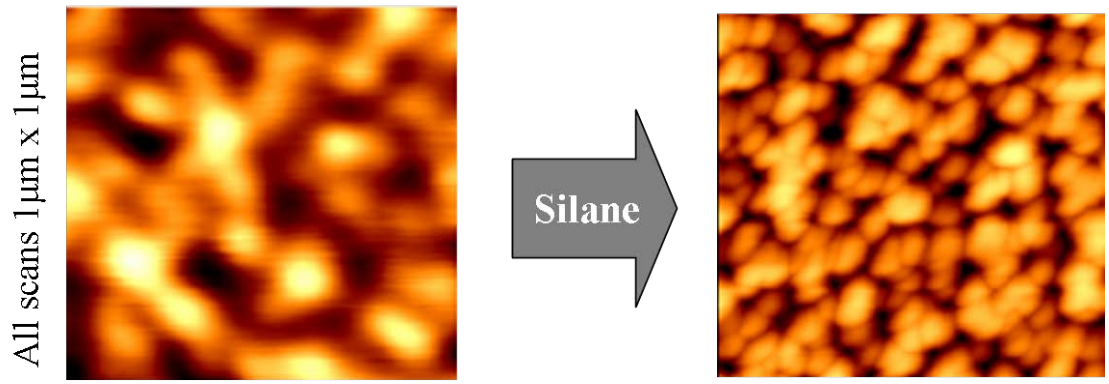

Figure 6.6: AFM images showing the effect of silane as an anti-surfactant for GaN nanostructures growth.

6.5.2. Effect of Growth Temperature

The strong impact of the growth temperature on the nanostructures' density and dimensions was confirmed by varying growth temperatures between 800 °C and 1100 °C. At a typical GaN growth temperature of 1050 °C, very large islands with diameters greater than 200 nm were formed. However as the temperature is reduced to 810 °C, the size of the islands formed decreases, which result in reduced nanostructures with diameters of less than 70 nm (Figure 6.7).

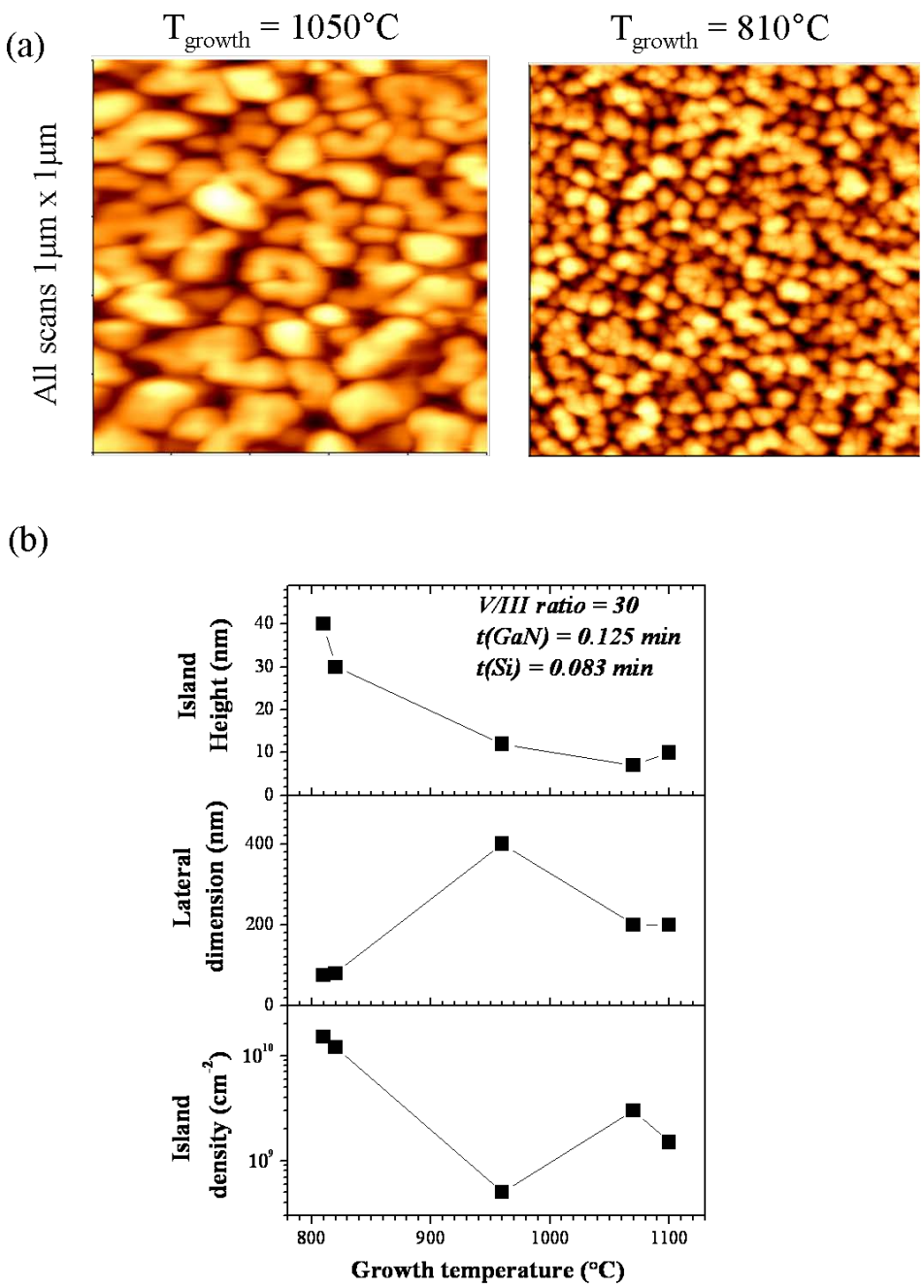

Figure 6.7: (a) AFM images showing the effect of temperature on GaN nanostructures, (b) graph depicting the effect of temperature on dimensions and density of GaN nanostructures.

The growth temperature was not reduced below 800 °C as the ammonia cracking efficiency decreases significantly below this temperature. It is inferred that the low growth temperature reduces both the kinetic energy of the atoms at the surface and the diffusion length, thereby supporting a 3D growth mode [220]. In this process the atoms are localized at the sites where they arrive at the surface instead of migrating to the edges of extended islands.

6.5.3. Effect of V-III Ratio

The V/III ratio is very important in nanostructure growth. Therefore, a wide range from 4.5-3500 was explored to determine the optimum conditions for QD formation. Figure 6.8 depicts the effect of V/III ratio on the dimensions and density of GaN nanostructures. It is apparent that at a growth temperature of 810 °C and at high V/III ratios (around 2000) the nanostructure diameter can be as large as 1000 nm, but reduces down to around 200 nm at V/III ratios below 35 (Figure 6.8a). This decrease in size is attributed to the fact that low V/III ratios favor 3D growth as it creates a metal rich condition that enhances the mobility of Ga atoms and nucleation. However, beyond a V/III ratio of 20 no significant change was seen in the nanostructure sizes, making a thermal activation step necessary to reduce the dimensions of the structures further (Figure 6.8b). This is described in the next section. Relatively low temperatures and extremely low V/III ratios are needed to form GaN nanostructures as shown in GaN QD growth on SiC [226, 231].

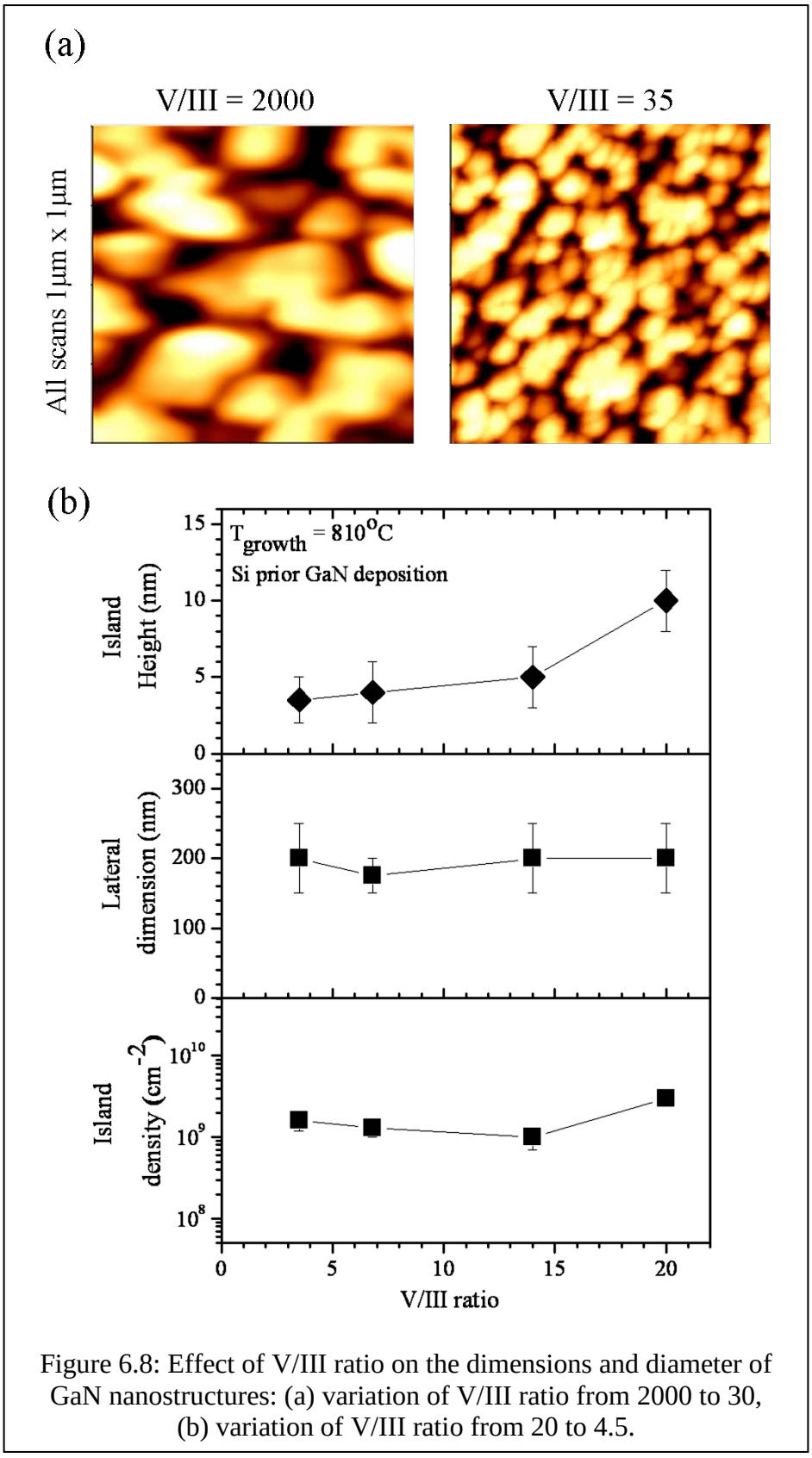

Figure 6.8: Effect of V/III ratio on the dimensions and diameter of GaN nanostructures: (a) variation of V/III ratio from 2000 to 30, (b) variation of V/III ratio from 20 to 4.5.

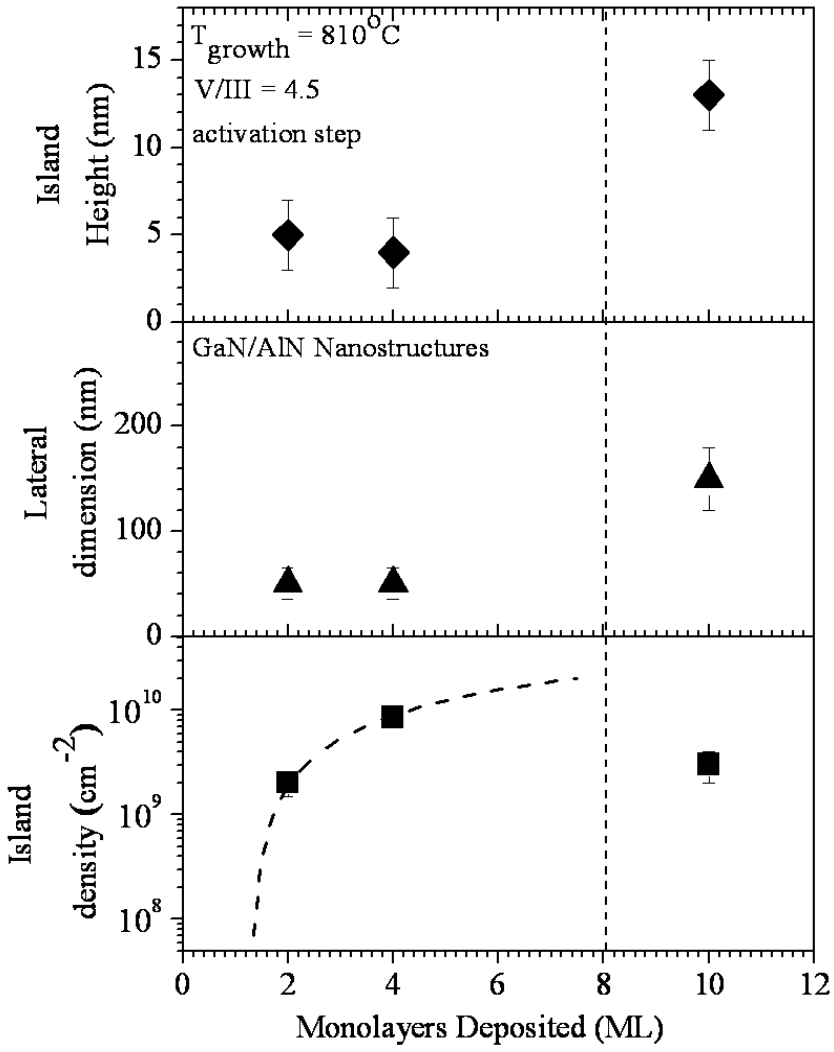

Figure 6.9: Graph depicting the monolayers deposited and its effect on the dimensions and density of the nanostructures.

It must be pointed out that the deposition time was determined to control the size of the nanostructures and the amount of material deposited. Deposition time was kept as low as possible to enable a GaN deposition of between two and 20 monolayers. The critical thickness for the transition from 2D to 3D growth occurred at 2 ML, which is consistent with the reports on GaN nanostructures grown on SiC [222, 226]. Beyond a deposition of 8 ML, the nanostructures begin to increase in diameter and reduce in density and 2D

growth process becomes dominant (Figure 6.9). The existence of an initial critical thickness of 2 ML followed by a ripening process beyond 8 ML of deposition are characteristic of SK-like nanostructure growth. It can be inferred that there exists a narrow deposition window that favors GaN nanostructure growth.

6.5.4. Thermal Activation of Nanostructures

A further reduction in the nanostructure dimensions and an increase in their density was achieved by applying a thermal activation step after the deposition [217]. A temperature ramp was immediately applied in the reactor under a nitrogen atmosphere after GaN deposition for the activation step. A clear transition to 3D growth mode was observed for temperatures up to 850 °C (Figure 6.10).

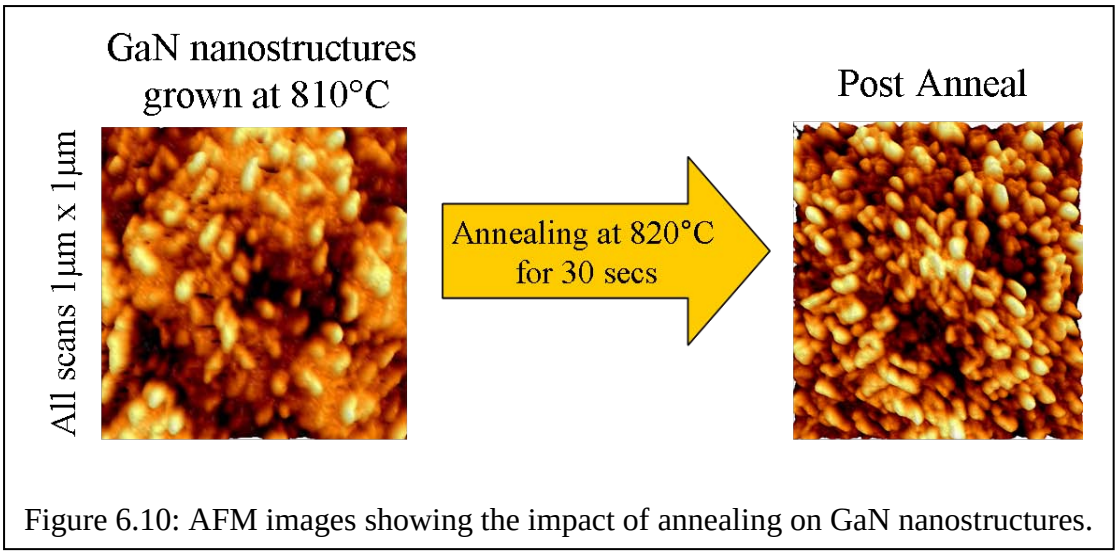

Figure 6.10: AFM images showing the impact of annealing on GaN nanostructures.

This is because the temperature ramp increases the energy of the GaN atoms, which coalesce to form islands with smaller dimensions and larger height. AFM scans revealed nanostructures with a lateral dimension of 40 nm and height of approximately 4 nm with island densities of $1x10^{10}$ cm^{-2}. Temperature ramps above 1000 °C result in an increase in lateral dimensions which can be attributed to the ripening of the islands. A similar

technique for the formation of nanostructures by an in-situ activation step has been demonstrated for CdSe/ZnSe QDs [232]. The optimized ramp temperature was determined to be 820 °C for 30 seconds in a nitrogen atmosphere (Figure 6.11).

To summarize, the optimal growth conditions for GaN nanostructures on AlN buffer layers by MOCVD were determined to be the application of 5 μmole of Si as an anti-surfactant for 5 seconds, followed by GaN growth at a temperature of 810 °C, with a V/III ratio of less than 20 and a post anneal temperature of 820 °C for 30 seconds in an N_2 atmosphere. The optimized GaN nanostructures had lateral dimensions of 50 nm, with a height of 5 nm and density of 1 x 10^{10} cm^{-2} as shown in Figure 6.11.

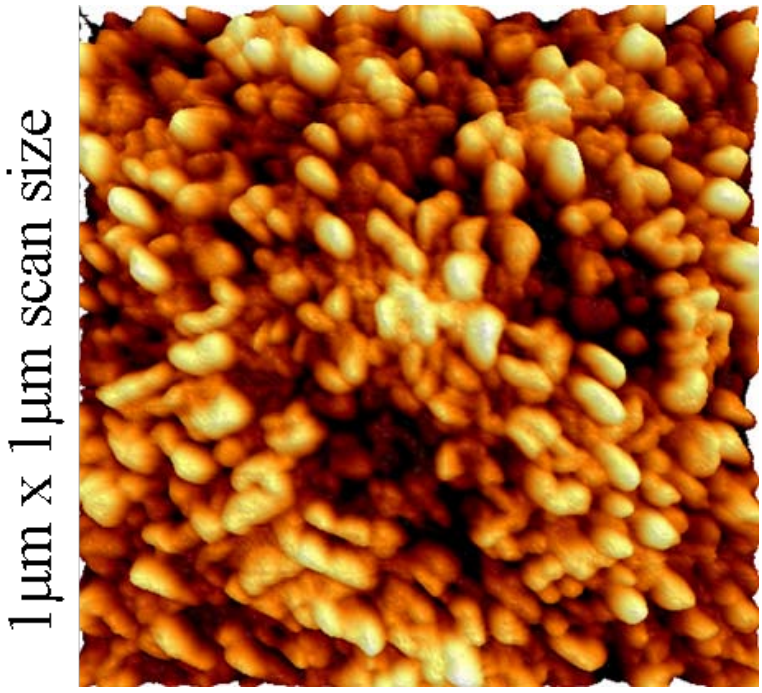

Figure 6.11: AFM image of optimized GaN nanostructures.

6.6. Crystalline and Optical Quality of GaN Nanostructures

The crystalline quality of the GaN nanostructures was determined by micro-Raman spectroscopy and the data obtained for the nanostructures grown at a temperature of 810 °C with a V/III ratio of 4.5 followed by an activation step at 820 °C is shown in Figure 6.12

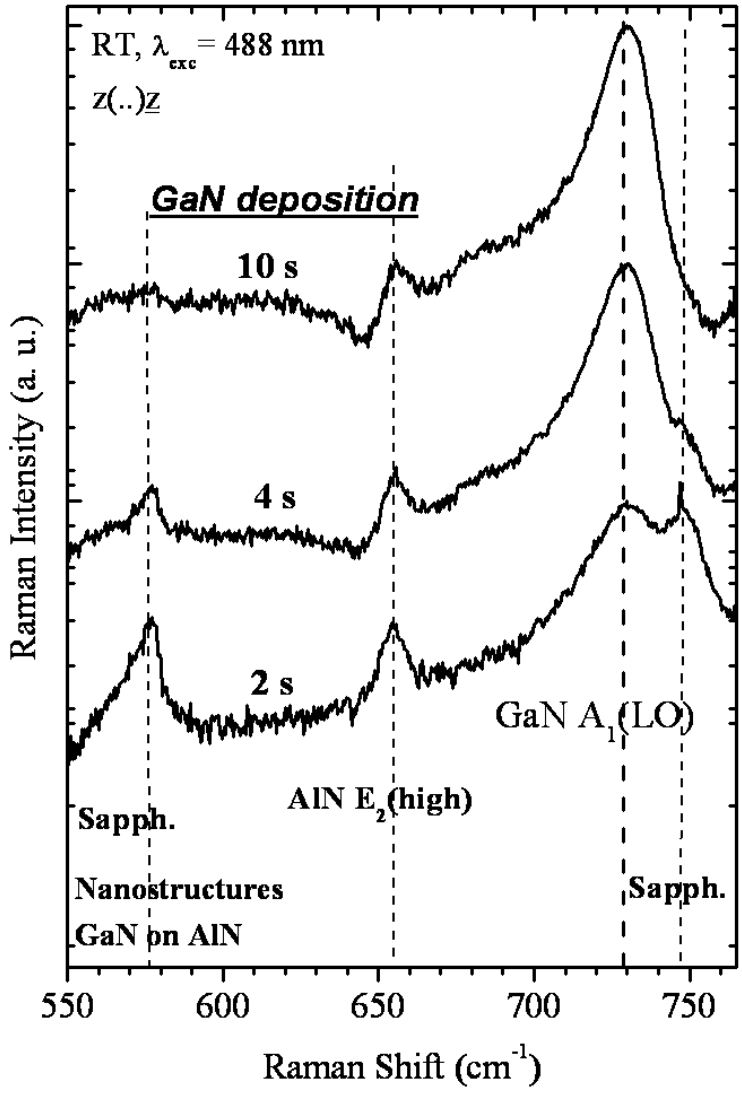

Figure 6.12: Raman spectra of GaN nanostructures for different GaN deposition times. The intensity of the GaN modes increases with increasing deposition time.

The presence of the GaN A_1(LO) mode confirms the high crystalline quality of the nanostructures despite the extremely low V/III ratio and low growth temperature. Furthermore, the intensity of the GaN related Raman mode increases with deposition time (i.e. monolayer deposited), whereas the intensity of the observed AlN and sapphire related modes decreases.

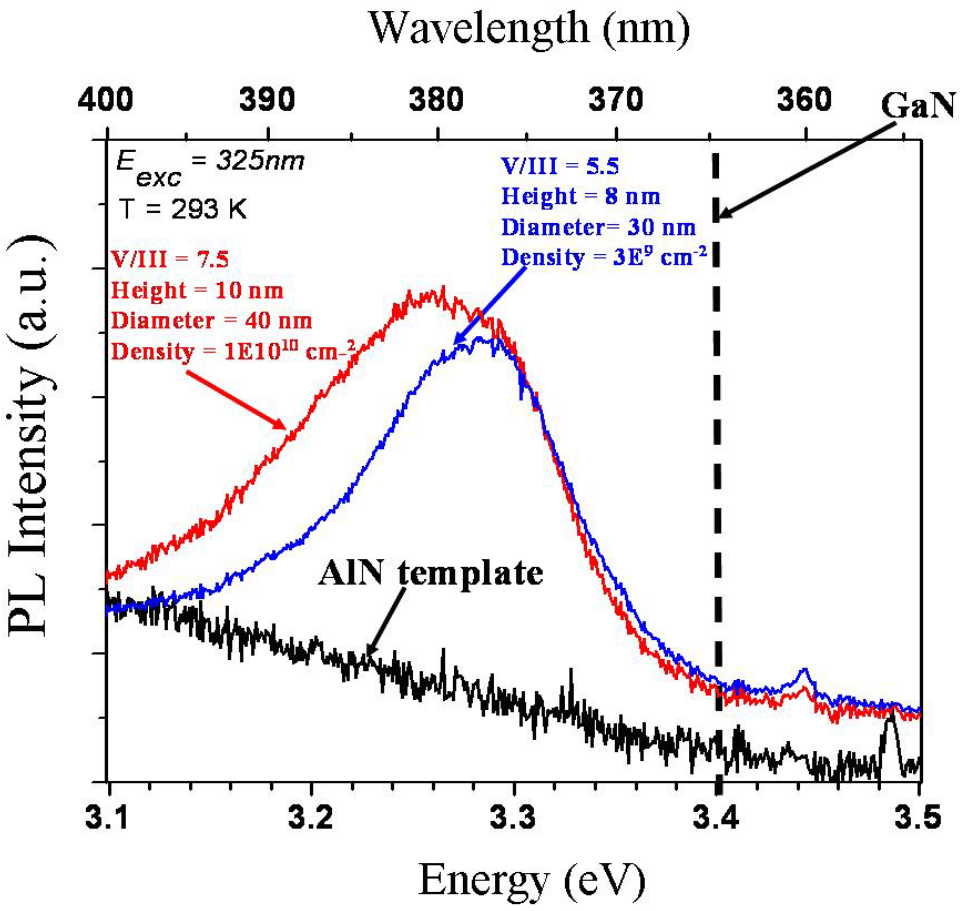

Figure 6.13: PL measurement data for GaN nanostructures. A blue shift is seen with a decrease in nanostructure size. This shift to higher energy is due to the decrease in piezoelectric effect.

PL measurements were conducted on GaN nanostructures capped with a thin AlN layer of approximately 50 nm. As seen in Figure 6.13, optically active nanostructures were obtained. The lattice mismatch between the AlN template and GaN islands, results

in strained islands that increase the piezoelectric fields along the c-axis. The measured transition energies of the QDs were determined to be the result of an interplay between the quantum size effect and the large piezoelectric field along the c-axis as outlined by Daudin et al. [224]. The red shift is attributed to the piezoelectric effect, which is caused by the strain, whereas the blue shift is attributed to quantum confinement. Thus size dependent emission is obtained from these nanostructures. In addition, the intensity of the PL is dependent on the density of the nanostructures. A higher PL intensity is obtained with a higher density of nanostructures.

6.7. $Ga_{1-x}TM_xN$ Nanostructures

TM doping of GaN nanostructures was carried out to study the magnetic properties of Nitrides at the nanoscale. $Ga_{1-x}TM_xN$ nanostructures were grown by introducing Mn and Fe to GaN flows under the optimal conditions for the formation of nanostructures. The amount of TM incorporated was calibrated by secondary ion mass spectroscopy measurements for bulk $Ga_{1-x}TM_xN$ layers. The doping concentration for Mn was varied from 0 to 2 % and from 0 to 3 % for Fe. Strain effects are not deemed to be significant at this level of composition as apparent from the $Ga_{1-x}TM_xN$ thin film results in chapter 4. The surface morphology was strongly affected by the presence of TM atoms. The AFM characterization (Figure 6.14) revealed that in comparison to the GaN nanostructures, a reduced diameter of 30 nm and height of 2 nm is obtained upon 2 % Mn incorporation. Furthermore, the island density increased up to 3.0 $x10^{10}$ cm^{-2}. Similarly, Fe doping of GaN nanostructures resulted in nanostructures with a diameter of 50 nm, heights ranging from 2 to 5 nm and a density of 10^{10} cm^{-2}. It must be noted that an anti-surfactant was not applied during the growth of $Ga_{1-x}TM_xN$ nanostructures. Thus TM doping in GaN

enhances nucleation. This result supports the findings of chapter 4 which show that there is a strong driving force for TMs to cluster in the GaN host semiconductor.

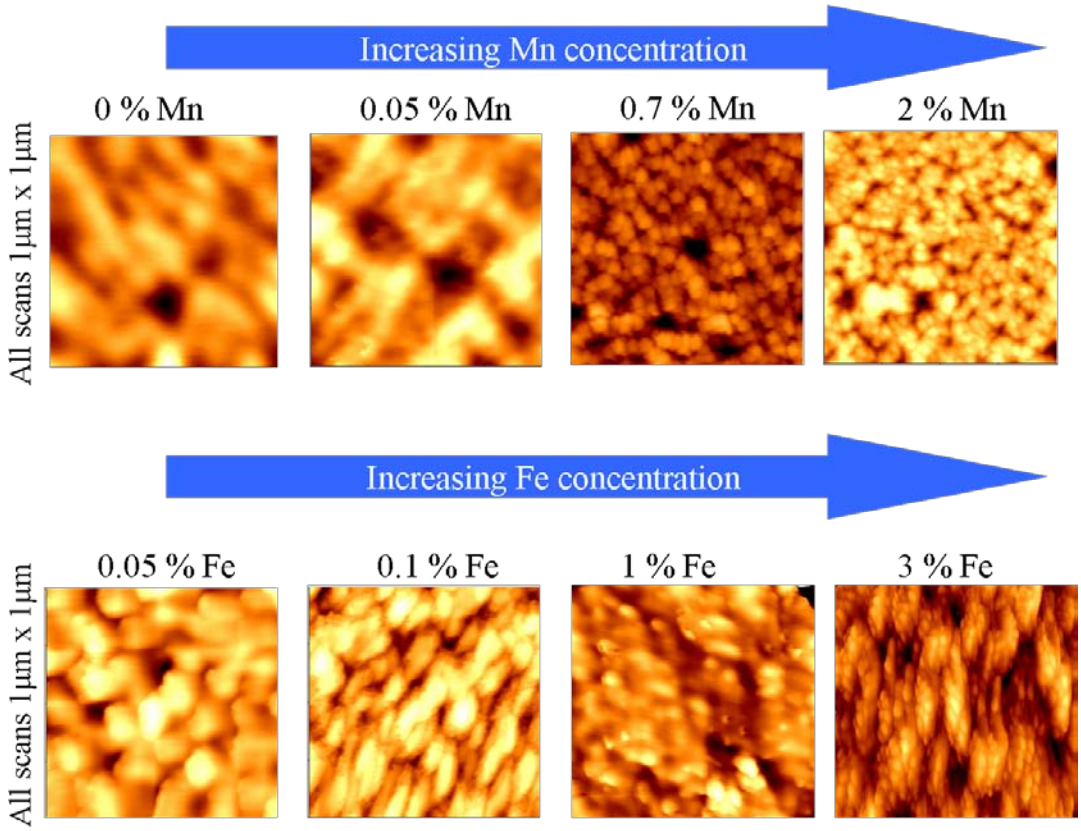

Figure 6.14: Effect of Mn and Fe doping on GaN nanostructures.

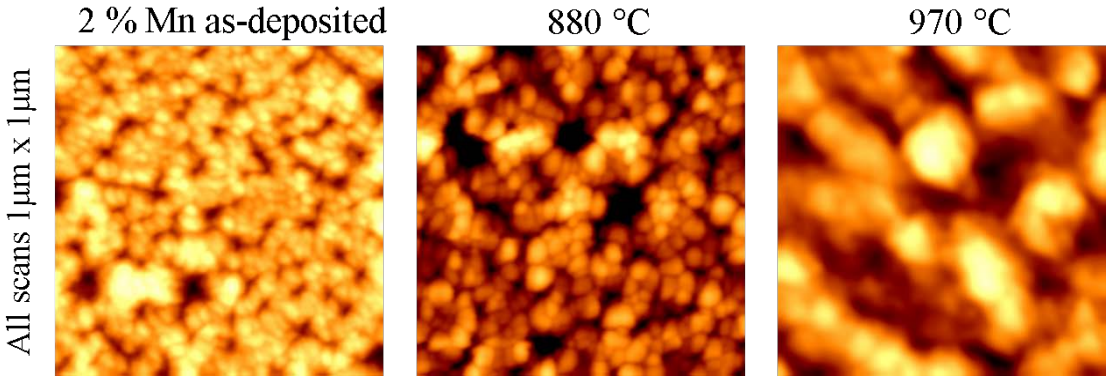

Figure 6.15: Effect of annealing temperature on GaN nanostructures doped with Mn.

Furthermore, it was determined that, unlike GaN nanostructures, an annealing step was not necessary to provide small $Ga_{1-x}TM_xN$ nanostructures of high density. Applying an activation temperature above 880 °C facilitated a ripening processes leading to increased island dimensions and smaller island densities (Figure 6.15).

The magnetization data for the $Ga_{1-x}TM_xN$ nanostructures were obtained at room and low temperature using a superconducting quantum interference device (SQUID) (Figure 6.16). Low temperature measurements conducted at 5 K revealed hysteresis curves with low magnetization of ~40 μemu. However, as the temperature was increased to 300 K, the magnetization loop closed up, leaving very little area in the hysteresis loop and thus resulting in minimal coercive field. This is indicative of superparamagnetic behavior, which is to be expected in nanoclusters.

It is apparent that with regards to GaN nanostructures, TM doping facilitates nanostructure formation, and the TM-TM interactions are superparamagnetic and result in weak magnetic moments as compared to their thin film counterparts. Furthermore, TM doping of GaN nanostructures did not result in increased T_C as in the Arsenide-based nanostructures.

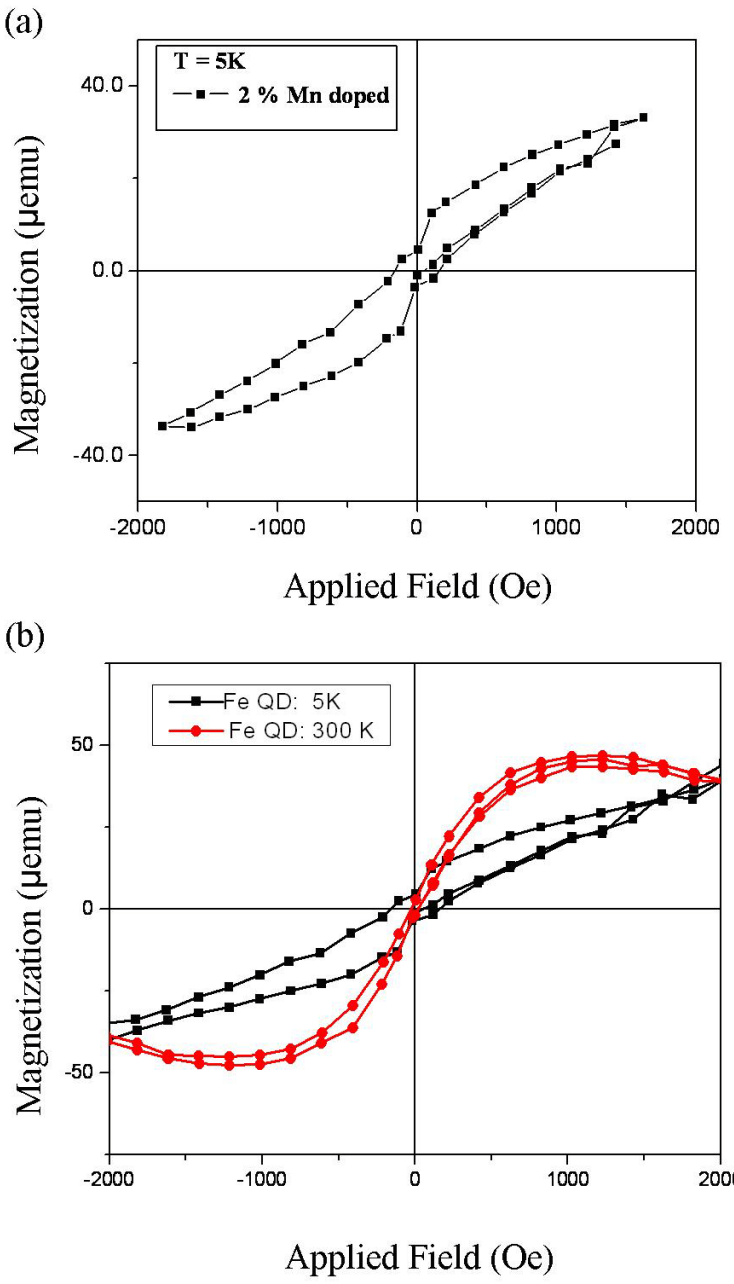

Figure 6.16: Magnetization data measured by SQUID for 2 % Mn and 3 % Fe doped GaN nanostructures.

6.7. Conclusions

Optically active GaN nanostructures that exhibit a SK-like growth mode were successfully grown on AlN template layers by MOCVD. Silicon was introduced as an

anti-surfactant prior to GaN deposition to promote nucleation. A low growth temperature of 810 °C and a V/III ratio less than 20 was shown to promote nanostructure growth. An in-situ activation step involving a temperature ramp up to 820 °C for 30 seconds in a nitrogen atmosphere was successfully applied after GaN deposition to initialize a 3D growth process. Nanostructures with a lateral dimension of 50 nm and a height of approximately 5 nm with island densities of ~10^{10} cm^{-2} were obtained. The presence of the GaN A_1(LO) mode in Raman measurements confirms the high crystalline quality of the nanostructures despite the extremely low V/III ratio growth conditions at relatively low deposition temperatures. A blue shift was observed in the PL for smaller GaN nanostructures.

TM doping of GaN nanostructures was successfully carried out to study the magnetic properties of the $Ga_{1-x}TM_xN$ at the nano-scale. It was determined that TM doping enhances the nucleation of GaN nanostructures resulting in lateral dimension of 30 nm and a height of 2 nm with increased island density of 3 x 10^{10} cm^{-2}. Additionally, unlike the GaN nanostructures, an activation step was not required to enhance nucleation in the $Ga_{1-x}TM_xN$ nanostructures. Magnetization measurements revealed superparamagnetic behavior for these nanostructures with low magnetization strengths of ~40 μemu. At this time the thin film $Ga_{1-x}TM_xN$ are better developed and display hysteresis with higher magnetization. However, the exploration of TM doping in GaN nanostructures performed by this research has provided further proof that the TMs enhance nucleation (or clustering) even in the absence of an anti-surfactant and an annealing step, and thereby result in superparamagnetic interactions.

CHAPTER 7

CONCLUSIONS AND FUTURE WORK

7.1. Conclusions

Transition metal (TM) and rare earth (RE) doping of GaN by metal organic chemical vapor deposition (MOCVD) has been successfully carried out in this study. The transition metal series consisting of chromium, manganese and iron was analyzed to obtain a better understanding of the effect of the number of unpaired spins and the acceptor level on the magnetic properties of GaN. Structural characterization showed the films to be of good crystalline quality and free of strain. Optical measurements revealed that the TM in GaN are deep acceptors and do not generate any free carriers. This observation was confirmed by Hall measurements that showed the films to be highly resistive. Thus the requirement of having 5 % Mn with hole concentrations of 3.5 x 10^{20} cm^{-3} as put forth by Dietl's theoretical model to realize room temperature carrier mediated magnetism in the Nitrides was found to be not realistic [15]. Magnetization measurements revealed hysteresis curves for all the transition metal doped GaN films, with the maximum magnetization obtained being 16 emu/cm^3 for GaN doped with 1.5 % Mn. First principle theoretical calculations suggest that this magnetization is a result of double exchange interactions [140]. However, the transition metal concentrations are well below the percolation limit of 20 % and this makes the mechanism inefficient for room temperature magnetization [61]. Furthermore, the effect of n- and p-doping on the magnetic properties of the $Ga_{1-x}TM_xN$ films was analyzed and in-depth magnetic measurement studies were carried out. In particular, it was observed that silicon doping results in a reduction of the

saturation magnetizations, and a significant splitting exists between the zero field cooled (ZFC) and field cooled (FC) curves. This is due to the fact that silicon is an anti-surfactant and promotes cluster formation. Additionally, silicon altered the charge state of the atoms and resulted in Coulombic interactions that favor the formation of magnetic clusters [17]. Through the magnetization studies it was determined that there is a strong tendency for TMs to clusters and the observed magnetization is due to magnetic clusters rather than an ideal DMS.

Transition metal doping was also explored in GaN nanostructures to study their properties at the nanoscale. The GaN nanostructures were grown on AlN buffer layers which provided a lattice mismatch to support Stranski-Krastanow-like growth. It was determined that both a low temperature of 810 °C and a V/III ratio of less than 20 were essential for nanostructure formation. Manganese and Fe doping were found to support nanostructure formation in these growth conditions, producing nanostructures with a diameter of approximately 30 nm, height of 2 nm, and a density of 3×10^{10} cm^{-2}. Magnetization measurements revealed these films to be superparamagnetic with very low magnetization moments on the order of 40 μemu.

Gadolinium, a rare earth dopant, was tested as an alternative route to obtaining a dilute magnetic semiconductor whose magnetic properties can be controlled through n- and p-doping and with the aim of developing conductive films that can eventually be integrated into semiconductor devices to produce multifunctional spintronic devices. Rare earth ions have unpaired spins in both the d and f orbitals and thus allow for s-d, s-f, p-d, and p-f exchange interactions. In the MOCVD grown films in this study it was observed that, despite Gd being a large atom, no strain or degradation of the film crystalline quality

occurs for up to 4 % Gd doping levels. Furthermore, optical measurements showed no degradation of the GaN bandedge emission and also no significant enhancement of the yellow luminescence. Additionally, low temperature optical measurements revealed the presence of donor-acceptor pairs with peaks in the 3.0-3.3 eV range.

Room temperature magnetometry displayed high magnetization strengths of 20 emu/cm^3 for 2 % Gd doping, which is equivalent to a magnetic moment of 2.5 μ_B/Gd. It was found that this magnetization can be enhanced significantly by silicon and magnesium doping. The n- and p-dopants resulted in saturation magnetization strengths of 110 emu/cm^3 and 500 emu/cm^3 respectively. Additionally, the as-grown and the n- and p-doped $Ga_{1-x}Gd_xN$ films obtained in this study are conductive that makes them promising for device applications. Gadolinium doping in GaN is isovalent and thus the n-type behavior observed for the $Ga_{1-x}Gd_xN$ films is due to intrinsic donors that exist in GaN. The Gd-Gd interactions in $Ga_{1-x}Gd_xN$ are antiferromagnetic and it is the intrinsic donors (i.e. nitrogen vacancies) that stabilize the ferromagnetic phase. Upon increasing the Gd concentration the magnetization strength decreases as the mean free path between the Gd ions decreases and antiferromagnetic interactions become dominant. Furthermore, it is possible that at increased concentrations, secondary phases with low T_C, such as GdN, begin to form and the overall room temperature magnetization decreases.

Doping with donors results in spin-splitting of the conduction band and allows for s-f (or s-d) coupling, which enhances the ferromagnetic interactions. On the other hand p-doping results in the introduction of holes and a significant difference in the splitting of the spin-up and spin-down states of the d orbitals of the Gd atoms. This allows for p-d coupling, which has an extremely strong exchange interaction and results in films with

significantly enhanced magnetization moments (25 times greater than $Ga_{1-x}Gd_xN$). Overall, ferromagnetism in $Ga_{1-x}Gd_xN$ can be stabilized by electrons and holes and is facilitated by the RKKY exchange mechanism. This work has shown experimentally that holes result in greater exchange interaction and result in higher magnetization strengths as compared to electrons. Additionally, all the $Ga_{1-x}Gd_xN$ films obtained in this work are conductive and can be integrated into devices structures without significantly increasing the turn on voltage of the devices.

The magnetic properties of as-grown TM and RE doped GaN are shown in Figure 7.1.

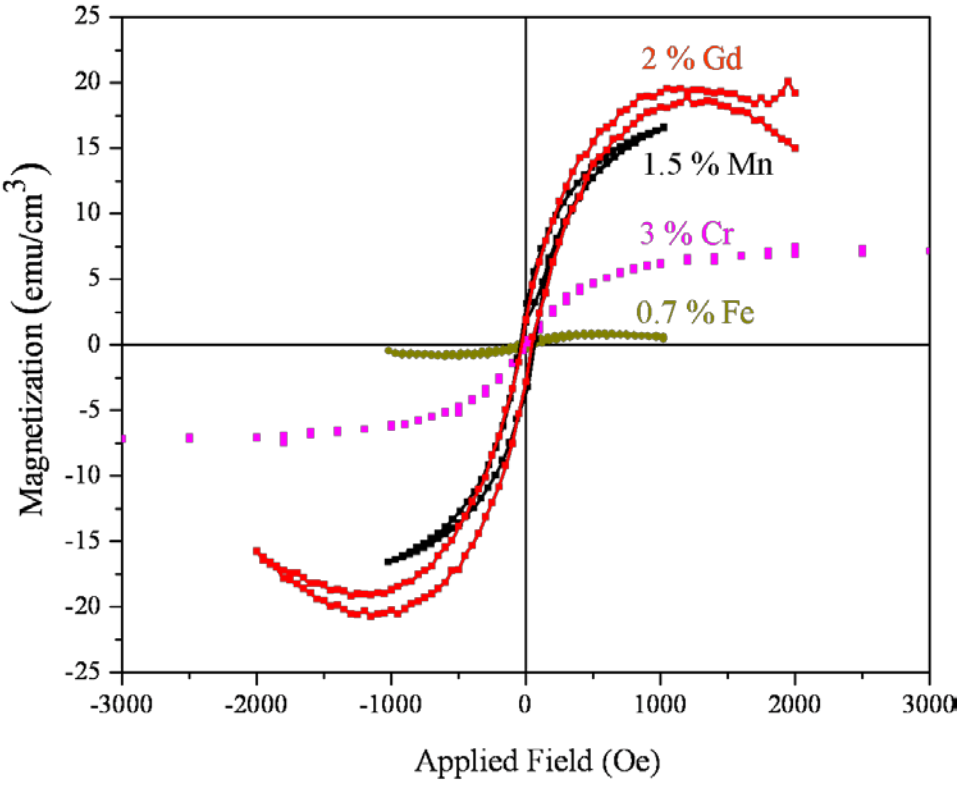

Figure 7.1: Summary of room temperature magnetization results for transition metal and rare earth dopants carried out in this study.

This research has successfully employed MOCVD growth technique to develop a Nitride-based dilute magnetic semiconductor that is conductive and possesses magnetic properties that can be controlled through the magnetic dopant concentration and n- and p-doping levels. The advantage of Gd doping in GaN is that it allows the development of both an n-type and p-type DMS that can be integrated into semiconductor devices to allow for spin injection of both electrons and holes.

7.2. Future Work

$Ga_{1-x}Gd_xN$ is extremely promising DMS as it shows RT ferromagnetism and the magnetic properties can be altered by doping it with donors or acceptors. Furthermore, this DMS is conducting and provides promise for creating a spintronic device. Although it is widely believed that Gd is incorporated on to the Ga lattice site in the 3^+ charge state, it is essential that this be experimentally verified. Electron paramagnetic resonance measurements could be conducted on these films to determine the Gd charge state and to observe the effect of n- and p-doping on the charge state of the RE ion. Furthermore, there is no consensus till date on where the 4f levels lie in the GaN host lattice. Advanced optical spectroscopy measurements and Zeeman spectroscopy measurements should be carried out to identify the location of the Gd ions and also to identify the excitation mechanisms. Additionally, magneto-optic investigation such as magnetic circular dichroism and Kerr effect measurements would be beneficial as they could provide insight into the magnetic behavior of this material.

In the past, development of a spintronic device that could operate at room temperature was limited by the lack of a DMS that was conductive and had a Curie temperature above room temperature. With the development of conductive $Ga_{1-x}Gd_xN$

and n- and p-doped $Ga_{1-x}Gd_xN$ films this obstacle has been overcome and thus their investigation in heterostructures is warranted. The spin injection analysis of the spin-LED devices grown in this work was limited due to the reduced spin lifetimes caused by the strain from the InGaN MQWs. Additionally, spin devices grown on polar substrates result in fast spin relaxation due to the large overlap in the A and B excitons, such that even under optimal growth conditions, the predicted output light polarization would only be about 5 % from basal plane (c-axis) sapphire. In order to improve the polarized emission resulting from the spin-LEDs and better understand the mechanism of spin injection within the structures, it is imperative to analyze other methods for improving the spin injection efficiency; by moving away from the basal plane emission and going where C excitons rather than B excitons are competing for recombination, the predicted polarized emission efficiency should increase several-fold. Thus spin-LEDs based on the $Ga_{1-x}Gd_xN$ should be investigated on non-polar substrates as this would allow for increased spin lifetimes and by analyzing the polarization of the emitted light great insight can be obtained into the spin dynamics of DMS in device structures.

The $Ga_{1-x}Gd_xN$ films can potentially be used to develop spin photodetectors, which would have a similar structure to the LEDs shown in Figure 5.22. These devices would undergo photoexcitation when illuminated with circularly polarized light. Laser light from HeCd laser can be chopped and passed through a quarter wave plate to produce either left or right circularly polarized light that then passes through the device. The absorption of circularly polarized light obeys the optical selection rules, and so these films would have different transmission and reflection coefficients for left and right circularly polarized light (for a given film magnetization). A change in the polarization

will cause modulation of the light intensity reaching the ferromagnetic semiconductor/semiconductor interface and produce a polarization-dependent photoresponse that imitates the effects of polarization-dependent spin transport that can be detected by a photodetector [233].

To conclude, the transition metal and rare earth doping of GaN has provided great insight into the material properties and semiconductor physics of the Nitrides. Although transition metal doped GaN has proven to be an unlikely DMS candidate for spintronic devices, the rare earth doping results obtained in this study provide an avenue towards room temperature spintronic devices potentially offering enhanced device functionality and efficiency.

REFERENCES

[1] S. A. Wolf, A. Y. Chtchelkanova, and D. M. Treger, IBM Journal of Research and Development 50 (2006) 101.

[2] S. J. Pearton, D. P. Norton, R. Frazier, S. Y. Han, C. R. Abernathy, and J. M. Zavada, IEE Proceedings-Circuits, Devices and Systems 152 (2005) 312.

[3] S. A. Wolf, D. D. Awschalom, R. A. Buhrman, J. M. Daughton, S. von Molnar, M. L. Roukes, A. Y. Chtchelkanova, and D. Treger, Science 294 (2001) 1488.

[4] G. Schmidt, D. Ferrand, L. W. Molenkamp, A. T. Filip, and B. J. van Wees, Physical Review B (Condensed Matter and Materials Physics) 62 (2000) R4790.

[5] V. F. Motsnyi, J. De Boeck, J. Das, W. Van Roy, G. Borghs, E. Goovaerts, and V. I. Safarov, Applied Physics Letters 81 (2002) 265.

[6] V. F. Motsnyi, P. Van Dorpe, W. Van Roy, E. Goovaerts, V. I. Safarov, G. Borghs, and J. De Boeck, Physical Review B 68 (2003) 245319.

[7] T. Manago and H. Akinaga, Applied Physics Letters 81 (2002) 694.

[8] B. T. Jonker, G. Kioseoglou, A. T. Hanbicki, C. H. Li, and P. E. Thompson, Nature Physics 3 (2007) 542.

[9] S. Datta and B. Das, Applied Physics Letters 56 (1990) 665.

[10] S. Das Sarma, American Scientist 89 (2001) 516.

[11] H. Ohno, Science 281 (1998) 951.

[12] M. Tanaka, Journal of Crystal Growth 278 (2005) 25.

[13] J. K. Furdyna, Journal of Applied Physics 64 (1988) R29.

[14] K. Y. Wang, R. P. Campion, K. W. Edmonds, M. Sawicki, T. Dietl, C. T. Foxon, and B. L. Gallagher, in Physics of Semiconductors: 27th International Conference on the Physics of Semiconductors - ICPS-27, Vol. 772, AIP, Flagstaff, Arizona (USA), 2005, p. 333.

[15] T. Dietl, H. Ohno, F. Matsukura, J. Cibert, and D. Ferrand, Science 287 (2000) 1019.

[16] C. Liu, F. Yun, and H. Morkoc, Journal of Materials Science-Materials in Electronics 16 (2005) 555.

[17] T. Dietl, Journal of Applied Physics 103, (2008) 07D111.

[18] K. Sato, P. H. Dederichs, H. Katayama-Yoshida, and J. Kudrnovsky, Physica B 340-342 (2003) 863.

[19] T. Graf, M. Gjukic, M. S. Brandt, M. Stutzmann, and O. Ambacher, Applied Physics Letters 81 (2002) 5159.

[20] P. Mahadevan and A. Zunger, Applied Physics Letters 85 (2004) 2860.

[21] G. H. Zhong, J. Lwang, and Z. Zeng, Journal of Physics-Condensed Matter 20 (2008) 295221.

[22] S. Dhar, L. Perez, O. Brandt, A. Trampert, K. H. Ploog, J. Keller, and B. Beschoten, Physical Review B (Condensed Matter and Materials Physics) 72 (2005) 245203.

[23] D. Loss and D. P. DiVincenzo, Physical Review A 57 (1998) 120.

[24] D. Bimberg, M. Grundmann, and N. N. Ledentsov, Quantum Dot Heterostructures Wiley, New York, 1991.

[25] S. Ghosh and P. Bhattacharya, Applied Physics Letters 80 (2002) 658.

[26] S. Montanari. *III-V compound semiconductor material systems* [cited; Available from: http://web.tiscali.it/decartes/phd_html/III-Vms-latgap.png.

[27] S. Nakamura, Y. Harada, and M. Seno, Applied Physics Letters 58 (1991) 2021.

[28] H. Amano, N. Sawaki, I. Akasaki, and Y. Toyoda, Applied Physics Letters 48 (1986) 353.

[29] S. Nakamura, Japanese Journal of Applied Physics Part 2-Letters 30 (1991) L1705.

[30] S. Nakamura, T. Mukai, M. Senoh, and N. Iwasa, Japanese Journal of Applied Physics Part 2-Letters 31 (1992) L139.

[31] H. Amano, M. Kito, K. Hiramatsu, and I. Akasaki, Japanese Journal of Applied Physics Part 2-Letters 28 (1989) L2112.

[32] B. Gil, Group III Nitride Semiconductor Compounds, Oxford University Press, England, 1998.

[33] S. Nakamura and S. F. Chichibu, Introduction to Nitride Semiconductor Blue Lasers and Light Emitting Diodes, Taylor & Francis 2000.

[34] O. Ambacher, Journal of Physics D-Applied Physics 31 (1998) 2653.

[35] R. Stepniewski, M. Potemski, W. Wysmolek, K. Pakula, J. M. Baranowski, J. Lusakowski, I. Grzegory, S. Porowski, G. Martinez, and P. Wyder, Physical Review B (Condensed Matter) 60 (1999) 4438.

[36] D. Jiles, Introduction to Magnetism and Magnetic Materials, Chapman & Hall, New York, 1991.

[37] M. Getzlaff, Fundamentals of Magnetism, Springer, Berlin, 2008.

[38] *The Hysteresis Loop and Magnetic Properties* [cited 2009 02/19/2009]; Available from:http://www.ndted.org/EducationResources/CommunityCollege/MagParticle/Physics/HysteresisLoop.htm.

[39] Z. L. Wang, Y. Liu, and Z. Zhang, Handbook of nanophase and nanostructured materials, Kluwer Academic, New York, 2003.

[40] J. Stöhr and H. C. Siegmann, Magnetism: From Fundamentals to Nanoscale Dynamics, Springer, Berlin, 2006.

[41] M. A. Ruderman and C. Kittel, Physical Review 96 (1954) 99.

[42] T. Kasuya, Progress of Theoretical Physics 16 (1956) 45.

[43] K. Yosida, Physical Review 1 (1957) 893.

[44] H. Ohno, A. Shen, F. Matsukura, A. Oiwa, A. Endo, S. Katsumoto, and Y. Iye, Applied Physics Letters 69 (1996) 363.

[45] H. Ohno and F. Matsukura, Solid State Communications 117 (2001) 179.

[46] C. Zener, Physical Review 82 (1951) 403.

[47] H. Akai, Physical Review Letters 81 (1998) 3002.

[48] H. A. Kramers, Physica 1 (1934) 182.

[49] P. W. Anderson, Physical Review 79 (1950) 350.

[50] M. Zajac, J. Gosk, M. Kaminska, A. Twardowski, T. Szyszko, and S. Podsiadlo, Applied Physics Letters 79 (2001) 2432.

[51] A. Bonanni, Semiconductor Science and Technology 22 (2007) R41.

[52] J. M. D. Coey, M. Venkatesan, and C. B. Fitzgerald, Nat Mater 4 (2005) 173.

[53] M. Venkatesan, C. B. Fitzgerald, J. G. Lunney, and J. M. D. Coey, Physical Review Letters 93 (2004) 177206.

[54] V. Litvinov and V. Dugaev, Physical Review Letters 86 (2001) 5593.

[55] K. Sato, H. Katayama-Yoshida, and P. H. Dederichs, Kluwer Academic/Plenum Publ, 2003, p. 31.

[56] L. Bergqvist, O. Eriksson, J. Kudrnovsky, V. Drchal, P. Korzhavyi, and I. Turek, Physical Review Letters 93 (2004) 4.

[57] K. Sato, W. Schweika, P. H. Dederichs, and H. Katayama-Yoshida, Physical Review B 70 (2004) 4.

[58] M. van Schilfgaarde and O. N. Mryasov, Physical Review B (Condensed Matter and Materials Physics) 63 (2001) 233205.

[59] G. P. Das, B. K. Rao, P. Jena, and Y. Kawazoe, Elsevier Science Bv, 2006, p. 84.

[60] T. Dietl and H. Ohno, Materials Today 9 (2006) 18.

[61] H. Katayama-Yoshida, K. Sato, T. Fukushima, M. Toyoda, H. Kizaki, V. A. Dinh, and P. H. Dederichs, Wiley-V C H Verlag Gmbh, 2007, p. 15.

[62] D. Ferrand, J. Cibert, A. Wasiela, C. Bourgognon, S. Tatarenko, G. Fishman, T. Andrearczyk, J. Jaroszynski, S. Kolesnik, T. Dietl, B. Barbara, and D. Dufeu, Physical Review B 6308 (2001).

[63] M. Sawicki, K. Le van, L. Hansen, D. Ferrand, L. W. Molenkamp, A. Waag, and T. Dietl, 2002, p. 717.

[64] A. A. Maksimov, G. Bacher, A. McDonald, V. D. Kulakovskii, A. Forchel, C. R. Becker, G. Landwehr, and L. W. Molenkamp, Physical Review B 62 (2000) R7767.

[65] S. Mackowski, T. Gurung, T. A. Nguyen, H. E. Jackson, L. M. Smith, G. Karczewski, and J. Kossut, Applied Physics Letters 84 (2004) 3337.

[66] D. J. Norris, N. Yao, F. T. Charnock, and T. A. Kennedy, Nano Letters 1 (2001) 3.

[67] S. W. Jung, S. J. An, and G.-C. Yi, Applied Physics Letters 80 (2002) 4561.

[68] D. P. Norton, M. E. Overberg, S. J. Pearton, K. Pruessner, J. D. Budai, L. A. Boatner, M. F. Chisholm, J. S. Lee, Z. G. Khim, Y. D. Park, and R. G. Wilson, Applied Physics Letters 83 (2003) 5488.

[69] H. J. Lee, S. Y. Jeong, C. R. Cho, and C. H. Park, Applied Physics Letters 81 (2002) 4020.

[70] P. Sharma, A. Gupta, K. V. Rao, F. J. Owens, R. Sharma, R. Ahuja, J. M. Osorio Guillen, B. Johansson, and G. A. Gehring, Nature Materials 2 (2003) 673.

[71] K. Ueda, H. Tabata, and T. Kawai, Applied Physics Letters 79 (2001) 988.

[72] T. Wakano, N. Fujimura, Y. Morinaga, N. Abe, A. Ashida, and T. Ito, Physica E: Low-dimensional Systems and Nanostructures 10 (2001) 260.

[73] H. Saeki, H. Tabata, and T. Kawai, Solid State Communications 120 (2001) 439.

[74] J. H. Kim, H. Kim, D. Kim, Y. E. Ihm, and W. K. Choo, Journal of Applied Physics 92 (2002) 6066.

[75] T. Fukumura, Z. Jin, M. Kawasaki, T. Shono, T. Hasegawa, S. Koshihara, and H. Koinuma, Applied Physics Letters 78 (2001) 958.

[76] S. J. Pearton, W. H. Heo, M. Ivill, D. P. Norton, and T. Steiner, Semiconductor Science and Technology 19 (2004) 59.

[77] S.-J. Han, T. H. Jang, Y. B. Kim, B.-G. Park, J.-H. Park, and Y. H. Jeong, Applied Physics Letters 83 (2003) 920.

[78] T. Fukumura, Z.-w. Jin, A. Ohtomo, H. Koinuma, and M. Kawasaki, Applied Physics Letters 75 (1999) 3366.

[79] D. A. Schwartz, K. R. Kittilstved, and D. R. Gamelin, Applied Physics Letters 85 (2004) 1395.

[80] D. Chiba, K. Takamura, F. Matsukura, and H. Ohno, Applied Physics Letters 82 (2003) 3020.

[81] K. C. Ku, S. J. Potashnik, R. F. Wang, S. H. Chun, P. Schiffer, N. Samarth, M. J. Seong, A. Mascarenhas, E. Johnston-Halperin, R. C. Myers, A. C. Gossard, and D. D. Awschalom, Applied Physics Letters 82 (2003) 2302.

[82] H. Ohno, H. Munekata, S. Vonmolnar, and L. L. Chang, Amer Inst Physics, 1991, p. 6103.

[83] T. Slupinski, H. Munekata, and A. Oiwa, 2002, p. 1331.

[84] R. Fiederling, M. Keim, G. Reuscher, W. Ossau, G. Schmidt, A. Waag, and L. W. Molenkamp, Nature 402 (1999) 787.

[85] B. T. Jonker, Y. D. Park, B. R. Bennett, H. D. Cheong, G. Kioseoglou, and A. Petrou, Physical Review B 62 (2000) 8180.

[86] Y. Ohno, D. K. Young, B. Beschoten, F. Matsukura, H. Ohno, and D. D. Awschalom, Nature 402 (1999) 790.

[87] M. Holub, S. Chakrabarti, S. Fathpour, P. Bhattacharya, Y. Lei, and K. Ghosh, Applied Physics Letters 85 (2004) 973.

[88] S. Chakrabarti, M. A. Holub, P. Bhattacharya, T. D. Mishima, M. B. Santos, M. B. Johnson, and D. A. Blom, Nano Letters 5 (2005) 209.

[89] R. Didchenko, J. E. Alix, and R. H. Toeniskoetter, Journal of Inorganic and Nuclear Chemistry 14 (1960) 35.

[90] H. M. Manasevit, Applied Physics Letters 12 (1968) 156.

[91] H. M. Manasevit and W. I. Simpson, Journal of the Electrochemical Society 115 (1968) C66.

[92] G. B. Stringfellow, Organometallic vapor-phase epitaxy: theory and practice, Academic Press, San Diego, 1989.

[93] M. Razeghi, The MOCVD challenge:A Study of GaInAsP-GaAs for Photonic and Electronic Device Applications, Institute of Physics Bristol, U.K., 1995.

[94] M. Razeghi, Fundamentals of Solid State Engineering, Springer, 2002.

[95] R. D. Dupuis, Journal of Crystal Growth 178 (1997) 56.

[96] B. C. Harrison and E. H. Tompkins, Inorganic Chemistry 1 (1962) 951.

[97] L. Liu and J. H. Edgar, Materials Science & Engineering R-Reports 37 (2002) 61.

[98] M. Ilegems, Journal of Crystal Growth 13-14 (1972) 360.

[99] A. Shintani and S. Minagawa, Journal of Crystal Growth 22 (1974) 1.

[100] S. Yoshida, S. Misawa, and S. Gonda, Applied Physics Letters 42 (1983) 427.

[101] S. Nakamura, M. Senoh, and T. Mukai, Japanese Journal of Applied Physics Part 2-Letters 32 (1993) L8.

[102] S. Keller, B. P. Keller, Y. F. Wu, B. Heying, D. Kapolnek, J. S. Speck, U. K. Mishra, and S. P. DenBaars, Applied Physics Letters 68 (1996) 1525.

[103] K. Uchida, A. Watanabe, F. Yano, M. Kouguchi, T. Tanaka, and S. Minagawa, Journal of Applied Physics 79 (1996) 3487.

[104] O. Briot, J. P. Alexis, M. Tchounkeu, and R. L. Aulombard, Elsevier Science Sa Lausanne, 1997, p. 147.

[105] *Reflectance measurements for real-time optical control of epitaxial growth*. 2008 01/01/2008 [cited 2008 09/01/2008]; Available from: http://www.laytec.de/fileadmin/laytec/applinotes/Info-Reflectance20080131.pdf.

[106] H. Harima, Journal of Physics: Condensed Matter 14 (2002) R967.

[107] G. Drenkow. *What is an atomic force microscope?* 2007 June 21.2007 [cited 2009 02/19/2009]; Available from: http://nano.tm.agilent.com/blog/wp-content/uploads/2007/06/how-an-atomic-force-microscope-works.bmp.

[108] C. F. Klingshirn, Semiconductor Optics Springer, 1997.

[109] *SQUID Magnetometer* [cited 2009 02/19/2009]; Available from: http://hyperphysics.phy-astr.gsu.edu/HBASE/Solids/imgsol/squide.gif.

[110] M. E. Overberg, C. R. Abernathy, S. J. Pearton, N. A. Theodoropoulou, K. T. McCarthy, and A. F. Hebard, Applied Physics Letters 79 (2001) 1312.

[111] S. Sonoda, H. Hori, Y. Yamamoto, T. Sasaki, M. Sato, S. Shimizu, K. I. Suga, and K. Kindo, Magnetics, IEEE Transactions on 38 (2002) 2859.

[112] T. Sasaki, S. Sonoda, Y. Yamamoto, K. I. Suga, S. Shimizu, K. Kindo, and H. Hori, Vol. 91, AIP, 2002, p. 7911.

[113] U. Gerstmann, A. T. Blumenau, and H. Overhof, Physical Review B 63 (2001) 075204.

[114] P. Mahadevan and A. Zunger, Physical Review B 69 (2004) 16.

[115] J. Baur, K. Maier, M. Kunzer, U. Kaufmann, and J. Schneider, Applied Physics Letters 65 (1994) 2211.

[116] B. Han, B. W. Wessels, and M. P. Ulmer, Applied Physics Letters 86 (2005) 3.

[117] C. G. van de Walle and J. Neugebauer, Journal of Applied Physics 95 (2004) 3851.

[118] A. Zunger, in Solid State Physics, Vol. 39 (H. Ehrenreich and D. Turnbull, eds.), Academic Press, New York, 1986, p. 275.

[119] T. Graf, T. B. Goennenwein, and M. S. Brandt, Physica status solidi (b) 239 (2003) 277.

[120] S. T. Oyama, The Chemistry of Transition Metals Carbides and Nitrides, Springer, 1996.

[121] N. Newman, S. Y. Wu, H. X. Liu, J. Medvedeva, L. Gu, R. K. Singh, Z. G. Yu, I. L. Krainsky, S. Krishnamurthy, D. J. Smith, A. J. Freeman, and M. van Schilfgaarde, Physica Status Solidi a-Applications and Materials Science 203 (2006) 2729.

[122] S. E. Park, H.-J. Lee, Y. C. Cho, S.-Y. Jeong, C. R. Cho, and S. Cho, Applied Physics Letters 80 (2002) 4187.

[123] J. Wang, P. Chen, X. Guo, Z. Li, and W. Lu, Journal of Crystal Growth 275 (2005) 393.

[124] M. Hashimoto, Y. K. Zhou, M. Kanamura, H. Katayama-Yoshida, and H. Asahi, Journal of Crystal Growth 251 (2003) 327.

[125] S. Subashchandran, S. Kimura, M. S. Kim, S. Kobayashi, Y. K. Zhou, S. Hasegawa, and H. Asahi, 2006, p. 3522.

[126] H. X. Liu, S. Y. Wu, R. K. Singh, L. Gu, D. J. Smith, N. Newman, N. R. Dilley, L. Montes, and M. B. Simmonds, Applied Physics Letters 85 (2004) 4076.

[127] A. Y. Polyakov, N. B. Smirnov, A. V. Govorkov, N. Y. Pashkova, A. A. Shlensky, S. J. Pearton, M. E. Overberg, C. R. Abernathy, J. M. Zavada, and R. G. Wilson, Journal of Applied Physics 93 (2003) 5388.

[128] Y. S. Cho, N. Kaluza, V. Guzenko, T. Schapers, H. Hardtdegen, H. P. Bochem, U. Breuer, M. R. Ghadimi, M. Fecioru-Morariu, B. Beschoten, and H. Luth, Physica Status Solidi (A) Applications and Materials 204 (2007) 72.

[129] M. Zajac, R. Doradzinski, J. Gosk, J. Szczytko, M. Lefeld-Sosnowska, M. Kaminska, A. Twardowski, M. Palczewska, E. Grzanka, and W. Gebicki, Applied Physics Letters 78 (2001) 1276.

[130] N. Theodoropoulou, A. F. Hebard, M. E. Overberg, C. R. Abernathy, S. J. Pearton, S. N. G. Chu, and R. G. Wilson, Applied Physics Letters 78 (2001) 3475.

[131] M. L. Reed, N. A. El-Masry, H. H. Stadelmaier, M. K. Ritums, M. J. Reed, C. A. Parker, J. C. Roberts, and S. M. Bedair, Applied Physics Letters 79 (2001) 3473.

[132] M. H. Kane, A. Asghar, A. M. Payne, C. R. Vestal, M. Strassburg, J. Senawiratne, Z. J. Zhang, N. Dietz, C. R. Summers, and I. T. Ferguson, Semiconductor Science & Technology 20 (2005) L5.

[133] E. Sarigiannidou, F. Wilhelm, E. Monroy, R. M. Galera, E. Bellet-Amalric, A. Rogalev, J. Goulon, J. Cibert, and H. Mariette, Physical Review B (Condensed Matter and Materials Physics) 74 (2006) 041306.

[134] Y. L. Soo, G. Kioseoglou, S. Kim, S. Huang, Y. H. Kao, S. Kuwabara, S. Owa, T. Kondo, and H. Munekata, Applied Physics Letters 79 (2001) 3926.

[135] S. Kuroda, E. Bellet-Amalric, X. Biquard, J. Cibert, R. Giraud, S. Marcet, and H. Mariette, Physica Status Solidi B-Basic Research 240 (2003) 443.

[136] H. Nakayama, H. Mashita, E. Kulatov, R. Funahashi, and H. Ohta, Journal of Magnetism and Magnetic Materials 258-259 (2003) 323.

[137] M. J. Reed, F. E. Arkun, E. A. Berkman, N. A. Elmasry, J. Zavada, M. O. Luen, M. L. Reed, and S. M. Bedair, Applied Physics Letters 86 (2005) 102504.

[138] S. Heikman, S. Keller, S. P. DenBaars, and U. K. Mishra, Applied Physics Letters 81 (2002) 439.

[139] R. P. Vaudo, X. P. Xu, A. Salant, J. Malcarne, and G. R. Brandes, Wiley-V C H Verlag Gmbh, 2003, p. 18.

[140] K. Sato and H. Katayama-Yoshida, Semiconductor Science & Technology 17 (2002) 367.

[141] N. Theodoropoulou, A. F. Hebard, S. N. G. Chu, M. E. Overberg, C. R. Abernathy, S. J. Pearton, R. G. Wilson, and J. M. Zavada, Applied Physics Letters 79 (2001) 3452.

[142] Y. Shon, Y. H. Kwon, Y. S. Park, S. U. Yuldashev, S. J. Lee, C. S. Park, K. J. Chung, S. J. Yoon, H. J. Kim, W. C. Lee, D. J. Fu, T. W. Kang, X. J. Fan, Y. J. Park, and H. T. Oh, Journal of Applied Physics 95 (2004) 761.

[143] Y. Shon, Y. S. Park, S. Lee, H. C. Jeon, Y. H. Kwon, T. W. Kang, J. S. Min, E. K. Kim, C. K. Kim, and C. S. Yoon, 2007, p. 78.

[144] H. Akinaga, S. Nemeth, J. De Boeck, L. Nistor, H. Bender, G. Borghs, H. Ofuchi, and M. Oshima, Applied Physics Letters 77 (2000) 4377.

[145] H. Ofuchi, M. Oshima, M. Tabuchi, Y. Takeda, H. Akinaga, S. Nemeth, J. De Boeck, and G. Borghs, Applied Physics Letters 78 (2001) 2470.

[146] S. Kuwabara, K. Ishii, S. Haneda, T. Kondo, and H. Munekata, Physica E: Low-dimensional Systems and Nanostructures 10 (2001) 233.

[147] J. Gosk, M. Zajac, M. Byszewski, M. Kaminska, J. Szczytko, A. Twardowski, B. Strojek, and S. Podsiadlo, Journal of Superconductivity 16 (2003) 79.

[148] H. Przybylinska, A. Bonanni, A. Wolos, M. Kiecana, M. Sawicki, T. Dietl, H. Malissa, C. Simbrunner, M. Wegscheider, and H. Sitter, Materials Science and Engineering: B 126 (2006) 222.

[149] A. Bonanni, M. Kiecana, C. Simbrunner, T. Li, M. Sawicki, M. Wegscheider, M. Quast, H. Przybylinska, A. Navarro-Quezada, R. Jakiela, A. Wolos, W. Jantsch, and T. Dietl, Physical Review B (Condensed Matter and Materials Physics) 75 (2007) 125210.

[150] S. Shanthi, M. Hashimoto, Y. K. Zhou, S. Kimura, M. S. Kim, S. Emura, N. Hasuike, H. Harima, S. Hasegawa, M. Ishimaru, Y. Hirotsu, and H. Asahi, Journal of Applied Physics 98 (2005) 013526.

[151] H. Harima, Journal of Physics: Condensed Matter 16 (2004) S5653–S5660.

[152] W. Limmer, W. Ritter, R. Sauer, B. Mensching, C. Liu, and R. Rauschenbach, Applied Physics Letters 72 (1998) 2589.

[153] M. A. Reshchikov and H. Morkoc, Physica B-Condensed Matter 376 (2006) 428.

[154] A. Y. Polyakov, A. V. Govorkov, N. B. Smirnov, N. Y. Pashkova, G. T. Thaler, M. E. Overberg, R. Frazier, C. R. Abernathy, S. J. Pearton, J. Kim, and F. Ren, Journal of Applied Physics 92 (2002) 4989.

[155] J. M. Baik, J.-L. Lee, Y. Shon, and T. W. Kang, Journal of Applied Physics 93 (2003) 9024.

[156] O. Gelhausen, E. Malguth, M. R. Phillips, E. M. Goldys, M. Strassburg, A. Hoffmann, T. Graf, M. Gjukic, and M. Stutzmann, Applied Physics Letters 84 (2004) 4514.

[157] M. H. Kane, M. Strassburg, W. E. Fenwick, A. Asghar, J. Senawiratne, D. Azamat, Z. Hu, E. Malguth, S. Graham, U. Perera, W. Gehlhoff, A. Hoffmann, N. Dietz, C. J. Summers, and I. T. Ferguson, physica status solidi (c) 3 (2006) 2237.

[158] S. Marcet, D. Ferrand, S. Kuroda, E. Gheeraert, R. M. Galera, J. Cibert, and H. Mariette, Materials Science and Engineering: B 126 (2006) 240.

[159] A. Y. Polyakov, N. B. Smirnov, A. V. Govorkov, G. T. Thaler, R. M. Frazier, C. R. Abernathy, and S. J. Pearton, Journal of Vacuum Science & Technology B 23 (2005) 1.

[160] B. K. Rao and P. Jena, Physical Review Letters 89 (2002) 185504.

[161] K. H. Kim, K. J. Lee, D. J. Kim, C. S. Kim, H. C. Lee, C. G. Kim, S. H. Yoo, H. J. Kim, and Y. E. Ihm, Journal of Applied Physics 93 (2003) 6793.

[162] E. Kartheuser, S. Rodriguez, and M. Villeret, Physical Review B 48 (1993) 14127.

[163] X. Y. Cui, J. E. Medvedeva, B. Delley, A. J. Freeman, N. Newman, and C. Stampfl, Physical Review Letters 95 (2005)

[164] Q. Wang, Q. Sun, B. K. Rao, P. Jena, and Y. Kawazoe, Journal of Chemical Physics 119 (2003) 7124.

[165] S. Tanaka, M. Takeuchi, and Y. Aoyagi, Japanese Journal of Applied Physics Part 2-Letters 39 (2000) L831.

[166] T. Dietl, Nature Materials 9 (2006) 673.

[167] T. Dietl, Physical Review B (Condensed Matter and Materials Physics) 77 (2008) 085208.

[168] A. Y. Polyakov, N. B. Smirnov, A. V. Govorkov, J. Kim, F. Ren, M. E. Overberg, G. Thaler, C. R. Abernathy, S. J. Pearton, C.-M. Lee, J.-I. Chyi, R. G. Wilson, and J. M. Zavada, Solid State Electronics 47 (2003) 963.

[169] G. T. Thaler, R. M. Frazier, J. Stapleton, C. R. Abernathy, S. J. Pearton, J. Kelly, R. Rairigh, A. F. Hebard, and J. M. Zavada, Electrochemical and Solid-State Letters 7 (2004) G34.

[170] A. Y. Polyakov, N. B. Smirnov, A. V. Govorkov, K. Jihyun, F. Ren, G. T. Thaler, M. E. Overberg, R. Frazier, C. R. Abernathy, S. J. Pearton, C. M. Lee, J. I. Chyi, R. G. Wilson, and J. M. Zavada, Solid-State Electronics 47 (2003) 981.

[171] I. A. Buyanova, M. Izadifard, W. M. Chen, J. Kim, F. Ren, G. Thaler, C. R. Abernathy, S. J. Pearton, C. C. Pan, G. T. Chen, J. I. Chyi, and J. M. Zavada, Applied Physics Letters 84 (2004) 2599.

[172] M. Julier, A. Vinattieri, M. Colocci, P. Lefebvre, B. Gil, D. Scalbert, C. A. Tran, R. F. K. Jr, and J. P. Lascaray, physica status solidi (b) 216 (1999) 341.

[173] S. Nagahara, M. Arita, and Y. Arakawa, Applied Physics Letters 86 (2005) 242103.

[174] A. J. Steckl, J. C. Heikenfeld, D. S. Lee, M. J. Garter, C. C. Baker, Y. Q. Wang, and R. Jones, IEEE Journal of Selected Topics in Quantum Electronics 8 (2002) 749.

[175] A. J. Steckl, J. Heikenfeld, D. S. Lee, and M. Garter, Materials Science and Engineering B 81 (2001) 97.

[176] A. J. Kenyon, Progress in Quantum Electronics 26 (2002) 225.

[177] R. Birkhahn, R. Hudgins, D. Lee, A. J. Steckl, R. J. Molnar, A. Saleh, and J. M. Zavada, Vol. 17, AVS, 1999, p. 1195.

[178] N. Teraguchi, A. Suzuki, Y. Nanishi, Y. K. Zhou, M. Hashimoto, and H. Asahi, Solid State Communications 122 (2002) 651.

[179] D. X. Li, Y. Haga, H. Shida, T. Suzuki, Y. S. Kwon, and G. Kido, Journal of Physics-Condensed Matter 9 (1997) 10777.

[180] P. Heller, Reports on Progress in Physics 30 (1967) 731.

[181] F. Leuenberger, A. Parge, W. Felsch, K. Fauth, and M. Hessler, Physical Review B 72 (2005).

[182] Z. Lipinska, M. Pawlowski, H. Zolnierowicz, A. Wysmolek, M. Palczewska, M. Kaminska, A. Twardowski, M. Bockowski, and I. Grzegory, 2006, p. 243.

[183] J. K. Hite, R. M. Frazier, R. P. Davies, T. Thaler, C. R. Abernathy, S. J. Pearton, J. M. Zavada, E. Brown, and U. Hommerich, Journal of Electronic Materials 36 (2007) 391.

[184] Y. K. Zhou, S. W. Choi, S. Emura, S. Hasegawa, and H. Asahi, Applied Physics Letters 92 (2008)

[185] S. Dhar, O. Brandt, M. Ramsteiner, V. F. Sapega, and K. H. Ploog, Physical Review Letters 94 (2005) 4.

[186] G. M. Dalpian and S. H. Wei, Physica Status Solidi B-Basic Solid State Physics 243 (2006) 2170.

[187] H. Asahi, Y. K. Zhou, M. Hashimoto, M. S. Kim, X. J. Li, S. Emura, and S. Hasegawa, 2004, p. S5555.

[188] S. Dhar, O. Brandt, A. Trampert, L. Daweritz, K. J. Friedland, K. H. Ploog, J. Keller, B. Beschoten, and G. Guntherodt, Applied Physics Letters 82 (2003) 2077.

[189] Y. K. Zhou, S. W. Choi, S. Kimura, S. Emura, S. Hasegawa, and H. Asahi, 2007, p. 429.

[190] J. Hejtmanek, K. Knizek, M. Marysko, Z. Jirak, D. Sedmidubsky, Z. Sofer, V. Perina, H. Hardtdegen, and C. Buchal, Journal of Applied Physics 103 (2008)

[191] Y. Gohda and A. Oshiyama, Physical Review B 78 (2008)

[192] L. Liu, P. Y. Yu, Z. Ma, and S. S. Mao, Phys Rev Lett 100 (2008) 127203.

[193] P. Larson and S. Satpathy, Physical Review B 76 (2007) 8.

[194] J. W. Gerlach, J. Mennig, and B. Rauschenbach, Applied Physics Letters 90 (2007) 61919.

[195] U. Haboeck, H. Siegle, A. Hoffmann, and C. Thomsen, Physica Status Solidi C 0 (2003) 1710.

[196] T. Kozawa, T. Kachi, H. Kano, H. Nagase, N. Koide, and K. Manabe, Journal of Applied Physics 77 (1995) 4389.

[197] A. L. Rosa, J. Neugebauer, J. E. Northrup, C.-D. Lee, and R. M. Feenstra, Applied Physics Letters 80 (2002) 2008.

[198] H. G. Grimmeiss and B. Monemar, Journal of Applied Physics 41 (1970) 4054.

[199] G. H. Dieke and L. Leopold, Journal of the Optical Society of America 47 (1957) 944.

[200] M. A. Reshchikov and H. Morkoc, Journal of Applied Physics 97 (2005) 95.

[201] R. T. Wegh, A. Meijerink, R. J. Lamminmaki, and J. Holsa, Elsevier Science Bv, 2000, p. 1002.

[202] B. Witek, A. Wysmolek, M. Kaminska, A. Twardowski, M. Potemski, M. Bockowski, and I. Grzegory, Acta Physica Polonica A 114 (2008) 1425.

[203] N. A. Kulagin, Optics and Spectroscopy 101 (2006) 402.

[204] V. N. Snytnikov, V. O. Stoyanovskii, V. A. Ushakov, and V. N. Parmon, Kinetics and Catalysis 46 (2005) 260.

[205] S. W. Choi, S. Emura, S. Kimura, M. S. Kim, Y. K. Zhou, N. Teraguchi, A. Suzuki, A. Yanase, and H. Asahi, 2006, p. 717.

[206] M. Hashimoto, S. Emura, R. Asano, H. Tanaka, N. Teraguchi, A. Suzuki, Y. Nanishi, T. Honma, N. Umesaki, and H. Asahi, physica status solidi (c) 0 (2003) 2650.

[207] W. M. Temmerman and P. A. Sterne, Journal of Physics-Condensed Matter 2 (1990) 5529.

[208] M. H. Kane, M. Strassburg, A. Asghar, W. E. Fenwick, J. Senawiratne, Q. Song, C. J. Summers, Z. J. Zhang, N. Dietz, and I. T. Ferguson, Materials Science and Engineering B-Solid State Materials for Advanced Technology 126 (2006) 230.

[209] S. Dhar, O. Brandt, and K. H. Ploog, in Compound Semiconductors 2004, Proceedings, Vol. 184, 2005, p. 175.

[210] M. Hong, J. Kwo, A. R. Kortan, J. P. Mannaerts, and A. M. Sergent, Science 283 (1999) 1897.

[211] M. Leskela and M. Ritala, Academic Press Inc Elsevier Science, 2003, p. 170.

[212] M. H. Ham, S. Yoon, Y. Park, L. F. Bian, M. Ramsteiner, and J. M. Myoung, Journal of Physics-Condensed Matter 18 (2006) 7703.

[213] Introduction to Nitride Semiconductor Blue Laser and Light Emitting Diodes, CRC Press, 2000.

[214] T. Steiner, ed., Semiconductor Nanostructures for Optoelectronic Applications, Artech House, 2004

[215] D. L. Huffaker, G. Park, Z. Zou, O. B. Shchekin, and D. G. Deppe, Applied Physics Letters 73 (1998) 2564.

[216] S. J. Xu, S. J. Chua, T. Mei, X. C. Wang, X. H. Zhang, G. Karunasiri, W. J. Fan, C. H. Wang, J. Jiang, S. Wang, and X. G. Xie, Applied Physics Letters 73 (1998) 3153.

[217] S. Gupta, H. Kang, M. Strassburg, A. Asghar, M. Kane, W. E. Fenwick, N. Dietz, and I. T. Ferguson, Journal of Crystal Growth 287 (2006) 596.

[218] D. J. Eaglesham and M. Cerullo, Physical Review Letters 64 (1990) 1943.

[219] I. Daruka and A. L. Barabasi, Physical Review Letters 79 (1997) 3708.

[220] F. Widmann, B. Daudin, G. Feuillet, Y. Samson, J. L. Rouviere, and N. T. Pelekanos, J. Appl. Phys. 83 (1998) 7618.

[221] B. Daudin, Phys. Rev. B 56 (1997) 7069.

[222] N. Gogneau, D. Jalabert, E. Monroy, T. Shibata, S. Tanaka, and B. Daudin, J. Appl. Phys. 94 (2003) 2254.

[223] K. Hoshino, S. Kako, and Y. Arakawa, Physica Status Solidi B-Basic Research 240 (2003) 322.

[224] F. Widmann, J. Simon, N. T. Pelekanos, B. Daudin, G. Feuillet, J. L. Rouviere, and G. Fishman, Microelectronics Journal 30 (1999) 353.

[225] S. Kako, M. Miyamura, K. Tachibana, K. Hoshino, and Y. Arakawa, Applied Physics Letters 83 (2003) 984.

[226] M. Miyamura, K. Tachibana, and Y. Arakawa, Appl. Phys. Lett. 80 (2002) 3937.

[227] Y. Ohba, H. Yoshida, and R. Sato, Japanese Journal of Applied Physics Part 2-Letters 36 (1997) L1565.

[228] C. H. Chen, H. Liu, D. Steigerwald, W. Imler, C. P. Kuo, M. G. Craford, M. Ludowise, S. Lester, and J. Amano, Journal of Electronic Materials 25 (1996) 1004.

[229] Q. Paduano and D. Weyburne, Japanese Journal of Applied Physics Part 1-Regular Papers Short Notes & Review Papers 42 (2003) 1590.

[230] S. Gupta, H. Kang, M. Strassburg, A. Asghar, J. Senawiratne, N. Dietz , and I. T. Ferguson, Mat. Res. Soc. Symp. Proc. 901E (2006) 0901.

[231] G. S. Solomon, J. A. Trezza, and J. S. Harris, Appl. Phys. Lett. 66 (1995) 3161.

[232] P. Kratzert, M. Rabe, and F. Henneberger, Phys. Stat. sol.(b) 224 (2001) 179.

[233] C. E. Tanner, T. Williams, S. Schwall, S. T. Ruggiero, P. Shaklee, S. Potashnik, J. M. Shaw, and C. M. Falco, Optics Communications 259 (2006) 704.